

© 2009 Matthew Walter Kunz

THE NONISOTHERMAL STAGE OF MAGNETIC STAR FORMATION

BY

MATTHEW WALTER KUNZ

B.A., University of Virginia, 2003

M.S., University of Illinois at Urbana-Champaign, 2004

DISSERTATION

Submitted in partial fulfillment of the requirements
for the degree of Doctor of Philosophy in Physics
in the Graduate College of the
University of Illinois at Urbana-Champaign, 2009

Urbana, Illinois

Doctoral Committee:

Professor John D. Stack, Chair

Professor Telemachos Ch. Mouschovias, Director of Research

Professor James N. Eckstein

Assistant Professor Leslie W. Looney

Assistant Professor Paul M. Ricker

Abstract

We follow the formation and subsequent evolution of fragments (or cores) in magnetically-supported, self-gravitating molecular clouds in two spatial dimensions. The six-fluid (neutrals, electrons, molecular and atomic ions, positively-charged, negatively-charged, and neutral grains) physical system is governed by the radiative, nonideal magnetohydrodynamic (RMHD) equations. The magnetic flux is not assumed to be frozen in any of the charged species. Its evolution is determined by a newly-derived generalized Ohm's law, which accounts for the contributions of both elastic and inelastic collisions to ambipolar diffusion and Ohmic dissipation. The species abundances are calculated using an extensive chemical-equilibrium network. The thermal evolution of the protostellar core and its affect on the dynamics are followed by employing the grey flux-limited diffusion approximation. Realistic temperature-dependent grain opacities are used that account for a variety of grain compositions. We have augmented the publicly-available Zeus-MP code to take into consideration all these effects and have modified several of its algorithms to improve convergence, accuracy and efficiency. We present results of magnetic star formation simulations that accurately track the evolution of a protostellar fragment over eleven orders of magnitude in density, from the early ambipolar-diffusion-initiated fragmentation phase, the magnetically-supercritical dynamical collapse phase, and the magnetic decoupling stage, all the way to the nonisothermal phase, including the formation and evolution of a hydrostatic core of radius ≈ 2 AU, density $\approx 10^{14}$ cm $^{-3}$, temperature ≈ 300 K, magnetic field strength ≈ 0.2 G, luminosity $\sim 10^{-3}$ L $_{\odot}$, and mass $\sim 10^{-2}$ M $_{\odot}$.

*Lo duca e io per quel cammino ascoso
intrammo a ritornar nel chiaro mondo;
e senza cura aver d'alcun riposo,
salimmo sù, el primo e io secondo,
tanto ch'i' vidi de le cose belle
che porta 'l ciel, per un pertugio tondo.
E quindi uscimmo a riveder le stelle.*

Into that hidden passage my guide and I
entered, to find again the world of light,
and, without thinking of a moment's rest,
we climbed up, he first and I behind him,
far enough to see, through a round opening,
a few of those fair things the heavens bear.
Then we came forth, to see again the stars.

Dante, *Inferno*, Canto XXXIV

Acknowledgements

It is my pleasure to thank . . .

- ... Telemachos Mouschovias, for his relentless passion, cogent idealism, infinite patience, immutable trust, and steadfast allegiance to his students, both past and present. In *Doctor Faustus*, Thomas Mann described a teacher as “the personification of the apprentice’s own conscience, confirming his doubts, explaining his discontents, prodding his own urge to improve.” Thank you for being all those things to me;
- ... Kostas Tassis and Vaso Pavlidou, for their scientific camaraderie and exceptional friendship. The quality of this Thesis would have suffered greatly if it were not for your generosity, support, and counsel;
- ... Steve Balbus, for preparing me well for research in astrophysical fluid dynamics, selflessly offering guidance in times of crisis, and being a strong advocate;
- ... Duncan Christie, for being a great sounding-board, carefully reading a draft of this Thesis and providing useful comments, and bringing a much-needed *esprit de corps* to our group;
- ... Steve Desch, for leaving behind a transparent Thesis, which made my work much easier;
- ... Leslie Looney, for ennobling my scientific opinions by virtue of his trust and confidence in me, and for serving on my committee;
- ... Paul Ricker, for candid postdoctoral advice and for serving on my committee;
- ... Jim Eckstein, for voluntarily taking a keen interest in my work, being a rewarding Professor to TA for, and serving on my committee;
- ... John Stack, for assigning me great teaching assistantships, granting me opportune summer research assistantships, and serving as the chair of my committee;
- ... Alex Schekochihin and Steve Cowley, for believing in my abilities as a scientist, offering me a job, and allowing my wife and I to start a new adventure abroad;

- ... Fabian Heitsch, einer der offensten, aufrichtigsten, und gerechtesten Wissenschaftler, die ich jemals getroffen habe;
- ... John Hayes, for his assistance with the Zeus-MP code;
- ... Dmitry Semenov and Thomas Henning, for generously providing the dust opacities used in this Thesis;
- ... Michael Campbell and the folks at the Turing cluster (maintained and operated by the Computational Science and Engineering Program at UIUC), by whom the costly numerical simulations for this Thesis were made possible;
- ... the Department of Physics, for financial support through numerous teaching and summer research assistantships, a travel grant to attend a conference on cosmic magnetism, and a Graduate Assistance in Areas of National Need (GAANN) fellowship during my first year of graduate school;
- ... Dan Stark, whose friendship and support, both scientific and personal, has removed an element of anxiety from my upcoming move to England;
- ... Tom Mulherin, for being a true friend and confidante and for providing a welcome distraction in music, literature, theology, and philosophy;
- ... Andrew Robertson, for his genuine friendship, good will, and emotional support;
- ... Bryan Fischer, for his loyalty and for never holding my long absences against me;
- ... Yannis Tsekouras & Jill Burlingame and Chris Fields & Natasha Capell, for being the friends my wife and I needed during our Champaign-Urbana years;
- ... Woojin Kwon and Hsin-Fang Chiang, for being great observational counterparts and taking an interest in my work;
- ... Patrick and Gracie, our cats, for keeping me company during the day and teaching me the virtues of relaxation;
- ... my parents-in-law, for welcoming me into their family and treating me like their son;
- ... my parents, for offering me choices, supporting my decisions, and loving me regardless of the outcomes;
- ... Jessica, my wife, my companion, my editor-in-chief, my best friend, and my everlasting love, for encouraging me in everything I do, caring for me when it's most inconvenient, and faithfully and unequivocally standing behind all my decisions, no matter what they may bring;
- ... God, for all of the above.

Table of Contents

List of Tables	viii
List of Figures	ix
Chapter 1 Introduction	1
1.1 Observed Properties of Molecular Clouds and Protostellar Cores	1
1.2 Self-Gravity	5
1.3 Magnetic Fields	8
1.4 Rotation	12
1.5 Grain Effects	14
1.6 MHD Waves and/or Turbulence	15
1.7 Radiative Transfer	21
1.8 Summary and Outline	23
Chapter 2 Formulation of the Problem	26
2.1 Outline	26
2.2 Basic Properties of the Model Cloud	27
2.3 The Six-Fluid RMHD Description of Magnetic Star Formation	29
2.4 The Chemical Model	35
2.4.1 Ionization Rate	35
2.4.2 Grain Size Distribution	38
2.4.3 Chemical Network	40
2.5 Magnetic Flux Loss and Electrical Resistivity	43
2.5.1 Resistivity of a Magnetic Gas	43
2.5.2 Generalized Ohm's Law	46
2.5.3 Attachment of Species to Magnetic Field Lines	49
2.5.4 Grain Continuity Equation	51
2.5.5 Joule Heating	52
2.6 Radiative Transfer	53
2.6.1 The Flux-Limited Diffusion Approximation	53
2.6.2 Dust Opacities	55
2.7 Summary	55

Chapter 3	Method of Solution	59
3.1	Introduction	59
3.2	Incorporating Nonideal MHD Into Zeus-MP	62
3.2.1	Ideal Magnetohydrodynamics in Zeus-MP	62
3.2.2	Nonideal Magnetohydrodynamics in Zeus-MP	70
3.3	Chemical Abundances and Magnetic Resistivity	74
3.4	Adaptive Grid	76
3.5	Radiative Transfer Routine	77
3.6	Gravitational Potential Solver	77
3.7	Initial and Boundary Conditions	79
3.8	Summary	82
Chapter 4	Results	83
4.1	The Physical Model	83
4.2	Overall Evolution	83
4.3	Evolution of Central Quantities	98
4.4	Evolution of Spatial Structure of the Model Cloud	116
4.4.1	Density and Temperature	119
4.4.2	Magnetic Field and Alfvén Speed	119
4.4.3	Forces	131
4.4.4	Velocities	135
4.4.5	Contribution of Electric Current Density by Different Species	141
4.4.6	Ambipolar Diffusion and Ohmic Dissipation	147
4.4.7	Mass, Magnetic Flux, and Mass Infall Rate	147
4.4.8	Radiation Flux and Luminosity	154
Chapter 5	Parameter Study	157
5.1	Introduction	157
5.2	^{26}Al as an Alternative Radionuclide	158
Chapter 6	Summary	167
Appendix A	Rate Coefficients	174
Appendix B	Generalized Ohm’s Law	176
B.1	Derivation	176
B.2	Modification due to a Grain Size Distribution	180
Appendix C	Derivation of Species Velocities	182
Appendix D	Definitions	184
References		187
Vita		200

List of Tables

1.1	Summary of best-fit mean axis ratios in star-forming objects	3
2.1	Chemical reaction network used in the calculation of the abundances of charged species.	27

List of Figures

1.1	Inferred magnetic field vectors from dust polarimetry in a variety of sources	10
1.2	Linewidth–size relation for 31 observed objects	18
1.3	Linewidth–size–magnetic-field relation for 31 observed objects	19
2.1	Ratio of specific heats for H ₂ vs temperature	36
2.2	Planck mean absorption coefficients for various grain sizes vs temperature	56
2.3	Rosseland mean extinction coefficients for various grain sizes vs temperature	57
3.1	Modified Zeus-MP program control	61
3.2	Centering of magnetic field variables in Zeus-MP	64
3.3	Space-time diagram of Alfvén wave characteristics	68
4.1	Central number density of neutrals vs time	84
4.2	Central mass-to-flux ratio vs central number density of neutrals	85
4.3	Spatial structure of the entire model cloud when the central number density of neutrals is $3 \times 10^3 \text{ cm}^{-3}$	88
4.4	Spatial structure of the entire model cloud when the central number density of neutrals is $3 \times 10^4 \text{ cm}^{-3}$	89
4.5	Spatial structure of the entire model cloud when the central number density of neutrals is $3 \times 10^5 \text{ cm}^{-3}$	90
4.6	Spatial structure of the innermost 10% of the model cloud when the central number density of neutrals is $3 \times 10^6 \text{ cm}^{-3}$	92
4.7	Spatial structure of the innermost 1% of the model cloud when the central number density of neutrals is $3 \times 10^9 \text{ cm}^{-3}$	93
4.8	Spatial structure of the innermost 0.01% of the model cloud when the central number density of neutrals is $3 \times 10^{11} \text{ cm}^{-3}$	94
4.9	Spatial structure of the innermost 0.01% of the model cloud when the central number density of neutrals is $3 \times 10^{12} \text{ cm}^{-3}$	95
4.10	Spatial structure of the innermost 0.01% of the model cloud when the central number density of neutrals is $3 \times 10^{13} \text{ cm}^{-3}$	96
4.11	Spatial structure of the innermost 0.01% of the model cloud when the central number density of neutrals is 10^{14} cm^{-3}	97
4.12	Thermal structure of the innermost 0.01% of the model cloud when the central number density of neutrals is $3 \times 10^{11} \text{ cm}^{-3}$	99

4.13	Thermal structure of the innermost 0.01% of the model cloud when the central number density of neutrals is $3 \times 10^{12} \text{ cm}^{-3}$	100
4.14	Thermal structure of the innermost 0.01% of the model cloud when the central number density of neutrals is $3 \times 10^{13} \text{ cm}^{-3}$	101
4.15	Thermal structure of the innermost 0.01% of the model cloud when the central number density of neutrals is 10^{14} cm^{-3}	102
4.16	Central gas and radiation temperatures vs central number density of neutrals	103
4.17	Effective adiabatic index vs central number density of neutrals	104
4.18	Exponent in the central column-density–number-density power-law relation	106
4.19	Central magnetic field strength vs central number density of neutrals	108
4.20	Exponent in the central magnetic-field-strength–density power-law relation	109
4.21	Central ionization rate vs central number density of neutrals	110
4.22	Central species abundances vs central number density of neutrals	111
4.23	Central magnetic resistivities vs central number density of neutrals	114
4.24	Central magnetic conductivities vs central number density of neutrals . . .	115
4.25	Fraction of central parallel magnetic conductivity carried by each species vs central number density of neutrals	117
4.26	Fraction of central perpendicular magnetic conductivity carried by each species vs central number density of neutrals	118
4.27	Neutral density along midplane and axis	120
4.28	Radial derivative along midplane of neutral density	121
4.29	Gas temperature along midplane and axis	122
4.30	Radial derivative along midplane of gas temperature	123
4.31	Magnetic field strength along midplane and axis	124
4.32	Radial derivative along midplane of magnetic field strength	125
4.33	Maximum strength of the radial component of the magnetic field	127
4.34	Ratio of Alfvén and local isothermal sound speeds along midplane and axis	128
4.35	Mass-to-flux ratio vs radius	130
4.36	Ratio of thermal-pressure and gravitational forces along midplane	132
4.37	Ratio of magnetic and gravitational forces along midplane	133
4.38	Ratio of thermal-pressure and magnetic forces along midplane	134
4.39	Neutral velocity along midplane and axis	136
4.40	Magnetic field-line velocity along midplane	138
4.41	Species velocities and direct attachment parameters along midplane	139
4.42	Total electric current density along midplane	142
4.43	Positively-charged grain electric current density along midplane	143
4.44	Negatively-charged grain electric current density along midplane	144
4.45	Ion electric current density along midplane	145
4.46	Electron electric current density along midplane	146
4.47	Ratio of Ohmic and ambipolar resistivities along midplane	148
4.48	Cumulative mass vs radius	149
4.49	Cumulative magnetic flux vs radius	151
4.50	Mass infall rate vs radius	152
4.51	Normalized mass infall rate vs radius	153
4.52	Radiation flux along midplane and axis	155

5.1	²⁶ Al: Central ionization rate vs central number density of neutrals	159
5.2	²⁶ Al: Central species abundances vs central number density of neutrals . . .	160
5.3	²⁶ Al: Central magnetic resistivities vs central number density of neutrals . .	162
5.4	²⁶ Al: Central magnetic conductivities vs central number density of neutrals	163
5.5	²⁶ Al: Fraction of central parallel magnetic conductivity carried by each species vs central number density of neutrals	164
5.6	²⁶ Al: Fraction of central perpendicular magnetic conductivity carried by each species vs central number density of neutrals	165
5.7	²⁶ Al: Ratio of Ohmic and ambipolar resistivities along midplane	166

Chapter 1

Introduction

1.1 Observed Properties of Molecular Clouds and Protostellar Cores

Stars form in fragments within interstellar molecular clouds, which have sizes ranging from 1 to 5 pc, masses from a few tens to $10^5 M_{\odot}$, mean densities $\sim 10^3 \text{ cm}^{-3}$, and temperatures $\simeq 10 \text{ K}$ (Myers 1985; Heiles 1987). Their spectral lines have Doppler-broadened linewidths that suggest supersonic (but subAlfvénic) internal motions. In the deep interiors of such clouds, high-energy cosmic rays ($> 100 \text{ MeV}$) maintain a degree of ionization $x_i \lesssim 10^{-7}$, whereas ultraviolet (UV) ionization is responsible for a much greater degree of ionization $x_i \gtrsim 10^{-5}$ in the outer envelopes (Caselli et al. 1998; Williams et al. 1998; Bergin et al. 1999). Studies of giant molecular clouds (GMCs) indicate that only a small fraction of their mass, $\lesssim 10\%$, is actually converted into stars, with star-formation rates inferred to be in the range $\sim 10 - 100 M_{\odot} \text{ Myr}^{-1}$ (e.g., Lada 1992; Evans et al. 2009).

Low-mass molecular cloud fragments, often referred to by observers as “starless cores” or “prestellar cores”,¹ are prestellar condensations characterized by relatively small radii ($\approx 0.05 - 0.2 \text{ pc}$) and masses ($\approx 0.3 - 10 M_{\odot}$). Such fragments are denser ($\approx 10^4 - 10^5 \text{ cm}^{-3}$) than their surrounding gas, but their similar temperatures ($\simeq 10 \text{ K}$) make them difficult to

¹The recent review by Ward-Thompson et al. (2007) suggests the following classification scheme: a “dense core” is defined as “any region in a molecular cloud that is observed to be significantly over-dense relative to its surroundings”; a “starless core” is defined as “any dense core that does not contain any evidence that it harbours a protostar, young stellar object or young star”; and “prestellar cores” are defined as a “subset of starless cores which are gravitationally bound and hence are expected to participate in the star formation process.”

distinguish from their backgrounds. They are typically observed by looking for emission from molecules that trace higher density gas, such as CS, H₂CO, NH₃, N₂H⁺, H¹³CO⁺, DCO⁺, and C¹⁸O. More recently, the advent of large millimeter and submillimeter radiotelescopes has made possible the identification of starless cores through extensive dust continuum surveys at 450 μ m and 850 μ m (using the Submillimeter Common-User Bolometer Array [SCUBA] on the James Clerk Maxwell Telescope), 1.3 mm (using the Max Planck Institut für Radioastronomie Bolometer Arrays on the Institut für Radioastronomie im Millimeterbereich 30 meter telescope), and 3 mm (using the Owens Valley Radio Observatory) — e.g., see reviews by Andre et al. (2000) and Ward-Thompson et al. (2007).

An important piece of information that may be extracted from such observational surveys is the distribution of core shapes. While observations of the shapes of molecular cloud cores can serve as a powerful discriminator between different theories of molecular cloud fragmentation and core formation, uncovering a core’s intrinsic shape is no easy task, as it is not possible to directly deproject the shape of each observed core. Instead, statistical techniques must be used. Early efforts to derive intrinsic core shapes from observations, assuming axial symmetry, seemed to favor prolate cores (Myers et al. 1991; Ryden 1996). However, subsequent investigations that relaxed the axisymmetry assumption have consistently yielded triaxial, preferentially oblate core shapes (Jones et al. 2001; Jones & Basu 2002; Goodwin et al. 2002; Tassis 2007), independently of tracer, core sample, and statistical technique. (See Table 1.1 for a summary.) Coupled with the fact that prestellar cores are generally observed in states of low angular momentum (i.e., the ratios of rotational and gravitational energy in cores are observed to be typically less than a few percent; e.g., Goodman et al. 1993; Caselli et al. 2002), and therefore are not rotationally flattened, this strongly suggests that magnetic fields play a role in the fragmentation process (see below).

Another important diagnostic that may be retrieved from observational surveys of cores is their initial mass function, i.e., the number of cores per mass interval. If the core mass spectrum is written as $dN/dM \propto M^{-\alpha}$, it is generally found that, for core masses $M \gtrsim$

Table 1.1: Summary of best-fit mean axis ratios (long-to-short: ξ ; middle-to-short: ζ).

Data Set	Object Type	ξ	ζ
Onishi et al. 1996; Tachihara et al. 2000	Molecular cloud cores	0.4 ^a	0.9 ^a
Jijina et al. 1999	Molecular cloud cores	0.5 ^a	0.9 ^a
Jijina et al. 1999	Molecular cloud cores	0.4 ^b	0.8 ^b
Lee & Myers 1999	Molecular cloud cores	0.3 ^a	0.9 ^a
Clemens & Barvainis 1998	Bok globules	0.4 ^a	0.9 ^a
Bourke et al. 1995	Bok globules	0.4 ^a	0.9 ^a
Motte et al. 1998	Prestellar cores	0.4 ^a	0.9 ^a
Motte et al. 2001	Prestellar cores	0.4 ^a	0.9 ^a
Nutter & Ward-Thompson 2007	Prestellar cores	0.5 ^c	1 ^c

^aAs determined by Jones & Basu (2002) from a least-squares analysis; $\sigma_\xi = \sigma_\zeta = 0.1$.

^bAs determined by Goodwin et al. (2002) from a least-squares analysis; $\sigma_\xi = 0.2$, $\sigma_\zeta = 0.1$.

^cAs determined by Tassis (2007) from a Bayesian analysis; given axis ratios \approx the values with the maximum likelihood.

$0.5 M_\odot$, $\alpha \simeq 2 - 2.5$, with 2.35 being typical, whereas for $M \lesssim 0.5 M_\odot$, $\alpha \simeq 1.5$ (Motte et al. 1998; Testi & Sargent 1998; Johnstone et al. 2000, 2001; Motte et al. 2001; Johnstone et al. 2006; Stanke et al. 2006; Enoch et al. 2006; Nutter & Ward-Thompson 2007). Johnstone et al. (2000) caution that the flattening below $0.5 M_\odot$ in ρ Oph may be from incompleteness due to limited sensitivity around $\sim 0.4 M_\odot$, close to the turnover. Observations by Motte et al. (1998) in ρ Oph also fail to find a mass turnover down to their completeness limit of $\sim 0.1 M_\odot$. However, compilation of SCUBA data from Orion shows a mass turnover at $\sim 1 M_\odot$ (Nutter & Ward-Thompson 2007), well above their completeness limit, indicating that the turnover may not be a selection effect and that the mass at which the turnover occurs may depend on the cloud environment. The fact that the initial core mass function is very similar to the observed initial stellar mass function suggests (but does not prove) that the early fragmentation process may determine the mass spectrum of stars as well (Simpson et al. 2008).

Once a prestellar core fragments out of its natal molecular cloud, its evolution as a young stellar object (YSO) towards the main sequence proceeds through several stages: the collapse of the core, followed by protostar and disk formation; the subsequent accretion of disk material onto the forming star; and, finally, the dissipation of the disk by planet

formation, evaporation, etc. (Shu et al. 1987). These stages reveal themselves by engendering their spectral energy distributions (SEDs; i.e., $\log \lambda F_\lambda$ vs. $\log \lambda$) with observationally-distinguishable characteristics. Motivated by the realization (Lada & Wilking 1984) that observed SEDs of YSOs were falling naturally into distinct morphological classes, Lada (1987) codified an empirical class system based upon the determination of the near-/mid-infrared spectral index $\alpha_{\text{IR}} \equiv d \log \lambda F_\lambda / d \log \lambda$: for class I sources, $0 < \alpha_{\text{IR}} \lesssim 3$; for class II sources, $-2 \lesssim \alpha_{\text{IR}} \leq 0$; and for class III sources, $-3 < \alpha_{\text{IR}} \lesssim -2$.² Comparison with the predictions of contemporary star formation theory (Adams et al. 1987) allowed for the association of the different empirically-defined classes with the various theoretically-motivated evolutionary stages of a YSO. Class I sources are believed to be relatively evolved protostars with both circumstellar disks and envelopes, whereas Class II sources are believed to be pre-main-sequence stars with significant protoplanetary disks (classical T Tauri stars). Class III sources are pre-main-sequence stars that are no longer accreting significant amounts of matter and are surrounded by a debris disk (weak-lined T Tauri stars).

Submillimeter dust continuum maps of molecular clouds detected several condensations that appeared to be associated with formed, hydrostatic YSOs. These were designated “Class 0” protostars by Andre et al. (1993) and were defined by the following observational properties:

1. Indirect evidence for a central young stellar object, as indicated by, e.g., the detection of a compact centimeter radio continuum source, a collimated CO outflow, or an internal heating source;
2. Centrally peaked but extended submillimeter continuum emission tracing the presence of a spheroidal circumstellar dust envelope (as opposed to just a disk);

²Subsequent revisions have shifted the boundaries to $0 < \alpha_{\text{IR}}$ (Class I), $-1.5 < \alpha_{\text{IR}} < 0$ (Class II), and $\alpha_{\text{IR}} < -1.5$ (Class III) — see, e.g., Andre et al. (2000, § III.A) and Evans et al. (2009, § 5.1) for more on the historical development of the YSO class system.

3. High ratio of submillimeter to bolometric luminosity, suggesting that the envelope mass exceeds the central stellar mass: $L_{\text{smm}}/L_{\text{bol}} > 0.5\%$, where L_{smm} is measured longward of $350 \mu\text{m}$. In practice, this often means an SED resembling a single-temperature blackbody at $T \sim 15 - 30 \text{ K}$.

Using luminosity as a proxy for mass, the fact that most of the confirmed Class 0 objects have $L_{\text{smm}}/L_{\text{bol}} \gg 0.5\%$ indicates that they are likely to be at the beginning of the main accretion phase with the mass of the envelope much greater than the protostellar mass (i.e., $M_{\text{env}} \gg M_*$). Class 0 objects are therefore thought to be very young accreting protostars in which a hydrostatic core has formed but not yet accumulated the majority of its final mass. The boundary between Class 0 and Class I is marked by $M_{\text{env}} \approx M_*$.

This Thesis uses analytical and numerical methods to discern the evolution of a single molecular cloud fragment from mean molecular cloud densities and temperatures to densities and temperatures approaching those characteristic of a newly-formed Class 0 protostar. Using the terminology suggested by Boss & Yorke (1995), we are in effect studying the formation and evolution of a “Class –I” (pre-Class 0) protostar, i.e., the first (molecular) hydrostatic core (see § 1.7). The formulation of a theory of star formation is no easy task, however. It requires understanding of the nonlinear interactions among self-gravity, magnetic fields, rotation, chemistry (including grain effects), turbulence, and radiation, any one of which presents formidable challenges of its own.

1.2 Self-Gravity

Early efforts to develop a theory of star formation sought to quantify the obvious importance of self-gravity. It has been 107 years since Sir James Jeans first showed via a linear plane-wave analysis of an infinite uniform medium that a cloud (or rather part of a cloud) becomes unstable and collapses if it lacks sufficient thermal-pressure support to balance the force of gravity. A necessary condition for collapse of a density fluctuation is that its

wavelength be larger than the critical Jeans length,

$$\lambda_J = c_s \left(\frac{\pi}{G\rho} \right)^{1/2} \quad (1.1a)$$

$$= 0.67 \left(\frac{T}{10 \text{ K}} \right)^{1/2} \left(\frac{n}{10^3 \text{ cm}^{-3}} \right)^{-1/2} \text{ pc}, \quad (1.1b)$$

where ρ is the volume density, T the temperature, $c_s = (k_B T / \mu m_H)^{1/2}$ the isothermal sound speed, n the number density ($= \rho / \mu m_H$), and μ ($= 2.33$, accounting for the standard 20% He abundance by number) the mean mass per particle in units of the atomic hydrogen mass, m_H . Assuming that the density fluctuations have similar dimensions in all three directions, the corresponding minimum mass for gravitational instability can be estimated as

$$M_J = \rho \lambda_J^3 \quad (1.2a)$$

$$= 17.2 \left(\frac{T}{10 \text{ K}} \right)^{3/2} \left(\frac{n}{10^3 \text{ cm}^{-3}} \right)^{-1/2} M_\odot. \quad (1.2b)$$

This critical mass is referred to as the Jeans mass.³

The Jeans analysis is rather specious, though. The infinite, uniform medium on top of which the linear analysis was performed is not in an equilibrium state, and its inevitable collapse, which may overwhelm the collapse of individual Jeans-unstable density fluctuations, had been conveniently ignored (the so-called ‘‘Jeans swindle’’; e.g., see Binney & Tremaine 2008). In response, more rigorous (nonlinear) stability analyses have been performed for a wide variety of equilibrium configurations. One particularly notable example, the stability of an isothermal, nonrotating, nonmagnetic spherical cloud, was first examined by Bonnor (1956) and Ebert (1957). They calculated the critical mass, M_{BE} , required for

³Some authors (e.g., Binney & Tremaine 2008) use a spherical definition of the Jeans mass, which gives a critical mass a factor $\pi/6$ smaller.

self-gravity to balance thermal-pressure forces:

$$M_{\text{BE}} = 1.18 \frac{c_s^4}{(G^3 P_{\text{ext}})^{1/2}} \quad (1.3a)$$

$$= 5.72 \left(\frac{T}{10 \text{ K}} \right)^{3/2} \left(\frac{n}{10^3 \text{ cm}^{-3}} \right)^{-1/2} M_{\odot}, \quad (1.3b)$$

where P_{ext} is the external pressure. Given the relative rigor involved in the Bonnor-Ebert sphere calculation, it is rather surprising that the mathematically-inconsistent Jeans analysis overestimated the critical mass by only a factor $\simeq 3$. Regardless, the critical masses obtained are orders of magnitude smaller than the observed masses of typical molecular clouds. Nevertheless, molecular clouds as a whole are not collapsing (e.g., see review by Zuckerman & Palmer 1974).

The evolution of an isothermal, nonrotating, nonmagnetic spherical cloud began to receive a great deal of attention in the 1970's through both numerical and analytical approaches. The debate at the time centered around what may be best considered as the initial conditions at the onset of gravitational collapse. The case advocated by Larson (1969) and Penston (1969) and extended by Hunter (1977) begins with a static cloud of constant density and follows the formation of a r^{-2} density profile. At the time when the protostar forms (i.e., when the central density reaches infinity in this idealized calculation), the collapse is highly dynamic, with an infall velocity of $3.3c_s$. Consequently, the mass infall rate onto the star is large, rapidly increasing from $\dot{M}_{\text{in}} = 29c_s^3/G$ at the moment of protostar formation to $\dot{M}_{\text{in}} = 47c_s^3/G$.

In an opposing point-of-view advocated by Shu (1977), the evolution to the r^{-2} density profile is thought to occur quasi-statically (i.e., with negligible velocity). Once an unstable hydrostatic equilibrium forms (the ‘‘singular isothermal sphere’’), the flow evolves in a self-similar fashion, collapsing initially at the center and subsequently at the location of an expansion wave that propagates outwards at the sound speed. Hence, this solution has been referred to as ‘‘inside-out’’ collapse. For radii greater than the instantaneous location of the

expansion wave, the density is that of a singular isothermal sphere, $\rho = c_s^2/(2\pi Gr^2)$; for radii less than the instantaneous location of the expansion wave, the gas accelerates until it reaches free-fall, with an infall velocity $v = (2GM_*/r)^{1/2}$ and density profile $\rho \propto r^{-3/2}$. (M_* is the instantaneous mass of the central protostar.) The mass infall rate is constant in time, $\dot{M}_{\text{in}} = 0.975c_s^3/G$, considerably less than that of the Larson-Penston-Hunter solution.

While the singular isothermal sphere solution has its obvious pitfalls (observed protostellar cores are neither singular, nor isothermal, nor spheres), its simplicity and ease of modification has allowed it to enjoy widespread use by the observational community (e.g., Zhou et al. 1990, 1993, 1994; Choi et al. 1995; Zhou et al. 1996; Ceccarelli et al. 1996; Gregersen et al. 1997). However, the increasing sophistication of present-day observations, made manifest in subarcsecond interferometric surveys (e.g., Looney et al. 2003), has provided ever-tightening constraints on the structure and evolution of protostellar cores, thereby casting a pessimistic view on the applicability of idealized self-similar models such as the Larson-Penston-Hunter and Shu solutions. The abstract of Looney et al. (2003) itself is rather telling:

We suggest that either there is some overall time scaling of the self-similar solutions that invalidates the age estimates or, more likely, we are at the limit of the usefulness of these models. With our observations we have begun to reach the stage at which models need to incorporate more of the fundamental physics of the collapse process, probably including magnetic fields and/or turbulence.

1.3 Magnetic Fields

The possible importance of magnetic fields to the support of interstellar clouds and to the regulation of star formation was first studied by Chandrasekhar & Fermi (1953), Mestel & Spitzer (1956), and Mestel (1965) using the virial theorem. Similar investigations by Strittmatter (1966a,b) and Spitzer (1968) followed. Mestel (1966) calculated the magnetic

forces on a spherically-symmetric, gravitationally-bound cloud. Self-consistent calculations by Mouschovias (1976a,b) produced exact equilibria of initially uniform, isothermal, magnetic clouds embedded in a hot and tenuous, electrically-conducting external medium. Mouschovias & Spitzer (1976) used these equilibrium states to find the critical mass-to-flux ratio

$$\left(\frac{M}{\Phi_B}\right)_{\text{cr}} = \left(\frac{1}{63G}\right)^{1/2} \quad (1.4)$$

that must be exceeded for collapse against the magnetic forces to set in. This condition can be rewritten to give a critical mass,

$$M_{\text{crit}} = 1.82 \times 10^2 \left(\frac{R}{Z}\right)^2 \left(\frac{B}{30 \mu\text{G}}\right)^3 \left(\frac{n}{10^3 \text{ cm}^{-3}}\right)^{-2} M_{\odot}, \quad (1.5)$$

where B is the magnetic field strength and the quantity (R/Z) is the major-to-minor axis ratio of the cloud. Under typical molecular cloud conditions, the mean magnetic field can support cloud masses ≈ 30 times greater than those supported by thermal pressure alone. Scott & Black (1980) performed numerical simulations of the collapse of a supercritical (as a whole) magnetic cloud. A picture of molecular clouds emerged in which magnetic fields play a central role in their support and evolution (Mouschovias 1978).

Subsequent observations lent credence to this picture by revealing the importance of magnetic fields through both dust polarization measurements and Zeeman observations. Polarization studies have exhibited large-scale ordered magnetic fields connecting protostellar cores to their surrounding envelopes (Vrba et al. 1981; Heyer et al. 1987; Novak et al. 1989, 1997; Lai et al. 2001, 2003; Crutcher et al. 2004; Matthews et al. 2005; Alves et al. 2008), often with an hourglass morphology (Schleuning 1998; Hildebrand et al. 1999; Girart et al. 1999; Schleuning et al. 2000; Lai et al. 2002; Matthews & Wilson 2002; Houde et al. 2004; Cortes & Crutcher 2006; Girart et al. 2006; Vaillancourt et al. 2008; Tang et al. 2009; Kirby 2009), as predicted by the theoretical calculations (Mouschovias 1976b; Fiedler & Mouschovias 1993). (See Figure 1.1 for some notable examples.) A large body

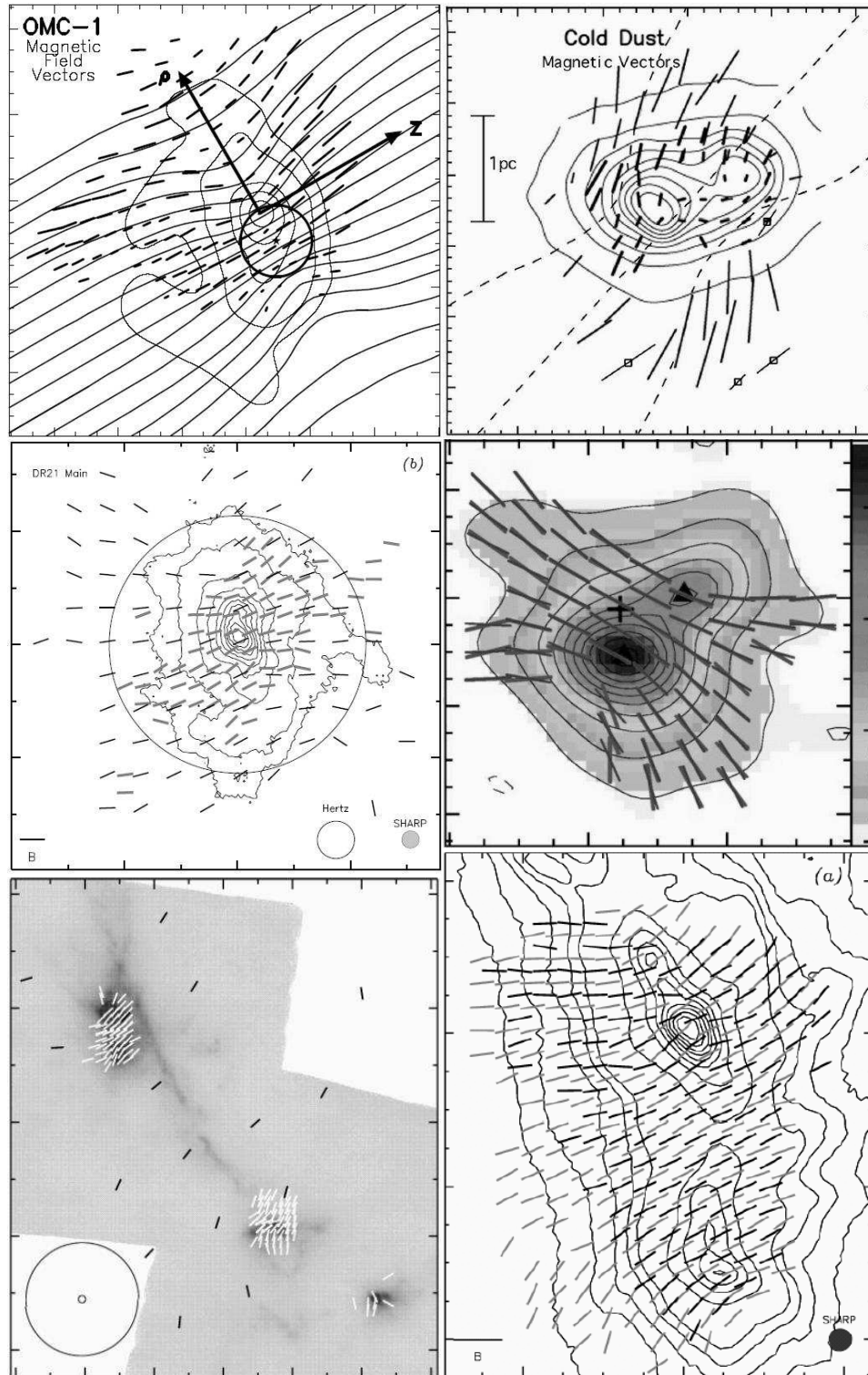


Figure 1.1: Inferred magnetic field vectors from dust polarimetry in a variety of sources (*clockwise from top right*): W3 (Schleuning et al. 2000), NGC 1333 IRAS 4A (Girart et al. 2006), OMC-1 (Vaillancourt et al. 2008), NGC 6334 (Li et al. 2006; Dotson et al. 2008), DR21-Main (Kirby 2009), and the OMC-1 ridge (Schleuning 1998).

of Zeeman observations (Crutcher & Kazès 1983; Kazès & Crutcher 1986; Troland et al. 1986; Crutcher et al. 1987; Goodman et al. 1989; Crutcher et al. 1993, 1994, 1996; Troland et al. 1996; Crutcher et al. 1999a,b; Crutcher 1999; Heiles & Crutcher 2005; Cortes et al. 2005) revealed magnetic fields in the range $\simeq 10 - 200 \mu\text{G}$ in molecular clouds, from small isolated ones to massive star-forming ones. These values are more than sufficient to establish the importance of magnetic fields in molecular cloud dynamics.

It was recognized early on (e.g., see Babcock & Cowling 1953, p. 373) that the magnetic flux of an interstellar blob of mass comparable to a stellar mass is typically several orders of magnitude greater than that of magnetic young stars. This is the so-called “magnetic flux problem” of star formation. It lies in the fact that substantial flux loss must take place at some stage during star formation. Ambipolar diffusion (the relative motion between plasma and neutrals) was first proposed by Mestel & Spitzer (1956) as a means by which an interstellar cloud as a whole would reduce its magnetic flux and thereby collapse. Pneuman & Mitchell (1965) undertook a detailed calculation of the collapse of such (spherical) cloud. Spitzer (1968) calculated the ambipolar-diffusion timescale by assuming that the magnetic force on the ions is balanced by the (self-)gravitational force on the neutrals. Nakano (1979) followed the quasistatic contraction of a cloud due to ambipolar diffusion using a sequence of Mouschovias’ (1976b) equilibrium states, each one of which had a smaller magnetic flux than the previous one.

A new solution for ambipolar diffusion by Mouschovias (1979) showed that the essence of this process is a redistribution of mass in the central flux tubes of a molecular cloud, rather than a loss of magnetic flux by the cloud as a whole. He found the ambipolar-diffusion timescale to be typically three orders of magnitude smaller in the interior of a cloud than in the outermost envelope, where there is a much better coupling between neutral particles and the magnetic field because of the much greater degree of ionization. This suggested naturally a *self-initiated* fragmentation of (or core formation in) molecular clouds

on the ambipolar-diffusion timescale

$$\tau_{\text{AD}} \approx \frac{\tau_{\text{ff}}^2}{\tau_{\text{ni}}} \approx 2 \times 10^6 \left(\frac{x_i}{10^{-7}} \right) \text{ yr}, \quad (1.6)$$

where τ_{ff} and τ_{ni} are the free-fall timescale and neutral-ion collision timescale, respectively (Mouschovias 1979). This expression is essentially independent of geometry (see Mouschovias 1987). The inefficiency of star formation was thereby attributed to the self-initiated formation and contraction of molecular cloud fragments (or cores) due to ambipolar diffusion in otherwise magnetically supported clouds (Mouschovias 1976b, 1977, 1978, 1979). The *central* mass-to-flux ratio eventually exceeds its critical value for collapse,

$$\left(\frac{dM}{d\Phi_{\text{B}}} \right)_{\text{c,cr}} = \frac{3}{2} \left(\frac{M}{\Phi_{\text{B}}} \right)_{\text{cr}}, \quad (1.7)$$

(see Mouschovias 1976a, eq. 44), and dynamic contraction ensues. Detailed numerical calculations in slab (Paleologou & Mouschovias 1983; Mouschovias et al. 1985), cylindrical (Mouschovias & Morton 1991, 1992a,b), axisymmetric (Fiedler & Mouschovias 1992, 1993; Ciolek & Mouschovias 1993, 1994, 1995; Basu & Mouschovias 1994, 1995a,b; Ciolek & Königl 1998; Desch & Mouschovias 2001; Tassis & Mouschovias 2005a,b, 2007a,b,c), and nonaxisymmetric (Basu & Ciolek 2004; Li & Nakamura 2004; Ciolek & Basu 2006; Kudoh et al. 2007; Nakamura & Li 2008; Kudoh & Basu 2008; Basu et al. 2009) geometries transformed this scenario of star formation into a theory with predictive power.

1.4 Rotation

During the early, isothermal phase of star formation, a cloud (or a fragment) must also lose a large fraction of its angular momentum (e.g., see Spitzer 1968, p. 231). While the geometry of protostellar fragments is often disklike over a wide range of lengthscales

(Kaifu et al. 1984; Sargent et al. 1988; Lay et al. 1994; Tassis 2007), observations show that molecular clouds and embedded fragments (or cores) rarely exhibit rotation significantly greater than that of the background medium (Goldsmith & Arquilla 1985). Even when they do, their angular velocities (typical core rotational rates are $\Omega \lesssim 3 \times 10^{-14} \text{ s}^{-1}$) imply centrifugal forces much too small to impose a disklike geometry through rotational support perpendicular to the axis of rotation (Saito et al. 1995). If angular momentum were conserved from the initial galactic rotation (i.e., starting from an angular velocity $\Omega_0 \simeq 10^{-15} \text{ s}^{-1}$ at the mean density of the interstellar medium $\simeq 1 \text{ cm}^{-3}$; Goldsmith & Arquilla 1985), centrifugal forces would not allow even the formation of interstellar clouds (Mouschovias 1991a, § 2). Fragmentation does not alter this conclusion (Mouschovias 1977, § 1). This is referred to as the “angular momentum problem” of star formation.

As far as clouds and their cores are concerned, the angular momentum problem has been shown to be resolved by magnetic braking (i.e., the transport of angular momentum from a fragment to its surrounding medium through the propagation of torsional Alfvén waves along magnetic field lines connecting the fragment to the cloud envelope) analytically by Mouschovias & Paleologou (1979, 1980) and numerically by Basu & Mouschovias (1994, 1995a,b) and Mellon & Li (2009). Transient phenomena aside, Mouschovias & Paleologou (1979, 1980) found that the characteristic time for loss of angular momentum is essentially equal to the time it takes for torsional Alfvén waves to propagate away from a cloud (or core) and set into motion an amount of “external” matter with moment of inertia equal to that of the cloud (or core). The magnetic-braking timescale of a disk-shaped rotator with straight-parallel field lines was found to be

$$\tau_{\parallel} = \frac{\rho_{\text{cl}}}{\rho_{\text{ext}}} \frac{Z}{v_{\text{A,ext}}} \equiv \left(\frac{\pi}{\rho_{\text{ext}}} \right)^{1/2} \frac{M}{\Phi_{\text{B}}}, \quad (1.8)$$

where ρ_{cl} and ρ_{ext} are the densities of the cloud and external medium (or envelope), respectively, Z the half-thickness of the cloud, and $v_{\text{A,ext}}$ the Alfvén speed in the external

medium. A “standard” value of $\rho_{\text{ext}} = 0.01\rho_{\text{cl}}$ (Basu & Mouschovias 1994).

In the case in which the field lines “fan out” away from a rotator (i.e., the field strength decreases from its value in the cloud, through a transition region, to that of the “background” field), the magnetic-braking timescale acquires a multiplicative factor ≤ 1 , whose precise value depends on the moment of inertia of the transition region, I_{tr} . If $I_{\text{tr}} \lesssim I_{\text{cl}}$ then the magnetic braking timescale becomes

$$\tau_{\parallel, \text{fan}} = \tau_{\parallel} \left(\frac{R_{\text{cl}}}{R_0} \right)^4 \equiv \left(\frac{\pi}{\rho_{\text{ext}}} \right)^{1/2} \frac{M}{\Phi_{\text{B}}} \left(\frac{R_{\text{cl}}}{R_0} \right)^2, \quad (1.9)$$

where R_0 is the radius of the flattened cloud, when its density was $\rho_0 (> \rho_{\text{ext}})$ but its magnetic field was equal to that of the external medium (see Mouschovias 1983). It follows from this equation that, as a cloud (or core) contracts at constant M/Φ_{B} in an environment whose properties (ρ_{ext}) do not change much as a result of the cloud’s (or core’s) contraction, $\tau_{\parallel, \text{fan}}$ decreases as R_{cl}^2 ($\propto Z \propto \rho_{\text{cl}}^{-1/2}$ for isothermal contraction with balance of forces maintained along field lines). In other words, magnetic braking becomes progressively more effective because of the decreasing moment of inertia of the cloud.

Magnetic braking has been shown to be so effective that the centrifugal forces resulting from the cloud’s or core’s rotation have a negligible effect on the evolution of the contracting core, at least up to central densities of $\approx 10^{14} \text{ cm}^{-3}$ (see the last paragraph of Tassis & Mouschovias 2007b).

1.5 Grain Effects

Interstellar grains comprise about 1% of the mass in the interstellar medium (Spitzer 1978). Baker (1979) and Elmegreen (1979) suggested that charged grains may couple to the magnetic field and thereby play a role in ambipolar diffusion and star formation. Elmegreen (1979) and Nakano & Umeyayashi (1980) compared the ambipolar-diffusion timescale and the free-fall timescale and concluded that ambipolar diffusion occurs over too long a

timescale (roughly 10 times greater than free-fall) to be a relevant process in star formation. Refinements by the same authors (Elmegreen 1986; Umebayashi & Nakano 1990; Nishi et al. 1991) led to similar conclusions. Through detailed numerical simulations of core formation and evolution including the effects of (negative and neutral) dust grains, Ciolek & Mouschovias (1993, 1994) found that grains lengthen the timescale for the formation of a core because of grain-neutral collisions, but cautioned that the ambipolar-diffusion timescale should not be compared to the free-fall timescale in determining its relevance in magnetically-supported clouds, as originally pointed out by Mouschovias (1977), because molecular clouds are not free-falling. Velocities characteristic of such collapse have not been observed. Ciolek & Mouschovias (1995) extended these calculations by including UV ionization and a variety of atomic metal ions (C^+ , S^+ , Si^+ , Mg^+ , Na^+ , Fe^+). Attention was also paid to the complementary effect of protostellar evolution on the microscopic physics and chemistry (Ciolek & Mouschovias 1996, 1998).

1.6 MHD Waves and/or Turbulence

It has long been known that molecular clouds exhibit supersonic linewidths (see review by Zuckerman & Palmer 1974), which are inextricably linked to how such dense ($n \simeq 10^3 \text{ cm}^{-3}$), cold ($T \simeq 10 \text{ K}$) objects, whose masses are typically $10^2 - 10^4$ greater than the thermal (or Jeans, or Bonnor-Ebert) critical mass, could be supported against their self-gravity, or whether they are supported at all. Possible explanations for the linewidths are radial collapse (or expansion) (Shu 1973; Liszt et al. 1974; Goldreich & Kwan 1974; Scoville & Solomon 1974), random motions of clumps within clouds (Zuckerman & Evans 1974; Morris et al. 1974), supersonic turbulence (Larson 1981; Leung et al. 1982; Myers 1983; Myers & Gammie 1999; Heyer & Brunt 2004), or hydromagnetic waves (Arons & Max 1975; Mouschovias 1975; Zweibel & Josafatsson 1983; Mouschovias & Psaltis 1995; Mouschovias et al. 2006). While the first two possibilities have long been ruled out

(Zuckerman & Evans 1974; Mouschovias 1975), there still exists a debate over the latter two (Mac Low & Klessen 2004; Mouschovias et al. 2006).

The debate hinges upon a proper interpretation of the observed correlations between linewidth (a proxy for velocity dispersion), size, and column density. When Larson (1981) compiled data on linewidths on 54 clouds, clumps, and cores, and found a relation between the observed velocity dispersion Δv and the size (diameter) R of each object (the so-called “turbulence law” $\Delta v \propto R^{0.38}$, which was thought to be the signature of Kolmogorov turbulence), supersonic turbulence appeared to be a natural explanation. Subsequent work by Leung et al. (1982), Myers (1983), and Solomon et al. (1987) also found a power-law relation, albeit with a significantly greater exponent, $\simeq 0.5$. Due in part to the influence of Larson’s original work, it is widely believed even today that the characteristic scaling relations at the heart of theories of turbulence may still provide the most natural explanation of the linewidth–size relation (Myers & Gammie 1999; Heyer & Brunt 2004).

Despite the promise of such an explanation, it is well known that supersonic turbulence decays very rapidly ($\lesssim 1$ Myr) and has very high energy requirements (Mestel & Spitzer 1956; Goldreich & Kwan 1974). Moreover, relatively recent numerical simulations (Stone et al. 1998; Mac Low et al. 1998; Ostriker et al. 1999; Padoan & Nordlund 1999; Ostriker et al. 2001) show that magnetic fields cannot mediate the decay of such turbulence (often assumed to be initially superAlfvénic, although such an assumption lacks observational support; see below). In light of the arguments for long lifetimes of molecular clouds (Mouschovias et al. 2006), this relatively rapid decay poses a serious problem for a turbulent interpretation of the linewidth–size relation unless a suitable driving mechanism is found that can replenish the rapidly-decaying turbulence. From a theoretical point of view, these difficulties are compounded by the fact that different numerical studies of molecular cloud turbulence seem to offer a wide range of conflicting results on what the predicted linewidth–size relation ought to actually be (see Elmegreen & Scalo 2004, § 5.2).

Perhaps the most deleterious finding for a turbulent interpretation of the linewidth–size

relation is the very recent revelation that Larson’s scaling relationships, in fact, do *not* hold. The coefficient of the cloud structure functions, $\Delta v/R^{1/2}$, is *not* constant, but rather systematically varies with the surface density of the cloud as $\Sigma^{0.5}$ (Heyer et al. 2008).

This new relation is actually a special case of a more general result originally derived by Mouschovias (1987) (see also Mouschovias & Psaltis 1995) in the context of the magnetic support of molecular clouds. If (1) self-gravitating clouds are magnetically supported, and (2) the material velocities responsible for the supersonic linewidths are slightly sub-Alfvénic or Alfvénic, then the linewidths may be attributed to large-scale non-radial cloud oscillations, which are essentially *standing* large-amplitude, long-wavelength ($\lambda \sim 1$ pc) Alfvén waves. For such clouds, the Alfvén speed is always comparable to the free-fall speed, i.e.,

$$v_A \simeq \left(\frac{2GM}{R} \right)^{1/2} = (2\pi G \Sigma R)^{1/2}, \quad (1.10)$$

where the column density $\Sigma = M/\pi R^2$. Furthermore, self-gravitating, magnetically-supported clouds are expected to have $\Sigma \simeq \Sigma_{\text{crit}} = (1/63G)^{1/2} B$ (see eq. 1.4). Combining these relations, one immediately finds that the nonthermal linewidth $(\Delta v)_{\text{NT}}$ is related to the magnetic field strength B and the size R of the object by

$$(\Delta v)_{\text{NT}} \simeq 1.4 \left(\frac{B}{30 \mu\text{G}} \right)^{1/2} \left(\frac{R}{1 \text{ pc}} \right)^{1/2} \text{ km s}^{-1} \quad (1.11)$$

Equilibrium oscillations left over from the cloud formation process (Mouschovias 1975; Kudoh & Basu 2003; Galli 2005; Kudoh & Basu 2006) could be the origin of these waves.

Equation (1.11) was shown by Mouschovias et al. (2006) to be in excellent quantitative agreement with spectral line observations of clouds, cores, and embedded OH masers; they considered the 31 objects for which the linewidth, size, and magnetic field strength were reliably measured at the time (Myers & Goodman 1988; Crutcher 1999; Crutcher et al. 2004). We reproduce their Figures 1 and 2 here. In Figure 1.2a we plot $(\Delta v)_{\text{NT}}$ versus R ; errors bars are as in Myers & Goodman (1988), indicating an uncertainty of a factor

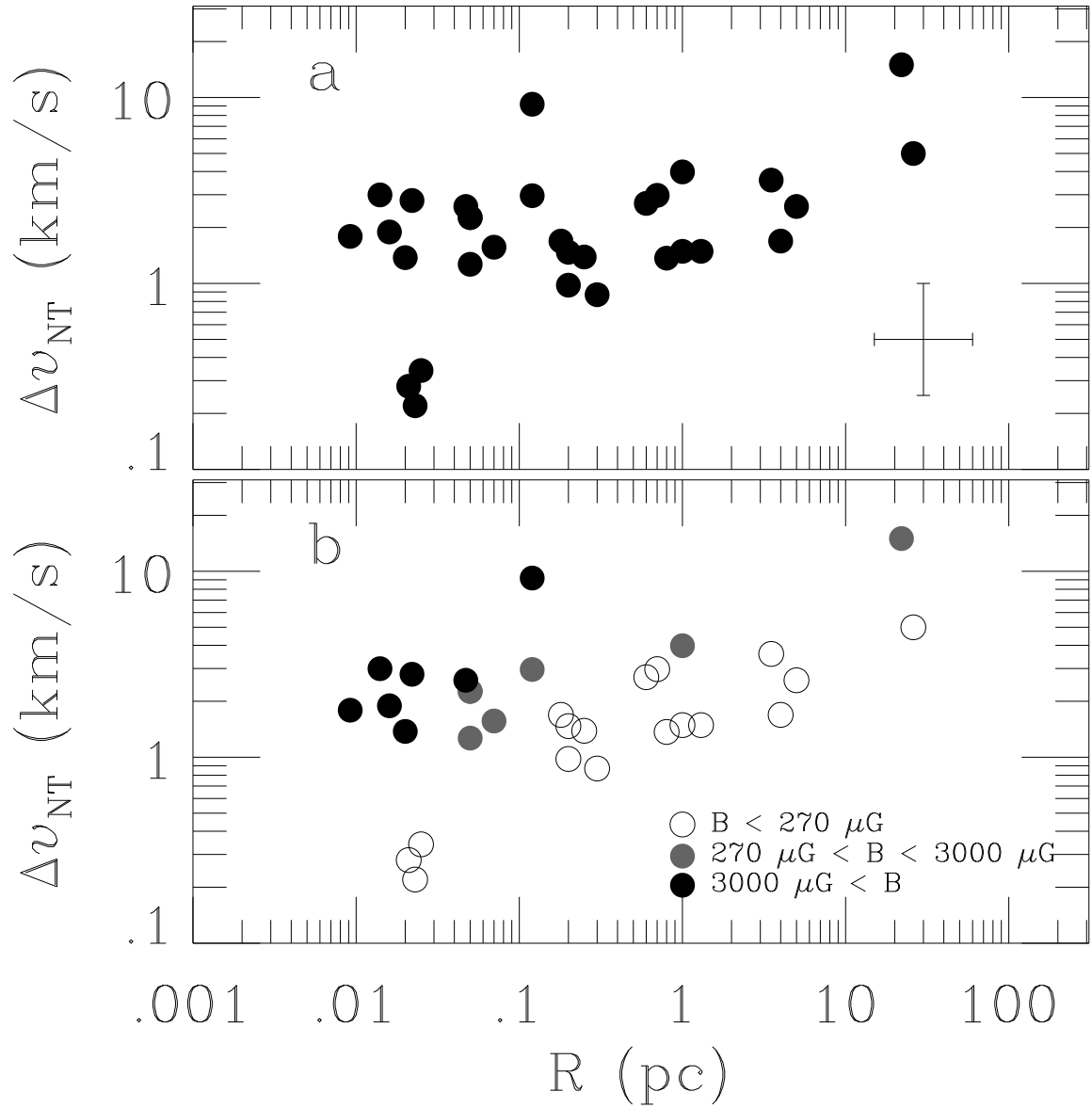


Figure 1.2: (a) Nonthermal linewidth versus (FWHM) size for 31 objects (data from Myers & Goodman 1988; Crutcher 1999; Crutcher et al. 2004). (b) Same linewidth-size data as in (a), but grouped according to the total magnetic field strength.

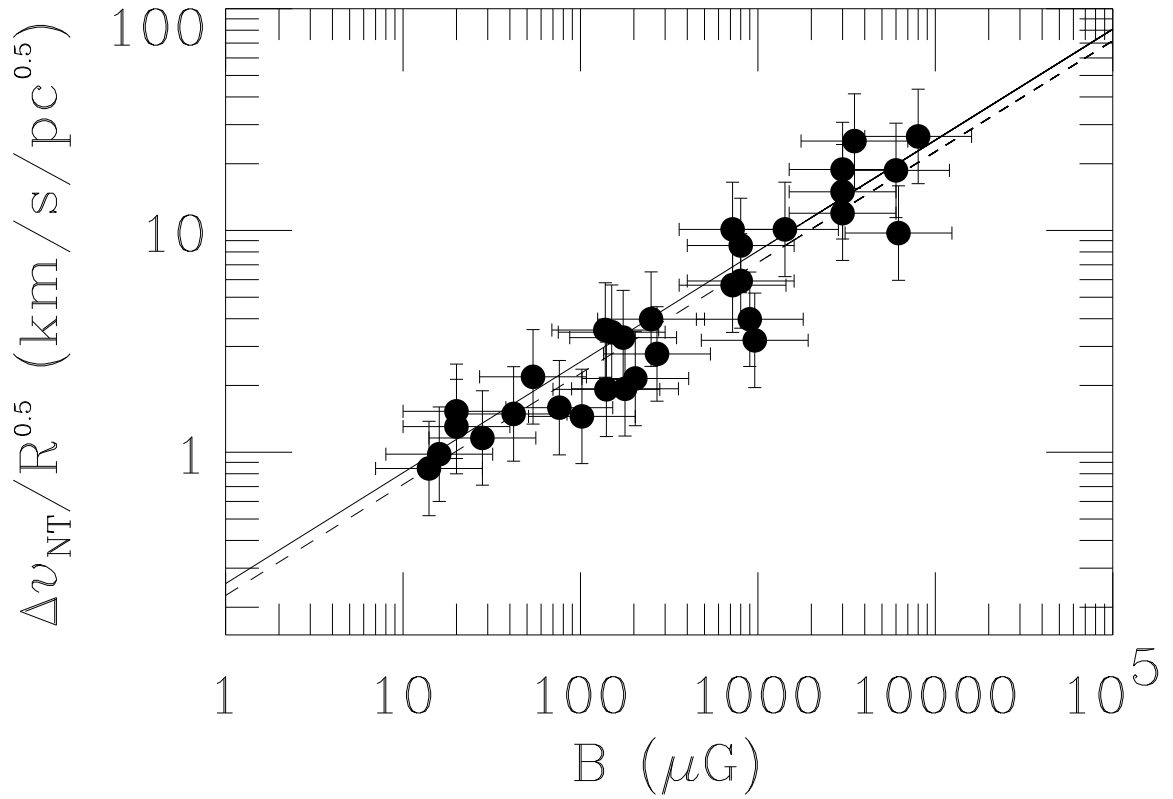


Figure 1.3: Same linewidth-size data as in Figure 1.2, but exhibiting the ratio $(\Delta v)_{\text{NT}}/R^{1/2}$ as a function of the total magnetic field strength B . Error bars are as in Figure 1.2. The theoretical prediction (eq. 1.11) is shown as a solid line. The dashed line is a least-squares fit to the data.

of 2. No single power law can meaningfully fit the data, in that the standard deviation would be too large. In Figure 1.2b we separate these points into weak-field ($B \leq 270 \mu\text{G}$; open circles), moderate-field ($270 \mu\text{G} < B < 3000 \mu\text{G}$; grey circles), and strong-field ($3000 \mu\text{G} \leq B$; black circles) regimes. There is a clear indication that sources of different magnetic-field strength follow different scaling laws. In Figure 1.3 we show the same data, but we plot the quantity $(\Delta v)_{\text{NT}}/R^{1/2}$ against B . Error bars are as in Figure 1.2. The solid line is the theoretical prediction, equation (1.11). The dashed line is a least-squares fit to the data. The quantitative agreement between theory and observations is remarkable. The theoretical prediction and the least-squares fit have exactly the same slope. In addition, the fact that the theoretical prediction is offset slightly higher than the least-squares fit indicates that the material motions responsible for the linewidths are slightly sub-Alfvénic.

Despite a lack of agreement on the origin of the linewidths, analytical (Mouschovias 1991a) and numerical calculations (Eng 2002) have demonstrated that turbulence plays an insignificant role in the star formation process once dynamical contraction of a fragment (or core) ensues. For typical molecular cloud parameters, the size of the region that can just become gravitationally unstable because of ambipolar diffusion happens to be essentially equal to the Alfvén lengthscale λ_A (Alfvén waves with wavelengths $\lambda \leq \lambda_A$ cannot propagate in the neutrals because of damping by ambipolar diffusion — see Mouschovias 1991a, eqs. 18a,b). In fact, it is precisely the decay of hydromagnetic waves due to ambipolar diffusion that removes part of the support against gravity over the critical thermal lengthscale and thus initiates fragmentation (or core formation) in molecular clouds (Mouschovias 1987). Observations showing narrowing and eventual thermalization of linewidths in protostellar cores (Baudry et al. 1981; Myers & Benson 1983; Myers et al. 1983; Bacmann et al. 2000) are in agreement with this conclusion.

1.7 Radiative Transfer

During the early phases of star formation, the energy produced by compressional heating is radiated away by the dust grains in the infrared. At higher densities ($\gtrsim 10^{10} \text{ cm}^{-3}$), the core traps and retains part of this heat and its temperature begins to rise. Considerable work has been conducted over the past several decades that attempts to discern the thermodynamic evolution of protostellar cores in the absence of magnetic fields. A large number of numerical simulations have been performed in one-dimensional spherically-symmetric (Bodenheimer 1968; Larson 1969, 1972b; Appenzeller & Tscharnuter 1975; Yorke & Kruegel 1977; Yorke 1979; Winkler & Newman 1980a,b; Masunaga et al. 1998), two-dimensional axially-symmetric (Larson 1972a; Black & Bodenheimer 1976; Tscharnuter 1975, 1978; Boss 1984; Bodenheimer et al. 1990; Yorke et al. 1993, 1995), and three-dimensional (Boss 1986, 1988, 1993; Boss & Myhill 1995; Whitehouse & Bate 2006) geometries, using widely varying initial conditions, approximations, and numerical techniques.

In the simplest case, the thermodynamic evolution of a protostellar core in the non-isothermal regime may be approximated (but substantially overestimated) by using an adiabatic equation of state (Boss 1981). More realistic equations of state have also been employed by, for example, Bate (1998). To accurately model the nonisothermal phase of protostellar contraction, however, one needs to include a proper treatment of radiative transfer.

Early efforts to include radiative transfer in (nonmagnetic) star formation calculations were confined to the use of the diffusion approximation (Bodenheimer 1968; Larson 1969, 1972b; Black & Bodenheimer 1975, 1976; Tscharnuter 1975; Yorke & Kruegel 1977). While the diffusion approximation is strictly applicable only to optically thick regions, its ease of implementation and relatively low computational cost make it an attractive choice. The Eddington approximation offers a slight improvement in that it retains some of the rigor of using moments of the radiative transfer equation, while making the simplifying assumption that the radiation field is everywhere isotropic. Its use in numerical calculations

of (nonmagnetic) star formation has been documented in Tscharnuter (1978), Tscharnuter & Winkler (1979), Winkler & Newman (1980a,b), Boss (1984, 1986, 1988), and Boss & Myhill (1995). By implicitly assuming that photons always travel a distance comparable to their mean-free path (even if this distance exceeds the free-flight distance $c\Delta t$, where Δt is the computational timestep), the Eddington approximation gives unphysical behavior in optically thin regions, in which the mean-free-path is huge. The result is a signal speed unbound by the speed of light, i.e., it violates causality (see Mihalas & Weibel Mihalas 1984, § 97).

Increasing the accuracy and realism of a radiative transfer algorithm often requires making limiting assumptions about the hydrodynamics in order to make the problem tractable (e.g., Yorke 1980; Masunaga et al. 1998). A full frequency- and angle-dependent treatment of the radiation is nearly always confined to postprocessing the results of a hydrodynamic calculation (Yorke 1977; Yorke & Shustov 1981; Adams & Shu 1985, 1986) or a grey (i.e., independent of frequency) radiation hydrodynamic calculation (Boss & Yorke 1990; Bodenheimer et al. 1990). By contrast, the flux-limited diffusion (FLD) approximation (Levermore & Pomraning 1981) is a propitious compromise that retains some of the advantages of the diffusion and Eddington approximations, while preserving causality and coupling self-consistently to the hydrodynamic equations.

Despite vast differences in the approximations and numerical techniques used in previous work, a consensus has emerged regarding the qualitative evolution of *nonmagnetic*, nonisothermal prestellar objects that is in broad agreement with the pioneering work of Larson (1969). Such objects have been shown to remain isothermal until central densities of $\approx 2 \times 10^{10} \text{ cm}^{-3}$ (or $\approx 2 \times 10^8 \text{ cm}^{-3}$, depending on the simulation) are reached. The subsequent rise in temperature ultimately leads to the formation of a hydrostatic core at a temperature $\sim 100 \text{ K}$ and central density $\approx 2 \times 10^{12} \text{ cm}^{-3}$. The initial mass and radius of the hydrostatic core are typically found to be $\approx 0.005 M_{\odot}$ and $\approx 4 \text{ AU}$, respectively. A thermal shock front forms at the core boundary as mass is accreted onto the hydrostatic

core, while small-amplitude oscillations occur about equilibrium. Finally, a temperature of 1000 K is reached at a central density $\approx 2 \times 10^{15} \text{ cm}^{-3}$. Soon thereafter, molecular hydrogen dissociates (at 2000 K), the ratio of specific heats γ dips below the critical value $4/3$, and material at the center of the core becomes unstable and collapses dynamically. Despite the ensuing highly dynamic evolution, the temperature rises only slowly since most of the gravitational energy goes into molecular dissociation. Once molecular hydrogen is nearly all dissociated, γ rises above $4/3$ and the thermal pressure rises rapidly, decelerating and ultimately halting the collapse at the center. A second (stellar) core forms, accompanied by another small rebound and subsequent radial pulsations. The mass and size of this core is $\approx 0.0015 M_{\odot}$ and $\approx 1.3 R_{\odot}$, respectively. Its central density $\approx 0.02 \text{ g cm}^{-3}$ and temperature $\approx 20,000 \text{ K}$.

1.8 Summary and Outline

The addition of magnetic fields to the theory of star formation has brought a myriad of interesting effects. Aside from the additional support that magnetic fields provide to counter self-gravity, the inclusion of magnetic fields has led to a qualitatively different picture of molecular cloud core fragmentation and evolution than earlier hydrodynamic calculations had suggested.

In an initially magnetically-subcritical cloud, gravitational infall occurs only as rapidly as allowed by ambipolar diffusion, the relative drift of neutral and charged particles. The neutrals fall in toward a local gravitating center, impeded by collisions with the charged particles, which remain nearly stationary along the magnetic field. Magnetic braking is very effective during this phase of contraction and is responsible for reducing the angular momenta of cloud cores to their observed low values and for resolving the angular momentum problem during the early, isothermal stage of contraction. The magnetically-subcritical phase continues until the neutral infall creates a central region with a supercritical mass-to-

flux ratio (typically between a central density $\lesssim 10^4 \text{ cm}^{-3}$ and $\approx 10^5 \text{ cm}^{-3}$). This region, referred to as a supercritical core, contracts more rapidly than its surroundings, evolving dynamically (though slower than free-fall) under near flux freezing, until the resurrection of ambipolar diffusion causes magnetic decoupling⁴ to set in at a density $\approx 10^{10} \text{ cm}^{-3}$. Magnetic decoupling occurs over a few orders of magnitude in central density enhancement and precedes the formation of a central stellar object. The isothermal evolution of a magnetic molecular cloud has been followed in detail up to central densities of $2 \times 10^{12} \text{ cm}^{-3}$ by Desch & Mouschovias (2001), who find that the magnetic field strength asymptotically approaches $\approx 0.1 \text{ G}$ in the innermost $\approx 20 \text{ AU}$ of the cloud.

Mostly due to the large numerical demands involved, the majority of magnetic star formation simulations have only been able to follow in detail the early isothermal phase of core fragmentation and evolution. There have been notable efforts, however, to incorporate radiative effects into these calculations. Unfortunately, these often involve sacrificing rigor in one aspect of the problem in deference to another. For example, the numerical simulations of Boss (1997, 1999, 2002, 2005, 2007, 2009) followed the thermodynamic evolution of a magnetic protostellar core with a reasonable degree of accuracy, via the Eddington approximation, while treating magnetic field effects and ambipolar diffusion crudely through various approximations and parameterizations based on previous isothermal MHD calculations. Tassis & Mouschovias (2007a,b,c) have taken the opposite approach by incorporating a detailed treatment of nonideal MHD and chemistry into their numerical simulations, while approximating the thermodynamic evolution via a piecewise adiabatic equation of state.

This Thesis represents a step forward in joining decades-old efforts to uncover the thermodynamic evolution of a nonmagnetic protostellar core with the modern realization that star formation is an intrinsically magnetohydrodynamic phenomenon. Magnetic fields are

⁴Complete magnetic decoupling refers to conditions such that the magnetic field has no significant effect on the dynamics of the neutral matter *and* the motion of the neutral matter no longer affects the magnetic field — see footnote 3 of Desch & Mouschovias (2001).

an importunate necessity in the formulation of a theory of star formation, and while the famous psychoanalyst Carl Jung was most assuredly not referring to magnetic fields when he wrote, “The artful denial of a problem will not produce conviction,” the quote itself seems rather appropriate.

The outline of the Thesis is as follows. In Chapter 2 we formulate the problem to be solved. Chapter 3 introduces the method of solution and provides the initial and boundary conditions of the numerical simulations, the results of which are presented in Chapter 4. Contact is made with both observations and prior theoretical work where appropriate. The results of a brief parameter study are given in Chapter 5. Finally, in Chapter 6 we close with a summary of results and predictions, as well as a discussion of their limitations and of possible future work.

Chapter 2

Formulation of the Problem

2.1 Outline

In this chapter we formulate the problem of the formation and evolution of protostellar fragments (or cores) in magnetically-supported, self-gravitating molecular clouds, including the effects of both ambipolar diffusion and Ohmic dissipation (which becomes important at high densities), grain chemistry and dynamics, and radiation. Using the results of Eng (2002) and Basu & Mouschovias (1994), we may safely ignore the effects of turbulence and rotation, respectively, on the evolution of the protostellar core for the densities considered here. The physical and chemical properties of the model cloud are summarized in Section 2.2. The radiation magnetohydrodynamic (RMHD) equations governing the evolution of the model cloud are presented and discussed in Section 2.3. In Section 2.4 we present the chemical model used in the calculations. The physics of magnetic diffusion (ambipolar and Ohmic) is handled by using a generalized Ohm's law, which is derived in Section 2.5. We treat the radiative transfer using the grey (i.e., independent of frequency) FLD approximation, with realistic grain opacities accounting for a variety of grain compositions (§ 2.6). Finally, we give the simplified set of equations and a brief summary in Section 2.7. Details, mostly mathematical, are left for the Appendix.¹

Table 2.1: Chemical reaction network used in the calculation of the abundances of charged species.

Relevant Chemical Reactions in Molecular Clouds			
Cosmic-Ray Ionization:	$\text{H}_2 + \text{CR}$	\rightarrow	$\text{H}_2^+ + \text{e}$
	$\text{H}_2^+ + \text{H}_2$	\rightarrow	$\text{H}_3^+ + \text{H}$
	$\text{H}_3^+ + \text{CO}$	\rightarrow	$\text{HCO}^+ + \text{H}_2$
Dissociative Recombination:	$\text{HCO}^+ + \text{e}$	\rightarrow	$\text{H} + \text{CO}$
Radiative recombination: ^a	$\text{A}^+ + \text{e}$	\rightarrow	$\text{A}^0 + h\nu$
Charge transfer: ^a	$\text{A}^0 + \text{HCO}^+$	\rightarrow	$\text{A}^+ + \text{HCO}$
e^- attachment onto grains:	$\text{e} + \text{g}_0$	\rightarrow	g_-
	$\text{e} + \text{g}_+$	\rightarrow	g_0
Atomic-ion attachment onto grains: ^a	$\text{A}^+ + \text{g}_-$	\rightarrow	$\text{A}^0 + \text{g}_0$
	$\text{A}^+ + \text{g}_0$	\rightarrow	$\text{A}^0 + \text{g}_+$
Molecular-ion attachment onto grains:	$\text{HCO}^+ + \text{g}_0$	\rightarrow	$\text{HCO} + \text{g}_+$
	$\text{HCO}^+ + \text{g}_-$	\rightarrow	$\text{HCO} + \text{g}_0$
Charge transfer by grain-grain collisions:	$\text{g}_+^\alpha + \text{g}_-^{\alpha'}$	\rightarrow	$\text{g}_0^\alpha + \text{g}_0^{\alpha'}$
	$\text{g}_\pm^\alpha + \text{g}_0^{\alpha'}$	\rightarrow	$\text{g}_0^\alpha + \text{g}_\pm^{\alpha'}$

^aA⁺ represents an atomic ion, such as Na⁺, Mg⁺, and K⁺, and A⁰ the corresponding neutral atom.

2.2 Basic Properties of the Model Cloud

We consider a self-gravitating, magnetic, weakly-ionized, axisymmetric model molecular cloud consisting of neutral particles (H₂ with 20% He by number), ions (both molecular HCO⁺ and atomic Na⁺, Mg⁺, K⁺), electrons, singly negatively-charged grains, singly positively-charged grains, and neutral grains. Following Desch & Mouschovias (2001), the abundances of all species (except the neutrals) are determined from the chemical reaction network shown in Table 2.1 and described below in Section 2.4.3. Cosmic rays of energy $\gtrsim 100$ MeV are mainly responsible for the degree of ionization in the cloud. Once column densities $\gtrsim 100 \text{ g cm}^{-2}$ are achieved, cosmic rays are appreciably attenuated. At even higher densities, cosmic rays are effectively shielded and radioactive decays become the dominant source of ionization. Finally, at temperatures on the order of 1000 K or higher, thermal ionization of potassium becomes important. UV radiation provides an additional ionization mechanism, but it only affects the outer envelope of molecular clouds (Hollen-

¹Published in ApJ Volume 693, Issue 2, pp. 1895–1911. Reproduction for this dissertation is authorized by the copyright holder.

bach et al. 1971; Glassgold & Langer 1974). We consider spherical grains whose radii are determined by either a uniform or an MRN (Mathis et al. 1977) size distribution. In the case of collisions of ions (molecular or atomic) with grains, we assume that the ions do not get attached to the grains, but rather that they get neutralized, with the resulting neutral particle escaping into the gas phase. Thus the total abundance of metals as well as the total HCO abundance remain constant. Grain growth is not considered here.

The ambipolar-diffusion-initiated evolution of the model cloud is followed in two dimensions from typical mean molecular cloud densities ($\simeq 300 \text{ cm}^{-3}$) to densities characteristic of the formation of a hydrostatic protostellar core. The axis of symmetry is aligned with the z -axis of a cylindrical polar coordinate system (r, ϕ, z) . Isothermality is an excellent approximation for the early stages of star formation, while the density is smaller than $\approx 10^{10} \text{ cm}^{-3}$ (Gaustad 1963; Hayashi 1966; Larson 1969). However, once the heat generated by released gravitational energy during core collapse is unable to escape freely (at a central number density of $n_{\text{opq}} \simeq 10^7 \text{ cm}^{-3}$), radiative transfer calculations are employed to determine the thermal evolution of the core.² This is an improvement over previous magnetic star formation calculations to reach these densities (Desch & Mouschovias 2001; Tassis & Mouschovias 2007a,b,c), which assumed an adiabatic equation of state beyond a critical density because of the high computational expense of radiative transfer calculations. Numerical techniques and computer hardware have matured enough by now to render these once impractical calculations feasible.

²We have varied the density n_{opq} at which we turn on the radiative transfer solver from 10^6 to 10^{11} cm^{-3} and found that $n_{\text{opq}} \lesssim 10^7 \text{ cm}^{-3}$ is necessary to achieve a smooth transition from isothermality. This numerical necessity does *not* mean that the isothermality assumption breaks down at as low a density as 10^7 cm^{-3} .

2.3 The Six-Fluid RMHD Description of Magnetic Star Formation

The RMHD equations governing the behavior of the six-fluid system (neutrals, electrons, ions, negative, positive, and neutral grains) are

$$\frac{\partial \rho_n}{\partial t} + \nabla \cdot (\rho_n \mathbf{v}_n) = 0, \quad (2.1a)$$

$$\frac{\partial(\rho_{g-} + \rho_{g0} + \rho_{g+})}{\partial t} + \nabla \cdot (\rho_{g-} \mathbf{v}_{g-} + \rho_{g0} \mathbf{v}_{g0} + \rho_{g+} \mathbf{v}_{g+}) = 0, \quad (2.1b)$$

$$\frac{\partial(\rho_n \mathbf{v}_n)}{\partial t} + \nabla \cdot (\rho_n \mathbf{v}_n \mathbf{v}_n) = -\nabla P_n - \rho_n \nabla \psi + \frac{1}{c} \mathbf{j} \times \mathbf{B} + \frac{1}{c} \chi_{\mathcal{F}} \mathcal{F}, \quad (2.1c)$$

$$0 = -en_e \left(\mathbf{E} + \frac{\mathbf{v}_e}{c} \times \mathbf{B} \right) + \mathbf{F}_{en}, \quad (2.1d)$$

$$0 = +en_i \left(\mathbf{E} + \frac{\mathbf{v}_i}{c} \times \mathbf{B} \right) + \mathbf{F}_{in}, \quad (2.1e)$$

$$0 = -en_{g-} \left(\mathbf{E} + \frac{\mathbf{v}_{g-}}{c} \times \mathbf{B} \right) + \mathbf{F}_{g-n} + \mathbf{F}_{g-g0,incl}, \quad (2.1f)$$

$$0 = +en_{g+} \left(\mathbf{E} + \frac{\mathbf{v}_{g+}}{c} \times \mathbf{B} \right) + \mathbf{F}_{g+n} + \mathbf{F}_{g+g0,incl}, \quad (2.1g)$$

$$0 = \mathbf{F}_{g0n} + \mathbf{F}_{g0g-,incl} + \mathbf{F}_{g0g+,incl}, \quad (2.1h)$$

$$\nabla \times \mathbf{B} = \frac{4\pi}{c} \mathbf{j}, \quad (2.1i)$$

$$\mathbf{j} = e (n_i \mathbf{v}_i - n_e \mathbf{v}_e + n_{g+} \mathbf{v}_{g+} - n_{g-} \mathbf{v}_{g-}), \quad (2.1j)$$

$$\frac{\partial \mathbf{B}}{\partial t} = -c \nabla \times \mathbf{E}, \quad (2.1k)$$

$$\nabla^2 \psi = 4\pi G \rho_n, \quad (2.1l)$$

$$\frac{\partial u_n}{\partial t} + \nabla \cdot (u_n \mathbf{v}_n) = -P_n \nabla \cdot \mathbf{v}_n - 4\pi \kappa_P \mathcal{B} + c \kappa_{\mathcal{E}} \mathcal{E} + \Gamma_{\text{diff}}, \quad (2.1m)$$

$$\frac{\partial \mathcal{E}}{\partial t} + \nabla \cdot (\mathcal{E} \mathbf{v}_n) = -\nabla \cdot \mathcal{F} - \nabla \mathbf{v}_n : \mathbf{P} + 4\pi \kappa_P \mathcal{B} - c \kappa_{\mathcal{E}} \mathcal{E}, \quad (2.1n)$$

$$\frac{\partial \mathcal{F}}{\partial t} + \nabla \cdot (\mathcal{F} \mathbf{v}_n) = -c^2 \nabla \cdot \mathbf{P} - c \chi_{\mathcal{F}} \mathcal{F}. \quad (2.1o)$$

The quantities ρ_s , n_s , and \mathbf{v}_s refer to the mass density, number density, and velocity of species s ; the subscripts n, i, e, \mathbf{g}_- , \mathbf{g}_+ , and \mathbf{g}_0 refer, respectively, to the neutrals, ions, electrons, negatively-charged grains, positively-charged grains, and neutral grains. The quantities \mathbf{E} and \mathbf{B} denote the electric and magnetic field, respectively, \mathbf{j} the total electric current density, u_n the internal energy density, P_n the gas pressure, and ψ the gravitational potential. The source term Γ_{diff} in the internal energy equation (2.1m) represents heating due to ambipolar diffusion and Ohmic dissipation (see § 2.5.5). The magnetic field satisfies the condition $\nabla \cdot \mathbf{B} = 0$ everywhere at all times.

The radiation variables are the Planck function \mathcal{B} , the total (frequency-integrated) radiation energy density \mathcal{E} , the total (frequency-integrated) radiation momentum density \mathcal{F} , and the total (frequency-integrated) radiation pressure tensor \mathbf{P} :

$$\mathcal{E}(\mathbf{x}, t) = \frac{1}{c} \int_0^\infty d\nu \oint d\Omega I(\mathbf{x}, t; \Omega, \nu), \quad (2.2a)$$

$$\mathcal{F}(\mathbf{x}, t) = \int_0^\infty d\nu \oint d\Omega I(\mathbf{x}, t; \Omega, \nu) \hat{\mathbf{n}}, \quad (2.2b)$$

$$\mathbf{P}(\mathbf{x}, t) = \frac{1}{c} \int_0^\infty d\nu \oint d\Omega I(\mathbf{x}, t; \Omega, \nu) \hat{\mathbf{n}} \hat{\mathbf{n}}. \quad (2.2c)$$

Here we have introduced the frequency ν , the extinction coefficient (i.e., opacity) $\chi(\nu)$ ($\equiv \kappa(\nu) + \sigma(\nu)$, where κ is the absorption coefficient and σ is the scattering coefficient), and the radiation specific intensity I . The material properties $\kappa_{\mathbf{P}}$, $\kappa_{\mathcal{E}}$, and $\chi_{\mathcal{F}}$ are the Planck and energy mean absorption coefficients, and the flux-weighted mean opacity, respectively; they are given by

$$\kappa_{\mathbf{P}} \equiv \frac{1}{\mathcal{B}} \int_0^\infty \kappa(\nu) \mathcal{B}(\nu) d\nu, \quad (2.3a)$$

$$\kappa_{\mathcal{E}} \equiv \frac{1}{\mathcal{E}} \int_0^\infty \kappa(\nu) \mathcal{E}(\nu) d\nu, \quad (2.3b)$$

$$\chi_{\mathcal{F}} \equiv \frac{1}{\mathcal{F}} \int_0^\infty \chi(\nu) \mathcal{F}(\nu) d\nu. \quad (2.3c)$$

Equations (2.1n) and (2.1o) are obtained from taking moments of the radiation transport equation

$$\left(\frac{1}{c} \frac{\partial}{\partial t} + \boldsymbol{\Omega} \cdot \boldsymbol{\nabla} \right) I(\mathbf{x}, t; \boldsymbol{\Omega}, \nu) = \chi(\mathbf{x}, t; \boldsymbol{\Omega}, \nu) [S(\mathbf{x}, t; \boldsymbol{\Omega}, \nu) - I(\mathbf{x}, t; \boldsymbol{\Omega}, \nu)] \quad (2.4)$$

under the assumptions that all the radiation variables are measured in the comoving frame of the fluid (in this frame the material properties are isotropic) and that the material properties are grey (Mihalas & Weibel Mihalas 1984).³ We have taken the source function S in the transport equation (2.4) to be given by

$$4\pi S_\nu = \frac{4\pi\kappa_\nu \mathcal{B}_\nu + c\sigma_\nu \mathcal{E}_\nu}{\kappa_\nu + \sigma_\nu}, \quad (2.5)$$

taking into account both establishment of local thermodynamic equilibrium and coherent isotropic scattering of radiation (Mihalas & Weibel Mihalas 1984).

The frictional force (per unit volume) on species s due to elastic collisions with neutrals is given by

$$\mathbf{F}_{sn} = \frac{\rho_s}{\tau_{sn}} (\mathbf{v}_n - \mathbf{v}_s), \quad s = \text{i, e, g}_-, \text{g}_+, \text{g}_0, \quad (2.6)$$

where the mean (momentum exchange) collision times, accounting for both s -H₂ and s -He collisions, is

$$\tau_{sn} = a_{\text{He}-s} \frac{m_{\text{H}_2} + m_s}{\rho_n \langle \sigma_{\text{coll}} w \rangle_{s\text{H}_2}}. \quad (2.7)$$

The quantity $a_{\text{He}-s}$ is the factor by which the presence of He lengthens the slowing-down time relative to the value it would have if only H₂- s collisions were considered, and is given

³We caution here that Preibisch et al. (1995) and Yorke & Sonnhalter (2002) have shown that multi-frequency calculations generally produce higher dust temperatures and greater degrees of anisotropy in the radiation field than corresponding grey calculations.

by (see Mouschovias 1996, § 2.1)

$$a_{\text{He}-s} = \begin{cases} 1.23 & \text{for } s = \text{i}, \\ 1.21 & \text{for } s = \text{e}, \\ 1.09 & \text{for } s = \text{g}_-, \text{g}_+, \text{ or } \text{g}_0. \end{cases} \quad (2.8)$$

The rate constant $\langle \sigma_{\text{coll}} w \rangle_{s\text{H}_2}$ for collisions between particles of species s and H_2 molecules is $1.69 \times 10^{-9} \text{ cm}^3 \text{ s}^{-1}$ for HCO^+ ions, with a similar value for Na^+ and Mg^+ ions (McDaniel & Mason 1973), and $1.3 \times 10^{-9} \text{ cm}^3 \text{ s}^{-1}$ for electrons (Mott & Massey 1971). In calculating these collisional rates, the Langevin approximation is used for ion-neutral collisions but not for electron-neutral collisions, for which the electron spin is important. For collisions between H_2 and grains of radius a , the rate constant is given by

$$\langle \sigma_{\text{coll}} w \rangle_{\text{gH}_2} = \pi a^2 (8k_{\text{B}}T/\pi m_{\text{H}_2})^{1/2}. \quad (2.9)$$

This rate is the same for both charged and neutral grains of radius $a \geq 10^{-6} \text{ cm}$ (the kind of grains we consider). Equation (2.9) is valid only if the velocity difference between a grain and a hydrogen molecule is smaller than the sound speed in the neutrals (Ciolek & Mouschovias 1993). Otherwise, one has to use

$$\langle \sigma_{\text{coll}} w \rangle_{\text{gH}_2} = \pi a^2 |\mathbf{v}_{\text{n}} - \mathbf{v}_{\text{g}}|. \quad (2.10)$$

By Newton's third law, i.e., $\mathbf{F}_{\text{ns}} = -\mathbf{F}_{\text{sn}}$, $\tau_{\text{ns}} = (\rho_{\text{n}}/\rho_{\text{s}})\tau_{\text{sn}}$.

The quantity $\mathbf{F}_{\gamma\delta,\text{inel}(k)}$ in equations (2.1f) – (2.1h) is the force per unit volume on grain fluid γ due to the conversion of dust particles of fluid δ into dust particles of fluid γ , with mass grain δm_{γ} (note that $m_{\gamma} = m_{\delta}$) via an inelastic process k , where k can be any one of the processes listed in Table 2.1 that involve grains. The momentum transferred to fluid γ

from fluid δ is

$$\Delta \mathbf{p} = |\delta m_\gamma| (\mathbf{v}_\delta - \mathbf{v}_\gamma), \quad (2.11)$$

and we can write

$$\mathbf{F}_{\gamma\delta,\text{inel}(k)} = m_\gamma \left| \frac{\partial n_\gamma}{\partial t} \right|_k (\mathbf{v}_\delta - \mathbf{v}_\gamma), \quad (2.12)$$

where the time rate of change of the number density of γ due to the inelastic process k is given by

$$\left| \frac{\partial n_\gamma}{\partial t} \right|_k = n_\eta n_\delta \langle \sigma_{\text{coll}} w \rangle_k = \frac{n_\delta}{\tau_{\delta\eta,\text{inel}}}, \quad (2.13)$$

and $\tau_{\delta\eta,\text{inel}}$ is the timescale for a particle δ to find a particle η and be converted into γ . Thus, in general, since $m_\gamma = m_\delta$,

$$\mathbf{F}_{\gamma\delta,\text{inel}(k)} = \frac{\rho_\delta}{\tau_{\delta\eta,\text{inel}}} (\mathbf{v}_\delta - \mathbf{v}_\gamma). \quad (2.14)$$

Furthermore, according to Newton's third law, the fluid δ will also experience an equal and opposite force

$$\mathbf{F}_{\delta\gamma,\text{inel}(k)} = -\mathbf{F}_{\gamma\delta,\text{inel}(k)} = \frac{\rho_\delta}{\tau_{\delta\eta,\text{inel}}} (\mathbf{v}_\gamma - \mathbf{v}_\delta). \quad (2.15)$$

The relevant timescales due to these inelastic processes are $\tau_{g_0e,\text{inel}} = (n_e \alpha_{eg_0})^{-1}$, $\tau_{g_0i,\text{inel}} = (n_i \alpha_{ig_0})^{-1}$, $\tau_{g_-i,\text{inel}} = (n_i \alpha_{ig_-})^{-1}$, $\tau_{g_+e,\text{inel}} = (n_e \alpha_{eg_+})^{-1}$, $\tau_{g_-g_+,\text{inel}} = (n_{g_+} \alpha_{g_+g_-})^{-1}$, $\tau_{g_+g_-,\text{inel}} = (n_{g_-} \alpha_{g_+g_-})^{-1}$, $\tau_{g_0g_\pm,\text{inel}} = (n_{g_\pm} \alpha_{g_\pm g_0})^{-1}$, and $\tau_{g_\pm g_0,\text{inel}} = (n_{g_0} \alpha_{g_\pm g_0})^{-1}$, where the reaction rates α_{eg_0} , α_{ig_0} , α_{ig_-} , α_{eg_+} , $\alpha_{g_+g_-}$, and $\alpha_{g_\pm g_0}$ are given in Appendix A.

In the force equations for the electrons, ions, and grains, the acceleration terms have been neglected due to the small inertia of these species. The acceleration term for the plasma was included by Mouschovias et al. (1985) and it was shown that the plasma reaches a terminal drift velocity very fast. Similarly, the thermal-pressure and gravitational forces have been dropped from the force equations of all species other than the neutrals because they are negligible compared to the electromagnetic and collisional forces. The inelastic momentum transfer by the electron and ion fluids due to attachment onto grains and neu-

tralization are negligible compared to the momentum transfer due to elastic collisions, and they have been omitted from the force equations (2.1d) and (2.1e) (see discussion in Ciolek & Mouschovias 1993, § 3.1). When considering a distribution of grain sizes, equations (2.1b), (2.1f) – (2.1h) apply to each grain size separately.

The full set of RMHD equations are closed with constitutive relations for the gas pressure, opacities, and the Planck function [i.e., $P_n = P_n(\rho_n, T)$, $\chi_{\mathcal{F}} = \chi_{\mathcal{F}}(\rho_g, T)$, $\kappa_{\mathcal{E}} = \kappa_{\mathcal{E}}(\rho_g, T)$, $\kappa_{\mathcal{P}} = \kappa_{\mathcal{P}}(\rho_g, T)$, and $\mathcal{B} = \mathcal{B}(T)$, where T is the gas temperature and $\rho_g \equiv \rho_{g-} + \rho_{g0} + \rho_{g+}$ is the total grain mass density]. In addition, we close the radiation moment equations with the tensor variable Eddington factor \mathbf{f} which is used to eliminate the radiation stress tensor \mathbf{P} in favor of the radiation energy density \mathcal{E} via

$$\mathbf{P} = \mathbf{f}\mathcal{E}. \quad (2.16)$$

The Eddington factor \mathbf{f} is determined by employing the FLD approximation (see § 2.6.1). The equation of state for an ideal gas is given by

$$P_n = (\gamma - 1)u_n, \quad (2.17)$$

where $\gamma = k_B/c_V + 1$ is the adiabatic index and c_V is the specific heat at constant volume per particle:

$$c_V = \frac{3}{2}k_B + c_V^{\text{vib}} + c_V^{\text{rot}}, \quad (2.18)$$

assuming that there is no coupling between the rotational and vibrational degrees of freedom of the molecule (in this case, H_2). The vibrational specific heat is

$$c_V^{\text{vib}} = k_B \left(\frac{\Theta_{\text{vib}}}{T} \right)^2 \frac{\exp(\Theta_{\text{vib}}/T)}{[\exp(\Theta_{\text{vib}}/T) - 1]^2}, \quad (2.19)$$

where $\Theta_{\text{vib}} = 6100 \text{ K}$; the rotational specific heat for a 3:1 mixture of ortho- and para-

hydrogen is

$$c_V^{\text{rot}} = \frac{3}{4}k_Bx^2 \frac{\partial^2}{\partial x^2} \ln Z_o + \frac{1}{4}k_Bx^2 \frac{\partial^2}{\partial x^2} \ln Z_p, \quad (2.20)$$

where Z_o and Z_p are the ortho- and para-hydrogen partition functions, respectively, given by

$$Z_o = \sum_{\text{odd } j} (2j + 1) \exp[-xj(j + 1)] \quad (2.21a)$$

$$Z_p = \sum_{\text{even } j} (2j + 1) \exp[-xj(j + 1)], \quad (2.21b)$$

and $x \equiv \Theta_{\text{rot}}/T = 85.4 \text{ K}/T$ (Kittel 1958). The dependence of γ on temperature T is shown in Figure 2.1.

Altogether, then, we have a system of 17 equations [(2.1a) – (2.1o), (2.16), and (2.17)], which contain 21 unknowns ($\rho_n, P_n, u_n, \mathbf{E}, \mathbf{B}, \mathbf{j}, \psi, \mathbf{v}_n, \mathbf{v}_e, \mathbf{v}_i, \mathbf{v}_{g-}, \mathbf{v}_{g+}, \mathbf{v}_{g0}, \rho_e, \rho_i, \rho_{g-}, \rho_{g+}, \rho_{g0}, \mathcal{E}, \mathcal{F}, \mathbf{P}$). To close the system, the densities of electrons, ions, and charged grains ($n_e, n_i, n_{g-},$ and n_{g+}) are calculated from the chemical-equilibrium model detailed below.

2.4 The Chemical Model

2.4.1 Ionization Rate

The rate of ionization per unit volume is given by ζn_{H_2} and is (in principle) due to the following ionization sources: UV radiation, cosmic rays, radioactivities, and thermal ionization. The presence of molecules in molecular clouds implies low levels of UV radiation, so it is usually neglected. UV radiation was included by Ciolek & Mouschovias (1995) in their numerical simulations of core formation and evolution. They found that UV ionization dominates cosmic-ray ionization for visual extinctions $A_V \lesssim 10$ and can increase the degree of ionization in the envelope by at least 2 orders of magnitude (see also McKee 1989). The increase in ionization was found to *speed up* core collapse by approximately 30% because the central gravitational field of a flattened cloud is stronger (i.e., less diluted by the

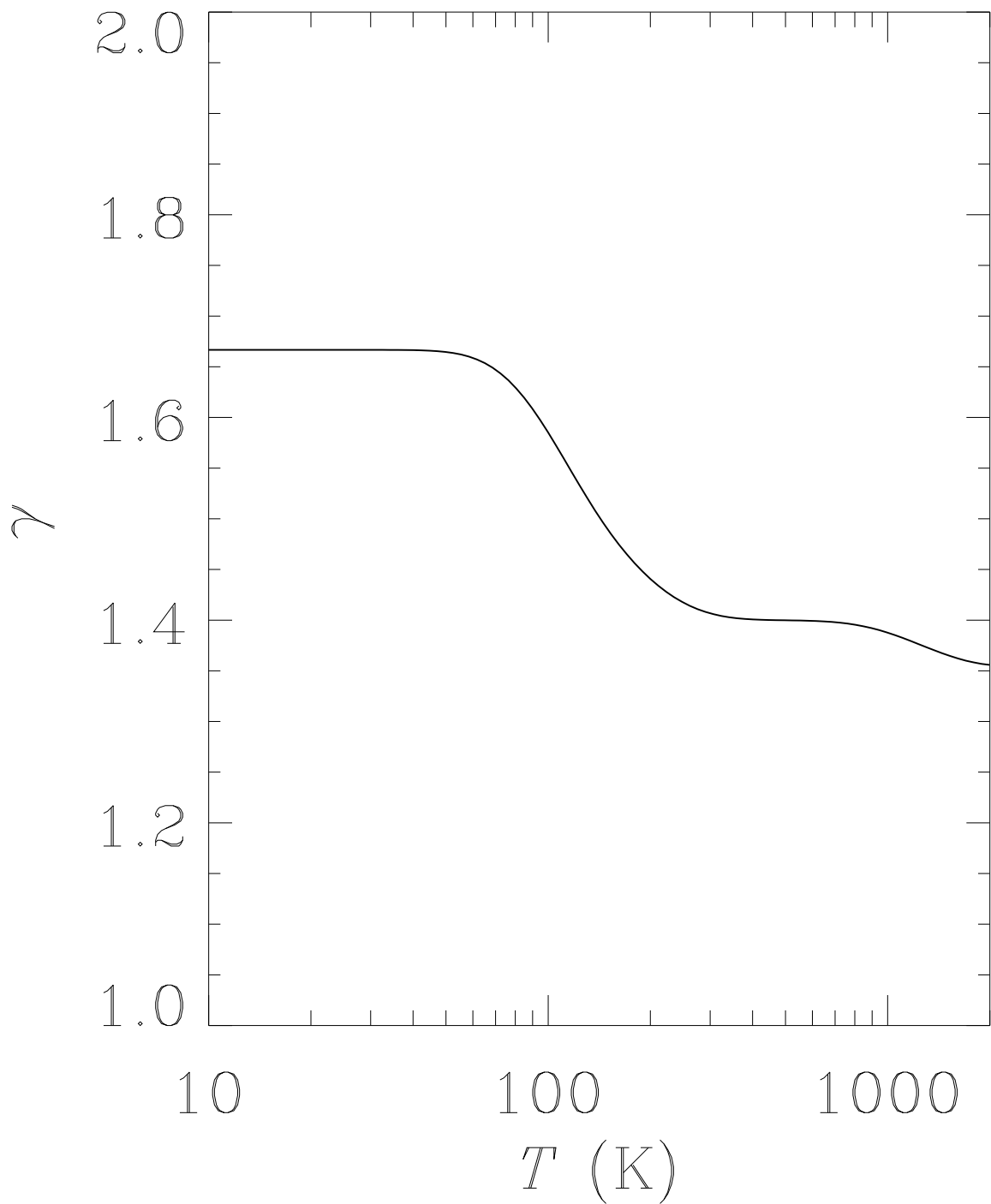


Figure 2.1: Dependence of γ (ratio of specific heats) on temperature T for H_2 .

mass of the envelope) when matter in the envelope is held farther away from the forming core. Once dynamical contraction ensues, it was found that UV radiation has little effect on the evolution of central quantities and therefore it is usually neglected. For numerical reasons, however, we add to the electron and ion number densities the second term in equation (4h) of Fiedler & Mouschovias (1992) ($= 467.64 n_{\text{H}_2}^{-2} \text{ cm}^{-3}$) so as to maintain a relatively large degree of ionization ($\sim 10^{-5} - 10^{-6}$) (and therefore negligible ambipolar diffusion) in the low-density ($n_{\text{H}_2} \lesssim 10^3 \text{ cm}^{-3}$) cloud envelope. This term qualitatively mimics the effect of cloud envelope penetration by UV photons, and has negligible quantitative effect on the formation and evolution of the core.

Cosmic rays, on the other hand, with typical energies of 100 MeV are able to penetrate deeper into molecular clouds. Umebayashi & Nakano (1980) have investigated the ionization due to a spectrum of cosmic rays. They found that the cosmic-ray ionization rate was well described by the following relation:

$$\zeta_{\text{CR}} = \zeta_0 \exp(-\Sigma_{\text{H}_2}/96 \text{ g cm}^{-2}), \quad (2.22)$$

where Σ_{H_2} is the column density of H_2 separating the point in question from the exterior of the cloud and $\zeta_0 = 5 \times 10^{-17} \text{ s}^{-1}$ is the canonical unshielded cosmic-ray ionization rate (Spitzer 1978). Tassis & Mouschovias (2007b) found that, when a typical core's central density exceeds $\simeq 10^{12} \text{ cm}^{-3}$, cosmic rays are shielded and an abrupt decrease in ionization occurs.

Once the core is shielded from high-energy cosmic rays, the dominant source of ionization is radioactive decay of ^{40}K or ^{26}Al . The isotope ^{40}K is the most common radionuclide invoked, due to its long half-life of 1.25 Gyr and its ubiquity in nature (0.012% of terrestrial potassium is ^{40}K). The density of potassium in the interstellar medium ($2.70 \times 10^{-7} n_{\text{H}_2}$) and the energy of the beta particle emitted as ^{40}K decays, 1.31 MeV, are used as inputs to calculate the ionization rate (e.g., see Glassgold 1995): $\zeta_{40} = 2.43 \times 10^{-23} \text{ s}^{-1}$. Con-

solmagno & Jokipii (1978) have suggested that ^{26}Al may have been a much more potent ionizer than ^{40}K . Performing a similar calculation for ^{26}Al , one finds $\zeta_{26} = 1.94 \times 10^{-19} \text{ s}^{-1}$, with the fraction of aluminum in the isotope ^{26}Al inferred to have existed in the solar nebula being 5×10^{-5} (Clayton & Leising 1987). Although ^{26}Al is four orders of magnitude more potent an ionizer than ^{40}K , its short half-life (0.716 Myr) makes it relevant only if the initial mass-to-flux ratio of the parent cloud is close to critical, so that the evolution is rapid enough to retain an adequate amount of this radionuclide. ^{26}Al can also become important if the core happens to get enriched because of a nearby Supernova explosion.

Finally, at temperatures on the order of 1000 K or higher, collisions between molecules are energetic enough to ionize those atoms with low ionization potentials, of which potassium and sodium are the most abundant. The abundance of sodium in the interstellar medium is greater than that of potassium (by a factor $\simeq 14$; Lequeux 1975), but the lower threshold of potassium (4.34 eV vs. 5.13 eV for sodium) makes it the dominant ion. The ionization occurs at a rate (Pneuman & Mitchell 1965) given by

$$\frac{d}{dt}(n_{\text{K}^+}) = 4.1 \times 10^{-15} n_{\text{H}_2} n_{\text{K}^0} \left(\frac{T}{1000 \text{ K}} \right)^{1/2} \exp \left(-\frac{5.04 \times 10^4 \text{ K}}{T} \right) \text{ cm}^3 \text{ s}^{-1}. \quad (2.23)$$

Because this process relies on collisions between two species, it is not expressed in terms of a quantity ζ .

2.4.2 Grain Size Distribution

Since the dust opacity, the conductivity of the gas, and the collision rates (see below) all depend on the (local) grain surface area, it is necessary to investigate the effect of a grain size distribution. The initial size distributions adopted here are a uniform distribution and the standard ‘‘MRN’’ distribution of interstellar dust (Mathis et al. 1977). In both cases, the density of the solid material of each grain is taken to be $\rho_{\text{S}} = 2.3 \text{ g cm}^{-3}$, the average density of silicates. For the uniform distribution, a fiducial grain size $a_0 = 0.0375 \text{ }\mu\text{m}$ is

used and the total mass density of dust $\rho_{g,\text{tot}} = 0.01\rho_{n,\text{tot}}$. For the MRN distribution, the number density of spherical dust grains with radii between a and $a + da$ is

$$dn_{g,\text{tot}}(a) = N_{\text{MRN}}a^{-3.5}da. \quad (2.24)$$

The distribution is truncated at a lower grain radius a_{min} and an upper grain radius a_{max} . The coefficient N_{MRN} is proportional to the dust-to-gas mass ratio in the cloud. Note that most of the grain surface area is contributed by small grains, because of their overwhelming abundance.

The grains are binned according to size and charge and treated as separate grain species. Each size bin represents a subset of the original distribution of grains, those with radii between a_{lower} and a_{upper} . The subset of grains in the α th ($\alpha = 1, 2, \dots, N$) size bin is replaced by a number density n_g^α of grains with identical radii, a_α . The total number of grains and the total surface area of grains in the size bin are constrained to match the total number and surface area of original grains incorporated into the size bin. Hence

$$n_g^\alpha = \int_{a_{\text{lower}}}^{a_{\text{upper}}} \frac{dn_{g,\text{tot}}}{da} da, \quad (2.25a)$$

$$n_g^\alpha a_\alpha^2 = \int_{a_{\text{lower}}}^{a_{\text{upper}}} a^2 \frac{dn_{g,\text{tot}}}{da} da. \quad (2.25b)$$

Applying these relations to the MRN grain size distribution, equation (2.24), if there are N size bins, then the α th bin is characterized by grains of number density and radii as follows:

$$n_g^\alpha = n_{g,\text{tot}} \xi^{2.5(\alpha-1)/N} \left(\frac{1 - \xi^{2.5/N}}{1 - \xi^{2.5}} \right), \quad (2.26a)$$

$$a_\alpha = a_{\text{min}} \xi^{-(\alpha-1)/N} \left[5 \left(\frac{1 - \xi^{0.5/N}}{1 - \xi^{2.5/N}} \right) \right]^{1/2}. \quad (2.26b)$$

The ratio of the lower and upper radii of the distribution is denoted by $\xi \equiv a_{\text{min}}/a_{\text{max}}$. The total number density of dust, $n_{g,\text{tot}}$, is determined by constraining the total grain mass

density in the size distribution to be $\rho_{g,\text{tot}}$:

$$n_{g,\text{tot}} = \left(\frac{\rho_{g,\text{tot}}}{\frac{4}{3}\pi\rho_S a_{\text{min}}^3} \right) \left[\frac{1}{5} \left(\frac{1 - \xi^{2.5}}{1 - \xi^{0.5}} \right) \right] \xi^{0.5}. \quad (2.27)$$

The lower and upper cutoffs to the size distribution are chosen to be $a_{\text{min}} = 0.0181 \mu\text{m}$ and $a_{\text{max}} = 0.9049 \mu\text{m}$, respectively. In equation (2.27), the total mass density of dust in the system, $\rho_{g,\text{tot}}$, is chosen in such a way that the total grain surface area in the size distribution is equal to that in the fiducial case of a single grain size a_0 . This constraint demands that $\rho_{g,\text{tot}}$ be increased by a factor $(a_{\text{min}}/a_0) \xi^{-0.5}$ over the fiducial value of $\rho_{g,\text{tot}}$. Only in this way can the effect of a size distribution, as distinct from just the surface area of grains, be determined. With the fiducial values $a_0 = 0.0375 \mu\text{m}$ and $\rho_{g,\text{tot}} = 0.01\rho_{n,\text{tot}}$ for the single grain case, $\rho_{g,\text{tot}} = 0.0341\rho_{n,\text{tot}}$ for the case of a size distribution. Empirically, it was found that a minimum of five size bins of grain radii were required for convergence of 1%. Since each size grain can be found in one of three possible charge states ($-e$, 0 , and $+e$), a total of 15 grain species are considered.

While we do not consider grain growth (and therefore fix the number of grains within each size bin), we do expect the grain size distribution to evolve spatially within the star-forming cloud. Ambipolar diffusion can alter a grain size distribution by acting more effectively on the larger grains, causing a spatial segregation of grain sizes that leaves the smaller grains behind in the cloud envelope. The result is a deficit of small grains ($a \lesssim 10^{-5} \text{ cm}$) in the cloud core. In fact, Ciolek & Mouschovias (1996) show how observations of grain abundances in the core and envelope of a molecular cloud can, at least in principle, be used to determine the initial mass-to-flux ratio of the cloud.

2.4.3 Chemical Network

We use a chemical-equilibrium network accounting for electrons (subscript e); molecular ions such as HCO^+ (subscript m⁺); neutral metal atoms (subscript A⁰) and atomic

ions (subscript A^+) of Mg, Na, and K; singly positively-charged grains (subscript g_+); singly negatively-charged grains (subscript g_-); and, neutral grains (subscript g_0). Multiply negatively- (positively-)charged grains may be neglected, because a singly negatively- (positively-)charged grain repels electrons (ions) thereby decreasing the rate of capture by the factor $\exp(-e^2/ak_B T)$ (Spitzer 1941). The equilibrium assumption is accurate provided that the dynamical timescales of interest are sufficiently longer than the chemical-reaction timescales. This is always the case for the density regime considered here. The relevant reactions are given below and explained briefly.

The production of molecular ions (such as HCO^+) is balanced by their destruction through charge-exchange reactions with atomic ions, by dissociative recombinations (collisions with electrons), or by collisions with and neutralization on the surfaces of grains:

$$\zeta n_{\text{H}_2} = n_{\text{m}+} n_{\text{A}^0} \beta + n_{\text{m}+} n_{\text{e}} \alpha_{\text{dr}} + \sum_{\alpha} n_{\text{m}+} n_{\text{g}_-^{\alpha}} \alpha_{\text{m}+ \text{g}_-^{\alpha}} + \sum_{\alpha} n_{\text{m}+} n_{\text{g}_0^{\alpha}} \alpha_{\text{m}+ \text{g}_0^{\alpha}}. \quad (2.28)$$

The index α denotes a grain size bin, and the sum is over all the size bins, which are treated as independent grain species. The production of atomic ions by charge-exchange reactions is balanced by radiative recombinations and by collisions with grains:

$$n_{\text{m}+} n_{\text{A}^0} \beta = n_{\text{A}^+} n_{\text{e}} \alpha_{\text{rr}} + \sum_{\alpha} n_{\text{A}^+} n_{\text{g}_-^{\alpha}} \alpha_{\text{A}^+ \text{g}_-^{\alpha}} + \sum_{\alpha} n_{\text{A}^+} n_{\text{g}_0^{\alpha}} \alpha_{\text{A}^+ \text{g}_0^{\alpha}}. \quad (2.29)$$

If the atomic ion in question is K^+ , there is the additional source term due to thermal ionization of potassium atoms, $n_{\text{K}^0} n_{\text{H}_2} \alpha_{\text{K}^0 \text{H}_2}$. Positively-charged grains are formed by the collisions of ions and neutral grains and by charge exchange between grains; they are destroyed by collisions with electrons, collisions with negative grains, and by charge exchange with

neutral grains:

$$\begin{aligned}
& n_{m^+} n_{g_0^\alpha} \alpha_{m^+ g_0^\alpha} + n_{A^+} n_{g_0^\alpha} \alpha_{A^+ g_0^\alpha} + \sum_{\alpha'} n_{g_+^{\alpha'}} n_{g_0^\alpha} \alpha_{g_+^{\alpha'} g_0^\alpha} \\
& = n_e n_{g_+^\alpha} \alpha_{e g_+^\alpha} + \sum_{\alpha'} n_{g_+^\alpha} n_{g_-^{\alpha'}} \alpha_{g_+^\alpha g_-^{\alpha'}} + \sum_{\alpha'} n_{g_+^\alpha} n_{g_0^{\alpha'}} \alpha_{g_+^\alpha g_0^{\alpha'}} .
\end{aligned} \tag{2.30}$$

Here the index α' runs over all the grain size bins, independently of the index α . Negatively-charged grains are formed by the collisions of electrons and neutral grains and by charge exchange between grains, and are destroyed by collisions with ions, collisions with positive grains, and by charge exchange with neutral grains:

$$\begin{aligned}
& n_e n_{g_0^\alpha} \alpha_{e g_0^\alpha} + \sum_{\alpha'} n_{g_-^{\alpha'}} n_{g_0^\alpha} \alpha_{g_-^{\alpha'} g_0^\alpha} \\
& = n_{m^+} n_{g_-^\alpha} \alpha_{m^+ g_-^\alpha} + n_{A^+} n_{g_-^\alpha} \alpha_{A^+ g_-^\alpha} + \sum_{\alpha'} n_{g_+^{\alpha'}} n_{g_-^\alpha} \alpha_{g_+^{\alpha'} g_-^\alpha} + \sum_{\alpha'} n_{g_-^\alpha} n_{g_0^{\alpha'}} \alpha_{g_-^\alpha g_0^{\alpha'}} .
\end{aligned} \tag{2.31}$$

We close this set of equations with constraints on the total number of grains in a given size bin,

$$n_{g_+^\alpha} + n_{g_0^\alpha} + n_{g_-^\alpha} = n_{g^\alpha} , \tag{2.32}$$

and the total number of an atomic species (neutral + positively-charged),

$$n_{A^0} + n_{A^+} = n_A , \tag{2.33}$$

and with charge neutrality:

$$n_{m^+} + n_{A^+} - n_e + \sum_{\alpha} (n_{g_+^\alpha} - n_{g_-^\alpha}) = 0 . \tag{2.34}$$

The rate coefficients in equations (2.28) – (2.34) are given in Appendix A.

The mass of molecular ions is taken to be that of HCO^+ , $m_{m^+} = 29 m_p$, while for the

atomic ions an average value $m_{A^+} = 23.5 m_p$, between the mass of Na ($m_{Na^+} = 23 m_p$) and the mass of Mg ($m_{Mg^+} = 24 m_p$), is used. Since the ion masses are all comparable, the fact that different ionic species dominate in different density regimes does not affect the evolution of the cloud cores. The total number density of metals (neutral + ionized) is fixed at $n_A = 2.05 \times 10^{-6} n_n$ (Morton 1974; Snow 1976).

2.5 Magnetic Flux Loss and Electrical Resistivity

The force equations (2.1d) – (2.1h) and the induction equation (2.1k) are not written in the most convenient form for our purposes. A useful simplification can be made, which amounts to a generalized version of Ohm’s law; namely, we replace equations (2.1d) – (2.1h) with a modified form of equation (2.1k). This auspiciously eliminates five variables ($\mathbf{v}_e, \mathbf{v}_i, \mathbf{v}_{g_0}, \mathbf{v}_{g_-},$ and \mathbf{v}_{g_+}), but not without a cost. The ensuing algebra is messy, and much of it is deferred to Appendix B.1. Here, we outline the simplification and highlight some results suitable for the present discussion.

2.5.1 Resistivity of a Magnetic Gas

The rate of change of magnetic flux across a surface S , comoving with a fluid with velocity \mathbf{v} , is given by

$$\frac{d\Phi_B}{dt} = \int_S \left[\frac{\partial \mathbf{B}}{\partial t} - \nabla \times (\mathbf{v} \times \mathbf{B}) \right] \cdot d\mathbf{S}. \quad (2.35)$$

Using Faraday’s law (2.1k), the integrand can be rewritten as

$$\frac{d\Phi_B}{dt} = -c \int_S \nabla \times \left(\mathbf{E} + \frac{\mathbf{v}}{c} \times \mathbf{B} \right) \cdot d\mathbf{S}, \quad (2.36)$$

and the current density can be calculated from

$$\mathbf{j} = \sigma \left(\mathbf{E} + \frac{\mathbf{v}}{c} \times \mathbf{B} \right). \quad (2.37)$$

The quantity \mathbf{v} is the velocity of the fluid, which for a weakly-ionized gas is essentially that of the neutrals \mathbf{v}_n , and $\boldsymbol{\sigma}$ is the conductivity tensor. The presence of a magnetic field introduces an anisotropy in the equations, which is the reason for which the conductivity must be described by a tensor. If we take the 3-direction to lie along the magnetic field, the conductivity tensor has the following representation (Parks 1991):

$$\boldsymbol{\sigma} = \begin{pmatrix} \sigma_{\perp} & -\sigma_{\text{H}} & 0 \\ \sigma_{\text{H}} & \sigma_{\perp} & 0 \\ 0 & 0 & \sigma_{\text{H}} \end{pmatrix}. \quad (2.38)$$

As $B \rightarrow 0$, the tensor must reduce to an isotropic form; i.e., $\sigma_{\text{H}} \rightarrow 0$ and $\sigma_{\perp} \rightarrow \sigma_{\parallel}$. Because magnetic forces vanish along the magnetic field, σ_{\parallel} must be independent of the magnetic field strength.

Equation (2.37) may be inverted to obtain the electric field, in which case a resistivity tensor $\boldsymbol{\eta}$ is defined by

$$\mathbf{E} + \frac{\mathbf{v}_n}{c} \times \mathbf{B} = \boldsymbol{\eta} \mathbf{j}, \quad (2.39)$$

where, in the same representation as $\boldsymbol{\sigma}$ written above,

$$\boldsymbol{\eta} = \begin{pmatrix} \eta_{\perp} & \eta_{\text{H}} & 0 \\ -\eta_{\text{H}} & \eta_{\perp} & 0 \\ 0 & 0 & \eta_{\parallel} \end{pmatrix}, \quad (2.40)$$

and

$$\eta_{\parallel} = \frac{1}{\sigma_{\parallel}}, \quad (2.41a)$$

$$\eta_{\perp} = \frac{\sigma_{\perp}}{\sigma_{\perp}^2 + \sigma_{\text{H}}^2}, \quad (2.41b)$$

$$\eta_{\text{H}} = \frac{\sigma_{\text{H}}}{\sigma_{\perp}^2 + \sigma_{\text{H}}^2}. \quad (2.41c)$$

The flux-freezing approximation corresponds to the limit $\boldsymbol{\eta} \rightarrow 0$.

If we write the current density \mathbf{j} in component form, it follows that we may write equation (2.39) as

$$\mathbf{E} + \frac{\mathbf{v}_n}{c} \times \mathbf{B} = \eta_{\parallel} \mathbf{j}_{\parallel} + \eta_{\perp} \mathbf{j}_{\perp} + \eta_H \mathbf{j} \times \mathbf{b}, \quad (2.42)$$

where \mathbf{j}_{\parallel} and \mathbf{j}_{\perp} are the components of the current density parallel and perpendicular to the magnetic field, respectively, and \mathbf{b} is a unit vector along the magnetic field. This relation between the electric field and the current density can be substituted in equation (2.36) to find that

$$\frac{d\Phi_B}{dt} = -c \int_S \nabla \times (\eta_{\parallel} \mathbf{j}_{\parallel} + \eta_{\perp} \mathbf{j}_{\perp} + \eta_H \mathbf{j} \times \mathbf{b}) \cdot d\mathbf{S}. \quad (2.43)$$

This is the general form of the equation describing the loss of magnetic flux from a parcel of neutral gas, written entirely in terms of the components of the resistivity tensor and current density.

For our model cloud, we have assumed axisymmetry and neglected rotation. In this case, the magnetic field is purely poloidal and the current density is purely toroidal by Ampere's law (2.1i). This geometry implies that the only nonvanishing component of the current density is the component perpendicular to the magnetic field, $\mathbf{j} = \mathbf{j}_{\perp}$. The evolution of the poloidal magnetic flux in the neutrals' reference frame is then given by

$$\frac{d\Phi_B}{dt} = -c \int_S \nabla \times (\eta_{\perp} \mathbf{j}_{\perp}) \cdot d\mathbf{S}. \quad (2.44)$$

The equivalent equation governing the evolution of the poloidal magnetic field is

$$\frac{\partial \mathbf{B}}{\partial t} = \nabla \times (\mathbf{v}_n \times \mathbf{B}) - c \nabla \times (\eta_{\perp} \mathbf{j}_{\perp}). \quad (2.45)$$

Equation (2.44) describes the evolution of magnetic flux in the neutrals' reference frame due to the motion of charges at right angles to the magnetic field and includes the effects of both ambipolar diffusion and Ohmic dissipation. The rate at which magnetic flux is lost equals the sum of the rates due to each process. Therefore, η_{\perp} can itself be written as the

sum of two components, one related to ambipolar diffusion (subscript AD) and the other to Ohmic dissipation (subscript OD):

$$\eta_{\perp} = \eta_{\perp\text{AD}} + \eta_{\perp\text{OD}}. \quad (2.46)$$

The issue of how to separate the resistivity η_{\perp} into its two components is discussed, for example, in Nakano & Umebayashi (1986a,b), Goldreich & Reisenegger (1992), and Desch & Mouschovias (2001). We quote the result here:

$$\eta_{\parallel\text{OD}} = \eta_{\parallel}, \quad (2.47\text{a})$$

$$\eta_{\perp\text{OD}} = \eta_{\parallel}, \quad (2.47\text{b})$$

$$\eta_{\parallel\text{AD}} = 0, \quad (2.47\text{c})$$

$$\eta_{\perp\text{AD}} = \eta_{\perp} - \eta_{\parallel}. \quad (2.47\text{d})$$

We now derive expressions for the resistivities from first principles.

2.5.2 Generalized Ohm's Law

We outline the derivation of a generalized Ohm's law, taking into account both elastic and inelastic collisions between neutrals, ions, electrons, and charged and neutral grains. We begin by writing the force equation for the charged species s :

$$0 = n_s q_s \left(\mathbf{E} + \frac{\mathbf{v}_s}{c} \times \mathbf{B} \right) + \frac{\rho_s}{\tau_{sn}} (\mathbf{v}_n - \mathbf{v}_s) + \frac{\rho_{g_0}}{\tau_{s,\text{inel}}} (\mathbf{v}_{g_0} - \mathbf{v}_s). \quad (2.48)$$

The subscript s runs over all the charged species, taking on the values $s = i, e, g_+,$ and g_- . Although we employ a grain size distribution, we consider only a single grain size in what follows for ease of presentation; a discussion of the consequences of a grain size distribution is deferred to Appendix B.2. The charge q_s of species s carries an algebraic

sign (e.g., it is negative for electrons). We write $\tau_{s,\text{inel}}$ to represent the timescale for species s to be created by or take part in any inelastic collision. For example,

$$\tau_{g^+, \text{inel}} = \left[\frac{1}{\tau_{g_0 i, \text{inel}}} + \frac{1}{\tau_{g_0 g^+, \text{inel}}} + \frac{\rho_{g^+}}{\rho_{g_0}} \left(\frac{1}{\tau_{g^+ e, \text{inel}}} + \frac{1}{\tau_{g^+ g^-, \text{inel}}} + \frac{1}{\tau_{g^+ g_0, \text{inel}}} \right) \right]^{-1} \quad (2.49)$$

is the timescale for a neutral grain to participate in *any* inelastic reaction involving conversion between positive and neutral grains. The first two terms represent the production of positive grains due to charge exchange between neutral grains and ions and between neutral grains and positive grains, respectively; the next two terms represent the conversion of positive grains to neutral grains via neutralization with electrons and negative grains, respectively; and, the final term represents the conversion of positive grains to neutral grains via charge exchange. Since these are processes occurring in parallel, the reciprocals of their respective collision times are added to obtain the net collision time. Similarly,

$$\tau_{g^-, \text{inel}} = \left[\frac{1}{\tau_{g_0 e, \text{inel}}} + \frac{1}{\tau_{g_0 g^-, \text{inel}}} + \frac{\rho_{g^-}}{\rho_{g_0}} \left(\frac{1}{\tau_{g^- i, \text{inel}}} + \frac{1}{\tau_{g^- g^+, \text{inel}}} + \frac{1}{\tau_{g^- g_0, \text{inel}}} \right) \right]^{-1} \quad (2.50)$$

is the timescale for a neutral grain to be involved in *any* inelastic reaction involving conversion between negative and neutral grains. The force equation for the neutral grains is

$$0 = \frac{\rho_{g_0}}{\tau_{g_0 n}} (\mathbf{v}_n - \mathbf{v}_{g_0}) + \sum_k \frac{\rho_{g_0}}{\tau_{k, \text{inel}}} (\mathbf{v}_k - \mathbf{v}_{g_0}), \quad (2.51)$$

where the index k runs over all the charged species.

We eliminate the velocity \mathbf{v}_s of species s in favor of a new velocity, \mathbf{w}_s , which is the velocity of species s with respect to the neutral gas ($\mathbf{w}_s \equiv \mathbf{v}_s - \mathbf{v}_n$). In addition, we define \mathbf{E}_n as the electric field in the frame of reference of the neutral gas ($\mathbf{E}_n \equiv \mathbf{E} + \mathbf{v}_n \times \mathbf{B}/c$). Equations (2.48) and (2.51) then become, respectively,

$$0 = \frac{\omega_s \tau_{sn}}{1 + \varrho_s} \left(\frac{c}{B} \mathbf{E}_n + \mathbf{w}_s \times \mathbf{b} \right) - \mathbf{w}_s + \frac{\varrho_s}{1 + \varrho_s} \mathbf{w}_{g_0}, \quad (2.52)$$

$$0 = \mathbf{w}_{g_0} - \sum_k \frac{\tau_0}{\tau_{k,\text{inel}}} \mathbf{w}_k, \quad (2.53)$$

where we have introduced the cyclotron frequency of species s , $\omega_s = q_s B / m_s c$, and have defined ϱ_s and τ_0 by

$$\varrho_s = \frac{\rho_{g_0}}{\rho_s} \frac{\tau_{sn}}{\tau_{s,\text{inel}}} \quad (2.54a)$$

$$\frac{1}{\tau_0} = \frac{1}{\tau_{g_0n}} + \sum_k \frac{1}{\tau_{k,\text{inel}}}. \quad (2.54b)$$

Equations (2.52) and (2.53) form the set of equations to be solved.⁴ The species velocities (relative to the neutrals) \mathbf{w}_s can be expressed in terms of \mathbf{E}_n and then substituted in the definition of the current density

$$\mathbf{j} = \sum_s n_s q_s \mathbf{w}_s, \quad (2.55)$$

where we have used charge neutrality ($\sum_s n_s q_s = 0$). This expression can then be inverted to find \mathbf{E}_n in terms of \mathbf{j} , which defines the resistivity tensor. The magnetic induction equation is then found by substitution into Faraday's law of induction:

$$\frac{\partial \mathbf{B}}{\partial t} - \nabla \times (\mathbf{v}_n \times \mathbf{B}) = -c \nabla \times \mathbf{E}_n. \quad (2.56)$$

Using this approach, we derive an induction equation generalized to include Ohmic dissipation, ambipolar diffusion, and the Hall effect for a six-fluid system including both elastic and inelastic collisions.

The ensuing calculation is tedious, and we defer the details to Appendix B.1. Here we give only the final result:

$$\mathbf{j} = \sigma_{\parallel} \mathbf{E}_{n,\parallel} + \sigma_{\perp} \mathbf{E}_{n,\perp} - \sigma_H \mathbf{E}_n \times \mathbf{b}, \quad (2.57)$$

⁴The quantity ϱ_s was written as r_s in Tassis & Mouschovias (2007a). We have renamed it here to avoid confusion with the cylindrical radial coordinate r .

where

$$\sigma_{\parallel} = \sum_s \sigma_s (1 - \zeta_s), \quad (2.58a)$$

$$\sigma_{\perp} = \sum_s \frac{\sigma_s (1 - \zeta_s)}{1 + \omega_s^2 \tau_{sn}^2 (1 - \varphi_s)} \Upsilon_s(\zeta), \quad (2.58b)$$

$$\sigma_H = - \sum_s \frac{\sigma_s \omega_s \tau_{sn} (1 - \varpi_s)}{1 + \omega_s^2 \tau_{sn}^2 (1 - \varphi_s)} \Upsilon_s(\varpi). \quad (2.58c)$$

The conductivity of species s is given by $\sigma_s = n_s q_s^2 \tau_{sn} / m_s$. The quantities ζ_s , ϖ_s , φ_s , and Υ_s are defined in Appendix D; they represent the effects of inelastic collisions on the conductivity of the gas. In the absence of inelastic collisions, these formulae reduce to their standard form (e.g., see Parks 1991):

$$\sigma_{\parallel} \rightarrow \sum_s \sigma_s, \quad \sigma_{\perp} \rightarrow \sum_s \frac{\sigma_s}{1 + \omega_s^2 \tau_{sn}^2}, \quad \sigma_H \rightarrow - \sum_s \frac{\sigma_s \omega_s \tau_{sn}}{1 + \omega_s^2 \tau_{sn}^2}.$$

Equation (2.57) may be inverted to give

$$\mathbf{E}_n = \eta_{\parallel} \mathbf{j}_{\parallel} + \eta_{\perp} \mathbf{j}_{\perp} + \eta_H \mathbf{j} \times \mathbf{b}, \quad (2.59)$$

with the resistivities η_{\parallel} , η_{\perp} , and η_H given by equations (2.41).

2.5.3 Attachment of Species to Magnetic Field Lines

It is possible to write the velocity of each species, \mathbf{v}_s , in terms of the velocity of the neutrals, \mathbf{v}_n , and the velocity of the field lines, \mathbf{v}_f , which is defined implicitly by

$$\mathbf{E} + \frac{\mathbf{v}_f}{c} \times \mathbf{B} = 0. \quad (2.60)$$

The algebra and some intermediate results of interest are given in Appendix C; here, we quote the main result and explain it physically:

$$\mathbf{v}_{s,\perp} = \mathbf{v}_{n,\perp} \frac{1}{\Theta_s + 1} + \mathbf{v}_{f,\perp} \frac{\Theta_s}{\Theta_s + 1} + (\mathbf{v}_f - \mathbf{v}_n) \times \mathbf{b} \Lambda_s, \quad (2.61a)$$

$$\mathbf{v}_s \times \mathbf{b} = \mathbf{v}_n \times \mathbf{b} \frac{1}{\Theta_s + 1} + \mathbf{v}_f \times \mathbf{b} \frac{\Theta_s}{\Theta_s + 1} - (\mathbf{v}_{f,\perp} - \mathbf{v}_{n,\perp}) \Lambda_s, \quad (2.61b)$$

where the expressions for Θ_s and Λ_s are given in Appendix C. The quantity Θ_s is the *attachment parameter* (i.e., for $\Theta_s \gg 1$, $\mathbf{v}_s \approx \mathbf{v}_f$ and species s is attached to the field lines, whereas for $\Theta_s \ll 1$, $\mathbf{v}_s \approx \mathbf{v}_n$ and species s is detached and comoves with the neutrals) — see, also, Ciolek & Mouschovias (1993, § 3.1.2). The function Λ_s quantifies the relation of one component of the species velocity to its mutually perpendicular component of the field line drift velocity, and essentially embodies Ampere’s law. Under the assumptions of this paper, the midplane velocities of the charged species s , written in cylindrical coordinates (r, ϕ, z) , are

$$\mathbf{v}_{s,\phi}(r, z = 0) = (\mathbf{v}_{n,r} - \mathbf{v}_{f,r}) \Lambda_s, \quad (2.62a)$$

$$\mathbf{v}_{s,r}(r, z = 0) = \mathbf{v}_{n,r} \frac{1}{\Theta_s + 1} + \mathbf{v}_{f,r} \frac{\Theta_s}{\Theta_s + 1}. \quad (2.62b)$$

The first equation says that the charged species move in such a way as to cause differential motion between the field lines and the neutrals (Ampere’s law). The second equation gives the radial velocity of any charged species in terms of the velocities of the neutrals and of the field lines. These may be combined to yield

$$\mathbf{w}_{s,r} = \mathbf{v}_{s,r} - \mathbf{v}_{n,r} = -\frac{\Theta_s}{\Theta_s + 1} \frac{\mathbf{v}_{s,\phi}}{\Lambda_s}. \quad (2.63)$$

In other words, the radial drift between species s and the neutrals is directly proportional to the contribution of species s to the azimuthal current.

2.5.4 Grain Continuity Equation

In the notation of Section 2.5.2, the grain continuity equation (2.1b) may be written as

$$\frac{\partial \rho_g}{\partial t} + \nabla \cdot (\rho_g \mathbf{v}_n) = -\nabla \cdot (\rho_{g-} \mathbf{w}_{g-} + \rho_{g_0} \mathbf{w}_{g_0} + \rho_{g+} \mathbf{w}_{g+}), \quad (2.64)$$

where $\rho_g = \rho_{g-} + \rho_{g_0} + \rho_{g+}$ is the total grain density. Eliminating \mathbf{w}_{g_0} using equation (2.53), we find that

$$\frac{\partial \rho_g}{\partial t} + \nabla \cdot (\rho_g \mathbf{v}_n) = -\nabla \cdot \left[\rho_{g+} \mathbf{w}_{g+} \left(1 + \frac{\tau_0}{\tau_{g+n}} \varrho_{g+} \right) + \rho_{g-} \mathbf{w}_{g-} \left(1 + \frac{\tau_0}{\tau_{g-n}} \varrho_{g-} \right) \right]. \quad (2.65)$$

We may use equation (C.1) to eliminate the differential velocities of the charged grain species to find, after some manipulation,

$$\frac{\partial \rho_g}{\partial t} + \nabla \cdot (\rho_g \mathbf{v}_n) = -\nabla \cdot (\eta_{\text{cont},\parallel} \mathbf{j}_{\parallel} + \eta_{\text{cont},\perp} \mathbf{j}_{\perp} + \eta_{\text{cont},\text{H}} \mathbf{j} \times \mathbf{b}), \quad (2.66)$$

where the components of the grain-continuity resistivity tensor, η_{cont} , are defined as

$$\eta_{\text{cont},\parallel} = \sum_{s=g+,g-} \frac{m_s}{q_s} \left[\eta_{\parallel} \sigma_{\parallel,s} \left(1 + \frac{\tau_0}{\tau_{sn}} \varrho_s \right) \right], \quad (2.67a)$$

$$\eta_{\text{cont},\perp} = \sum_{s=g+,g-} \frac{m_s}{q_s} \left[\eta_{\perp} \sigma_{\perp,s} \left(1 + \frac{\tau_0}{\tau_{sn}} \varrho_s \right) - \eta_{\text{H}} \sigma_{\text{H},s} \left(1 + \frac{\tau_0}{\tau_{sn}} \varrho_s \right) \right], \quad (2.67b)$$

$$\eta_{\text{cont},\text{H}} = \sum_{s=g+,g-} \frac{m_s}{q_s} \left[\eta_{\text{H}} \sigma_{\perp,s} \left(1 + \frac{\tau_0}{\tau_{sn}} \varrho_s \right) - \eta_{\perp} \sigma_{\text{H},s} \left(1 + \frac{\tau_0}{\tau_{sn}} \varrho_s \right) \right]. \quad (2.67c)$$

These equations apply to all grain sizes separately. Under the assumptions in this work, $\mathbf{j}_{\parallel} = 0$ and $\nabla \cdot \mathbf{j}_{\perp} = 0$ by axisymmetry. Equation (2.66) then becomes

$$\frac{\partial \rho_g}{\partial t} + \nabla \cdot (\rho_g \mathbf{v}_n) = -\nabla \cdot (\eta_{\text{cont},\text{H}} \mathbf{j} \times \mathbf{b}). \quad (2.68)$$

Note that if $\eta_{\text{cont,H}} = 0$, a quantitative implementation of flux-freezing, the grain species are advected with the neutrals, as expected.

2.5.5 Joule Heating

The rate Γ_{diff} at which collisions dissipate kinetic energy as heat per unit volume (in the reference frame of the neutrals) may be calculated by taking the dot product of equation (2.52) with \mathbf{w}_s and using equation (2.51):

$$\Gamma_{\text{diff}} = \left[\sum_s (1 + \varrho_s) \frac{\rho_s}{\tau_{\text{sn}}} |\mathbf{w}_s|^2 \right] - \left(\sum_s \frac{\rho_{\text{g0}}}{\tau_{\text{s,inel}}} \mathbf{w}_s \right) \cdot \left(\sum_k \frac{\tau_0}{\tau_{k,\text{inel}}} \mathbf{w}_k \right), \quad (2.69)$$

where the summation indices s and k run, as usual, over all charged species (including charged grains of different sizes if a grain size distribution is considered). Using equation (C.1) to eliminate the velocities in favor of the current density, we find after much simplification

$$\begin{aligned} \Gamma_{\text{diff}} = & \eta_{\parallel} |\mathbf{j}_{\parallel}|^2 \left[\sum_s \left(\frac{\sigma_{\parallel,s}}{\sqrt{\sigma_s \sigma_{\parallel}}} \sqrt{1 + \varrho_s} \right)^2 - \left(\sum_s \frac{\sigma_{\parallel,s}}{\sqrt{\sigma_s \sigma_{\parallel}}} \sqrt{\frac{\varrho_s \tau_0}{\tau_{s,\text{inel}}}} \right)^2 \right] \\ & + \eta_{\perp} |\mathbf{j}_{\perp}|^2 \left[\sum_s \left(\frac{\sigma_{\perp,s}}{\sqrt{\sigma_s \sigma_{\perp}}} \sqrt{1 + \varrho_s} \right)^2 - \left(\sum_s \frac{\sigma_{\perp,s}}{\sqrt{\sigma_s \sigma_{\perp}}} \sqrt{\frac{\varrho_s \tau_0}{\tau_{s,\text{inel}}}} \right)^2 \right] \\ & + \eta_{\text{H}} |\mathbf{j}_{\perp}|^2 \left[\sum_s \left(\frac{\sigma_{\text{H},s}}{\sqrt{\sigma_s \sigma_{\text{H}}}} \sqrt{1 + \varrho_s} \right)^2 - \left(\sum_s \frac{\sigma_{\text{H},s}}{\sqrt{\sigma_s \sigma_{\text{H}}}} \sqrt{\frac{\varrho_s \tau_0}{\tau_{s,\text{inel}}}} \right)^2 \right]. \end{aligned} \quad (2.70)$$

In the limit where inelastic collisions are negligible relative to elastic collisions (i.e., $\varrho_s \rightarrow 0$), this equation reduces to the usual expression

$$\Gamma_{\text{diff}} \rightarrow \eta_{\parallel} |\mathbf{j}_{\parallel}|^2 + \eta_{\perp} |\mathbf{j}_{\perp}|^2 = \eta_{\text{OD}} |\mathbf{j}|^2 + \eta_{\text{AD}} |\mathbf{j}_{\perp}|^2.$$

In the last step, we have used equations (2.47) to separate the contributions of Ohmic dissipation and ambipolar diffusion to the heating rate. Ohmic dissipation affects the total

current density, whereas ambipolar diffusion affects only the perpendicular component of the current density.

2.6 Radiative Transfer

2.6.1 The Flux-Limited Diffusion Approximation

Computing a formal solution of the full angle-frequency dependent non-LTE radiative transfer equation in a multidimensional numerical algorithm is a prohibitive task. Even if a rigorous yet tractable algorithm were developed to this end, the computational expense involved would prevent a solution in any reasonable amount of time. In fact, the sophisticated numerical code described in Stone et al. (1992) designed to solve this problem with as few approximations as possible never saw public release. The FLD approximation is an attractive method for handling transport phenomena that is relatively easy to implement, robust, and inexpensive. It has the advantage over other diffusive approximations in that it preserves causality in regions where significant spatial variation can occur over distances smaller than a mean free path. For example, the Eddington approximation consists of assuming the radiation field is everywhere isotropic, an assumption that is violated in the optically-thin limit where the radiation becomes streaming (Mihalas & Weibel Mihalas 1984).

The fundamental assumption of FLD is that the specific intensity is a slowly varying function of space and time. This is certainly valid in the diffusion and streaming limits (at least in one dimension); one hopes that it is approximately true in intermediate situations (and in multidimensions). Given this assumption, Levermore & Pomraning (1981) showed that the radiation flux can be expressed in the form of Fick's law of diffusion,

$$\mathcal{F} = -\mathcal{D}_{\text{FLD}} \nabla \mathcal{E} , \quad (2.71)$$

where the diffusion coefficient \mathcal{D}_{FLD} can be written as

$$\mathcal{D}_{\text{FLD}} = \frac{c\lambda_{\text{FLD}}}{\chi_{\mathcal{F}}}. \quad (2.72)$$

The dimensionless function $\lambda_{\text{FLD}} = \lambda_{\text{FLD}}(\mathcal{E})$ is called the flux limiter. Similarly, in FLD theory the radiation pressure tensor can be expressed in terms of the radiation energy density via

$$\mathbf{P} = \mathbf{f}\mathcal{E}, \quad (2.73)$$

where the components of the Eddington tensor \mathbf{f} are given by

$$\mathbf{f} = \frac{1}{2}(1 - f)\mathbf{I} + \frac{1}{2}(3f - 1)\hat{\mathbf{n}}\hat{\mathbf{n}}, \quad (2.74)$$

where $\hat{\mathbf{n}} = \nabla\mathcal{E}/|\nabla\mathcal{E}|$ is the normalized gradient of \mathcal{E} and the dimensionless function $f = f(\mathcal{E})$ is called the Eddington factor (Turner & Stone 2001). The flux limiter λ_{FLD} and Eddington factor f are related through implicit constraints between the moments \mathcal{F} and \mathbf{P} , so that

$$f = \lambda_{\text{FLD}} + \lambda_{\text{FLD}}^2 \mathcal{R}^2, \quad (2.75)$$

where \mathcal{R} is the dimensionless quantity $\mathcal{R} = |\nabla\mathcal{E}|/\chi_{\mathcal{F}}\mathcal{E}$. We have chosen the flux limiter derived by Levermore & Pomraning (1981, eq. 28), which is given by

$$\lambda_{\text{FLD}} = \frac{2 + \mathcal{R}}{6 + 3\mathcal{R} + \mathcal{R}^2}. \quad (2.76)$$

Its use in hydrodynamic simulations of star formation has been documented, for example, in Bodenheimer et al. (1990), Yorke et al. (1993, 1995), and Whitehouse & Bate (2006).

2.6.2 Dust Opacities

For temperature less than $\simeq 1500$ K, the contribution of dust to the total opacity dominates that from all other sources. We take $\kappa_{\mathcal{E}} = \kappa_{\mathcal{P}}$ and $\chi_{\mathcal{F}} = \chi_{\mathcal{R}}$ (see Mihalas & Weibel Mihalas 1984, § 82), where $\kappa_{\mathcal{P}}$ and $\chi_{\mathcal{R}}$ have been obtained from private communication with Dmitry Semenov and Thomas Henning. The major dust constituents are “iron-poor” silicates, troilite, organics, and water. Their relative mass fractions are taken from Pollack et al. (1994). These opacities (in $\text{cm}^2 \text{g}^{-1}$ of dust) are shown in Figures 2.2 and 2.3 for the five different grain size bins taken to represent an MRN distribution (see § 2.4.2). The major changes in the dust opacities are: for temperatures $T < 120$ K, all dust material are present; at $T \simeq 120$ K, water ice evaporates; at $T = 275$ K, volatile organics evaporate; at $T = 450$ K, refractory organics evaporate; at $T = 680$ K, troilite (FeS) evaporates.

2.7 Summary

In this chapter, we have formulated the problem of the formation and evolution of fragments (or cores) in magnetically-supported, self-gravitating molecular clouds in two spatial dimensions. The evolution is governed by the six-fluid RMHD equations. The magnetic flux is not assumed to be frozen in any of the charged species. Its evolution is determined by a newly-derived generalized Ohm’s law, which accounts for the contributions of both elastic and inelastic collisions to ambipolar diffusion and Ohmic dissipation. The species abundances (electrons, atomic and molecular ions, positively-charged grains, negatively-charged grains, and neutral grains) are calculated using an extensive chemical-equilibrium network. Both MRN and uniform grain size distributions are considered. The thermal evolution of the protostellar core and its effect on the dynamics are followed by employing the grey FLD approximation. Realistic temperature-dependent grain opacities are used that account for a variety of grain compositions.

We summarize here for convenience the simplified evolutionary equations discussed

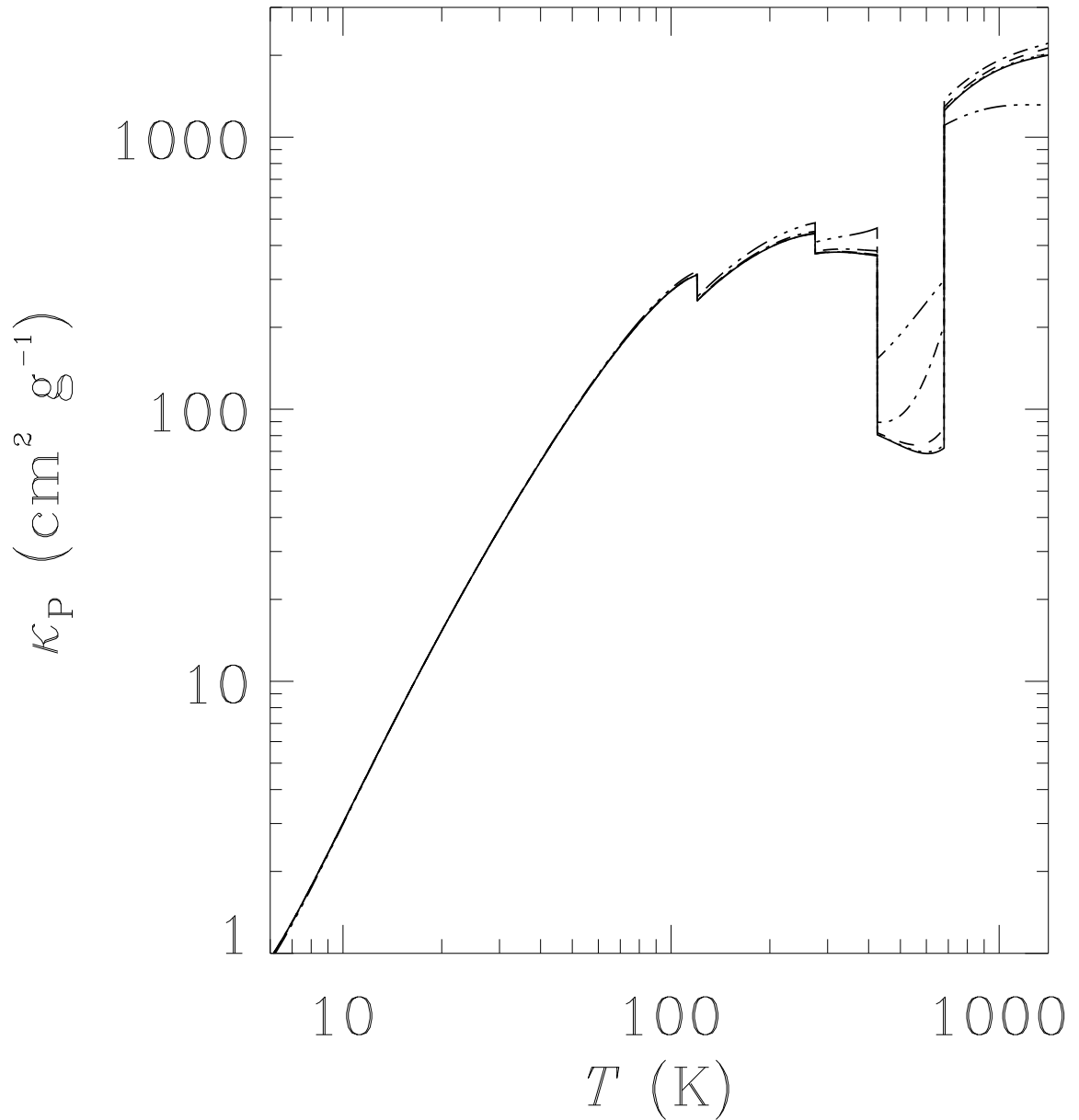


Figure 2.2: Planck mean absorption coefficients κ_P (in $\text{cm}^2 \text{g}^{-1}$ of dust) as a function of temperature T for grain sizes $a = 0.0256 \mu\text{m}$ (*solid line*), $0.0543 \mu\text{m}$ (*dotted line*), $0.1190 \mu\text{m}$ (*dashed line*), $0.2600 \mu\text{m}$ (*dash-dotted line*), and $0.5680 \mu\text{m}$ (*dashed-triple-dot line*).

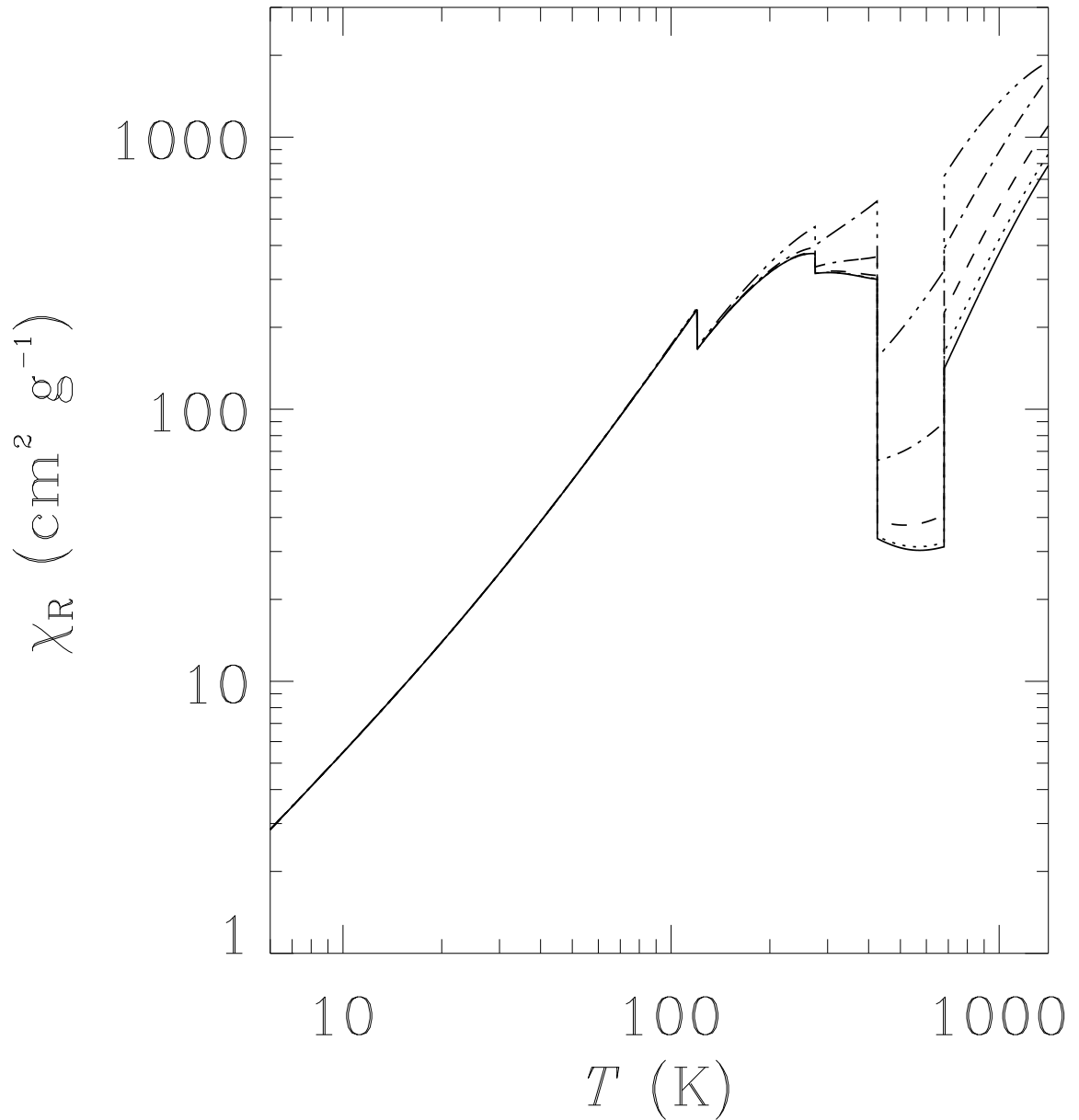


Figure 2.3: Rosseland mean extinction coefficients χ_R (in $\text{cm}^2 \text{g}^{-1}$ of dust) as a function of temperature T for grain sizes $a = 0.0256 \mu\text{m}$ (solid line), $0.0543 \mu\text{m}$ (dotted line), $0.1190 \mu\text{m}$ (dashed line), $0.2600 \mu\text{m}$ (dash-dotted line), and $0.5680 \mu\text{m}$ (dashed-triple-dot line).

above and used in our numerical simulations (see Chapter 3):

$$\frac{\partial \rho_n}{\partial t} + \nabla \cdot (\rho_n \mathbf{v}_n) = 0, \quad (2.77a)$$

$$\frac{\partial \rho_g}{\partial t} + \nabla \cdot (\rho_g \mathbf{v}_n) = -\nabla \cdot (\eta_{\text{cont,H}} \mathbf{j} \times \mathbf{b}), \quad (2.77b)$$

$$\frac{\partial(\rho_n \mathbf{v}_n)}{\partial t} + \nabla \cdot (\rho_n \mathbf{v}_n \mathbf{v}_n) = -\nabla P_n - \rho_n \nabla \psi + \frac{1}{4\pi} (\nabla \times \mathbf{B}) \times \mathbf{B} - \lambda_{\text{FLD}} \nabla \mathcal{E}, \quad (2.77c)$$

$$\frac{\partial \mathbf{B}}{\partial t} = \nabla \times \left(\mathbf{v}_n \times \mathbf{B} - \frac{c^2 \eta_{\perp}}{4\pi} \nabla \times \mathbf{B} \right), \quad (2.77d)$$

$$\nabla^2 \psi = 4\pi G \rho_n, \quad (2.77e)$$

$$\frac{\partial u_n}{\partial t} + \nabla \cdot (u_n \mathbf{v}_n) = -P_n \nabla \cdot \mathbf{v}_n - 4\pi \kappa_P \mathcal{B} + c \kappa_P \mathcal{E} + \Gamma_{\text{diff}}, \quad (2.77f)$$

$$\frac{\partial \mathcal{E}}{\partial t} + \nabla \cdot (\mathcal{E} \mathbf{v}_n) = \nabla \cdot \left(\frac{c \lambda_{\text{FLD}}}{\chi_R} \nabla \mathcal{E} \right) - \nabla \mathbf{v}_n : \mathbf{P} + 4\pi \kappa_P \mathcal{B} - c \kappa_P \mathcal{E}. \quad (2.77g)$$

These equations are considered together with the relations $P_n = (\gamma - 1)u_n$ and $\mathbf{P} = \mathbf{f}\mathcal{E}$.

Chapter 3

Method of Solution

3.1 Introduction

In order to solve for the evolution of the many complex, nonlinear systems of equations presented in Chapter 2, numerical techniques are necessary. Rather than extend the sophisticated fully implicit, nonorthogonal adaptive mesh, two-fluid MHD code of Fiedler & Mouschovias (1992) to include radiative transfer, we have opted instead to modify the publicly-available Zeus-MP RMHD code (Hayes et al. 2006).

Zeus-MP is a time-explicit, operator-split, massively-parallel RMHD code, distributed by the Laboratory for Computational Astrophysics at the University of California, San Diego. It offers a vast improvement over its namesake, the original Zeus-2D code documented in Stone & Norman (1992a,b), not only in its efficiency — being a Message Passing Interface (MPI) implementation of Zeus, it is designed for execution on massively parallel architectures — but also in its accuracy and stability. Zeus-MP offers an MHD algorithm which is better suited for multidimensional flows than the Zeus-2D module by virtue of modifications to the Method of Characteristics scheme first suggested by Hawley & Stone (1995). In addition, radiative transfer is already implemented in the code via an implicit FLD module. Arbitrary equations of state are supported. Zeus-MP is the first Zeus code to allow for the advection of multispecies fluids. We refer the reader to Hayes et al. (2006) for a more complete history of the Zeus code’s development.

The Zeus series was conceived with a discerning eye towards versatility and flexibility, in order to ease its use and modification by as wide an audience as possible. As a result,

each physical effect is modular, isolated from the others. Physical effects associated with advection are all calculated together in the “transport” part of each timestep, whereas physical effects associated with sources or sinks are grouped together in the “source” part of each timestep. The accommodation of a new physical effect by the code essentially amounts to the user providing a new module and placing it appropriately in either the transport or source step of the code.

We have altered the algorithms governing the evolution of the magnetic field in order to account for ambipolar diffusion and Ohmic dissipation. In addition, we have added routines to evolve the total grain density, update the gas energy density due to Joule heating, determine the local ratio of specific heats, and compute the species abundances from the chemical-equilibrium model detailed in § 2.4.3. Changes have also been made to Zeus-MP’s adaptive mesh module in order to track the collapsing core. New modules were written to improve both the efficiency of Zeus-MP’s implicit radiative transfer solver and the manner in which the gravitational potential is calculated. A brief description of these modifications follows this section.

For future code reference, the names of the relevant added and/or substantially modified routines are listed at the start of each corresponding section below. These routines have been incorporated into the program control in our modified version of Zeus-MP, which is diagrammed in Figure 3.1 as an adaptation of the original Zeus-MP flowchart given in Figure 2 of Hayes et al. (2006).¹

¹Portions of this chapter have been published in ApJ Volume 693, Issue 2, pp. 1895–1911. Reproduction for this dissertation is authorized by the copyright holder.

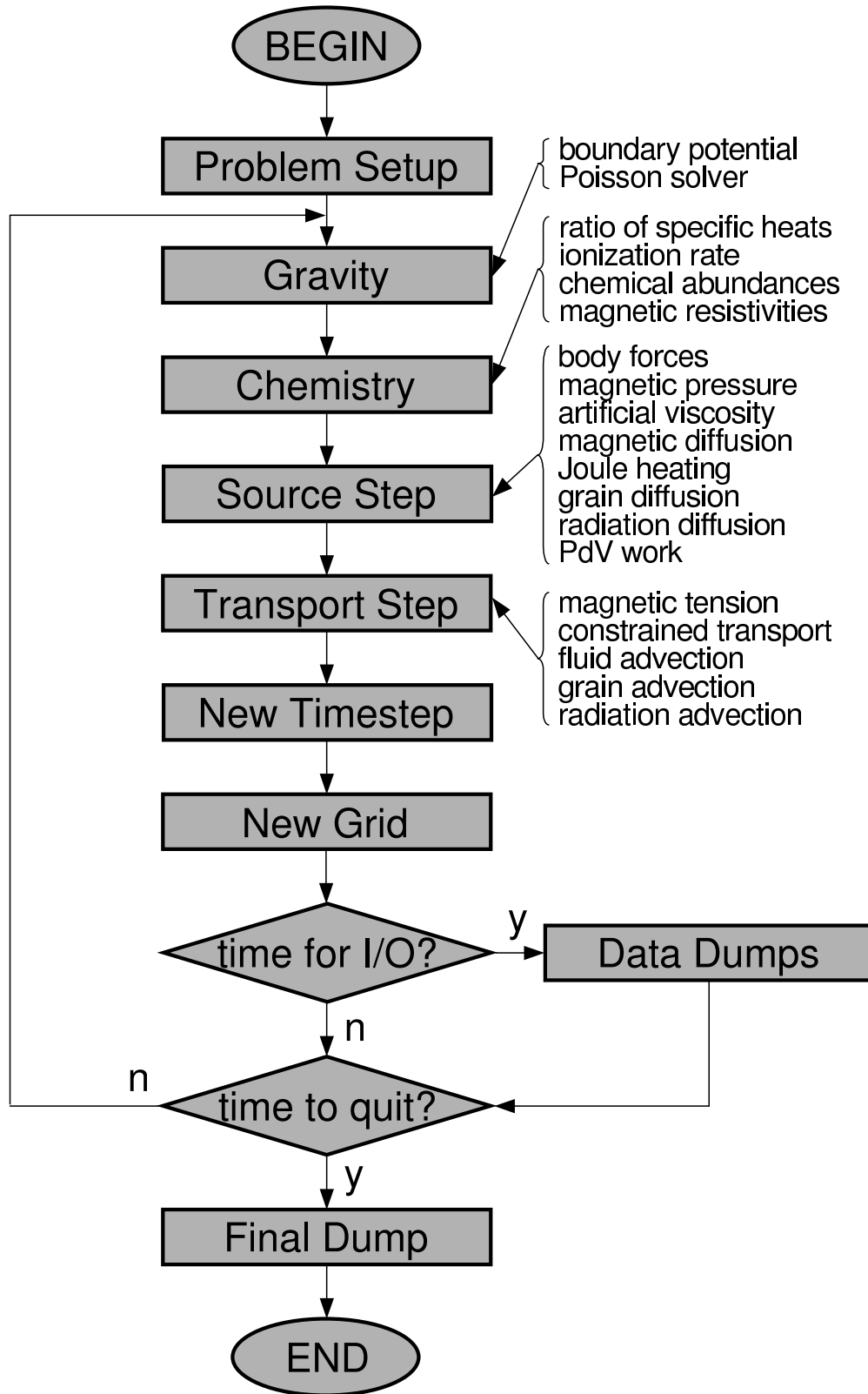


Figure 3.1: Modified Zeus-MP program control. Figure adapted from Hayes et al. (2006).

3.2 Incorporating Nonideal MHD Into Zeus-MP

3.2.1 Ideal Magnetohydrodynamics in Zeus-MP

The ability of the Zeus codes to accurately follow the evolution of magnetohydrodynamic processes stems from their use of an innovative algorithm, the Method of Characteristics / Constrained Transport (MOCCT) scheme. This scheme is a hybrid of two previous approaches to numerical MHD. The Constrained Transport (CT) method (Evans & Hawley 1988) is a robust method for evolving the magnetic field while preserving the divergence-free condition. The Method of Characteristics (MOC) is an accurate interpolation scheme which uses quantities that are upwind with respect to MHD waves. We review these methods in this section as they are currently used in the publicly-available Zeus-MP code, so that alterations to them (described in the next section) may be understood.

Magnetic fields engender new degrees of freedom to a physical system, and the consequent emergence of new families of wave modes necessitates a careful and relatively complex numerical treatment of wave advection. MHD waves may be longitudinal and compressive (e.g., fast and slow magnetosonic waves) or transverse and non-compressive (e.g., Alfvén waves). A naïve numerical implementation of the former wave family suffices; they may be treated in the source-step portion of the Zeus code in a similar fashion to their hydrodynamic analogs. Unfortunately, the same is not true for the latter family of waves. Alfvén waves couple directly to the magnetic induction equation and, when treated numerically, require knowledge of fluid quantities upwind. As a result, these non-compressive modes are computed in a separate step that necessarily follows the source step update but precedes the transport update.

These concerns may be put on a rigorous mathematical footing after noting that the Lorentz force in equation (2.77c) may be expanded as

$$(\nabla \times \mathbf{B}) \times \mathbf{B} = -\frac{1}{2} \nabla B^2 + (\mathbf{B} \cdot \nabla) \mathbf{B}. \quad (3.1)$$

The first term on the right-hand side is the gradient of the magnetic pressure. This term is responsible for providing a longitudinal force, which represents the contribution from the compressive magnetosonic waves. Numerically, this term is finite-differenced in space and time identically to the thermal pressure term and therefore is evaluated in the source step portion of the momentum equation. The second term on the right-hand side is typically thought of as representing the magnetic tension in curved field lines and is transverse to the gradient of \mathbf{B} . It is this term that couples to the magnetic induction equation to produce Alfvén waves. The magnetic tension force and the induction equation must therefore be solved simultaneously using the MOCCT method.

In Section 2.5.1, we gave the rate of change of magnetic flux across a surface S , which is comoving with a fluid with velocity \mathbf{v} (eq. 2.36). If, instead, we consider the surface to be one which moves with the grid at a velocity \mathbf{v}_{grid} , it is straightforward to show that

$$\frac{d\Phi_B}{dt} = -c \int_S \nabla \times \left(\mathbf{E} + \frac{\mathbf{v}_{\text{grid}}}{c} \times \mathbf{B} \right) \cdot d\mathbf{S} \quad (3.2a)$$

$$= \int_S \nabla \times (\mathbf{v} - \mathbf{v}_{\text{grid}}) \times \mathbf{B} \cdot d\mathbf{S} \quad (3.2b)$$

$$= \oint_C (\mathbf{v} - \mathbf{v}_{\text{grid}}) \times \mathbf{B} \cdot d\boldsymbol{\ell} \quad (3.2c)$$

$$\equiv \oint_C \boldsymbol{\varepsilon} \cdot d\boldsymbol{\ell}, \quad (3.2d)$$

where C is the closed boundary of the surface S . The quantity

$$\boldsymbol{\varepsilon} = (\mathbf{v} - \mathbf{v}_{\text{grid}}) \times \mathbf{B} \quad (3.3)$$

is referred to in the Zeus literature as the electromotive force (EMF) acting along the curve C . If $\mathbf{v}_{\text{grid}} = \mathbf{v}$, we recover the well-known flux-freezing result, $d\Phi_B/dt = 0$.

As discussed in Evans & Hawley (1988), Stone & Norman (1992b), Hawley & Stone (1995), and Hayes et al. (2006), equation (3.2d) guarantees divergence-free magnetic field transport when finite differenced, provided the EMFs are evaluated once and only once per

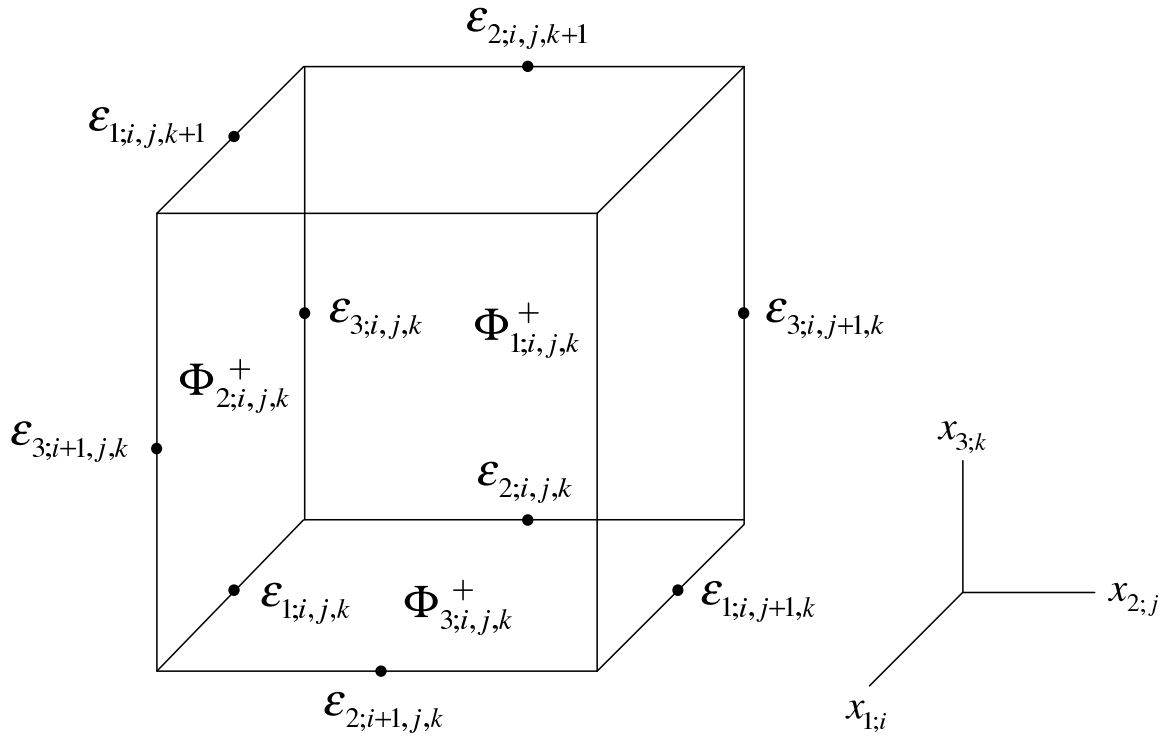


Figure 3.2: Centering of different components of the EMF (ϵ_1 , ϵ_2 , ϵ_3 ; black circles on the box edges) and the magnetic flux (Φ_1 , Φ_2 , Φ_3 ; crosses on the box faces) on a three-dimensional unit cell in Zeus-MP. Figure adapted from Hayes et al. (2006).

timestep. Referring to the unit computational cell diagrammed in Figure 3.2, we can write the discrete ($dt \rightarrow \Delta t$, $d\mathbf{x} \rightarrow \Delta\mathbf{x}$) form of equation (3.2d) as

$$\begin{aligned} \frac{\Phi_{1;i,j,k}^{n+1} - \Phi_{1;i,j,k}^n}{\Delta t} &= \varepsilon_{2;i,j,k} \Delta x_{2;i,j,k} + \varepsilon_{3;i,j+1,k} \Delta x_{3;i,j+1,k} \\ &\quad - \varepsilon_{2;i,j,k+1} \Delta x_{2;i,j,k+1} - \varepsilon_{3;i,j,k} \Delta x_{3;i,j,k} , \end{aligned} \quad (3.4a)$$

$$\begin{aligned} \frac{\Phi_{2;i,j,k}^{n+1} - \Phi_{2;i,j,k}^n}{\Delta t} &= \varepsilon_{1;i,j,k+1} \Delta x_{1;i,j,k+1} + \varepsilon_{3;i,j,k} \Delta x_{3;i,j,k} \\ &\quad - \varepsilon_{1;i,j,k} \Delta x_{1;i,j,k} - \varepsilon_{3;i+1,j,k} \Delta x_{3;i+1,j,k} , \end{aligned} \quad (3.4b)$$

$$\begin{aligned} \frac{\Phi_{3;i,j,k}^{n+1} - \Phi_{3;i,j,k}^n}{\Delta t} &= \varepsilon_{1;i,j,k} \Delta x_{1;i,j,k} + \varepsilon_{2;i+1,j,k} \Delta x_{2;i+1,j,k} \\ &\quad - \varepsilon_{1;i,j+1,k} \Delta x_{1;i,j+1,k} - \varepsilon_{2;i,j,k} \Delta x_{2;i,j,k} , \end{aligned} \quad (3.4c)$$

where the superscript n refers to the timestep number and the subscripts i, j, k refer to the three-dimensional location of the cell on the computational grid. Summing the contributions to the change in flux piercing all 6 sides yields zero. Therefore, the total magnetic flux penetrating the cube remains constant. Provided that the user supply an initially divergence-free magnetic field, the code will evolve the field conservatively, always ensuring that the divergence remains zero (to machine accuracy).

The power of the CT formalism is that, in principle, one could use *any* method to compute the EMF and still maintain a divergence-free magnetic field. However, the *accuracy* of the magnetic flux evolution is not guaranteed by the CT algorithm, and so a method must be used which stably and accurately propagates both MHD wave types: longitudinal-compressive (fast and slow magnetosonic) waves and transverse-non-compressive (Alfvén) waves. As noted earlier, the real difficulty arises in the treatment of the Alfvén waves.

The various properties of Alfvén waves suggest themselves what steps must be taken

to ensure a robust numerical algorithm. Unlike hydrodynamic waves, which steepen into shocks, Alfvén waves are not dissipative; this rules out the use of dissipative numerical algorithms. Alfvén waves tightly couple the evolution equations for the velocity and magnetic field components perpendicular to the direction of propagation; this rules out operator splitting these components. Finally, information about the characteristics of Alfvén waves must be included in the EMFs to ensure stability. All these requirements are satisfied by using the MOC to compute the EMFs, which may be written schematically as (ignoring \mathbf{v}_{grid} for simplicity)

$$\varepsilon_{1;i,j,k} = v_{2;i,j,k}^* B_{3;i,j,k}^* - v_{3;i,j,k}^* B_{2;i,j,k}^* \quad (3.5a)$$

$$\varepsilon_{2;i,j,k} = v_{3;i,j,k}^* B_{1;i,j,k}^* - v_{1;i,j,k}^* B_{3;i,j,k}^* \quad (3.5b)$$

$$\varepsilon_{3;i,j,k} = v_{1;i,j,k}^* B_{2;i,j,k}^* - v_{2;i,j,k}^* B_{1;i,j,k}^* . \quad (3.5c)$$

The starred quantities represent the upwinded values for these variables resulting from the solution of the characteristic equations at the centers of zone edges where the EMFs are located.

Since the MOC is applied to Alfvén waves only (longitudinal modes are adequately handled during the source step using finite difference methods), the equations of incompressible MHD may be used to derive Alfvén wave characteristics:

$$\frac{\partial \mathbf{B}}{\partial t} = -(\mathbf{v} \cdot \nabla) \mathbf{B} + (\mathbf{B} \cdot \nabla) \mathbf{v} , \quad (3.6a)$$

$$\frac{\partial \mathbf{v}}{\partial t} = -(\mathbf{v} \cdot \nabla) \mathbf{v} + \frac{1}{4\pi\rho} (\nabla \times \mathbf{B}) \times \mathbf{B} . \quad (3.6b)$$

To simplify the derivation, the magnetic field and velocity are assumed to be

$$\mathbf{B} = B_x \hat{\mathbf{e}}_x + B(x) \hat{\mathbf{e}}_y , \quad (3.7a)$$

$$\mathbf{v} = v_x \hat{\mathbf{e}}_x + v(x) \hat{\mathbf{e}}_y , \quad (3.7b)$$

so that both variables are functions of x and t only.² Then, the solenoidal nature of the velocity and magnetic field constrains v_x and B_x , respectively, to be spatially uniform and equations (3.6) reduce to

$$\frac{\partial B}{\partial t} = -v_x \frac{\partial B}{\partial x} + B_x \frac{\partial v}{\partial x}, \quad (3.8a)$$

$$\frac{\partial v}{\partial t} = -v_x \frac{\partial v}{\partial x} + \frac{B_x}{4\pi\rho} \frac{\partial B}{\partial x}. \quad (3.8b)$$

Multiplying the first equation by $(4\pi\rho)^{-1/2}$ and then adding and subtracting the two yields the characteristic equation

$$\frac{Dv}{Dt} \pm \frac{1}{\sqrt{4\pi\rho}} \frac{DB}{Dt} = 0, \quad (3.9)$$

where the comoving derivative

$$\frac{D}{Dt} \equiv \frac{\partial}{\partial t} + (v_x \mp v_A) \frac{\partial}{\partial x}, \quad (3.10)$$

and $v_A = B_x(4\pi\rho)^{-1/2}$ is the Alfvén speed associated with the background magnetic field. The upper (lower) sign in equations (3.9) and (3.10) corresponds to the characteristic equation along the forward- (backward-)facing characteristic C^\pm . Physically, equations (3.9) state that along characteristics, which are straight lines in space-time with slopes $v_x \pm v_A$, the changes in the velocity and magnetic field are not independent.

The characteristic equations (3.9) are used to determine the upwinded values of the velocity and magnetic field to be used in equations (3.5). These intermediate values, denoted v^* and B^* , are located at x^* , which is the boundary between neighboring cells. The Alfvén waves that reach x^* at timestep $n + 1/2$ (time $t_n + \Delta t/2$) initiated at timestep n (time t_n) from spatial locations denoted x^+ and x^- , which are referred to as the “footpoints”. (See Figure 3.3.) Once the characteristic speeds $v_x \pm v_A$ are used to compute the footpoint values

²Here we are in effect considering a linearly-polarized Alfvén wave. The subsequent derivation, however, may be trivially generalized for a circularly-polarized Alfvén wave by replacing the unit vector \hat{e}_y with $(1/\sqrt{2})(\hat{e}_y \pm i\hat{e}_z)$.

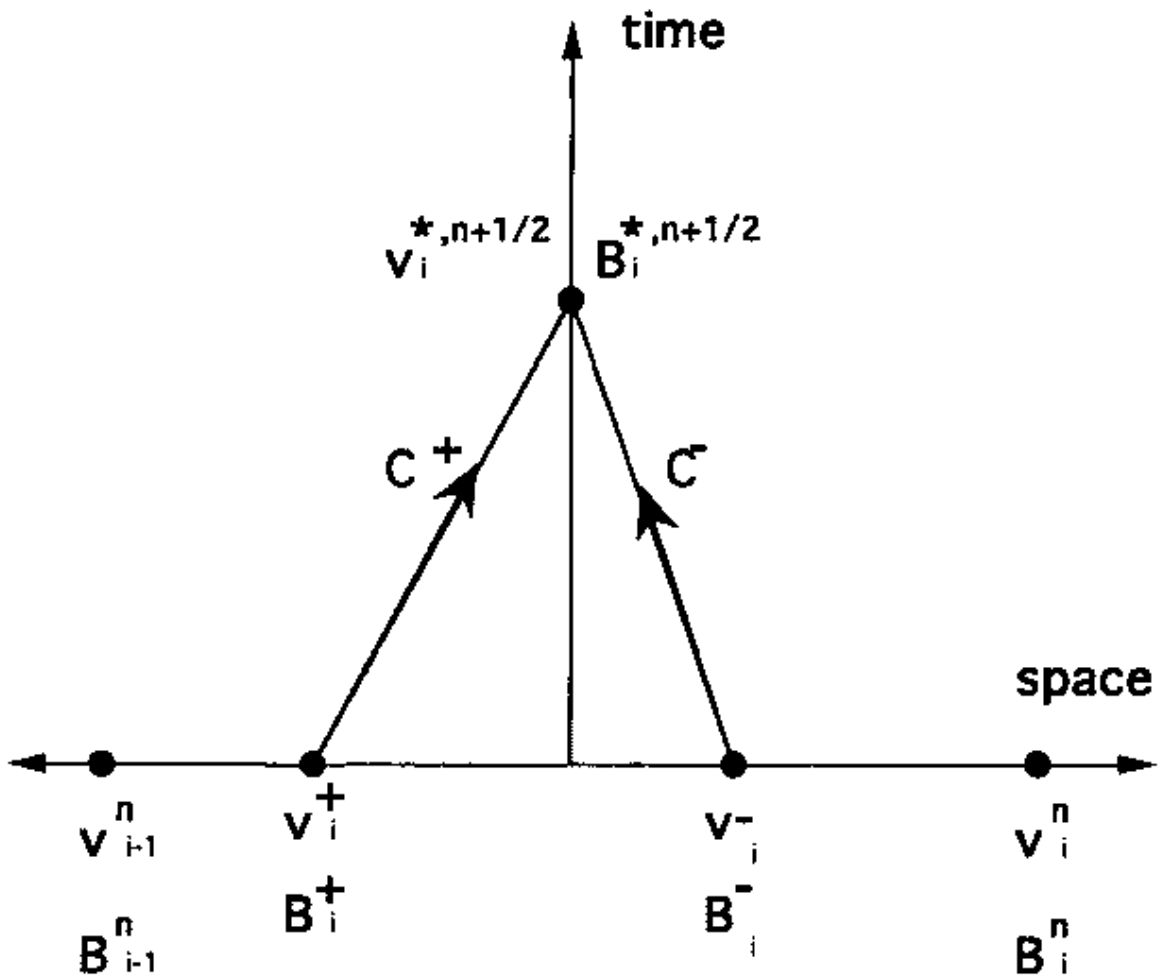


Figure 3.3: Space-time diagram illustrating how Alfvén waves originate at footpoints x^+ and x^- , propagate along characteristics C^+ and C^- , respectively, and meet at the point x^* at a time $t_n + \Delta t/2$. Figure taken from Stone & Norman (1992b).

v^\pm and B^\pm , the finite difference equations along C^+ and C^- become

$$\frac{v^* - v^\pm}{\Delta t/2} \pm \frac{1}{\sqrt{4\pi\rho^\pm}} \frac{B^* - B^\pm}{\Delta t/2} = 0. \quad (3.11)$$

(For simplicity, the Zeus code sets ρ^\pm equal to the mean density in the cell in which x^\pm lies, rather than using interpolated values for the time-centered density obtained by upwind differencing.) The two linear equations (3.11) are then solved algebraically for the two unknowns v^* and B^* .

The generalization of the above analysis to multiple dimensions is relatively straightforward, with the exception of an important subtlety in its implementation. For multidimensional calculations, the upwinding of variables along full characteristics is numerically impractical. This is circumvented by adopting the approach of Hawley & Stone (1995), in which only partial characteristics are used to upwind velocity and magnetic field components. This amounts to directionally splitting the advection on planes passing through the center of the cell and the cell edges where the EMFs are to be evaluated. Stability is improved, particularly in the presence of magnetic discontinuities, by combining Alfvén-upwinded quantities with quantities upwinded along hydrodynamic fluid-flow characteristics (coordinate axes) in a self-consistent fashion. Following the discussion in Appendix C1 of Hayes et al. (2006), we illustrate this process by calculating the numerical representation of ε_3 . First, B_2 and v_2 are van Leer average upwinded along the 1-axis according to v_1 to find $\overline{B}_2^{(1)}$ and $\overline{v}_2^{(1)}$, respectively. These quantities are then used to compute the Alfvén-characteristic speeds in the 2-direction:

$$v^{(2\pm)} = \overline{v}_2^{(1)} \mp \frac{|\overline{B}_2^{(1)}|}{\sqrt{4\pi\rho^\pm}}. \quad (3.12)$$

The third step amounts to van Leer average upwinding B_1 and v_1 along the \pm characteristics using these characteristic speeds; the result is $\overline{v}_1^{(2\pm)}$ and $\overline{B}_1^{(2\pm)}$. Finally, the characteristic equations are solved for B_1^* and v_1^* and the products $v_1^* \overline{B}_2^{(1)}$ and $\overline{v}_2^{(1)} B_1^*$ are stored. The

analogous process is executed for B_2^* and v_2^* by examining partial characteristics in the 1-direction, obtaining the products $v_2^* \bar{B}_1^{(2)}$ and $\bar{v}_1^{(2)} B_2^*$. The 3-EMF may then be written as

$$\begin{aligned} \varepsilon_{3;i,j,k} = & \frac{1}{2} \left(v_{1;i,j,k}^* \bar{B}_{2;i,j,k} + \bar{v}_{1;i,j,k} B_{2;i,j,k}^* \right) \\ & - \frac{1}{2} \left(v_{2;i,j,k}^* \bar{B}_{1;i,j,k} + \bar{v}_{2;i,j,k} B_{1;i,j,k}^* \right) , \end{aligned} \quad (3.13)$$

Because each component of the magnetic field (e.g., B_1) depends upon EMFs computed around both transverse axes (e.g., ε_2 and ε_3), the evolution of each magnetic-field component will depend upon the full set of characteristics.

The Lorentz accelerations are computed by a procedure analogous to the calculation of the EMFs. However, as the numerical algorithm involved in calculating and applying the Lorentz force update is unaffected by the incorporation of nonideal MHD, we do not describe it here but rather refer the reader to Appendix C2 of Hayes et al. (2006).

3.2.2 Nonideal Magnetohydrodynamics in Zeus-MP

Added Routines: EmfsOD, BValCrl, CTOD, DGSrc, Joule

Modified Routines: SrcStep, NewDT

Having described in the previous section the numerical solution to the problem of the stable and accurate advection of Alfvén waves, the incorporation of nonideal MHD into the algorithm is actually much simpler than one would expect. While the details are rather involved, the end result is surprisingly simple: as long as the nonideal MHD Courant condition

$$\Delta t \leq \Delta t_{\text{diff}} \equiv \frac{4\pi}{c^2 \eta_{\perp}} \frac{(\Delta x)^2}{2} \quad (3.14)$$

is satisfied, then the method of characteristics used to update the magnetic field due to advection by the neutral species remains valid (Mac Low et al. 1995) and we may use it without modification. Physically, this is because, for a sufficiently short timestep, ambipolar diffusion and/or Ohmic dissipation does not have time to alter the characteristics of

Alfvén waves.

This may be proved rigorously by writing down the nonideal MHD analogs of equations (3.6):

$$\frac{\partial \mathbf{B}}{\partial t} = -(\mathbf{v} \cdot \nabla) \mathbf{B} + (\mathbf{B} \cdot \nabla) \mathbf{v} - \nabla \times \left(\frac{c^2 \eta_{\perp}}{4\pi} \nabla \times \mathbf{B} \right), \quad (3.15a)$$

$$\frac{\partial \mathbf{v}}{\partial t} = -(\mathbf{v} \cdot \nabla) \mathbf{v} + \frac{1}{4\pi\rho} (\nabla \times \mathbf{B}) \times \mathbf{B}, \quad (3.15b)$$

where \mathbf{v} now refers to the motion of the neutral gas (rather than the flux-frozen bulk plasma). Inserting the previous Ansatz (3.7), the above equations can be reduced to

$$\frac{\partial B}{\partial t} = -v_x \frac{\partial B}{\partial x} + B_x \frac{\partial v}{\partial x} + \frac{\partial}{\partial x} \left(\frac{c^2 \eta_{\perp}}{4\pi} \frac{\partial B}{\partial x} \right), \quad (3.16a)$$

$$\frac{\partial v}{\partial t} = -v_x \frac{\partial v}{\partial x} + \frac{B_x}{4\pi\rho} \frac{\partial B}{\partial x}. \quad (3.16b)$$

These may be combined in the usual fashion to derive the new characteristic equation

$$\frac{Dv}{Dt} \pm \frac{1}{\sqrt{4\pi\rho}} \frac{DB}{Dt} = \pm \frac{1}{\sqrt{4\pi\rho}} \frac{\partial}{\partial x} \left(\frac{c^2 \eta_{\perp}}{4\pi} \frac{\partial B}{\partial x} \right). \quad (3.17)$$

The MOC including magnetic diffusion again utilizes information at the two footpoints x^{\pm} to compute v^* and B^* . The nonideal MHD analogue of equations (3.11) is

$$\frac{v^* - v^{\pm}}{\Delta t/2} \pm \frac{1}{\sqrt{4\pi\rho^{\pm}}} \frac{B^* - B^{\pm}}{\Delta t/2} = \pm \frac{1}{\sqrt{4\pi\rho^{\pm}}} \overline{\frac{\partial}{\partial x} \left(\frac{c^2 \eta_{\perp}}{4\pi} \frac{\partial B}{\partial x} \right)}. \quad (3.18)$$

The bar over the terms on the right-hand side of these equations denotes an average along the characteristic. This average is found by integrating along the characteristic, using the definition of the differential operator D/Dt . In what follows, we illustrate this averaging mathematically by examining the C^+ characteristic.

An Alfvén wave that follows the C^+ characteristic originates at position x^+ at time t_n and terminates at position x^* at time $t_n + \Delta t/2$. The average value over this characteristic

of the spatial derivative of some quantity Q , $\partial Q/\partial x$, is defined to be

$$\overline{\frac{\partial Q}{\partial x}} \Big|_+ \equiv \frac{\int_+^* (\partial Q/\partial x) Dt}{\int_+^* Dt} = \frac{1}{\Delta t/2} \int_+^* \frac{\partial Q}{\partial x} Dt. \quad (3.19)$$

Evaluation of the integral is aided by rewriting the spatial derivative of Q in terms of the differential operator D/Dt :

$$\frac{\partial Q}{\partial x} = \frac{1}{v_x + v_A} \left(\frac{DQ}{Dt} - \frac{\partial Q}{\partial t} \right), \quad (3.20)$$

so that

$$\overline{\frac{\partial Q}{\partial x}} \Big|_+ = \frac{1}{(v_x + v_A)(\Delta t/2)} \left[\int_+^* \frac{DQ}{Dt} Dt - \int_+^* \frac{\partial Q}{\partial t} Dt \right]. \quad (3.21)$$

The first integral is trivial to evaluate, but the second integral requires knowledge of the time derivative of Q along the characteristic. This information necessitates a knowledge of Q everywhere at time $t_n + \Delta t/2$, which demands an implicit solution algorithm. To avoid this problem, we make the approximation that $\partial Q/\partial t$ at all times and positions along the characteristic takes on the same values as $\partial Q/\partial t$ at the same times and at position $x = x^*$. Under this assumption, the second integral becomes

$$\int_0^* \frac{\partial Q}{\partial t} dt = Q|_* - Q|_0, \quad (3.22)$$

where the subscript “0” denotes evaluation at the space-time location (x^*, t) . Collecting all terms, using the relationship $x^* - x^+ = (v_x + v_A)(\Delta t/2)$, and simplifying, we obtain the following expression for the average value of the spatial derivative of Q along the characteristic:

$$\overline{\frac{\partial Q}{\partial x}} \Big|_+ = \frac{Q|_0 - Q|_+}{x^* - x^+}. \quad (3.23)$$

In other words, the average spatial derivative of Q along the characteristic is equal to its average value at time t_n .

If we associate Q with $(c^2\eta_{\perp}/4\pi)(\partial B/\partial x)$, equations (3.18) can be solved for the two unknowns B^* and v^* :

$$B^* = \frac{\left(\frac{B^+}{\sqrt{4\pi\rho^+}} + \frac{B^-}{\sqrt{4\pi\rho^-}}\right) - (v^+ - v^-) + \left(\frac{\Delta t}{2}\right) \left(\frac{(\overline{\partial Q/\partial x})_+}{\sqrt{4\pi\rho^+}} + \frac{(\overline{\partial Q/\partial x})_-}{\sqrt{4\pi\rho^-}}\right)}{\frac{1}{\sqrt{4\pi\rho^+}} + \frac{1}{\sqrt{4\pi\rho^-}}}, \quad (3.24a)$$

$$v^* = \frac{\left(v^+ \sqrt{4\pi\rho^+} + v^- \sqrt{4\pi\rho^-}\right) - (B^+ - B^-) - \left(\frac{\Delta t}{2}\right) \left(\left.\frac{\partial Q}{\partial x}\right|_+ - \left.\frac{\partial Q}{\partial x}\right|_-\right)}{\sqrt{4\pi\rho^+} + \sqrt{4\pi\rho^-}}. \quad (3.24b)$$

The terms in these equations can be shown to be on the order of

$$B^* \sim B \left[\mathcal{O}(1) + \mathcal{O}\left(\frac{v}{v_A} \frac{\Delta t}{\tau_A}\right) + \mathcal{O}\left(\frac{\Delta t}{\tau_{\text{diff}}}\right) \right], \quad (3.25a)$$

$$v^* \sim v_A \left[\mathcal{O}\left(\frac{v}{v_A}\right) + \mathcal{O}\left(\frac{\Delta t}{\tau_A}\right) + \mathcal{O}\left(\frac{\Delta t}{\tau_A} \frac{\Delta t}{\tau_{\text{diff}}}\right) \right], \quad (3.25b)$$

where τ_A is the Alfvén crossing time across a grid cell and τ_{diff} is the timescale associated with magnetic diffusion. As long as the Courant condition is met for all physical processes, including magnetic diffusion, for which equation (3.14) is the relevant timestep limitation, then the terms representing wave propagation and magnetic diffusion will remain only small corrections to the magnetic field or velocity. That is, B^* and v^* will approximately equal the magnetic field and velocity, respectively, in the neighborhood of x^* , with corrections that are derived from the MOC.

The only remaining issue regarding the implementation of ambipolar diffusion and Ohmic dissipation in Zeus-MP is the following: at what point in the code should the EMF due to magnetic diffusion be applied? The ability of the CT algorithm to preserve the divergence-free constraint on the magnetic field regardless of the EMF used suggests that

we merely replace the EMF given by equation (3.3) with

$$\boldsymbol{\varepsilon} = (\boldsymbol{v} - \boldsymbol{v}_{\text{grid}}) \times \boldsymbol{B} - \frac{c^2 \eta_{\perp}}{4\pi} \nabla \times \boldsymbol{B} \quad (3.26)$$

and let the current Zeus architecture handle the rest. Unfortunately, sending this EMF to the CT algorithm during the transport step of the Zeus code leads to numerical instabilities. Perhaps this is not too surprising, though. That the first term in equation (3.26) should be handled in the transport step makes a great deal of sense — it is this term that is associated with the advection of the magnetic flux. The same cannot be said, however, for the second term, which represents a sink due to magnetic diffusion and therefore ought to be placed in the source step. In this way, the physical interpretation of the terms in equation (3.26) itself suggests the proper construction of a stable and accurate nonideal MOCCT algorithm.

We employ a similar approach to the grain continuity equation (2.68). The right-hand side is treated as a source term in the source step part of the code. Then, the grain mass density is advected during the transport step using the multispecies advection module already present in Zeus-MP. Joule heating (eq. 2.70) is also applied to the internal energy during the source step.

3.3 Chemical Abundances and Magnetic Resistivity

Added Routines: Ohmic, GamCalc, Ionize, Chem, Resist

Modified Routines: BVal3D, ZeusMP

The starting point for calculating the chemical abundances and magnetic resistivities is to determine the gas temperature from the relation

$$T = \frac{u_{\text{n}}}{n_{\text{n}} c_{\text{V}}}. \quad (3.27)$$

Since c_{V} is a complicated function of temperature (see eq. 2.18 and Fig. 2.1), equation

(3.27) must be solved implicitly. The most straightforward way to accomplish this is by applying a Newton-Raphson iteration scheme using an initial guess for the temperature, which may be obtained from the previous timestep. (The internal energy u_n and neutral number density n_n are known at the current timestep.) Once the current temperature is known, the adiabatic index $\gamma = k_B/c_V + 1$ can be found.

The next step is to compute the local ionization rate in every computational cell. The cosmic-ray ionization rate is a sensitive function of the column density, which is computed by integrating from the point in question to the cloud surface following a path perpendicular to the disk midplane. This rate is then supplemented with the rates of alternate sources of ionization, such as UV, radioactivities, and thermal ionization of potassium (see Section 2.4.1). With the total ionization rate in hand, we may then proceed to calculate the chemical abundances.

The nonlinear system of equations (2.28) – (2.34), which quantifies our chemical-equilibrium network and thereby uniquely determines the chemical abundances, is best solved numerically via Gauss-Jordan elimination on the matrix equation derived by applying the Newton-Raphson iteration method. The abundance equations are a system of N variables x_i (the various abundances) and N equations $f_i(x_1, x_2, \dots, x_N) = 0$ (the rate equations or constraints), $i = 1, 2, \dots, N$. If \mathbf{X} denotes an array of the abundances, then in the neighborhood of the initial guess \mathbf{X}_0 , the functions f_i can each be expanded in a Taylor series to give

$$f_i(\mathbf{X}_0 + \delta\mathbf{X}) \approx f_i(\mathbf{X}_0) + \sum_{j=1}^N \frac{\partial f_i}{\partial x_j} \delta x_j. \quad (3.28)$$

Since one desires $f_i(\mathbf{X}_0 + \delta\mathbf{X}) = 0$ for all i , a matrix equation is formed for the corrections $\delta\mathbf{X}$:

$$\delta\mathbf{X} = \mathbf{R}^{-1}\boldsymbol{\xi}, \quad (3.29)$$

where

$$R_{ij} = \frac{\partial f_i}{\partial x_j}, \quad (3.30)$$

$$\xi_i = -f_i(\mathbf{X}_0). \quad (3.31)$$

This matrix equation is solved using Gauss-Jordan elimination, which yields a correction to the abundances. The matrix \mathbf{R} and the residual vector $\boldsymbol{\xi}$ are recomputed for the new set of abundances. This process is iterated to convergence, until $\boldsymbol{\xi} = \mathbf{0}$. In order to prevent unphysical negative abundances, corrected abundances are never allowed to drop by more than 50% during any one iteration.

Once the chemical abundances are found, the local values of the magnetic conductivities (eq. 2.58) and resistivities (eqs. 2.41 and 2.67) may be computed in each cell, since we also know the neutral density and gas temperature (to calculate the collision timescales τ_{sn} and $\tau_{s,incl}$) and the magnetic field strength (to calculate the gyrofrequency ω_s).

3.4 Adaptive Grid

Modified Routine: NewVG

We use an adaptive grid to track the evolution of the contracting core. The grid, which must resolve the core, has its innermost zone constrained so as to always have a width in the range $\lambda_{T,cr}/5 - \lambda_{T,cr}/7$, where $\lambda_{T,cr} \equiv 1.4c_s\tau_{ff}$ is the critical thermal lengthscale (Mouschovias 1991a) and $\tau_{ff} \equiv (3\pi/32G\rho_{n,c})^{1/2}$ is the spherical free-fall time. (The quantity $\rho_{n,c}$ is the neutral mass density at the cloud center.) The critical thermal lengthscale is the smallest scale on which there can be spatial structure in the density without thermal-pressure forces smoothing it out. The number of cells is fixed (80×80), and their positions are spaced logarithmically, so that the spacing between the i th and $i+1$ cells is a number greater than the spacing between the $i-1$ and i th cells. This ratio is kept spatially

uniform (with the same value in both the r and z directions) but is allowed to vary in time. At the end of the simulations presented in this Thesis, the smallest computational cell has a width ≈ 0.2 AU, which represents a tiny fraction ($\sim 10^{-6}$) of the width of the entire computational domain (0.75 pc — see below).

3.5 Radiative Transfer Routine

Modified Routines: `Opacity`, `MatProp`, `Grey_FLD`

Once the heat generated by released gravitational energy during core contraction is unable to escape freely (at a central number density of $n_{\text{opq}} \simeq 10^7 \text{ cm}^{-3}$), radiative transfer calculations are used to determine the thermal evolution of the core and its effect on the dynamics. For this, we employ the grey flux-limited diffusion (FLD) approximation. Fortunately, this approximation has already been built into the public-release version of Zeus-MP. As discussed in Hayes et al. (2006, § 3.8.1), Zeus-MP uses the diagonal preconditioned conjugate gradient method to solve the sparse matrix equation that results from spatially discretizing equations (2.1m) and (2.1n).

Diagonal preconditioning is an attractive technique due to its simple calculation, the fact that it poses no barrier to parallel implementation, and its fairly common occurrence in linear systems. However, it is only efficient for matrices in which the main diagonal elements are much greater in magnitude than the off-diagonal elements (a condition referred to as “diagonal dominance”). Unfortunately, this is generally not the case for the problem studied here. We have therefore replaced the diagonal preconditioner with an incomplete Cholesky decomposition preconditioner, similar to what was provided in the public-release version of Zeus-2D. The savings in computational cost has been enormous.

3.6 Gravitational Potential Solver

Added Routine: `GPBVCy1`

Modified Routine: Gravity

Zeus-MP computes the gravitational potential through a two-step process: first, the gravitational potential ψ is found on the computational boundaries; then ψ is found in the interior by iteratively solving the Poisson equation for ψ using a sparse matrix solver that relies on the preconditioned conjugate gradient method. For each boundary of the domain, there are two possible boundary types: (1) Neumann, in which the slope of the gravitational potential is set to zero, and (2) Dirichlet, in which the value of ψ in the ghost zones is specified. (There is actually a third possible boundary type — periodic boundary conditions — however, this boundary condition is not used here.) Neumann boundary conditions are used at symmetry boundaries (axis $r = 0$ and equatorial plane $z = 0$), while Dirichlet conditions are applied at the outer boundaries, far from most of the mass distribution. In the public-release version of Zeus-MP, Dirichlet boundary conditions are implemented by computing ψ on the domain boundaries using a multipole expansion formula, which we give here in spherical coordinates (z, θ, ϕ) for an axisymmetric mass distribution:

$$\psi(z, \theta) = -G \sum_{\ell=0,2} \left[\int \rho(z', \theta') P_{\ell}(\cos \theta') z'^{\ell} d^3 z' \right] \frac{P_{\ell}(\cos \theta)}{z^{\ell+1}}, \quad (3.32)$$

where P_{ℓ} is the Legendre polynomial of degree ℓ . Note that Zeus-MP uses only the monopole and quadrupole moments, in contrast to the earlier Zeus-2D code (Stone & Norman 1992a), which used arbitrarily high ℓ moments until a desired convergence was achieved. The term in brackets is denoted by q_{ℓ} , and is known as the multipole moment of order ℓ of the density distribution. In most situations, a dozen or so multipole moments are sufficient for convergence. They can be calculated once and then used to find the potential at many boundary points. However, we have found this subroutine inadequate for our purposes, as it fails to converge in situations when the distance z to the point at which one wishes to calculate the potential is greater than the distance to any mass element. In the axisymmetric geometry used in this work, this situation is inevitable: mass elements

near $(r, z) = (0, Z)$ or $(r, z) = (R, 0)$ are closer to the origin than are mass elements near $(r, z) = (R, Z)$. We, therefore, have followed Desch & Mouschovias (2001) in using the more general multipole expansion (Jackson 1999):

$$\psi(\boldsymbol{z}, \theta) = -G \sum_{\ell=0}^{\infty} \left[\int \rho(\boldsymbol{z}', \theta') P_{\ell}(\cos \theta') \frac{z_{<}^{\ell}}{z_{>}^{\ell+1}} d^3 \boldsymbol{z}' \right] P_{\ell}(\cos \theta), \quad (3.33)$$

where $z_{>}$ ($z_{<}$) is the greater (lesser) of z' and z , and ℓ may take arbitrarily large integral values until a desired convergence is achieved. An unfortunate consequence of this more general expansion is that it is *not* possible to perform one integration over all space and use the result of that integration (the multipole moment q_{ℓ}) to find the potential at all boundary points. Instead, a new integration over space must be performed for each boundary point, since the location of that boundary point will determine how the integral in equation (3.33) is separated into two integrals: one integral will have z' in the numerator of the integrand, and in the other integral z' will be in the denominator. This situation is further complicated by the use of parallelization, since comparisons of z and z' and subsequent integrations must take place across multiple processors.

3.7 Initial and Boundary Conditions

Added Routine: NewStar

The model cloud is evolved by using the six-fluid RMHD equations (2.77) from a nonequilibrium, uniform “reference” state, characterized by a number density of neutrals $n_{\text{n,ref}} = 300 \text{ cm}^{-3}$ (corresponding to a neutral mass density $\rho_{\text{n,ref}} \simeq 1.17 \times 10^{-21} \text{ g cm}^{-3}$), temperature $T_{\text{ref}} = 10 \text{ K}$ (corresponding to an isothermal sound speed $c_{\text{s,ref}} = 0.188 \text{ km s}^{-1}$), and magnetic field strength $B_{\text{ref}} = 15 \text{ } \mu\text{G}$ (corresponding to an Alfvén speed $v_{\text{A}} = 1.24 \text{ km s}^{-1}$). The cloud has radius R and half-thickness Z , both equal to 0.75 pc , implying a total mass of $45.5 M_{\odot}$. The central mass-to-flux ratio of the reference state in

units of the critical central value is then

$$\begin{aligned}\mu_{\text{ref}} &\equiv \frac{(dM/d\Phi_{\text{B}})_{\text{c}}}{(dM/d\Phi_{\text{B}})_{\text{c,cr}}} = \frac{2Z\rho_{\text{n,ref}}/B_{\text{ref}}}{(3/2)(63G)^{-1/2}} \\ &= 0.49 \left(\frac{n_{\text{n,ref}}}{300 \text{ cm}^{-3}} \right) \left(\frac{Z}{0.75 \text{ pc}} \right) \left(\frac{15 \mu\text{G}}{B_{\text{ref}}} \right),\end{aligned}\quad (3.34)$$

where $(dM/d\Phi_{\text{B}})_{\text{c,cr}} = (3/2)(63G)^{-1/2}$ is the central critical value for collapse originally determined by Mouschovias & Spitzer (1976) for objects initially having a spherical mass distribution threaded by a uniform magnetic field.

If the magnetic field were frozen in the matter, our “reference” state would relax along field lines and oscillate about an equilibrium state (denoted by a subscript “0”) in which gravity is balanced by thermal-pressure forces along field lines and mainly by magnetic forces perpendicular to field lines. An important dimensionless parameter in this equilibrium state is the ratio of the magnetic and thermal pressures,

$$\begin{aligned}\alpha_0 &\equiv \frac{B_0^2}{8\pi\rho_{\text{n},0}c_{\text{s},0}^2} \\ &= 6.48 \left(\frac{B_0}{15 \mu\text{G}} \right)^2 \left(\frac{10^3 \text{ cm}^{-3}}{n_{\text{n},0}} \right) \left(\frac{10 \text{ K}}{T_0} \right).\end{aligned}\quad (3.35)$$

In equilibrium, $\alpha_0\mu_0^2 \approx 0.71$ (see Mouschovias 1991b). Since $\mu_{\text{ref}} = \mu_0$ (i.e., flux-frozen contraction along field lines does not alter a fragment’s mass-to-flux ratio), the central density in the equilibrium state will be a factor $\approx 1.4\alpha_{\text{ref}}\mu_{\text{ref}}^2 \approx 7$ greater than that of the reference state. As in Fiedler & Mouschovias (1993), we have found little quantitative difference (for typical parameters) between a run in which ambipolar diffusion operates from the outset and one in which the cloud is allowed to reach equilibrium under flux-freezing before ambipolar diffusion is switched on. The physical reason for this is that the relaxation time along field lines is short compared to the ambipolar diffusion timescale, particularly for the low densities characteristic of the relaxation phase ($n_{\text{n}} \lesssim 10^3 \text{ cm}^{-3}$ — see below) when ionization due to UV radiation is important.

We pause here briefly to reemphasize an important point discussed in Mouschovias (1991b, § 2.3) — see also Fiedler & Mouschovias (1993). In the central flux tube of such an equilibrium state, one has that

$$\rho_{n,c} c_s^2 \approx \frac{\pi}{2} G \Sigma_{n,c}^2 \approx \frac{\mu_0^2}{0.71} \frac{B_c^2}{8\pi}, \quad (3.36)$$

where $\Sigma_{n,c} = 2\rho_{n,c}Z$ is the neutral column density of the central flux tube. Physically, this equation states that, in equilibrium, the thermal, gravitational, and magnetic pressures of a critical central flux tube ($\mu_0 = 1$) are approximately equal to one another. For subcritical central flux tubes ($\mu_0 < 1$), the *local* magnetic pressure exceeds the thermal and gravitational pressures. This does *not* imply that such flux tubes will expand. It simply means that the magnetic field in the core is comparable to that in envelope, and is confined by the massive envelope, not the core. Virial-theorem based arguments (McKee et al. 1993; Nakano 1998) miss this essential point, leading to the physical absurdity that magnetically-subcritical fragments cannot exist in nature.

Due to the assumed symmetry of the problem, we need only simulate the computational region bounded by $0 \leq r \leq R$ and $0 \leq z \leq Z$. Boundary conditions on the density and velocity are chosen so that no mass, flux, or thermal energy crosses any boundary. The magnetic field is constrained to cross the midplane ($z = 0$) and upper boundary ($z = Z$) normally, and to have no radial component at the axis ($r = 0$) and outer boundary ($r = R$). In order to prevent unrealistic densities near the upper boundary of the computational domain ($z = Z$), a floor is imposed on the neutral number density at $n_{n,\text{floor}} = 1 \text{ cm}^{-3}$. In addition, the gas and radiation temperatures are maintained $\geq 10 \text{ K}$ by imposing temperature floors.

3.8 Summary

In this chapter we described in detail the numerical method used to obtain the solution of the nonlinear evolutionary equations (2.77), which were derived in the previous chapter. The wide variety of physics encountered when attempting to numerically simulate the process of star formation places stringent demands on the type of code that can be employed quickly and effectively. Fortunately, the publicly-available Zeus-MP code is well-suited for this task, not only because of its well-documented and thoroughly-tested ability to accurately follow the dynamics of astrophysical fluids in the presence of both magnetic fields and radiation, but also because the code was designed with a discerning eye towards versatility and flexibility. This made our task of altering the algorithms governing the evolution of the magnetic field, in order to account for ambipolar diffusion and Ohmic dissipation, relatively straightforward and painless. Unfortunately, the same cannot be said for several of Zeus-MP's other algorithms, whose poor convergence and gross inefficiency were revealed by the demands of our particular problem. These faults were rectified either by the addition of new or the modification of existing modules, all of which have been catalogued in this chapter. We have also provided here the initial and boundary conditions imposed on the numerical simulations, the results of which are presented in the following chapter.

Chapter 4

Results

4.1 The Physical Model

A detailed discussion of the physical processes included in the calculations was presented in Chapter 2. In summary, we consider a two-dimensional, nonrotating, nonisothermal model molecular cloud, whose axis of symmetry is aligned with the z -axis of a cylindrical-polar coordinate system (r, ϕ, z) . The cloud is initially threaded by a uniform magnetic field oriented along the symmetry axis. The abundances of all species (except the neutrals) are determined from an extensive equilibrium chemical reaction network that includes cosmic rays, radioactive decays, thermal ionization, dissociative and radiative recombination, atomic and molecular ion charge transfer, electron and ion attachment onto grains, and charge transfer by grain–grain collisions. UV ionization is treated qualitatively. While the code described in Chapter 3 is designed to handle an MRN grain size distribution, we present here only the simpler case of a uniform grain size distribution. Results of numerical calculations that employ an MRN distribution will be presented as a part of a parameter study in a future publication (M. W. Kunz & T. Ch. Mouschovias 2010, in preparation).

4.2 Overall Evolution

In Figures 4.1 and 4.2, we show, respectively, the time evolution of the central number density of neutrals, $n_{n,c}$, and the central mass-to-flux ratio, $(dM/d\Phi_B)_c$, (normalized to the central critical value) as a function of $n_{n,c}$. There are three distinct phases of evolu-

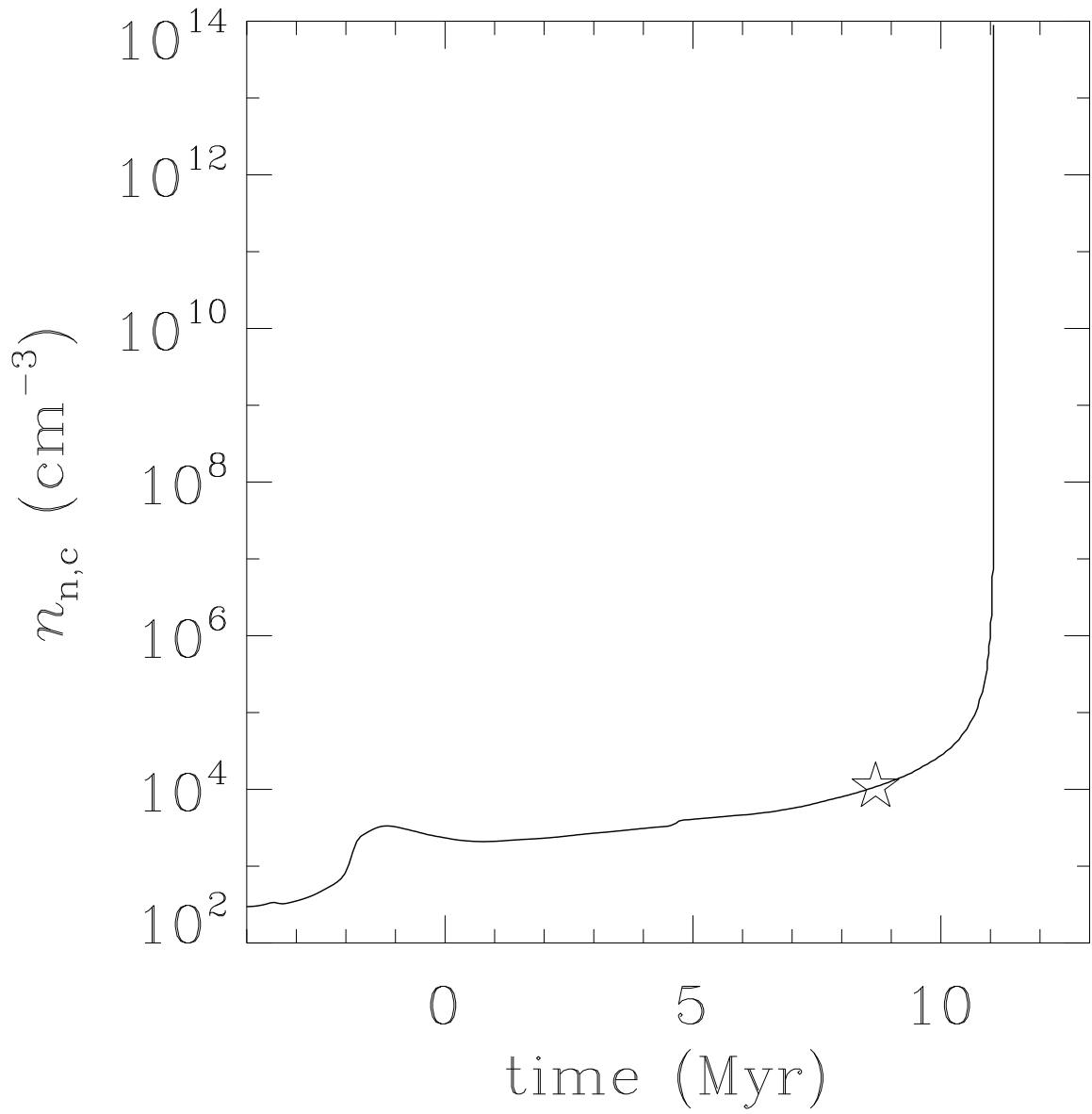


Figure 4.1: Central number density of neutrals, $n_{n,c}$, as a function of time. The “star” marks the time at which a supercritical core forms.

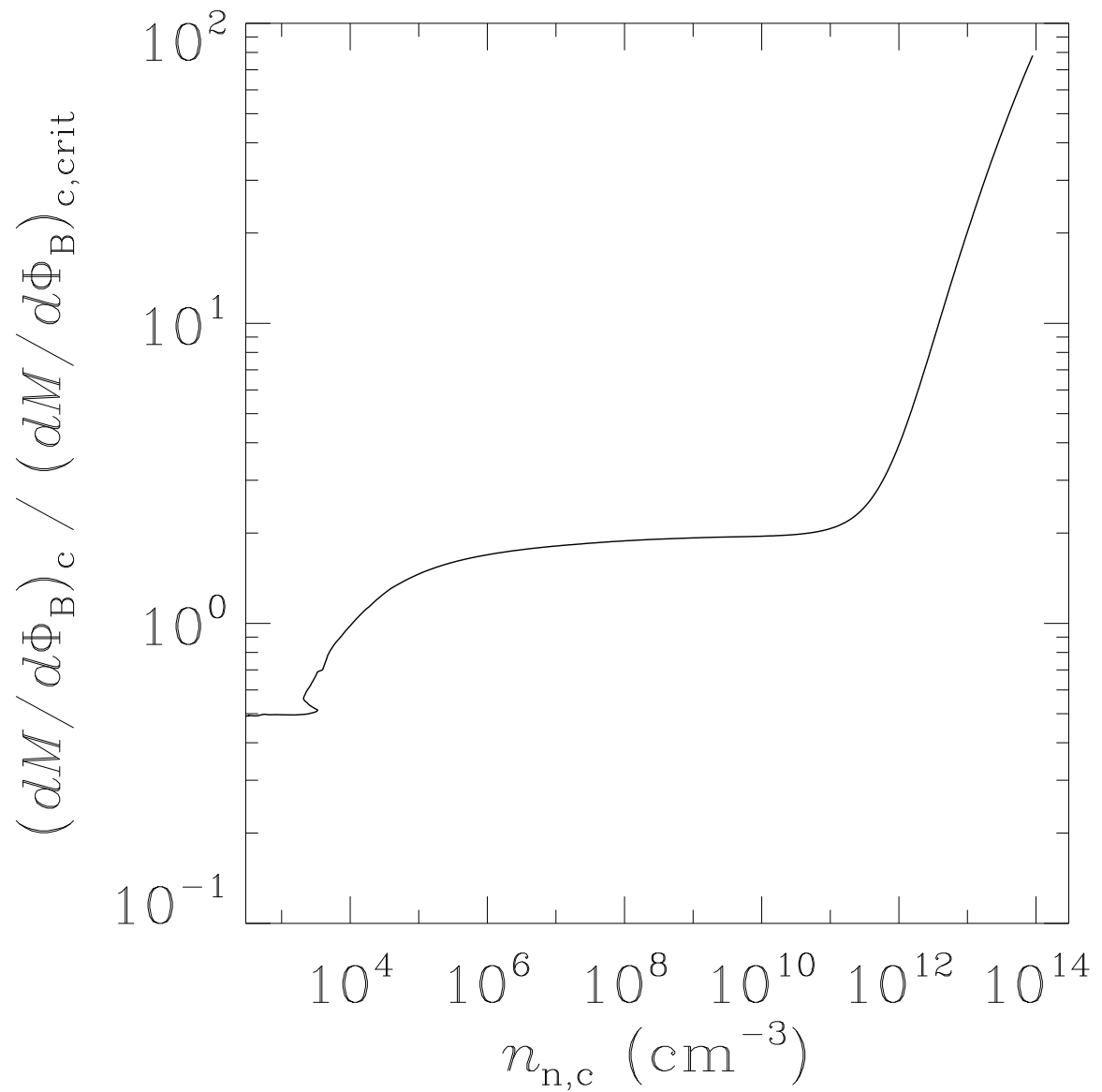


Figure 4.2: Central mass-to-flux ratio (normalized to the central critical value) as a function of $n_{n,c}$. The “star” marks the time at which a supercritical core forms.

tion: relaxation, quasistatic, and dynamic. First, the cloud relaxes along magnetic field lines from its uniform reference state to a quasi-equilibrium state whose central density $n_{n,c} \simeq 2280 \text{ cm}^{-3}$. Ambipolar diffusion is negligible during this phase, since it is marked by relatively low densities ($\lesssim 10^3 \text{ cm}^{-3}$) and therefore relatively large degrees of ionization ($\sim 10^{-6} - 10^{-5}$) due to UV radiation. Hence, the mass-to-flux ratio remains roughly constant. Once UV radiation is shielded, the fragment contracts quasistatically (i.e., negligible acceleration) under its own self-gravity via ambipolar diffusion until a supercritical core forms at $n_{n,c} \simeq 1.1 \times 10^4 \text{ cm}^{-3}$ and time $\approx 9 \text{ Myr}$ (denoted in the figure by the position of the “star”). The subsequent evolution is dynamic, although significantly slower than free-fall. The central mass-to-flux ratio asymptotes to roughly twice its critical value until ambipolar diffusion is “reawakened” at a central density $n_{n,c} \approx 10^{11} \text{ cm}^{-3}$. The mass-to-flux ratio then increases dramatically, reaching $\simeq 80$ times the central critical value for collapse by the end of the calculation (at a density $\simeq 10^{14} \text{ cm}^{-3}$). During the entire supercritical phase of evolution, the central density increases by ten orders of magnitude in 2.38 Myr.

Note that, by the time the core formed in this simulation becomes observable as a well-defined ammonia core (at a central density $2 \times 10^4 \text{ cm}^{-3}$), it has already become magnetically supercritical. Therefore, Zeeman observations of ammonia cores are predicted to preferentially measure supercritical mass-to-flux ratios. Indeed, this has already been seen by, e.g., Crutcher (1999). Also, the detectable (using ammonia as a tracer) lifetime of the core formed in this simulation is 1.46 Myr, compatible with the $\sim 1 \text{ Myr}$ lifetime of starless cores advocated by Lee & Myers (1999) and Jijina et al. (1999). (See Tassis & Mouschovias 2004 for a further discussion of this point and its importance in interpreting starless core statistics.)

The overall spatial and temporal evolution of the cloud is shown in Figures 4.3 – 4.11. The density (thin solid lines), magnetic field (thick solid lines), and velocity field (arrows) are given in each of the frames, which show portions of the cloud at the different times

when the central density $n_{n,c} = 3 \times (10^3, 10^4, 10^5, 10^6, 10^9, 10^{11}, 10^{12}, 10^{13}) \text{ cm}^{-3}$ and 10^{14} cm^{-3} . The velocity vectors are normalized to the maximum velocity in each frame (given in the figure captions). Every second isodensity contour indicates a change in density by a factor of 10.

In Figure 4.3, we show the entire model cloud ($-R \leq r \leq R, -Z \leq z \leq Z$) at the time when the central density $n_{n,c} = 3 \times 10^3 \text{ cm}^{-3}$. The cloud has settled into a quasi-equilibrium state and ambipolar diffusion has already commenced. The magnetic field lines remain relatively undeformed, while the neutrals contract through the magnetic field lines via their own self-gravity (their maximum radial velocity at this moment is 0.012 km s^{-1}). At large r and z , there is a small outward motion as the cloud rebounds from overshooting its equilibrium state.

In Figure 4.4 ($n_{n,c} = 3 \times 10^4 \text{ cm}^{-3}$), the central magnetic flux tubes of the cloud have just become magnetically supercritical and begun to bend into an hourglass morphology. Such a field morphology has been observed via dust polarimetry by, e.g., Schleuning (1998), Hildebrand et al. (1999), Girart et al. (1999), Schleuning et al. (2000), Lai et al. (2002), Matthews & Wilson (2002), Houde et al. (2004), Cortes & Crutcher (2006), Girart et al. (2006), Vaillancourt et al. (2008), Tang et al. (2009), and Kirby (2009). The maximum radial velocity has increased to 0.033 km s^{-1} . The outermost envelope of the cloud remains magnetically supported, whence the radial velocities there are very small. A shock has formed at $z \simeq 0.3 \text{ pc}$ (maximum vertical velocity $0.39 \text{ km s}^{-1} \approx 2c_s$) because of the rapid collapse along field lines.

In Figure 4.5 ($n_{n,c} = 3 \times 10^5 \text{ cm}^{-3}$), the magnetically-supercritical core is well into its dynamical (though slower than free-fall) stage of evolution and the maximum radial velocity has reached $\approx 0.1 \text{ km s}^{-1}$. By this point, the qualitative features of the outer envelope of the cloud, which is magnetically supported, have been largely determined and essentially do not evolve throughout the remainder of the simulation. The result is a highly nonhomologous collapse. We therefore focus on progressively smaller radii and track the

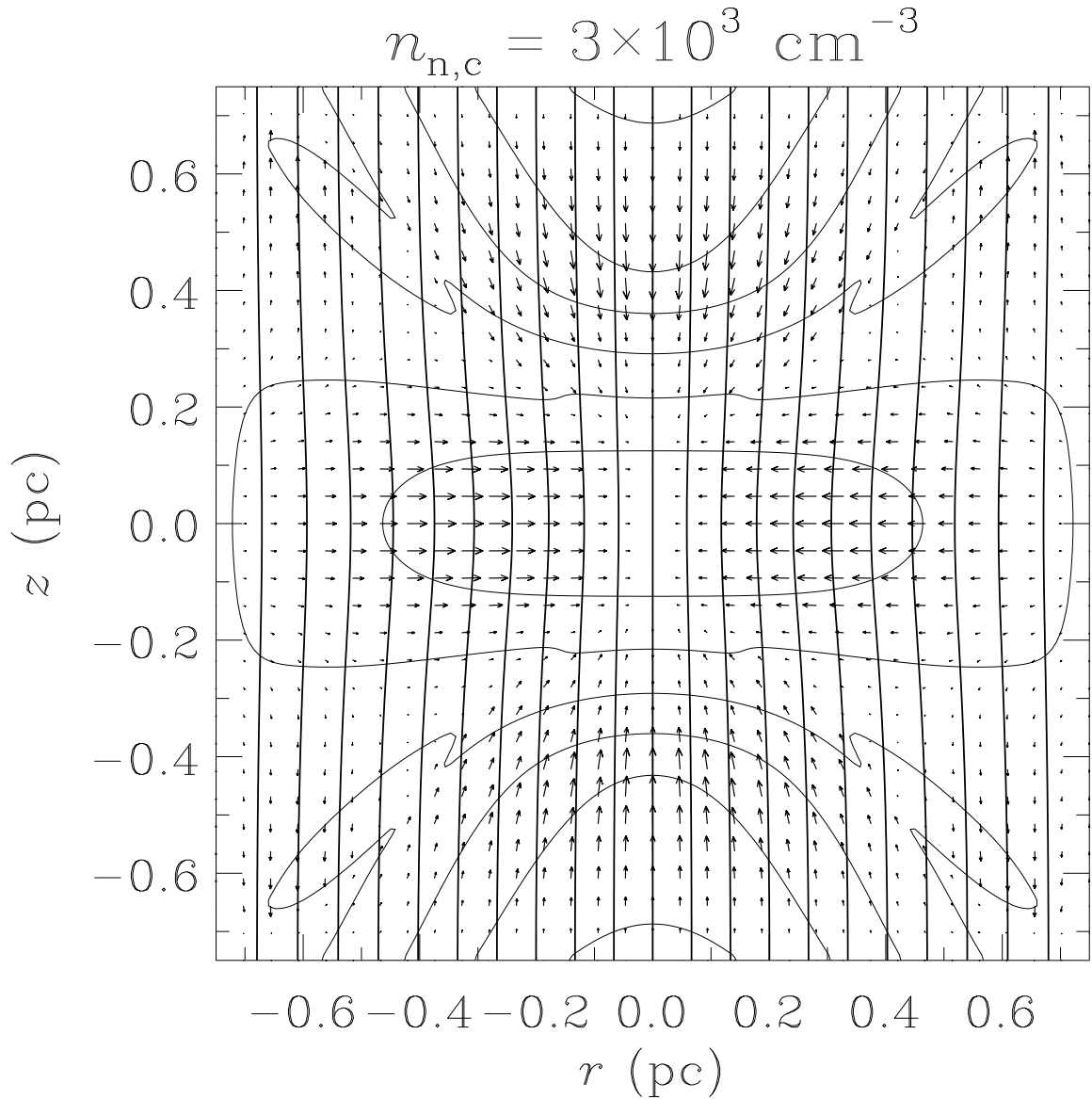


Figure 4.3: Spatial structure of the entire model cloud at the time when the central density $n_{n,c} = 3 \times 10^3 \text{ cm}^{-3}$. Isodensity contours (thin solid lines), magnetic field lines (thick solid lines), and velocity vectors (arrows) are shown. Every second isodensity contour indicates a change in density by a factor of 10. The innermost isodensity contour corresponds to 10^3 cm^{-3} . The velocity vectors are normalized to the maximum velocity in the frame (0.23 km s^{-1}).

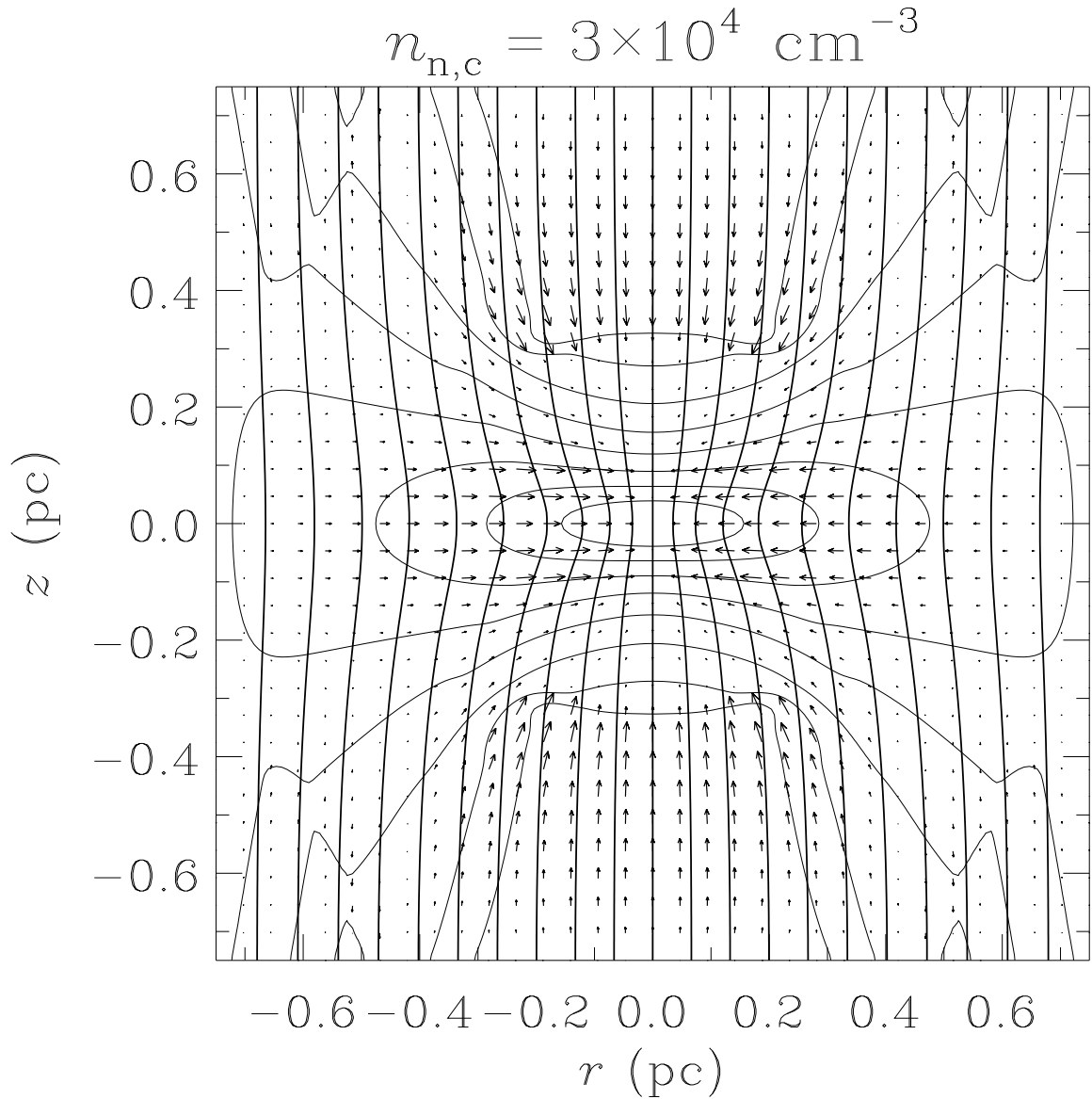


Figure 4.4: Spatial structure of the entire model cloud at the time when the central density $n_{n,c} = 3 \times 10^4 \text{ cm}^{-3}$. Isodensity contours (thin solid lines), magnetic field lines (thick solid lines), and velocity vectors (arrows) are shown. Every second isodensity contour indicates a change in density by a factor of 10. The innermost isodensity contour corresponds to 10^4 cm^{-3} . The velocity vectors are normalized to the maximum velocity in the frame (0.39 km s^{-1}).

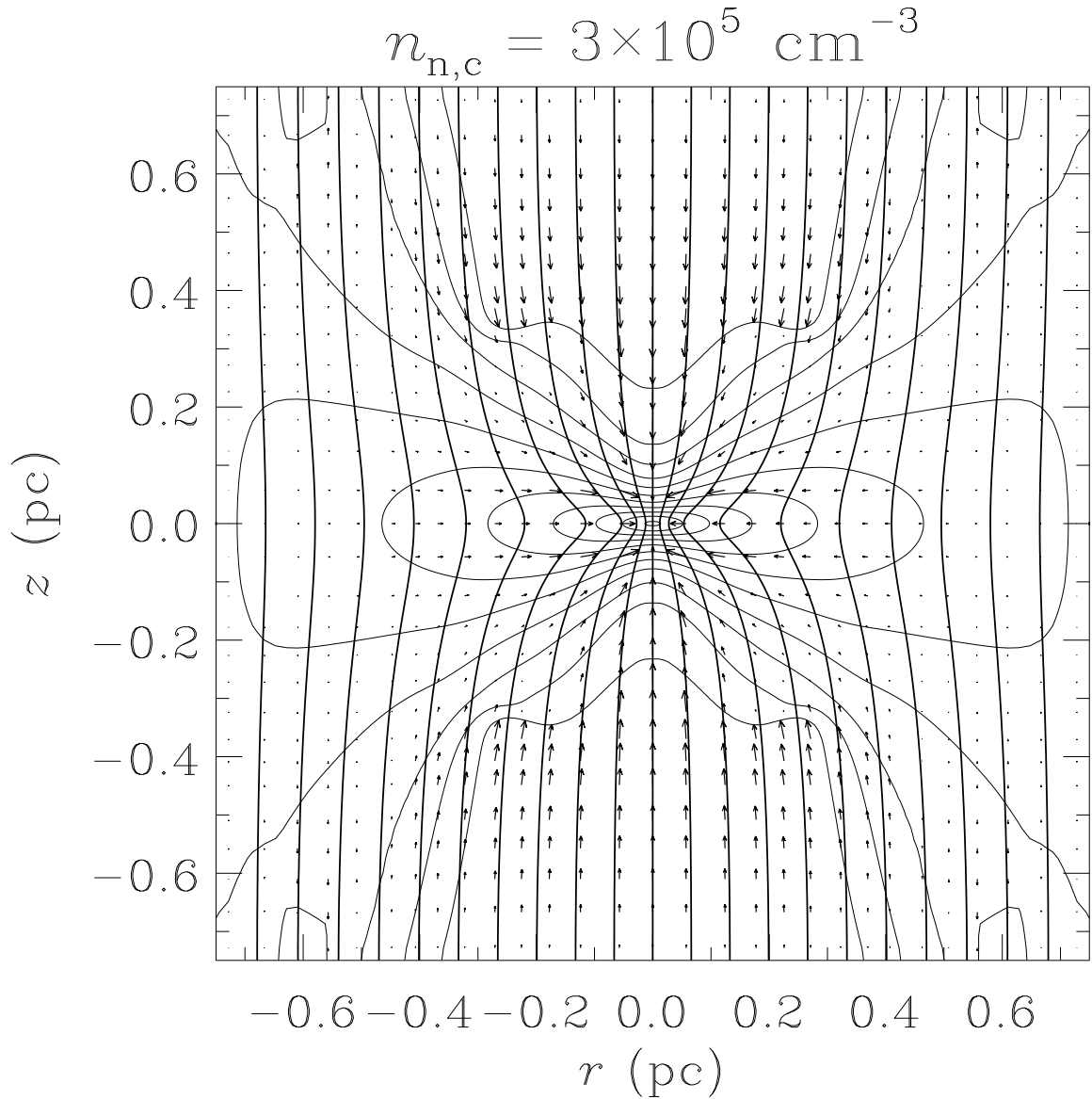


Figure 4.5: Spatial structure of the entire model cloud at the time when the central density $n_{n,c} = 3 \times 10^5 \text{ cm}^{-3}$. Isodensity contours (thin solid lines), magnetic field lines (thick solid lines), and velocity vectors (arrows) are shown. Every second isodensity contour indicates a change in density by a factor of 10. The innermost isodensity contour corresponds to $3 \times 10^5 \text{ cm}^{-3}$. The velocity vectors are normalized to the maximum velocity in the frame (0.42 km s^{-1}).

local evolution of the magnetically-supercritical core.

In Figure 4.6, we show the innermost 10% of the cloud when $n_{n,c} = 3 \times 10^6 \text{ cm}^{-3}$. The maximum radial (vertical) velocity is 0.18 km s^{-1} (0.47 km s^{-1}). It is clear that the core remains disklike down to smallest scales, even in the absence of rotation, a consequence of the presence of magnetic forces. In Figure 4.7, we show the innermost 1% of the cloud when $n_{n,c} = 3 \times 10^9 \text{ cm}^{-3}$. The maximum radial (vertical) velocity at this moment is 0.38 km s^{-1} (0.80 km s^{-1}). The similarities between these two figures suggest that the supercritical phase of core contraction is nearly self-similar, a fact that has been exploited by, e.g., Basu (1997), Contopoulos et al. (1998), and Krasnopolsky & Königl (2002), who derived semianalytic self-similar solutions for this stage of contraction that reproduce the main qualitative features found in detailed simulations.

The evolution departs from being nearly self-similar at higher densities, once the gas begins to decouple from the magnetic field and a spherical geometry is approached. In Figures 4.8 – 4.11, we zoom in on the innermost 0.01% of the cloud ($\simeq 15.5 \text{ AU} \times 15.5 \text{ AU}$) in order to highlight the formation of the hydrostatic core. In Figure 4.8, the central density $n_{n,c} = 3 \times 10^{11} \text{ cm}^{-3}$ and the maximum radial (vertical) velocity at this moment is 0.52 km s^{-1} (1.03 km s^{-1}). This is the last frame shown in which an oblate disklike geometry is exhibited in the innermost $r \lesssim 4 \text{ AU}$ of the cloud. In Figure 4.9 ($n_{n,c} = 3 \times 10^{12} \text{ cm}^{-3}$), this region has begun to assume a spherical geometry due to the increasing relative importance of thermal-pressure forces. The magnetic field has decoupled from the matter and the field lines are straight inside the $\simeq 3 \times 10^{11} \text{ cm}^{-3}$ density contour. The radial and vertical velocities attain their maxima (0.64 km s^{-1} and 1.14 km s^{-1} , respectively) just outside of the boundary of the newly-formed hydrostatic core, where shocks occur in both radial and vertical directions. These shocks are a result of the rapid deceleration of matter as it comes into contact with the hydrostatic core boundary. In Figure 4.10 ($n_{n,c} = 3 \times 10^{13} \text{ cm}^{-3}$), the hydrostatic core is clearly visible and exhibits a spherical geometry inside of $\simeq 2 \text{ AU}$. The magnetic field lines continue to remain straight within the

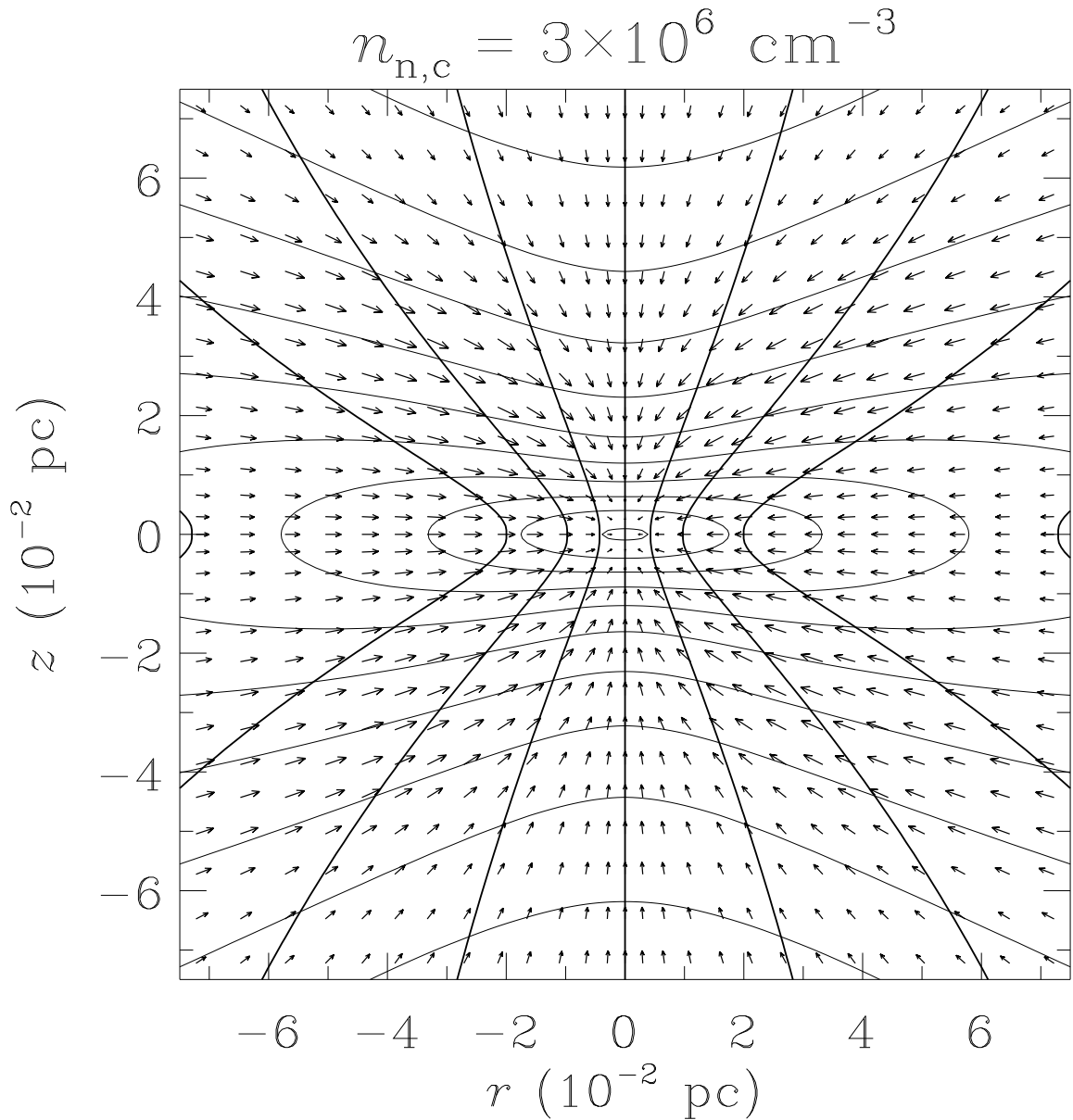


Figure 4.6: Spatial structure of the innermost 10% of the model cloud at the time when the central density $n_{n,c} = 3 \times 10^6 \text{ cm}^{-3}$. Isodensity contours (thin solid lines), magnetic field lines (thick solid lines), and velocity vectors (arrows) are shown. Every second isodensity contour indicates a change in density by a factor of 10. The innermost isodensity contour corresponds to $3 \times 10^6 \text{ cm}^{-3}$. The velocity vectors are normalized to the maximum velocity in the frame (0.47 km s^{-1}).

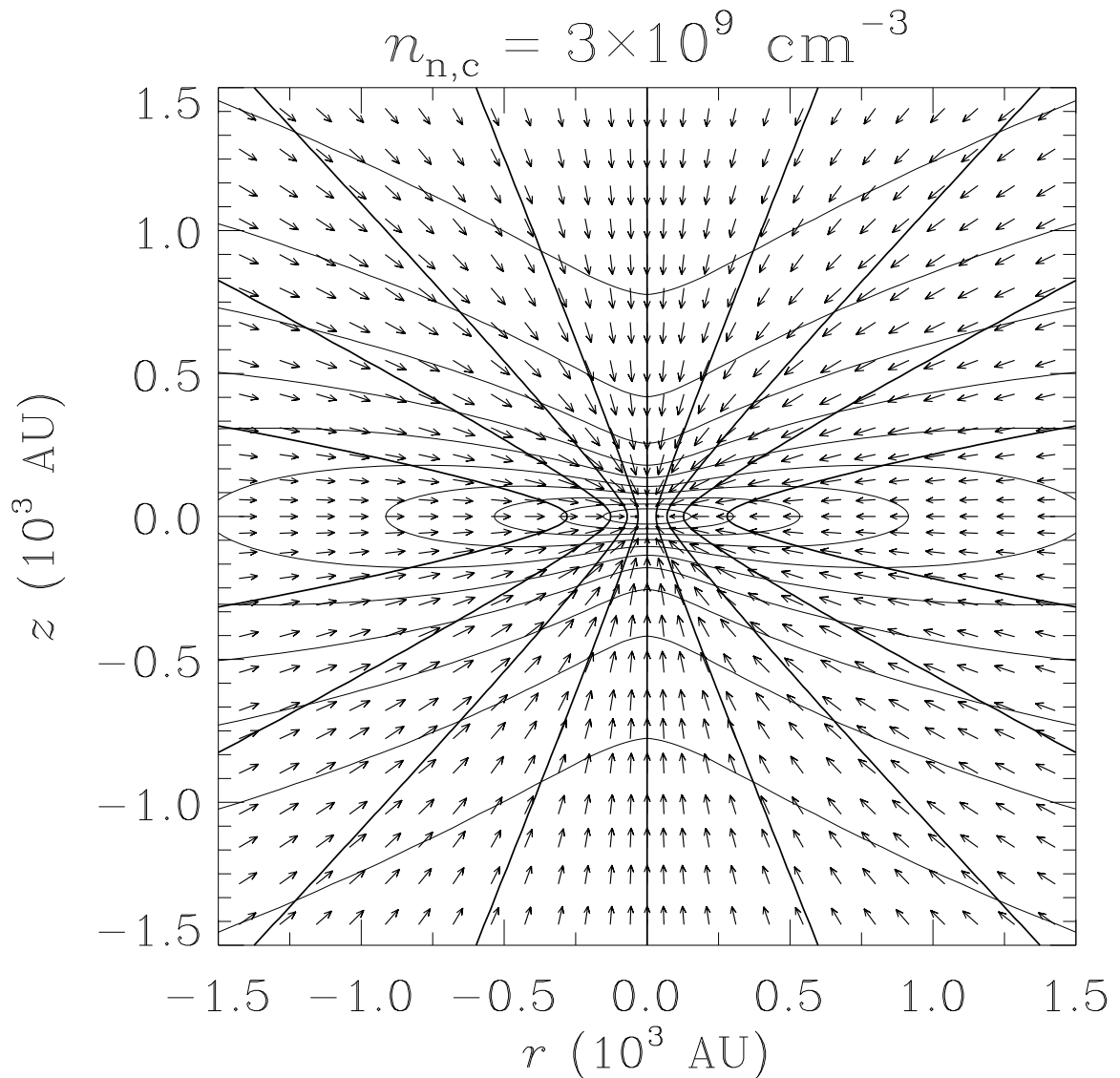


Figure 4.7: Spatial structure of the innermost 1% of the model cloud at the time when the central density $n_{n,c} = 3 \times 10^9 \text{ cm}^{-3}$. Isodensity contours (thin solid lines), magnetic field lines (thick solid lines), and velocity vectors (arrows) are shown. Every second isodensity contour indicates a change in density by a factor of 10. The innermost isodensity contour corresponds to 10^9 cm^{-3} . The velocity vectors are normalized to the maximum velocity in the frame (0.80 km s^{-1}).

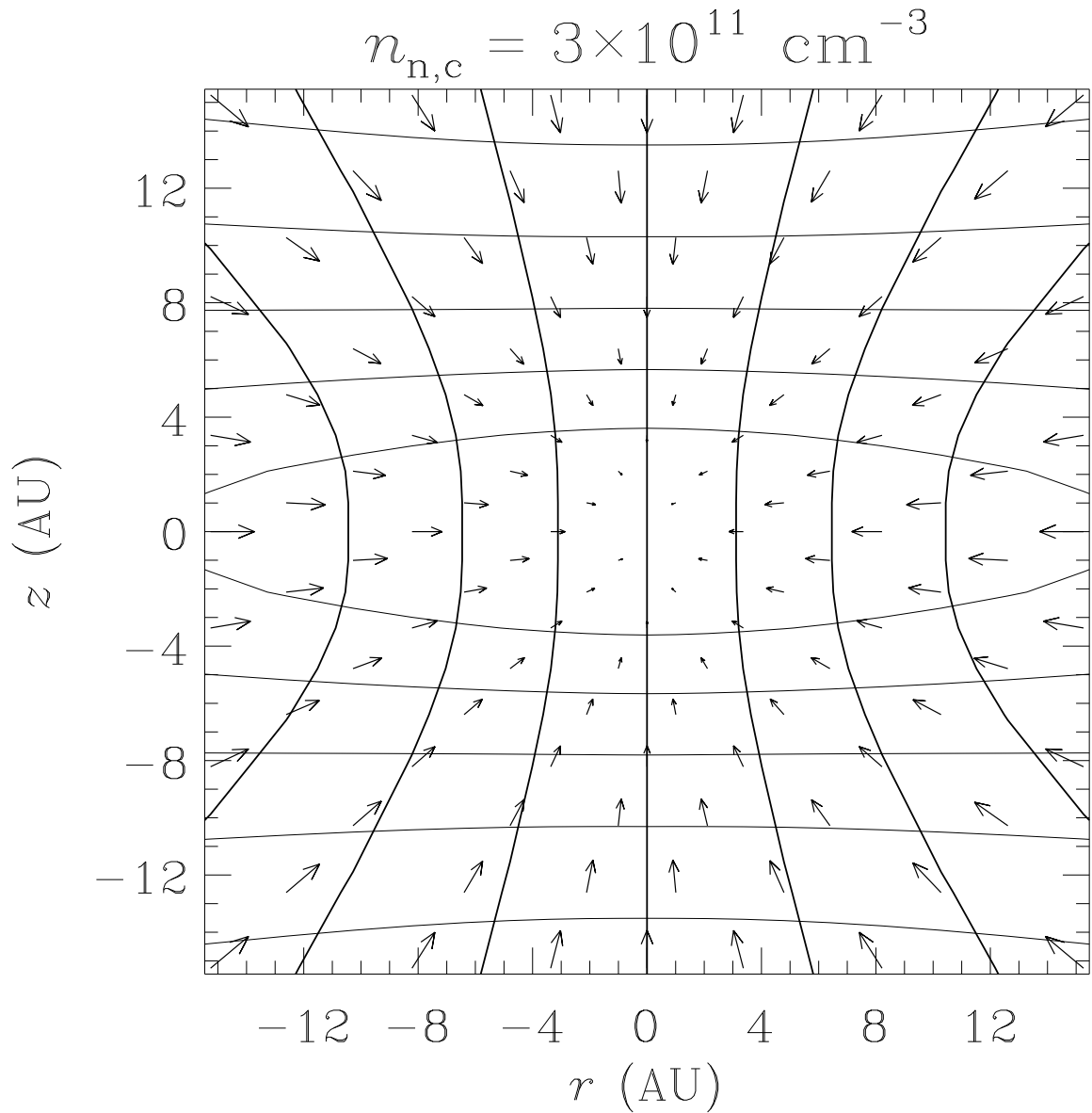


Figure 4.8: Spatial structure of the innermost 0.01% of the model cloud at the time when the central density $n_{n,c} = 3 \times 10^{11} \text{ cm}^{-3}$. Isodensity contours (thin solid lines), magnetic field lines (thick solid lines), and velocity vectors (arrows) are shown. Every second isodensity contour indicates a change in density by a factor of 10. The innermost isodensity contour corresponds to 10^{11} cm^{-3} . The velocity vectors are normalized to the maximum velocity in the frame (1.03 km s^{-1}).

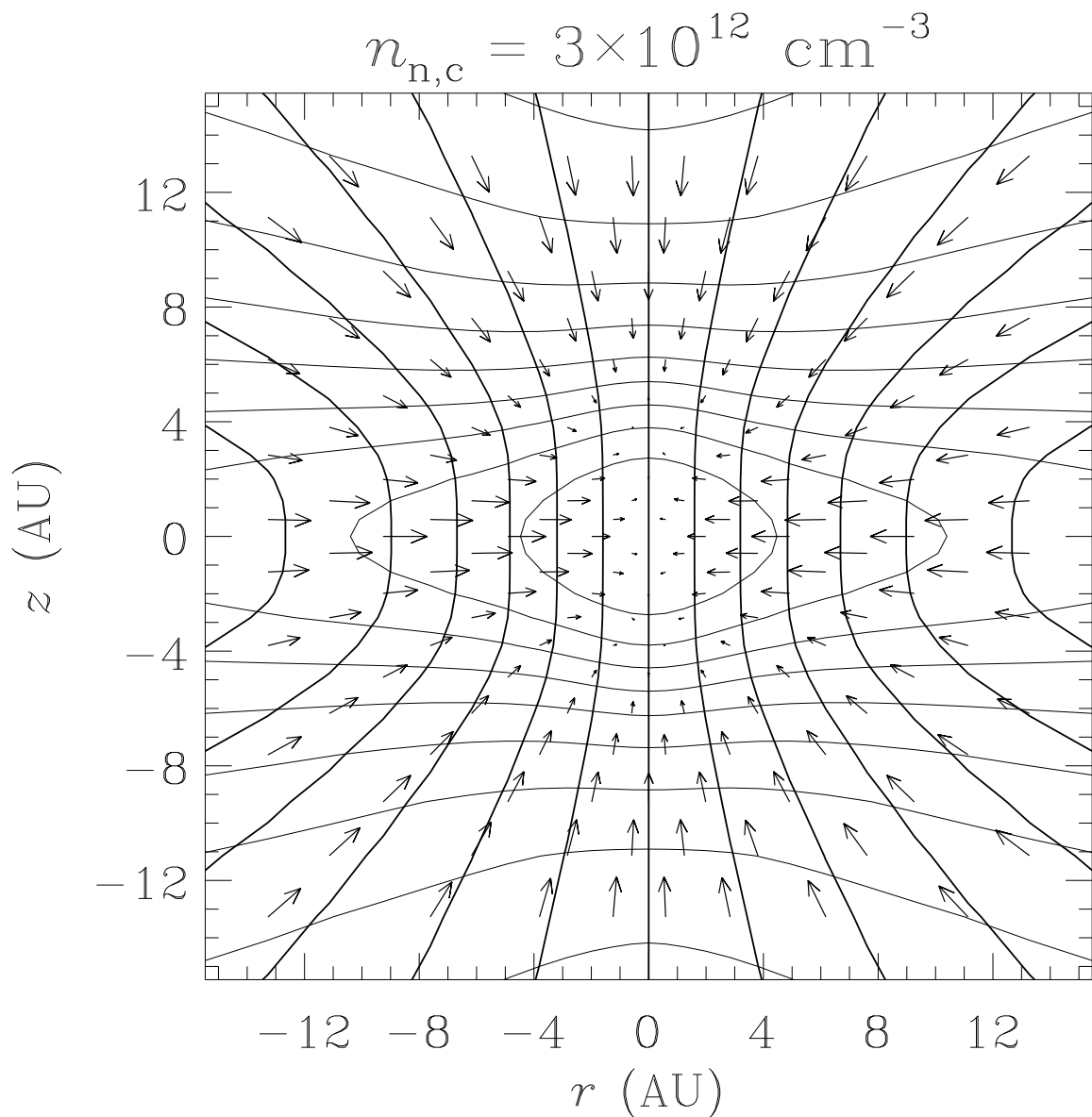


Figure 4.9: Spatial structure of the innermost 0.01% of the model cloud at the time when the central density $n_{n,c} = 3 \times 10^{12} \text{ cm}^{-3}$. Isodensity contours (thin solid lines), magnetic field lines (thick solid lines), and velocity vectors (arrows) are shown. Every second isodensity contour indicates a change in density by a factor of 10. The innermost isodensity contour corresponds to 10^{12} cm^{-3} . The velocity vectors are normalized to the maximum velocity in the frame (1.14 km s^{-1}).

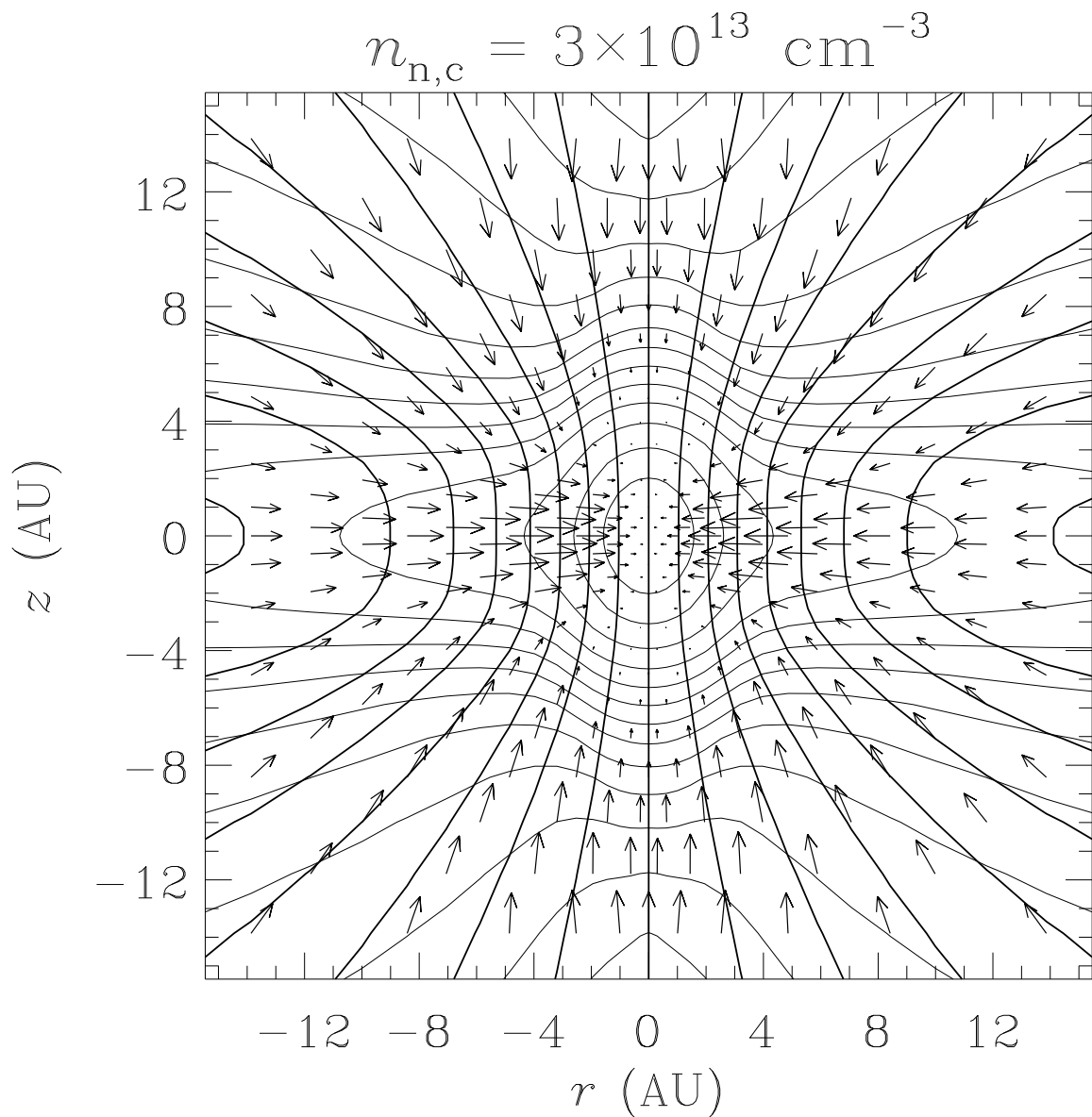


Figure 4.10: Spatial structure of the innermost 0.01% of the model cloud at the time when the central density $n_{n,c} = 3 \times 10^{13} \text{ cm}^{-3}$. Isodensity contours (thin solid lines), magnetic field lines (thick solid lines), and velocity vectors (arrows) are shown. Every second isodensity contour indicates a change in density by a factor of 10. The innermost isodensity contour corresponds to 10^{13} cm^{-3} . The velocity vectors are normalized to the maximum velocity in the frame (1.33 km s^{-1}).

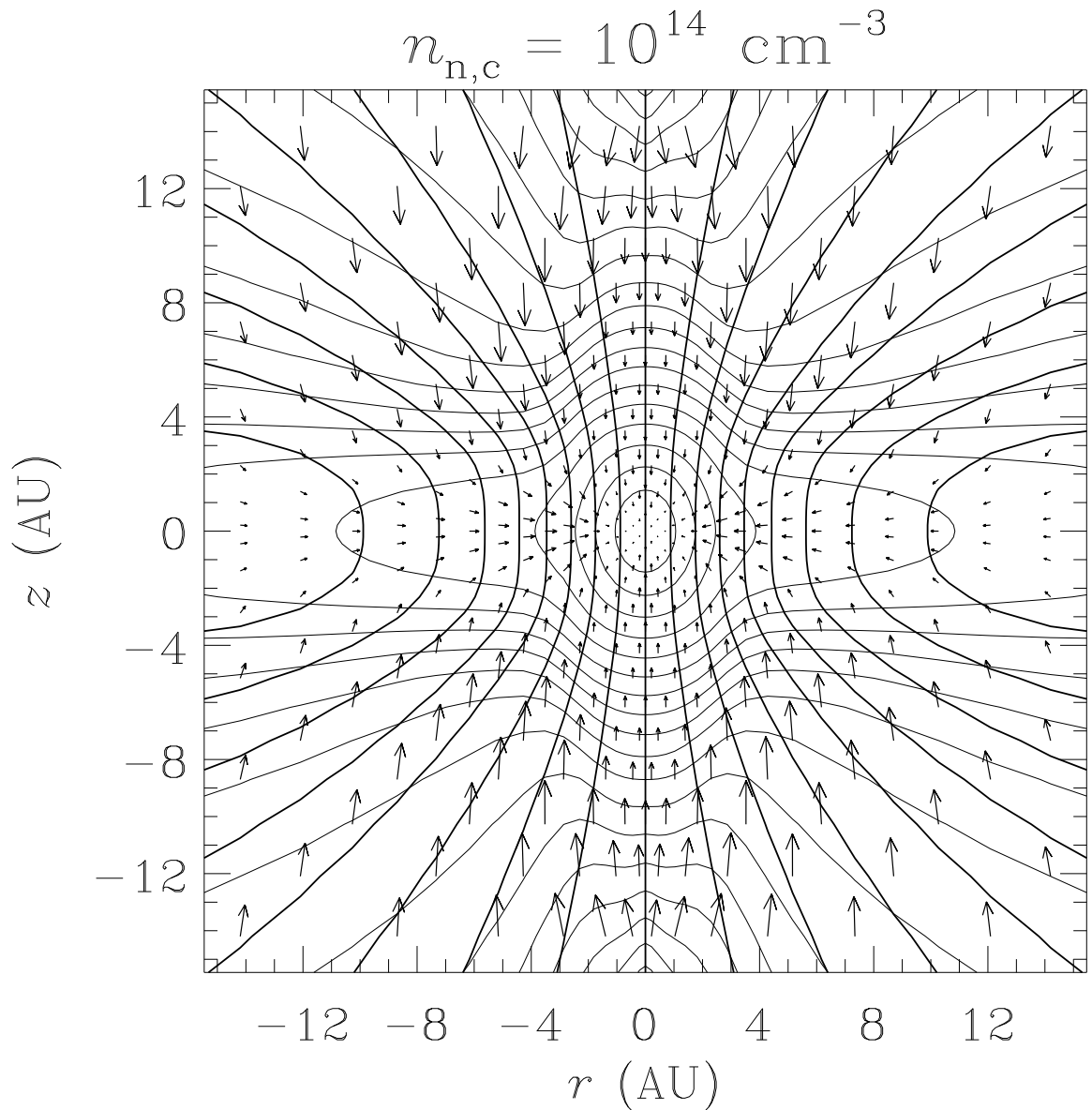


Figure 4.11: Spatial structure of the innermost 0.01% of the model cloud at the time when the central density $n_{n,c} = 10^{14} \text{ cm}^{-3}$. Isodensity contours (thin solid lines), magnetic field lines (thick solid lines), and velocity vectors (arrows) are shown. Every second isodensity contour indicates a change in density by a factor of 10. The innermost isodensity contour corresponds to $3 \times 10^{13} \text{ cm}^{-3}$. The velocity vectors are normalized to the maximum velocity in the frame (1.44 km s^{-1}).

$\simeq 3 \times 10^{11} \text{ cm}^{-3}$ density contour. The maximum radial (vertical) velocity in the frame is 1.13 km s^{-1} (1.27 km s^{-1}). A closer inspection reveals a small outward motion with speed of $\sim 0.1 \text{ km s}^{-1}$ along the vertical symmetry axis, a result of infalling gas rebounding after overshooting hydrostatic quasi-equilibrium. Throughout the evolution, the magnitude of the radial component of the magnetic field never becomes greater than the magnitude of the vertical component. Magnetic pinching forces remain small and magnetic reconnection does not occur. Figure 4.11 shows the innermost 0.01% of the cloud at the end of the simulation (when $n_{n,c} = 10^{14} \text{ cm}^{-3}$). The maximum radial (vertical) velocity in the frame is 1.44 km s^{-1} (1.24 km s^{-1}).

Figures 4.12 – 4.15 exhibit the thermal structure of the innermost 0.01% of the model cloud at times when the central density $n_{n,c} = 3 \times (10^{11}, 10^{12}, 10^{13}) \text{ cm}^{-3}$ and 10^{14} cm^{-3} . Isothermal (solid lines) and isodensity (dashed lines) contours are shown. The maximum temperatures in the three figures are 22.0 K, 72.9 K, 184.4 K, and 268.5 K respectively. Every tenth isothermal contour indicates a change in temperature by a factor of 10; every second isodensity contour indicates a change in density by a factor of 10. Note that, in all three figures, isothermal and isodensity contours coincide only within a region $z \equiv (r^2 + z^2)^{1/2} \lesssim 4 \text{ AU}$. Outside of this region, the temperature structure is appreciably more spherical than the density structure. This suggests that the assumption of a piecewise adiabatic equation of state not only substantially overestimates the temperature, but also results in a qualitatively incorrect thermal structure outwards of $\approx 4 \text{ AU}$.

4.3 Evolution of Central Quantities

Figure 4.16 exhibits the central gas (solid line) and radiation (dashed line) temperatures, T_c , as a function of the central number density of neutrals. The gas remains isothermal at 10 K until a density $n_{\text{opq}} \simeq 10^7 \text{ cm}^{-3}$, after which the heat generated by gravitational collapse is unable to escape efficiently. The central gas temperature then rises with density

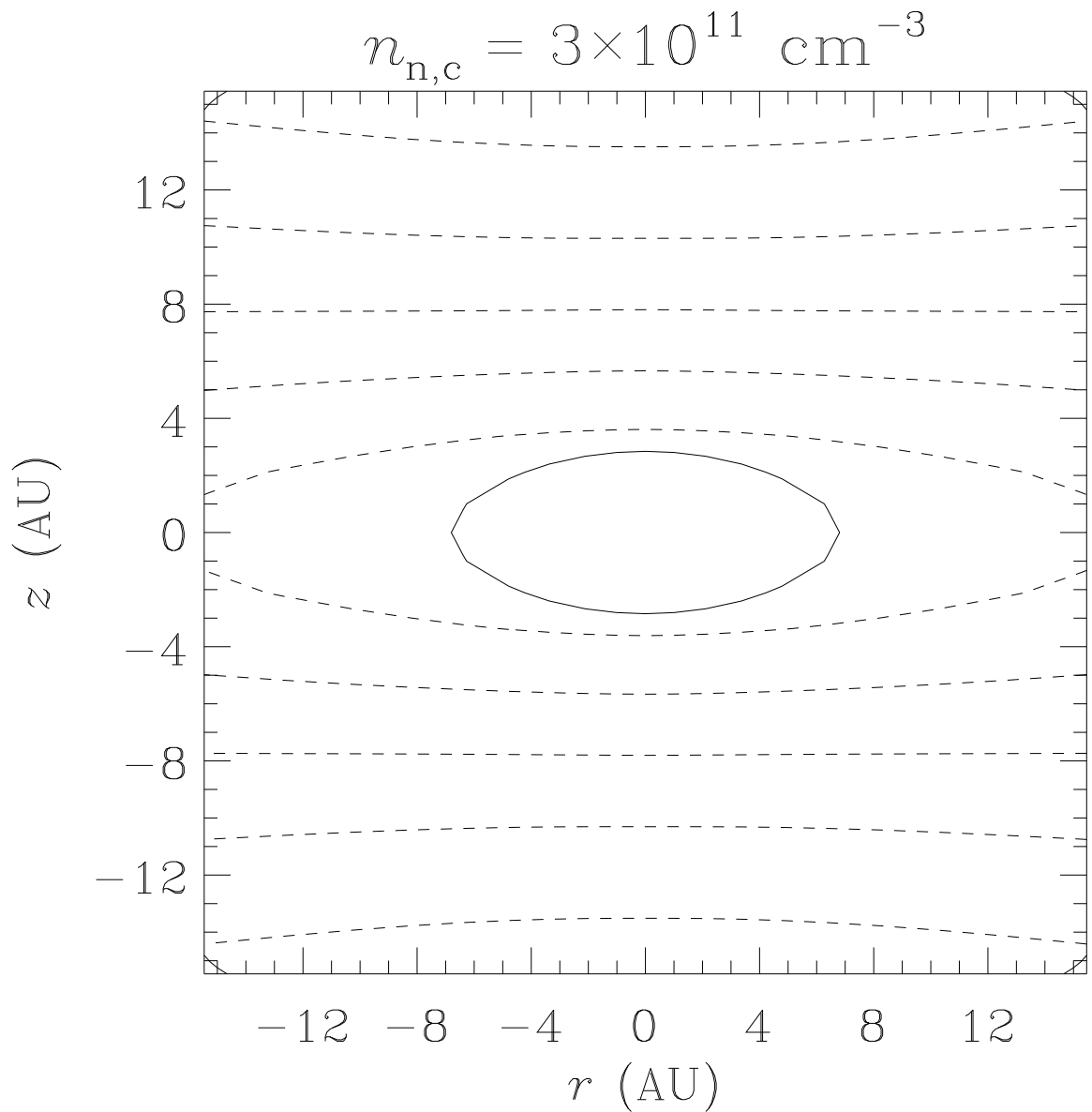


Figure 4.12: Thermal structure of the innermost 0.01% of the model cloud at the time when the central density $n_{n,c} = 3 \times 10^{11} \text{ cm}^{-3}$. The maximum temperature is 22.0 K. Isothermal contours (solid lines) and isodensity contours (dashed lines) are shown. Every tenth isothermal contour indicates a change in temperature by a factor of 10; every second isodensity contour indicates a change in density by a factor of 10. The innermost isothermal (isodensity) contour corresponds to 20 K (10^{11} cm^{-3}).

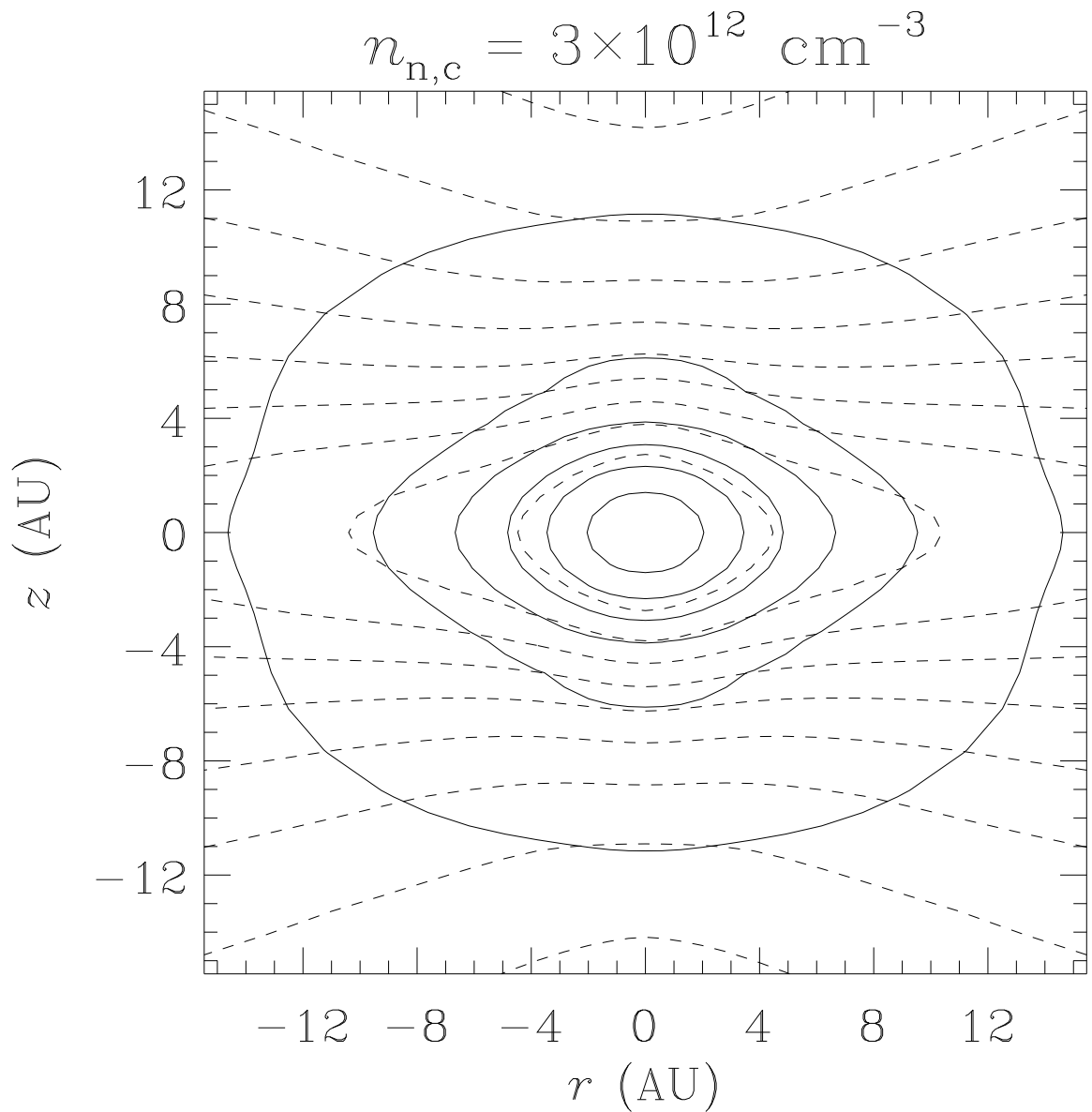


Figure 4.13: Thermal structure of the innermost 0.01% of the model cloud at the time when the central density $n_{n,c} = 3 \times 10^{12} \text{ cm}^{-3}$. The maximum temperature is 72.9 K. Isothermal contours (solid lines) and isodensity contours (dashed lines) are shown. Every tenth isothermal contour indicates a change in temperature by a factor of 10; every second isodensity contour indicates a change in density by a factor of 10. The innermost isothermal (isodensity) contour corresponds to 63 K (10^{12} cm^{-3}).

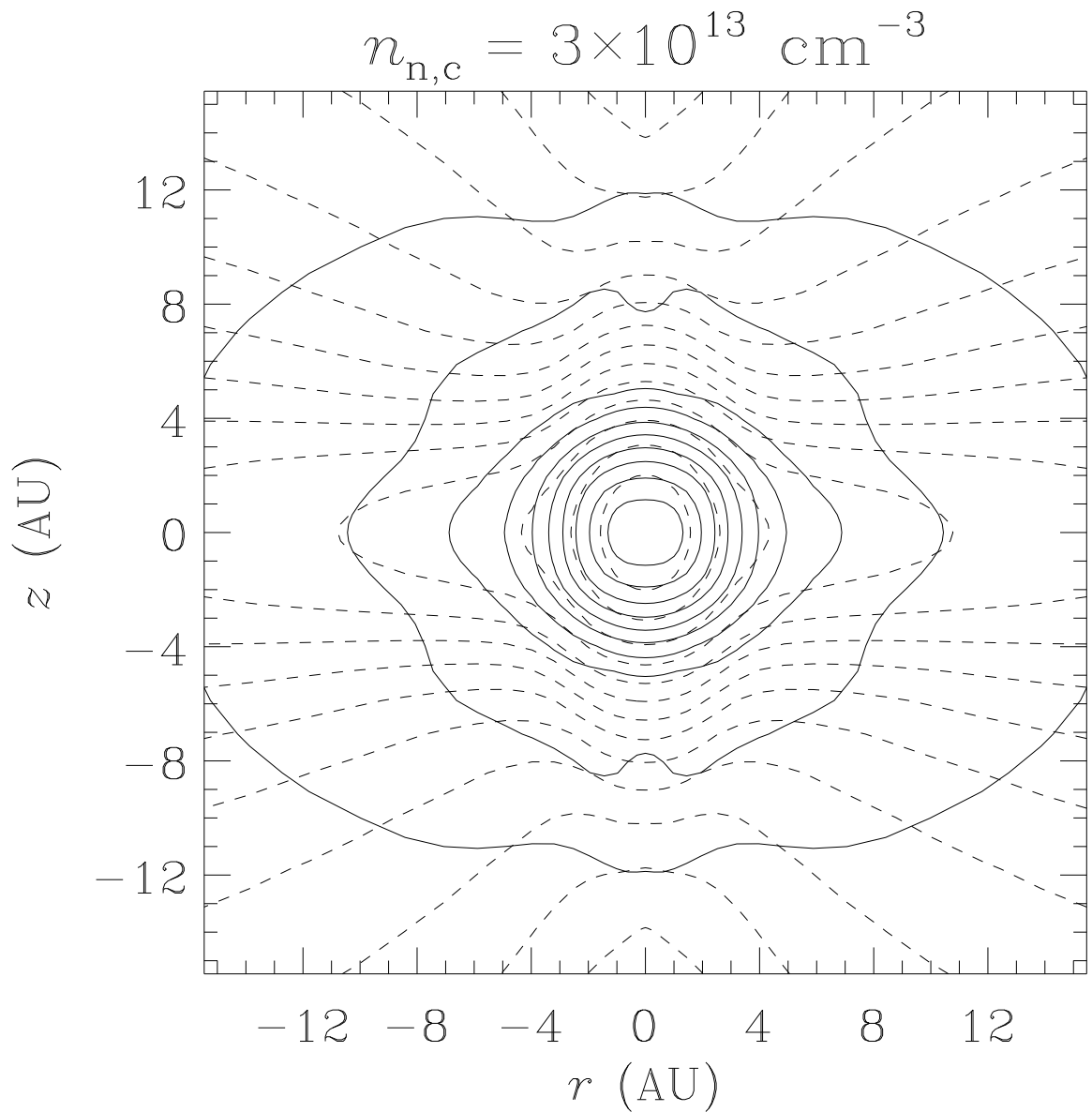


Figure 4.14: Thermal structure of the innermost 0.01% of the model cloud at the time when the central density $n_{n,c} = 3 \times 10^{13} \text{ cm}^{-3}$. The maximum temperature is 184.4 K. Isothermal contours (solid lines) and isodensity contours (dashed lines) are shown. Every tenth isothermal contour indicates a change in temperature by a factor of 10; every second isodensity contour indicates a change in density by a factor of 10. The innermost isothermal (isodensity) contour corresponds to 158 K (10^{13} cm^{-3}).

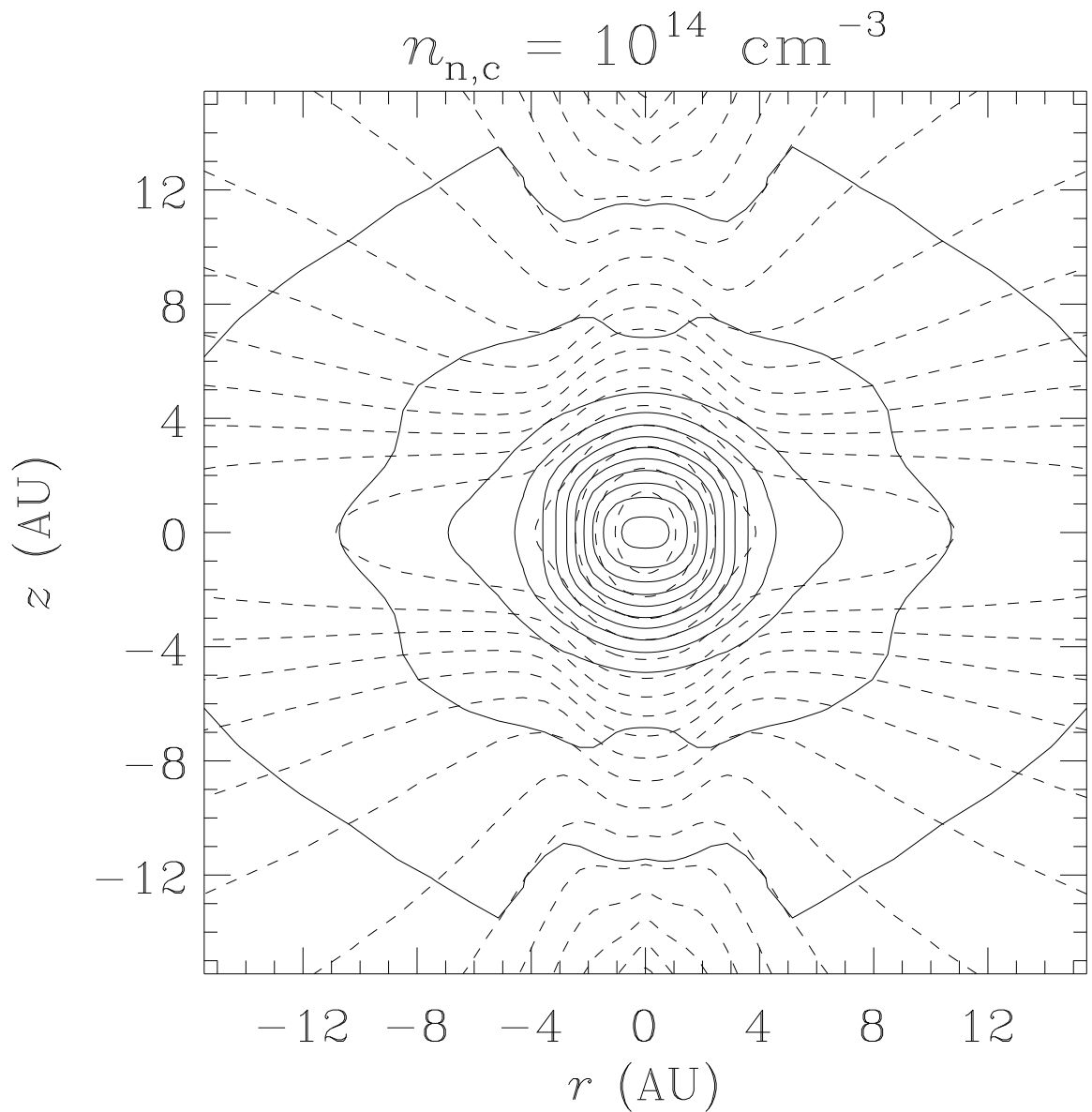


Figure 4.15: Thermal structure of the innermost 0.01% of the model cloud at the time when the central density $n_{n,c} = 10^{14} \text{ cm}^{-3}$. The maximum temperature is 268.5 K. Isothermal contours (solid lines) and isodensity contours (dashed lines) are shown. Every tenth isothermal contour indicates a change in temperature by a factor of 10; every second isodensity contour indicates a change in density by a factor of 10. The innermost isothermal (isodensity) contour corresponds to 251 K ($3 \times 10^{13} \text{ cm}^{-3}$).

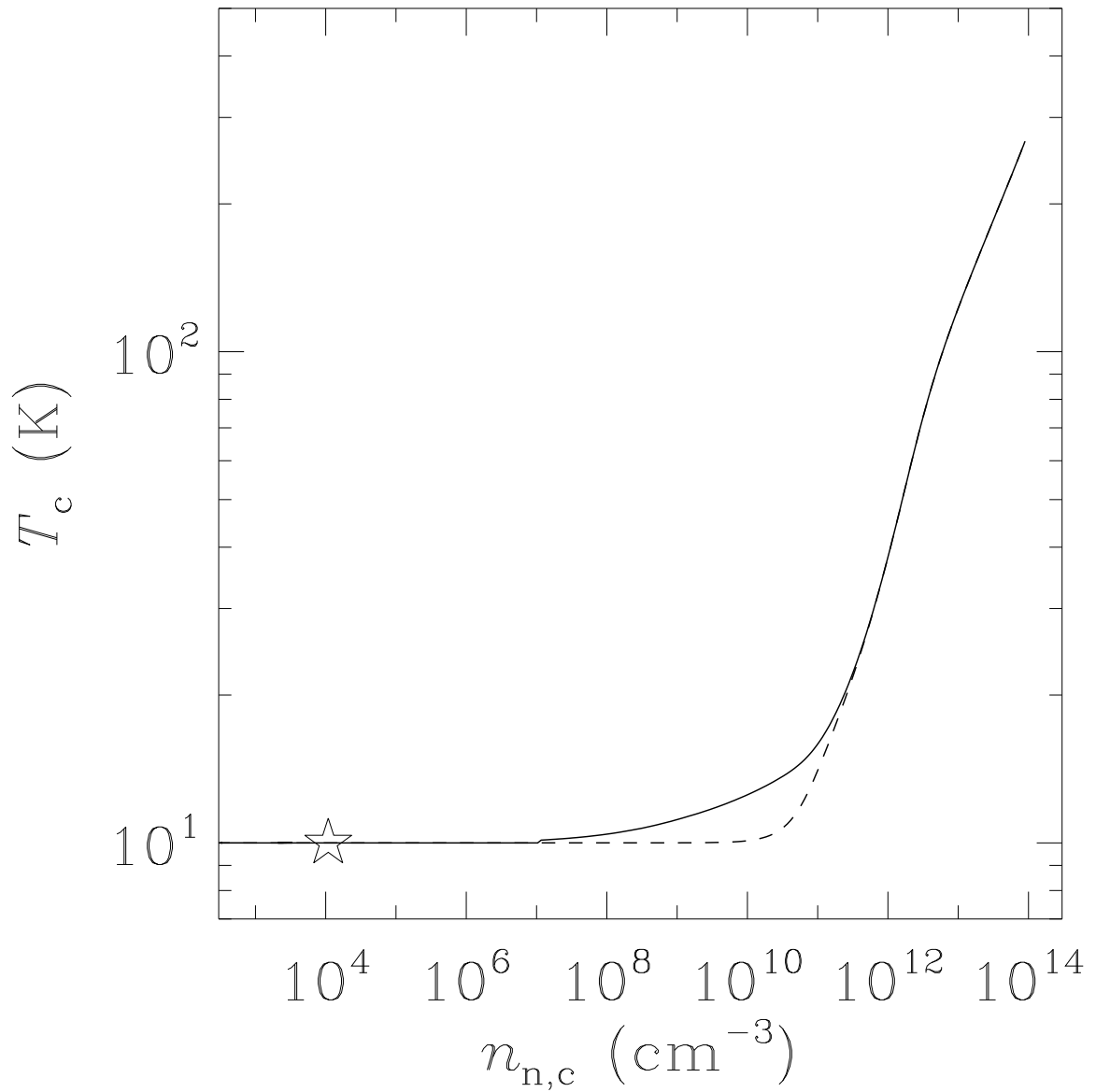


Figure 4.16: Evolution of the central gas (solid line) and radiation (dashed line) temperatures, T_c , as functions of the central number density of neutrals, $n_{n,c}$. The “star” marks the time at which a supercritical core forms.

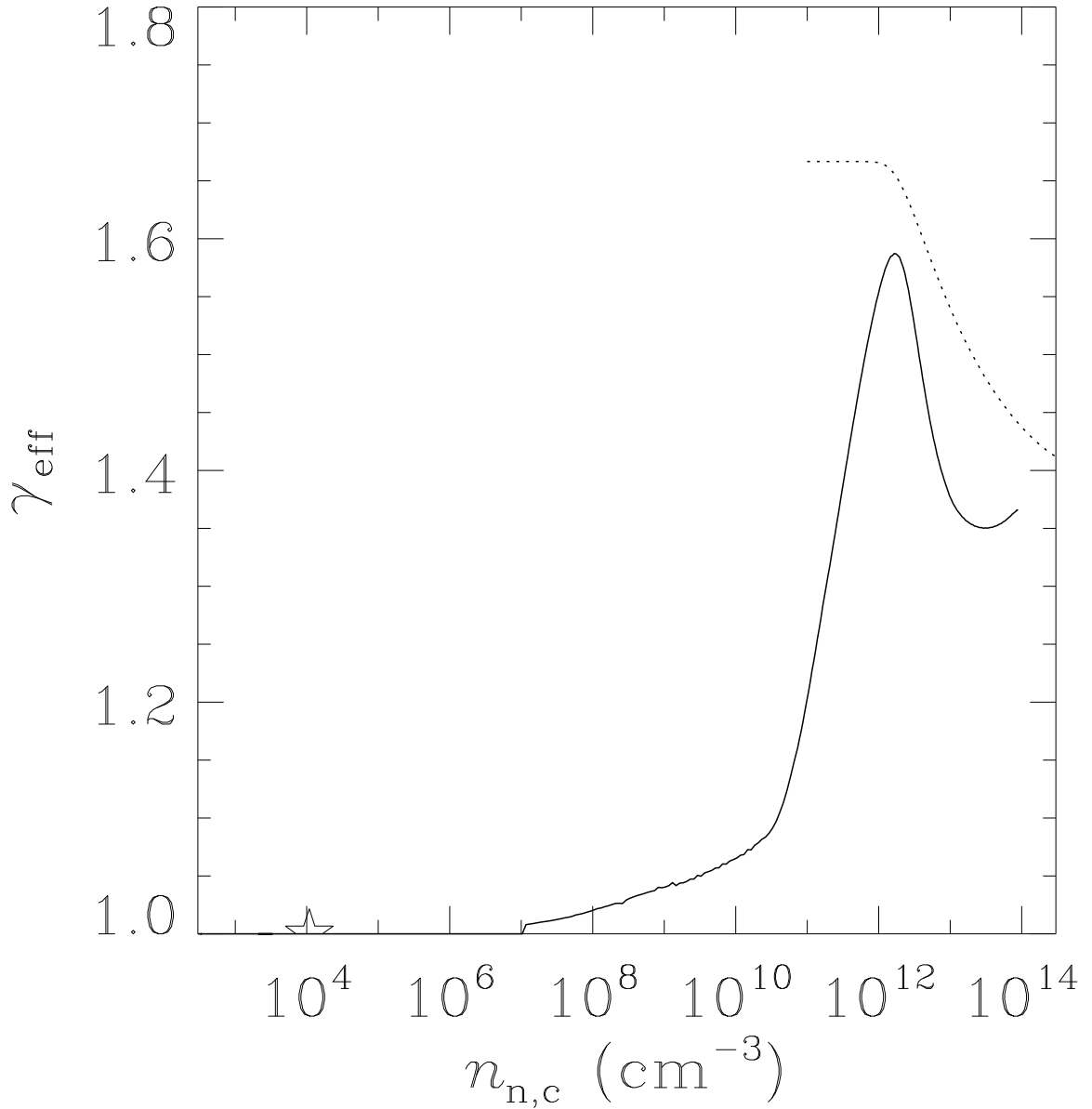


Figure 4.17: Evolution of the exponent γ_{eff} in the relation $T_c \propto n_{n,c}^{\gamma_{\text{eff}}-1}$ (solid line) as a function of the central number density of neutrals, $n_{n,c}$. The dotted line shows the exponent if the gas were to evolve adiabatically beyond a central density 10^{11} cm^{-3} . The “star” marks the time at which a supercritical core forms.

at a rate $\partial \ln T_c / \partial \ln n_{n,c} \equiv \gamma_{\text{eff}} - 1$, where γ_{eff} is the effective adiabatic index denoted by the solid line in Figure 4.17. The dotted line in Figure 4.17 shows this index if the gas were to evolve adiabatically beyond a central density 10^{11} cm^{-3} (as in, e.g., Tassis & Mouschovias 2007b). *The gas never evolves adiabatically during the simulation.* There is some indication that adiabaticity will set in at the cloud center by a central density $\sim 10^{15} \text{ cm}^{-3}$, after which $\gamma_{\text{eff}} \simeq 7/5$. The central temperature never evolves with an effective adiabatic index $\gamma_{\text{eff}} = 5/3$.

A central temperature of 100 K is reached when the central density is $\simeq 6 \times 10^{12} \text{ cm}^{-3}$. This is a significantly higher density than that found by, e.g., Larson (1969). There are two principal reasons for this difference. First, a disklike, rather than spherical, geometry allows the radiation to escape more easily, since the radiation is not isotropically confined by a spherical opacity distribution. Second, the early redistribution of mass by ambipolar diffusion is responsible for lowering the dust-to-gas ratio in the central flux tubes of the cloud from its usual interstellar medium value (see below). The fewer dust grains there result in a lowered opacity, and consequently allow radiation to escape more efficiently. This effect is complicated somewhat, however, as our opacities are temperature-dependent (see Figures 2.2 and 2.3), whereas Larson (1969) assumed a constant value $\chi_R = 15 \text{ cm}^2 \text{ g}^{-1}$ of dust (with a constant dust-to-gas ratio of 0.01).

The evolution of the central (gas) temperature assists in understanding the evolution of the quantity $\partial \ln \Sigma_{n,c} / \partial \ln n_{n,c}$ (shown in Figure 4.18), which is a quantitative indicator of the core geometry. For a disk, in which thermal-pressure forces balance gravity along magnetic field lines, $\partial \ln \Sigma_{n,c} / \partial \ln n_{n,c} = \gamma_{\text{eff}} / 2$ (whose value is denoted by the dotted line in the figure), whereas for a sphere, $\partial \ln \Sigma_{n,c} / \partial \ln n_{n,c} = 2/3$. After the rapid collapse along field lines, $\partial \ln \Sigma_{n,c} / \partial \ln n_{n,c}$ approaches and oscillates about $1/2$; the cloud has settled into a disklike quasi-equilibrium. Even during the magnetically-supercritical phase of dynamical contraction, the geometry remains disklike (as indicated by the near coincidence of the solid and dotted curves in the figure). This trend holds until central densities

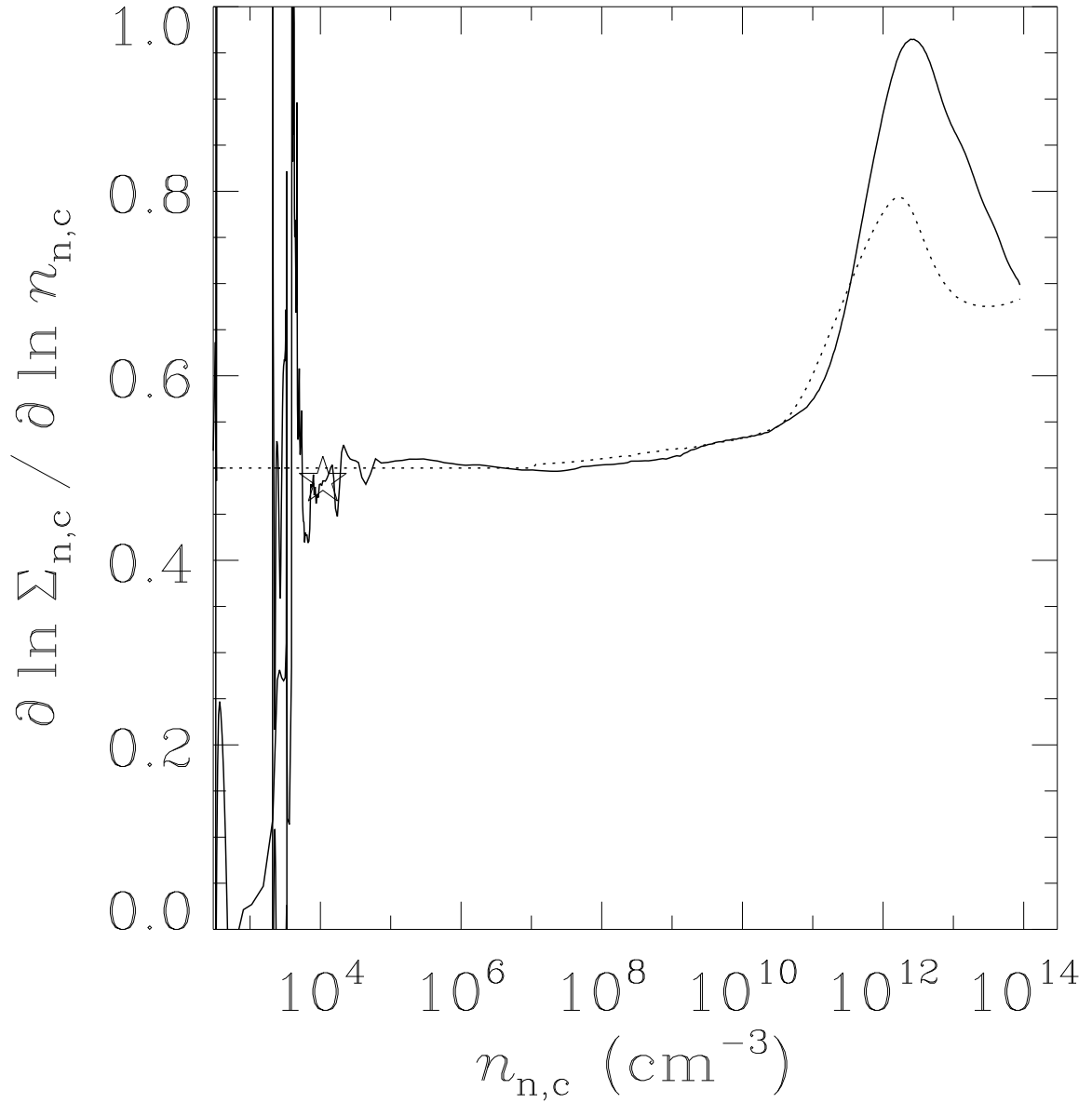


Figure 4.18: Evolution of the exponent $\partial \ln \Sigma_{n,c} / \partial \ln n_{n,c}$ (solid line) as a function of the central number density of neutrals, $n_{n,c}$. The dotted line shows the exponent if the geometry were to remain disklike throughout the evolution. The “star” marks the time at which a supercritical core forms.

$\approx 3 \times 10^{11} \text{ cm}^{-3}$ are attained, after which a spherical core geometry becomes increasingly apparent.

In Figure 4.19, we show the central magnetic field strength, B_c , as a function of central density. During the ambipolar-diffusion-controlled evolution (until the formation of a supercritical core, marked by the “star”), B_c increases by only $\simeq 47\%$ from $15 \mu\text{G}$ to $22 \mu\text{G}$. A phase of near flux-freezing subsequently follows, during which B_c resembles a power-law $B_c \propto n_{n,c}^\kappa$ with $\kappa \simeq 0.47$ (see Figure 4.20). This is in excellent agreement with the observed $\kappa = 0.47 \pm 0.08$ inferred from Zeeman detections of protostellar cores (Crutcher 1999). For a thin disk in the flux-freezing limit, $B_c \propto n_{n,c}^{1/2} T_c^{1/2}$, so that $\kappa = \gamma_{\text{eff}}/2$. Therefore, any nonisothermal evolution (i.e., $\gamma_{\text{eff}} > 1$) will result in $\kappa > 1/2$ (in the flux-freezing limit). This is evident briefly in Figure 4.20 for the central density range $n_{n,c} \sim 10^8 - 10^{11} \text{ cm}^{-3}$. This trend is halted once the magnetic field begins to decouple from the matter and κ decreases. Once the magnetic field is completely decoupled from the gas, $B_c \propto T_c^{1/2}$, so that $\kappa = (\gamma_{\text{eff}} - 1)/2$. This scaling will approximately hold until the core contracts spherically under flux-refreezing (after magnetic recoupling — see below) and κ approaches $2/3$.

Note that the rapid, large oscillations in κ seen in Figure 1f of Tassis & Mouschovias (2007b) after magnetic decoupling sets in are absent in our Figure 4.20. Those oscillations were due to the abrupt and (relatively) rapid adiabatic temperature increase in the core, which forced the contracting core to overshoot and subsequently oscillate about hydrostatic equilibrium. In the situation presented here, the much more gradual increase in the central temperature affords the core enough time to maintain hydrostatic force balance as it contracts. A close inspection of Figure 4.20 does indeed reveal small physical oscillations about a hydrostatic equilibrium.

Figures 4.21 and 4.22 show the evolution of quantities related to the chemistry as functions of central density: the ionization rate at the center of the cloud, ζ_c , due to all processes (UV radiation, cosmic rays, and radioactive decays) and the central abundances of differ-

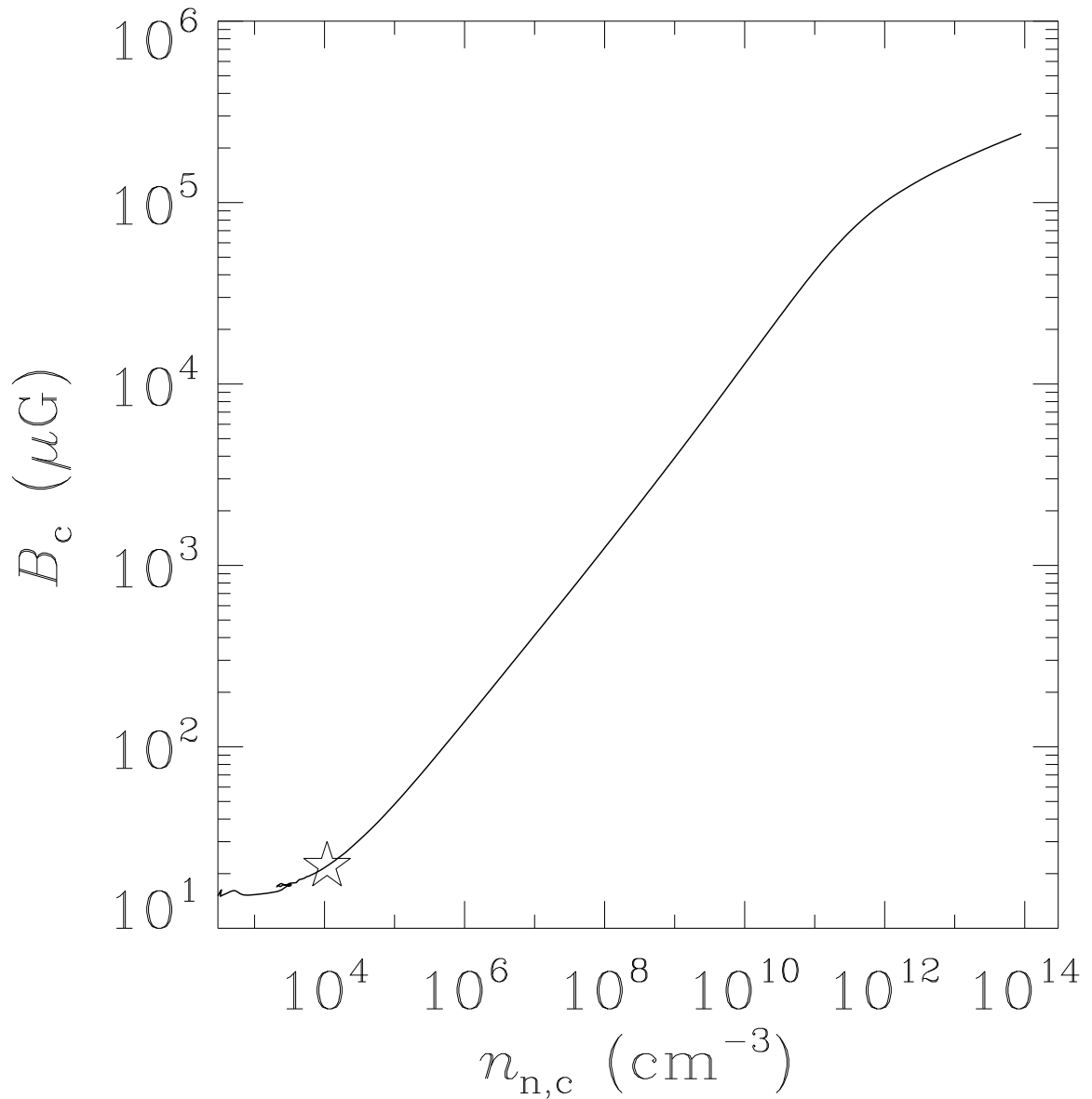


Figure 4.19: Evolution of the central magnetic field strength, B_c , as a function of the central number density of neutrals, $n_{n,c}$. The “star” marks the time at which a supercritical core forms.

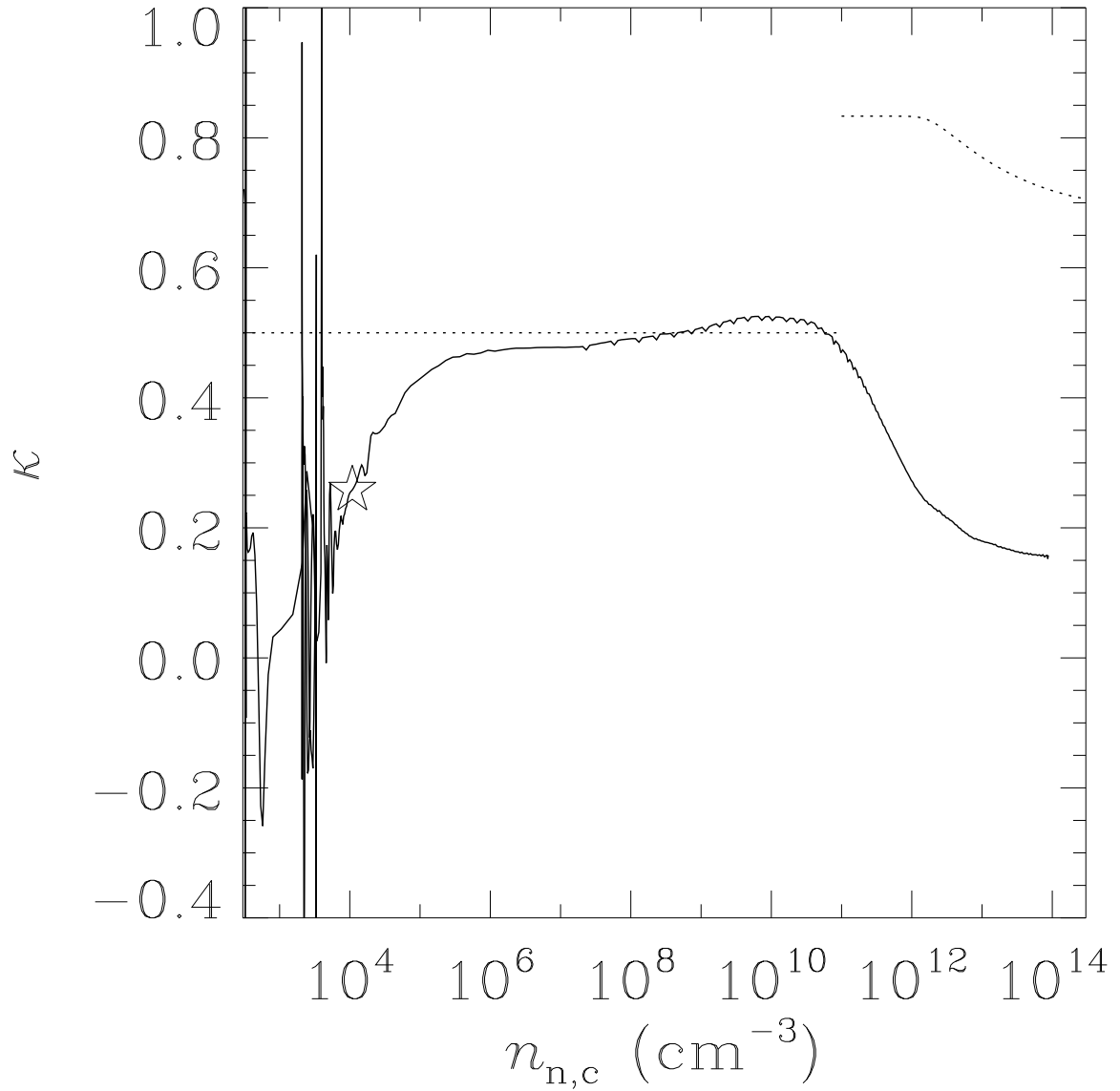


Figure 4.20: Evolution of the exponent κ in the relation $B_c \propto n_{n,c}^\kappa$ (solid line) as a function of the central number density of neutrals, $n_{n,c}$. The dotted line shows the exponent if the magnetic field were to evolve under strict flux-freezing and the gas were to behave adiabatically beyond a central density 10^{11} cm^{-3} . The “star” marks the time at which a supercritical core forms.

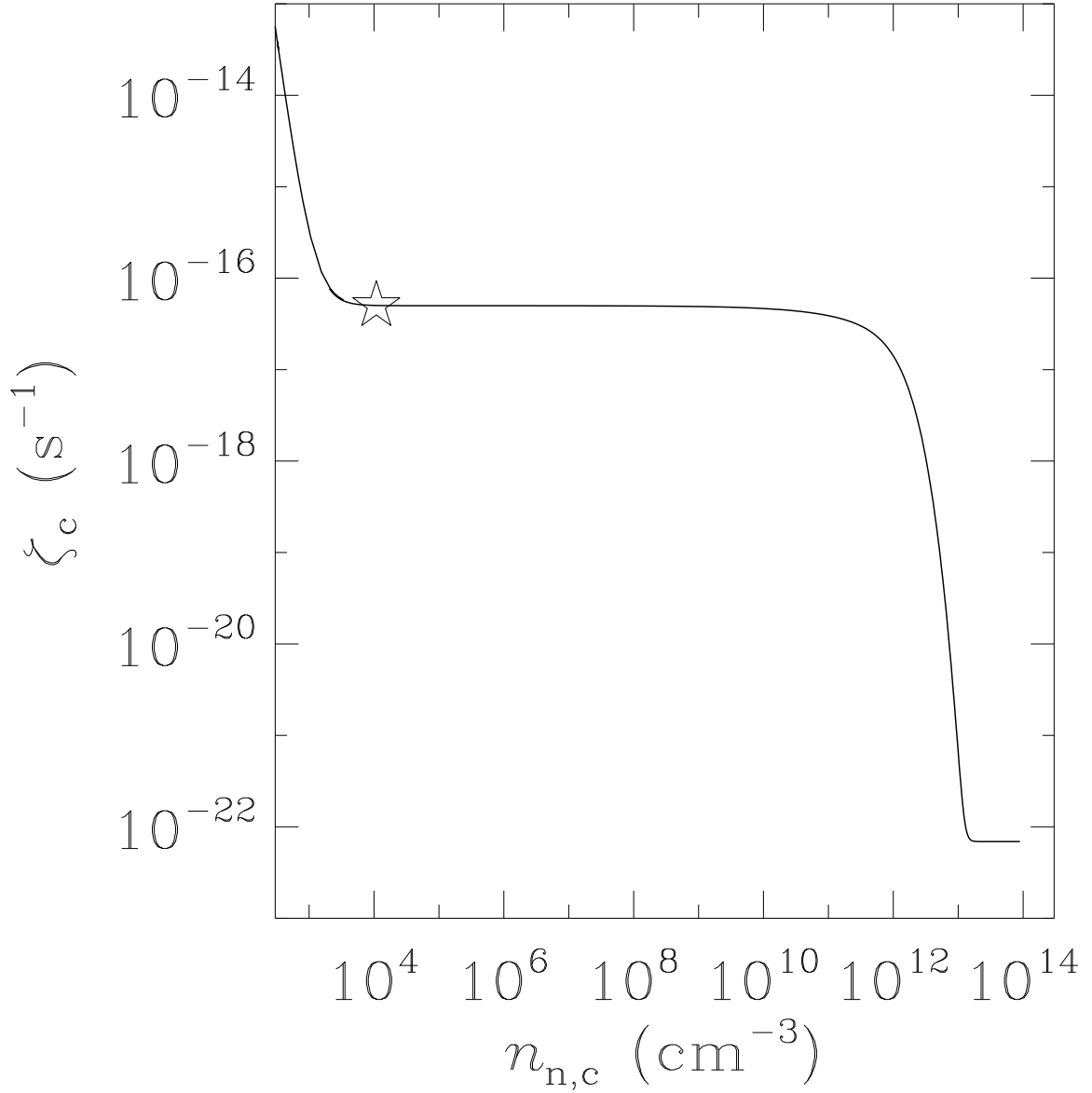


Figure 4.21: Evolution of the central ionization rate due to all processes (UV radiation, cosmic rays, and radioactive decays) as a function of the central number density of neutrals, $n_{n,c}$. The “star” marks the time at which a supercritical core forms.

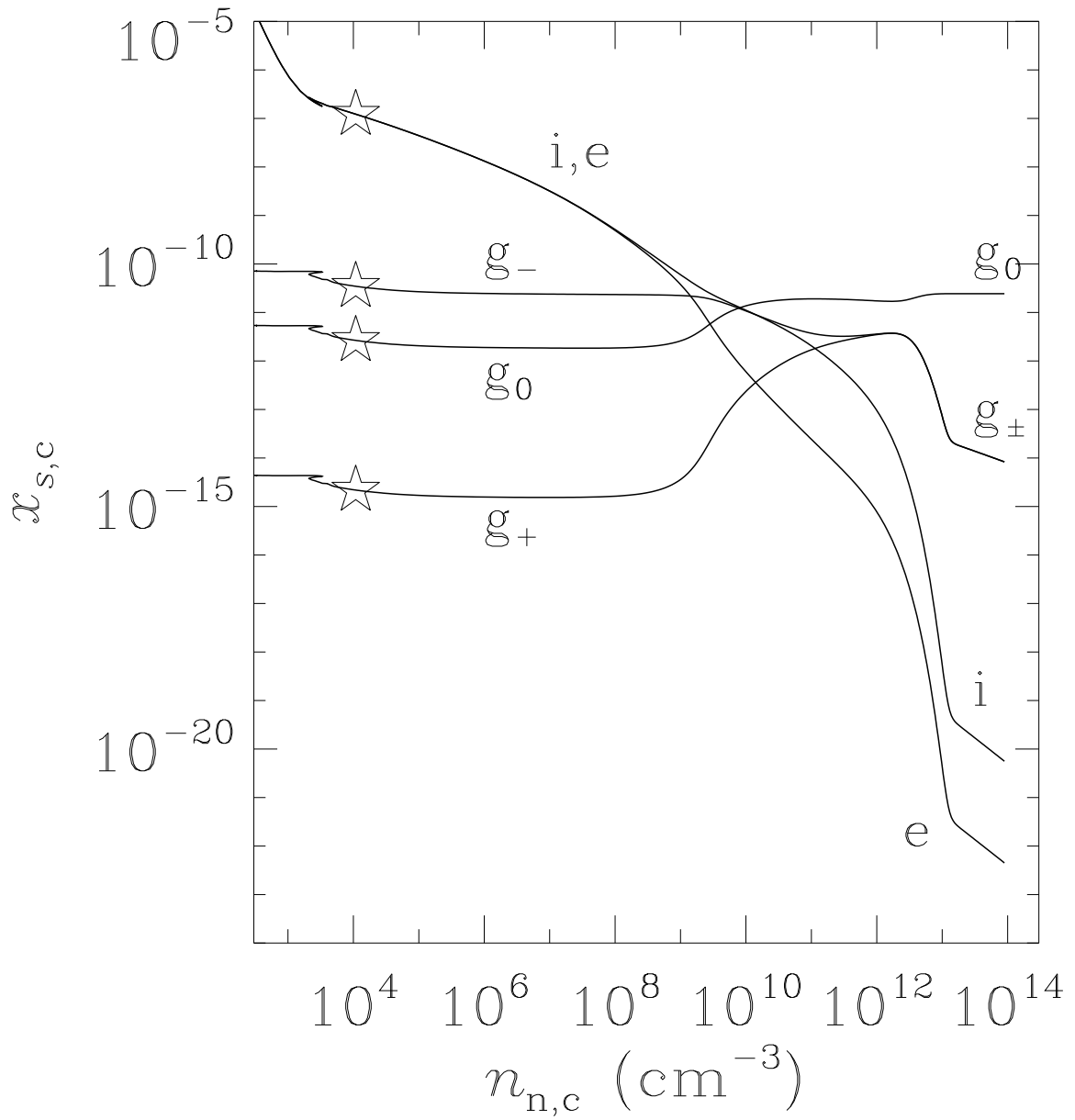


Figure 4.22: Evolution of the central abundances of species x_s (where $s = e, i, g_{-}, g_0, g_{+}$) as functions of the central number density of neutrals, $n_{n,c}$. The “star” marks the time at which a supercritical core forms.

ent species, $x_{s,c} \equiv n_{s,c}/n_{n,c}$ (where $s = e, i, g_-, g_0, g_+$). For $n_{n,c} \lesssim 1800 \text{ cm}^{-3}$, UV radiation dominates the ionization rate. Beyond this density, the ionization in the core is mainly due to cosmic rays. Its value is constant, $\zeta = 5 \times 10^{-17} \text{ s}^{-1}$, for densities up to $\approx 3 \times 10^{11} \text{ cm}^{-3}$, beyond which the column density exceeds $\approx 100 \text{ g cm}^{-2}$ and cosmic rays are appreciably attenuated. The ionization rate then decreases monotonically, until it is dominated by radioactive decays (mainly of ^{40}K) above a central density $\approx 10^{13} \text{ cm}^{-3}$ and reaches a constant value $\zeta = 6.9 \times 10^{-23} \text{ s}^{-1}$. Thermal ionization does not become important for the density range investigated in this Thesis, since the temperature never reaches $\simeq 10^3 \text{ K}$. A simple extrapolation of temperature based on our results indicates that such a temperature will not be reached until a central density $\approx 3 \times 10^{15} \text{ cm}^{-3}$. Therefore, we predict that *magnetic recoupling will not occur until central densities of at least several $\times 10^{15} \text{ cm}^{-3}$ are attained.*

The central species abundances are strongly affected not only by changes in the ionization rate, but also by microscopic interactions between the different species and by the macroscopic dynamics of the cloud. For central neutral densities $\lesssim 1800 \text{ cm}^{-3}$, UV ionization and (radiative and dissociative) recombinations dominate the ion and electron chemistry and the ion and electron abundances $x_{i,e} \propto n_n^{-3}$. Once UV radiation is effectively shielded and the ionization is primarily due to cosmic rays, $x_{i,e}$ decreases more slowly. However, the canonical relation $x_{i,e} \propto n_n^{k-1}$ with $k = \text{const} = 1/2$ is never established. In fact, during the subcritical phase of the evolution (i.e., $n_{n,c} \lesssim 10^5 \text{ cm}^{-3}$), k is always greater than $1/2$, an effect that is entirely due to ambipolar diffusion. As explained by Ciolek & Mouschovias (1998), during this phase of evolution charged and neutral dust grains are well attached to magnetic field lines, which are essentially “held in place” (Mouschovias 1978, 1979), and are “left behind” by the inwardly diffusing neutrals. This results in a decrease in the central dust-to-gas ratio by a factor roughly equal to the initial (dimensionless) central mass-to-flux ratio. One consequence is a significantly reduced inelastic capture of ions and electrons onto grains and therefore a greater number of gas-phase ions and electrons than

predicted by calculations that assume a constant dust-to-gas ratio.

Once a supercritical core forms, the grain abundances are frozen at their values until a central density of $\sim 10^9 \text{ cm}^{-3}$ is reached. Gas-phase ions and electrons are then quickly adsorbed onto grain surfaces and the grains become the main charge carriers (when $n_{n,c} \sim 10^{10} \text{ cm}^{-3}$). However, most grains remain neutral due to inadequate numbers of ions and electrons, whose abundances are determined by balancing their rates of production against their collision rates with neutral grains. Because these collision rates are inversely proportional to the square root of the ion/electron mass, the ions are more abundant than the lighter electrons by a factor $\simeq (m_i/m_e)^{1/2} \simeq 210$ (different sticking probabilities for ions and electrons reduce this value to $\simeq 125$). Since x_{g_0} approaches a constant, the densities of ions and electrons approach constant values, so their abundances relative to neutrals asymptote towards a n_n^{-1} dependence. Once cosmic rays become appreciably attenuated, however, this asymptotic behavior is interrupted and the abundances of electrons and ions decrease much more rapidly. An ionization floor is established by the radionuclide ^{40}K at densities $\approx 10^{13} \text{ cm}^{-3}$, after which the electron and ion abundances once again scale roughly as n_n^{-1} . The abundances of charged grains are proportional to $n_n^{-1/2}$, for the same reasons that applied to the abundances of electrons and ions at low densities.

The evolution of central quantities related to magnetic diffusion are demonstrated in Figures 4.23 – 4.26 as functions of central density. The magnetic diffusion coefficients related to ambipolar diffusion (AD), Ohmic dissipation (OD), and the Hall effect (H) are shown in Figure 4.23. As we are concerned here with the evolution of only the poloidal component of the magnetic field (recall that rotation has been justifiably ignored), the Hall effect plays no role in the dynamics of the cloud. Nevertheless, we have calculated the Hall resistivity (denoted by the dashed line) in order to highlight its importance relative to the other diffusion mechanisms. Ambipolar diffusion dominates the evolution of the cloud until a density $\simeq 7 \times 10^{12} \text{ cm}^{-3}$ is reached, after which Ohmic dissipation is the primary magnetic diffusion mechanism. Therefore, ambipolar diffusion still dominates

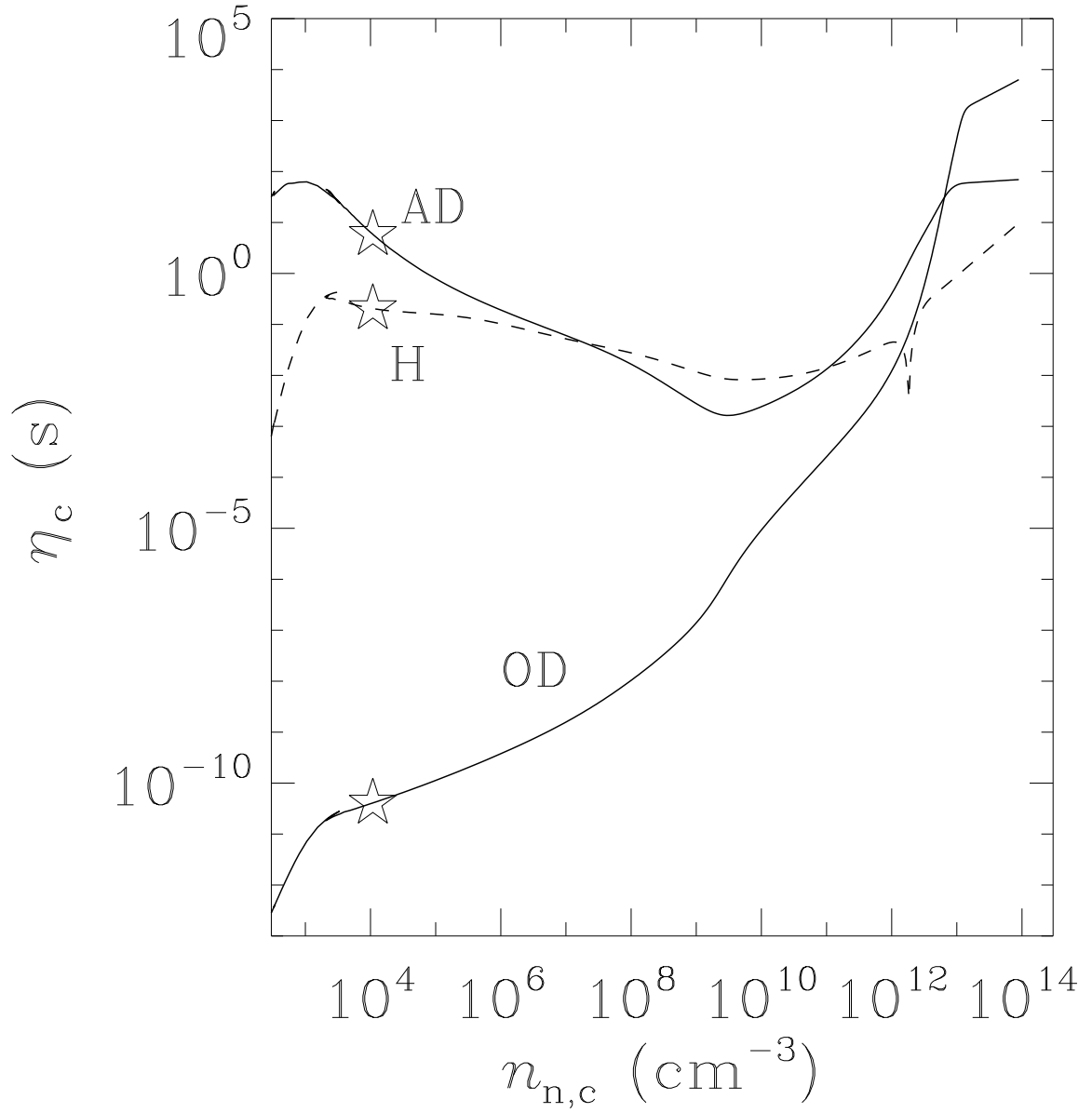


Figure 4.23: Evolution of the central magnetic resistivities associated with ambipolar diffusion (AD), Ohmic dissipation (OD), and the Hall effect (H) as functions of the central number density of neutrals, $n_{n,c}$. The “star” marks the time at which a supercritical core forms.

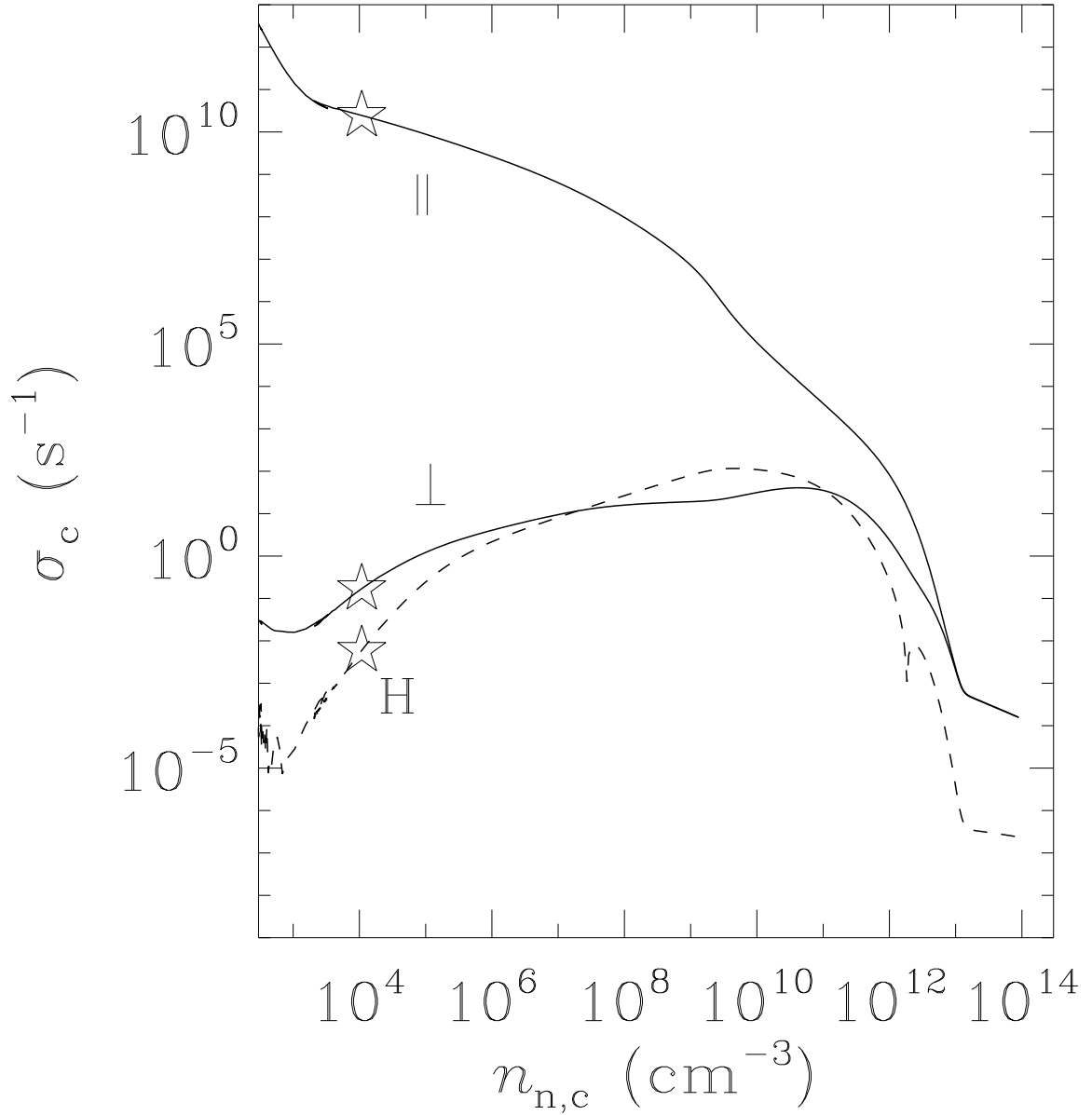


Figure 4.24: Evolution of the central parallel (\parallel), perpendicular (\perp), and Hall (H) magnetic conductivities as functions of the central number density of neutrals, $n_{n,c}$. The “star” marks the time at which a supercritical core forms.

Ohmic dissipation as a flux-reduction mechanism when the grains become the primary charge carriers, contrary to the expectations of Nakano & Umebayashi (1986a,b). Equality of the ambipolar-diffusion and Ohmic-dissipation rates occurs once the central mass-to-flux ratio $\simeq 16$ times its critical value and the grains become the dominant *current* carriers (see below).

In Figure 4.24, we show the parallel (\parallel), perpendicular (\perp), and Hall (H) conductivities. Figures 4.25 and 4.26 show the fraction of the parallel and perpendicular conductivities, respectively, carried by each species. (Absolute values have been taken; the cusps in the positive grain curves are due to the conductivity passing through zero as it changes sign.) The electrons dominate the parallel conductivity until Ohmic dissipation becomes the primary magnetic diffusion mechanism, after which the charged grains dominate the parallel conductivity. The ions dominate the perpendicular conductivity (and therefore the electrical current — see Section 4.4.5) until a central density $\simeq 3 \times 10^{12} \text{ cm}^{-3}$, after which the charged grains dominate. In other words, the grains begin to carry the majority of the current at roughly the same time that Ohmic dissipation becomes important. *Star formation and protostellar disk calculations that study the phase when Ohmic dissipation becomes an important magnetic diffusion mechanism must include not only the chemistry but also the magnetohydrodynamics of dust grains.*

4.4 Evolution of Spatial Structure of the Model Cloud

Figures 4.27 – 4.47 show radial midplane (solid line) and vertical symmetry-axis (dashed line) profiles of physical quantities at thirteen different times. Each curve corresponds to a time t_j when the central density has increased by a factor of 10^j relative to the initial uniform “reference” state (i.e., the central density $\simeq 3 \times 10^{2+j} \text{ cm}^{-3}$ at time t_j). The exception is the last curve (corresponding to t_{12}), which represents the time at which $n_{n,c} \simeq 10^{14} \text{ cm}^{-3}$.

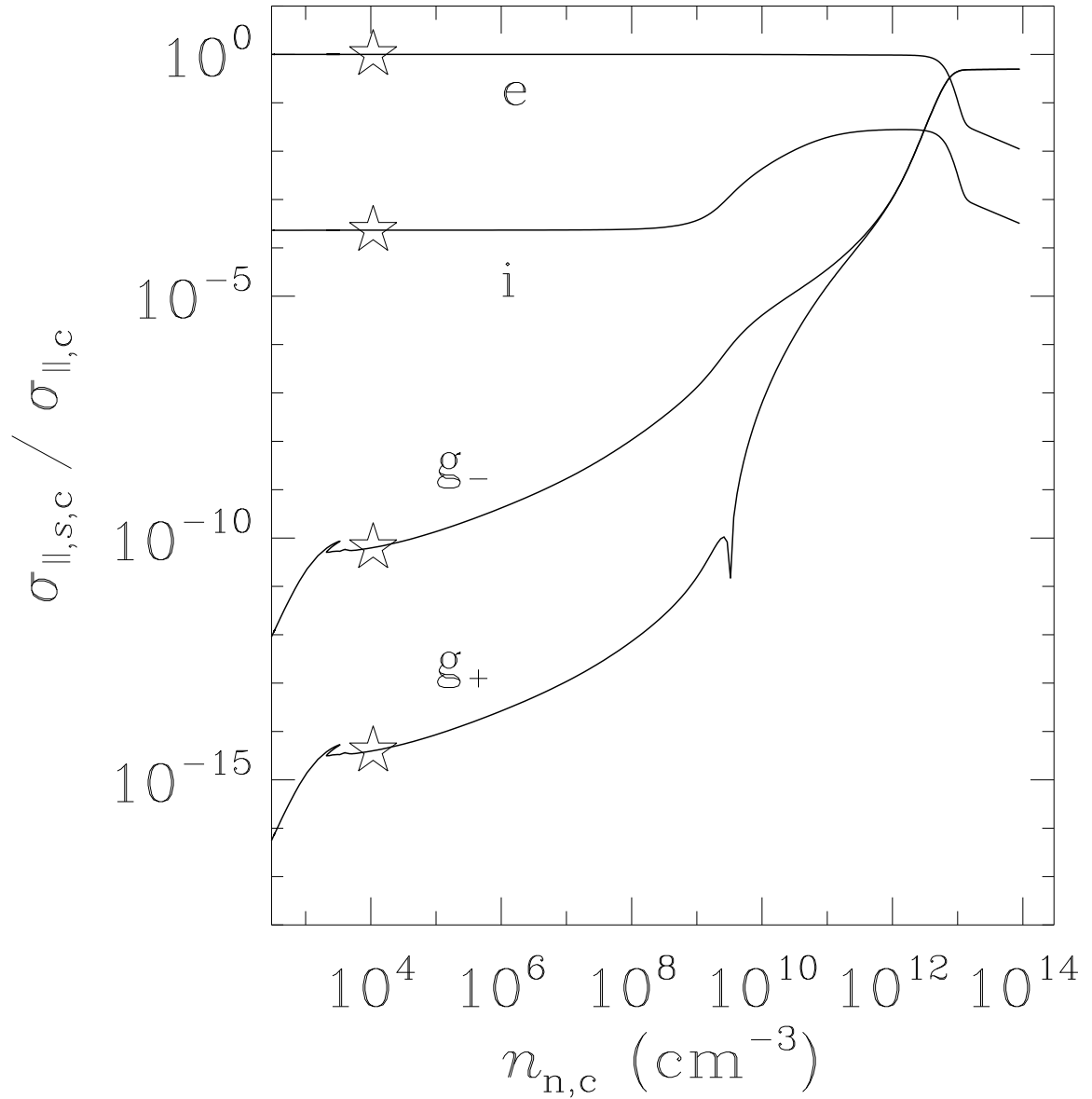


Figure 4.25: Evolution of the fraction of the central parallel magnetic conductivity carried by each species as a function of the central number density of neutrals, $n_{n,c}$. The “star” marks the time at which a supercritical core forms.

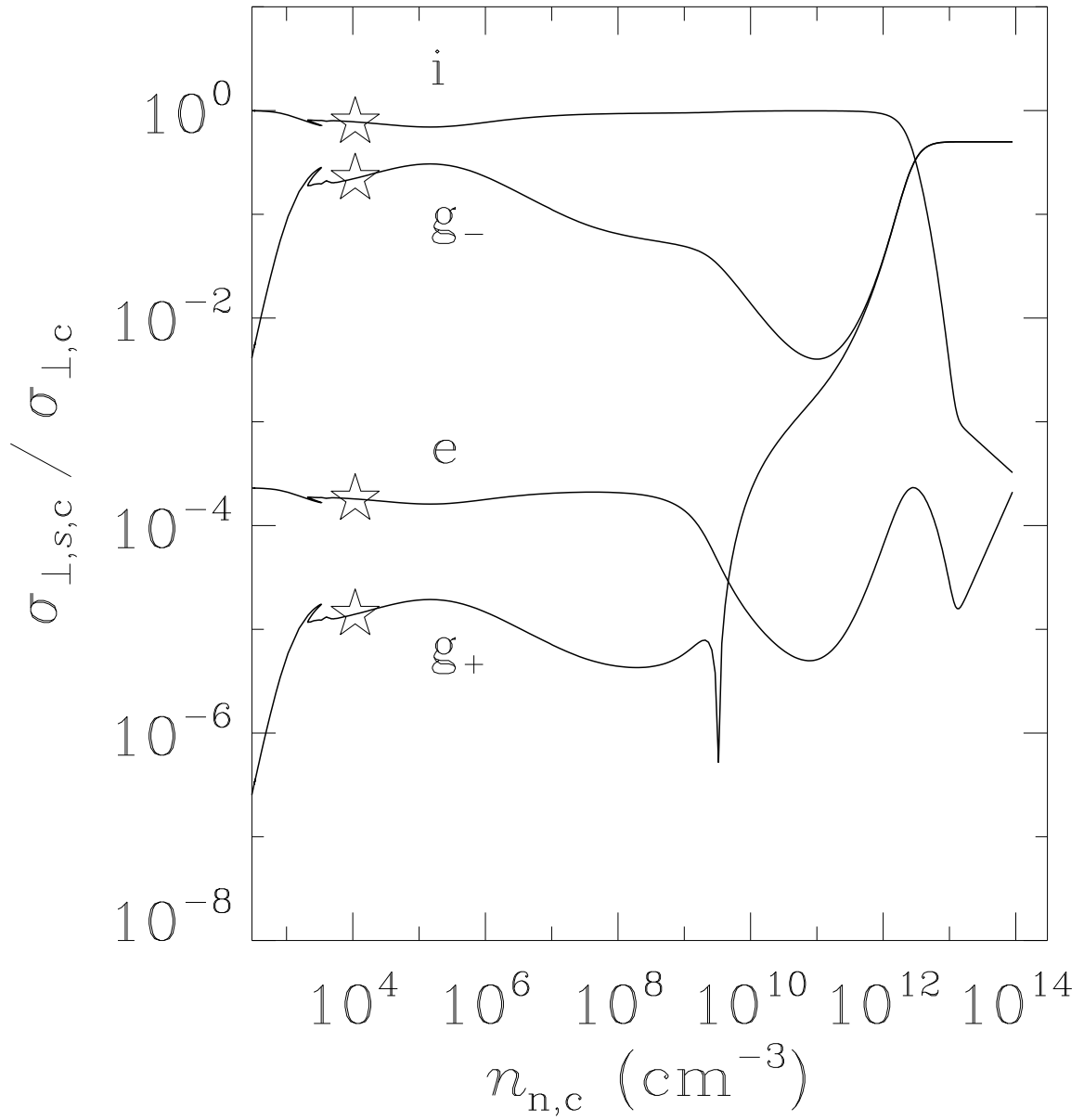


Figure 4.26: Evolution of the fraction of the central perpendicular magnetic conductivity carried by each species as a function of the central number density of neutrals, $n_{n,c}$. The “star” marks the time at which a supercritical core forms.

4.4.1 Density and Temperature

Figure 4.27 displays the number density of neutrals as a function of radius (r) and height (z) at the 13 different times given above. We also show the logarithmic slope of the (midplane) density profile versus radius, $\partial \ln n_n / \partial \ln r$, in Figure 4.28. A uniform central region is maintained (in the radial direction) for $r < \lambda_{T,cr}(t)$ by thermal pressure forces. Outside of this region, the density profile resembles a broken power-law. Inside the supercritical core, the slope has an average value $\simeq -2.2$ for $10^{-4} \text{ pc} \lesssim r \lesssim 10^{-1} \text{ pc}$. For smaller radii in the range $\approx 10^{-5} - 10^{-4} \text{ pc}$ ($\approx 2 - 20 \text{ AU}$), the slope increases briefly due to a local increase in magnetic support (see § 4.4.3). A transition to spherical geometry occurs at $r \simeq 4 \text{ AU}$ when the central density $\simeq 3 \times 10^{12} \text{ cm}^{-3}$. The radial and vertical density profiles are nearly identical inside this radius, with a slope approaching $\approx -10/3$, corresponding to hydrostatic force balance (with $\gamma_{\text{eff}} = 7/5$). Outside of the magnetically-supercritical core ($\approx 0.4 \text{ pc}$), there is an abrupt break in the slope because of significant magnetic support in the envelope. Very near the cloud radial boundary ($r = R = 0.75 \text{ pc}$) the slope decreases again to satisfy the boundary condition that the material has no radial velocity at this surface.

Figure 4.29 displays similar profiles for the (gas) temperature. The logarithmic slope of the (midplane) temperature versus radius, $\partial \ln T / \partial \ln r$, is shown in Figure 4.30. The molecular cloud and supercritical core evolve isothermally for densities $n_n \lesssim 10^7 \text{ cm}^{-3}$ and cylindrical polar radii $r \gtrsim 10^{-2} \text{ pc}$. Just inside the hydrostatic core ($r \lesssim 2 \text{ AU}$), the slope is closely approximated by $(\gamma_{\text{eff}} - 1)(\partial \ln n_n / \partial \ln r)$, whereas the temperature becomes constant very near the center of the core. For $2 \text{ AU} \lesssim r \lesssim 2000 \text{ AU}$, no single power-law can approximate the temperature profile.

4.4.2 Magnetic Field and Alfvén Speed

The z -component of the magnetic field is shown in Figure 4.31. In common with the density profile, there is an inner flat region [$r < \lambda_{T,cr}(t)$] where the magnetic field is near

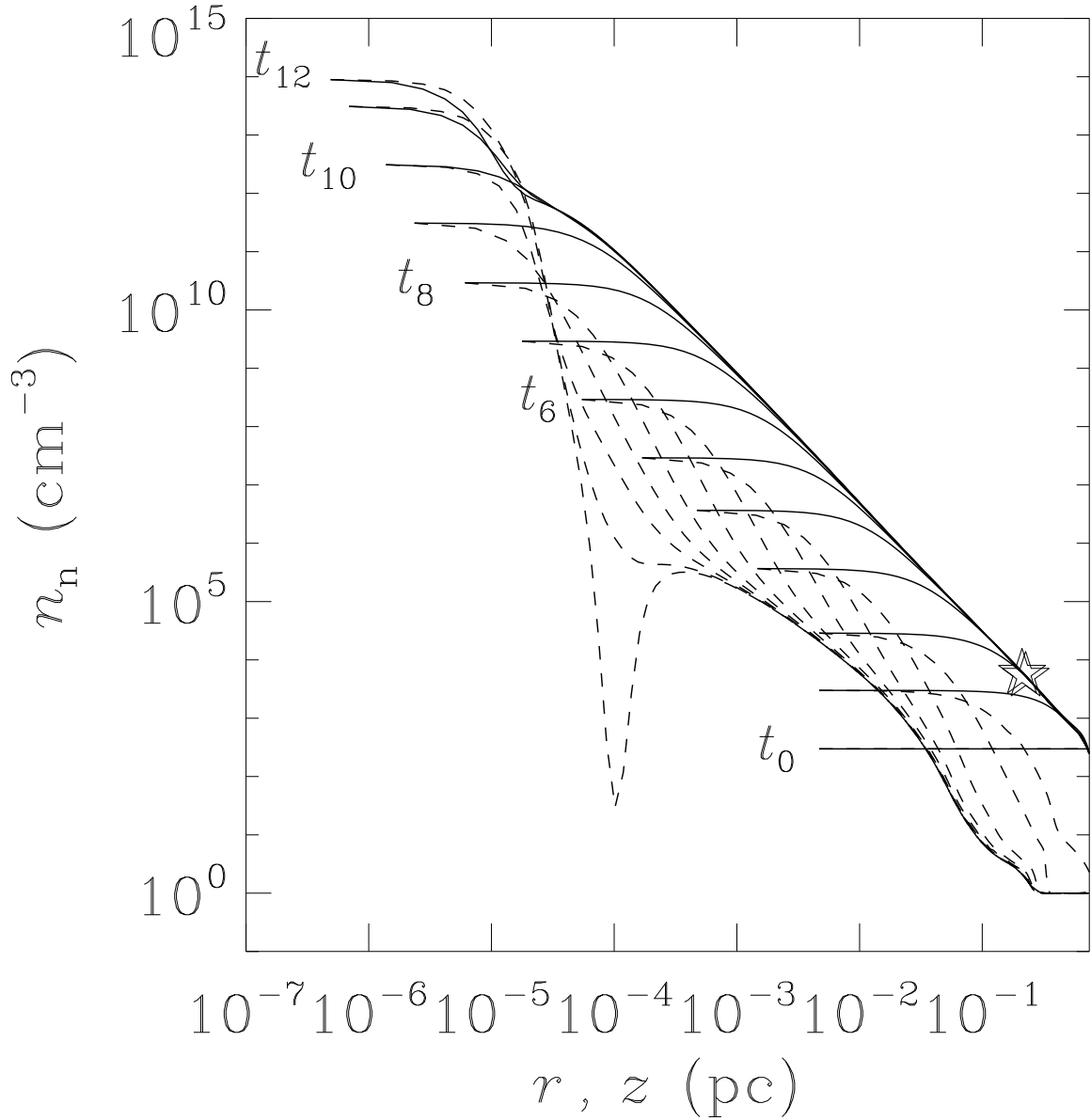


Figure 4.27: Radial midplane (solid line) and vertical symmetry-axis (dashed line) profiles of the number density of neutrals at twelve different times. The inner (outer) “star” on a radial profile curve, present only after a supercritical core forms, marks the initial (final) radius of the supercritical core.

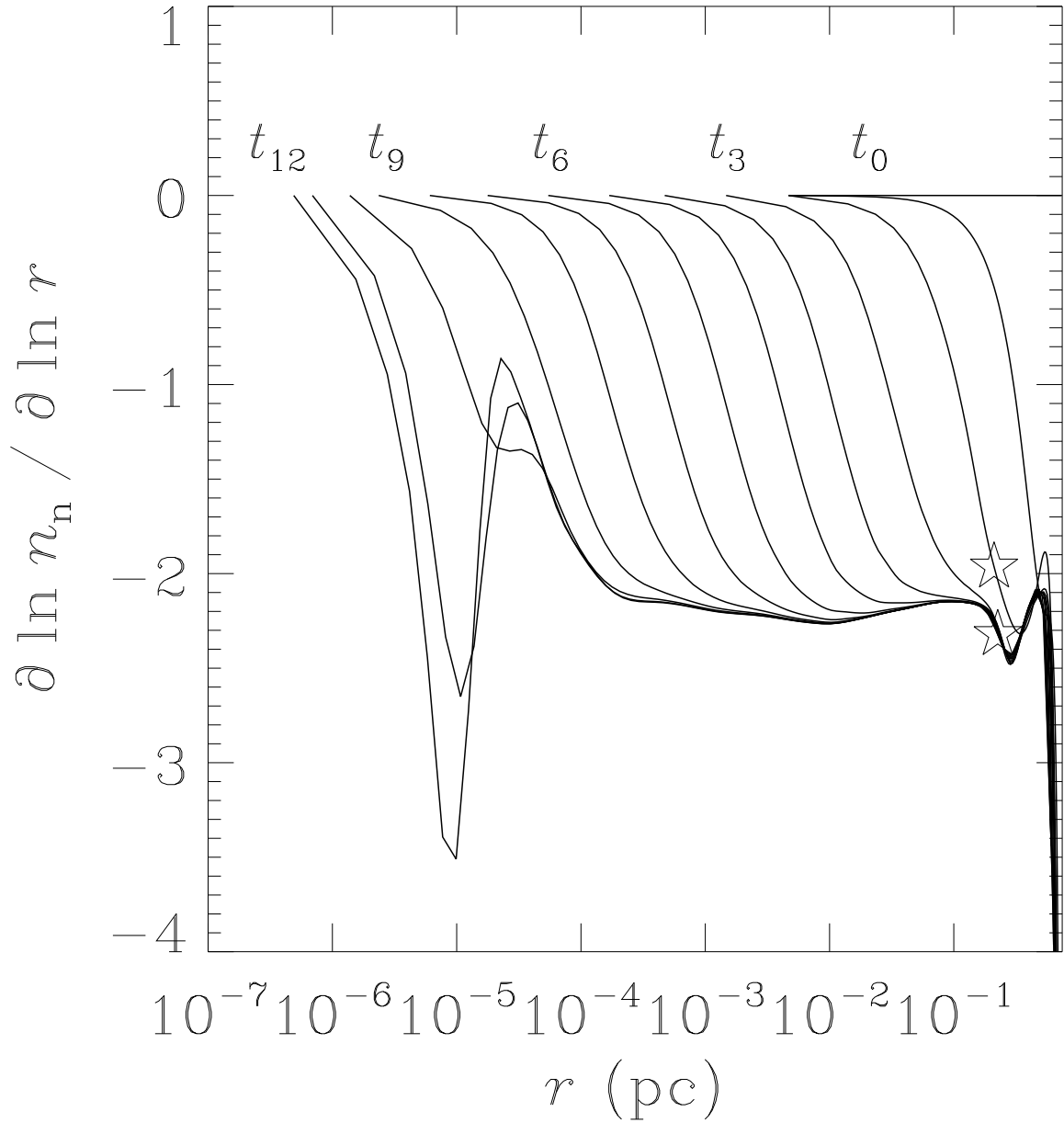


Figure 4.28: Radial derivative along the midplane of the density profile, $\partial \ln n_n / \partial \ln r$, at different times, as in Fig. 4.27. The inner (outer) “star” on a radial profile curve, present only after a supercritical core forms, marks the initial (final) radius of the supercritical core.

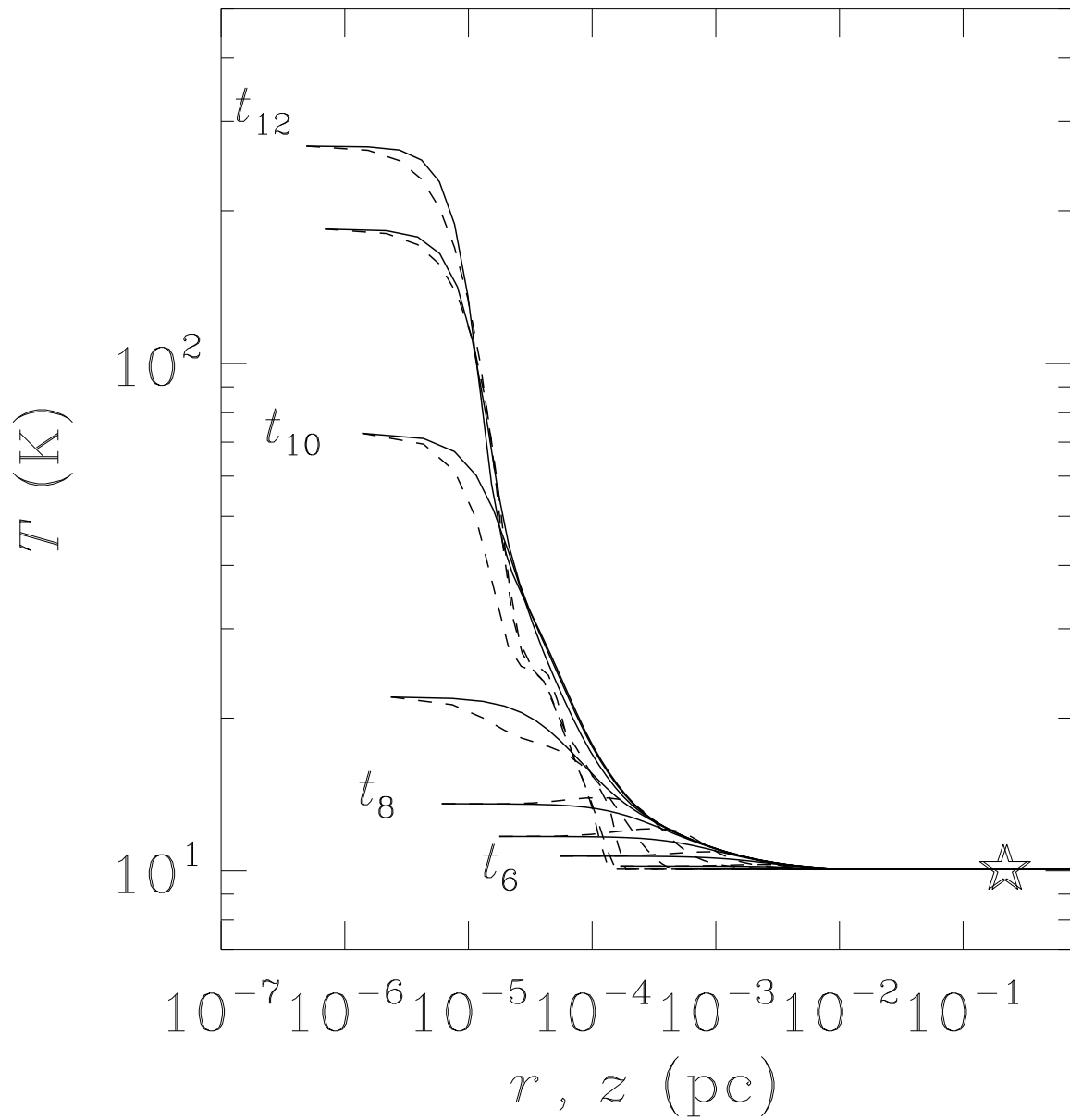


Figure 4.29: Radial midplane (solid line) and vertical symmetry-axis (dashed line) profiles of the gas temperature at different times, as in Fig. 4.27. The inner (outer) “star” on a radial profile curve, present only after a supercritical core forms, marks the initial (final) radius of the supercritical core.

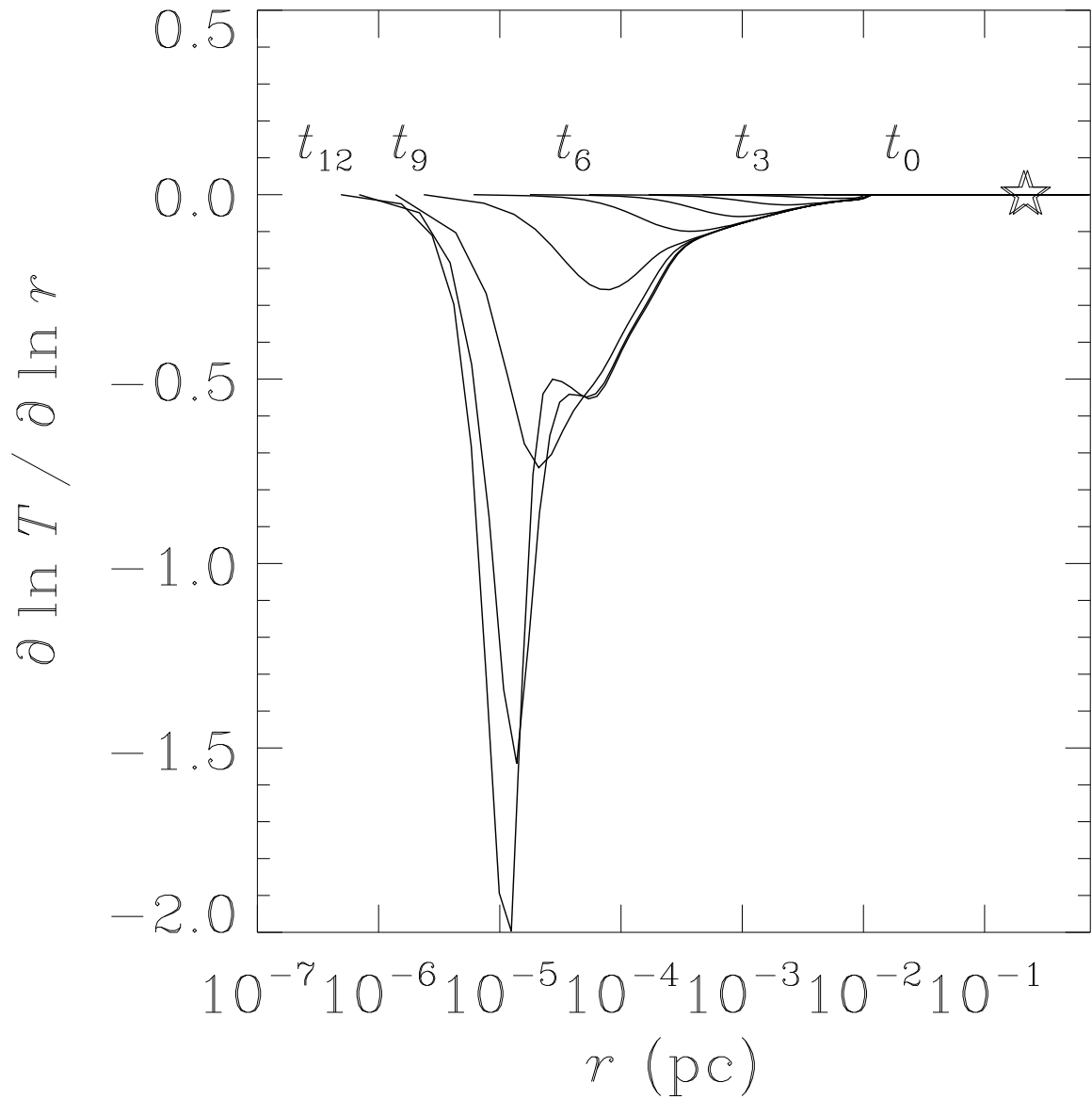


Figure 4.30: Radial derivative along the midplane of the (gas) temperature profile, $\partial \ln T / \partial \ln r$, at different times, as in Fig. 4.27. The inner (outer) “star” on a radial profile curve, present only after a supercritical core forms, marks the initial (final) radius of the supercritical core.

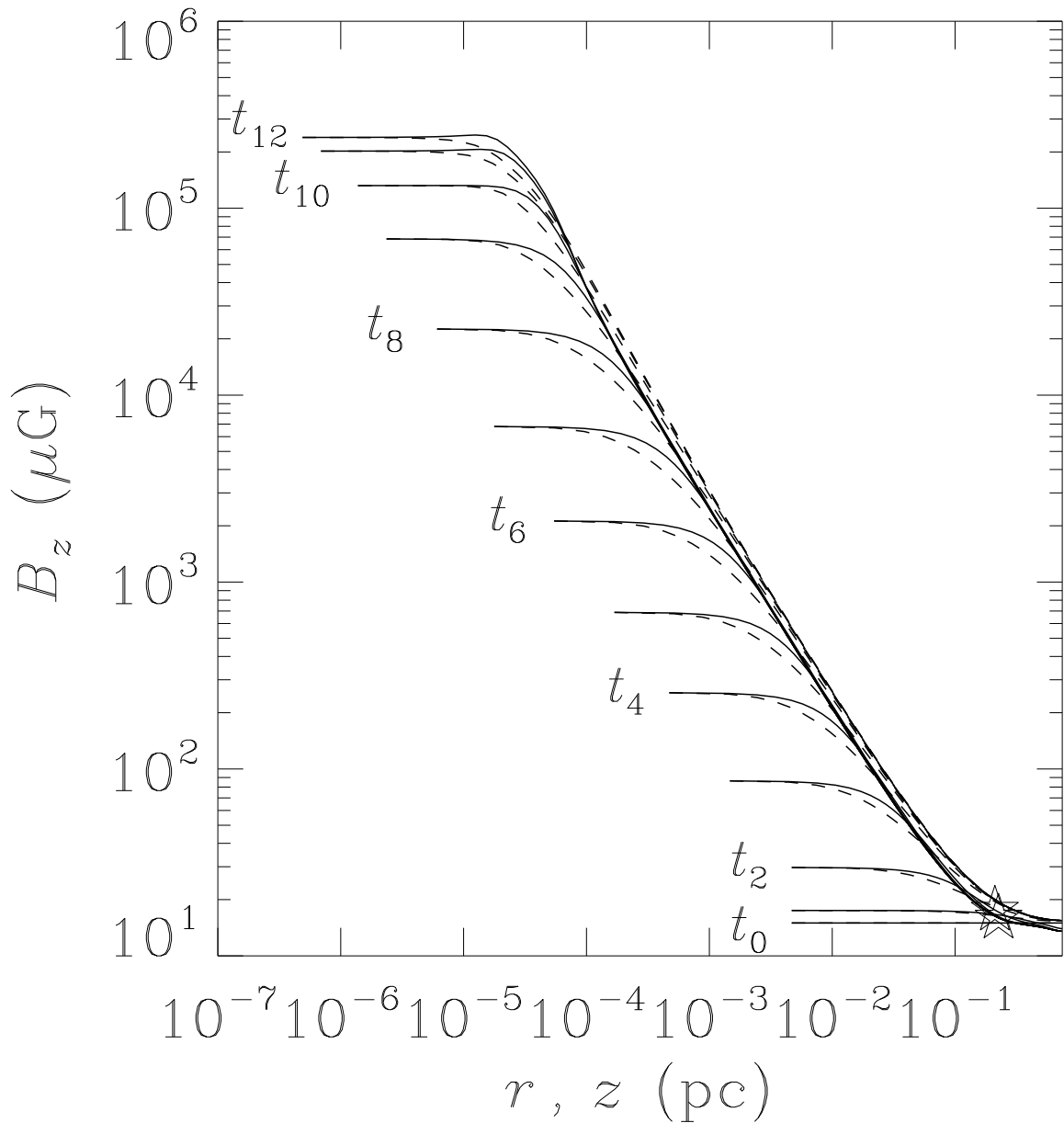


Figure 4.31: Radial midplane (solid line) and vertical symmetry-axis (dashed line) profiles of the z -component of the magnetic field at different times, as in Fig. 4.27. The inner (outer) “star” on a radial profile curve, present only after a supercritical core forms, marks the initial (final) radius of the supercritical core.

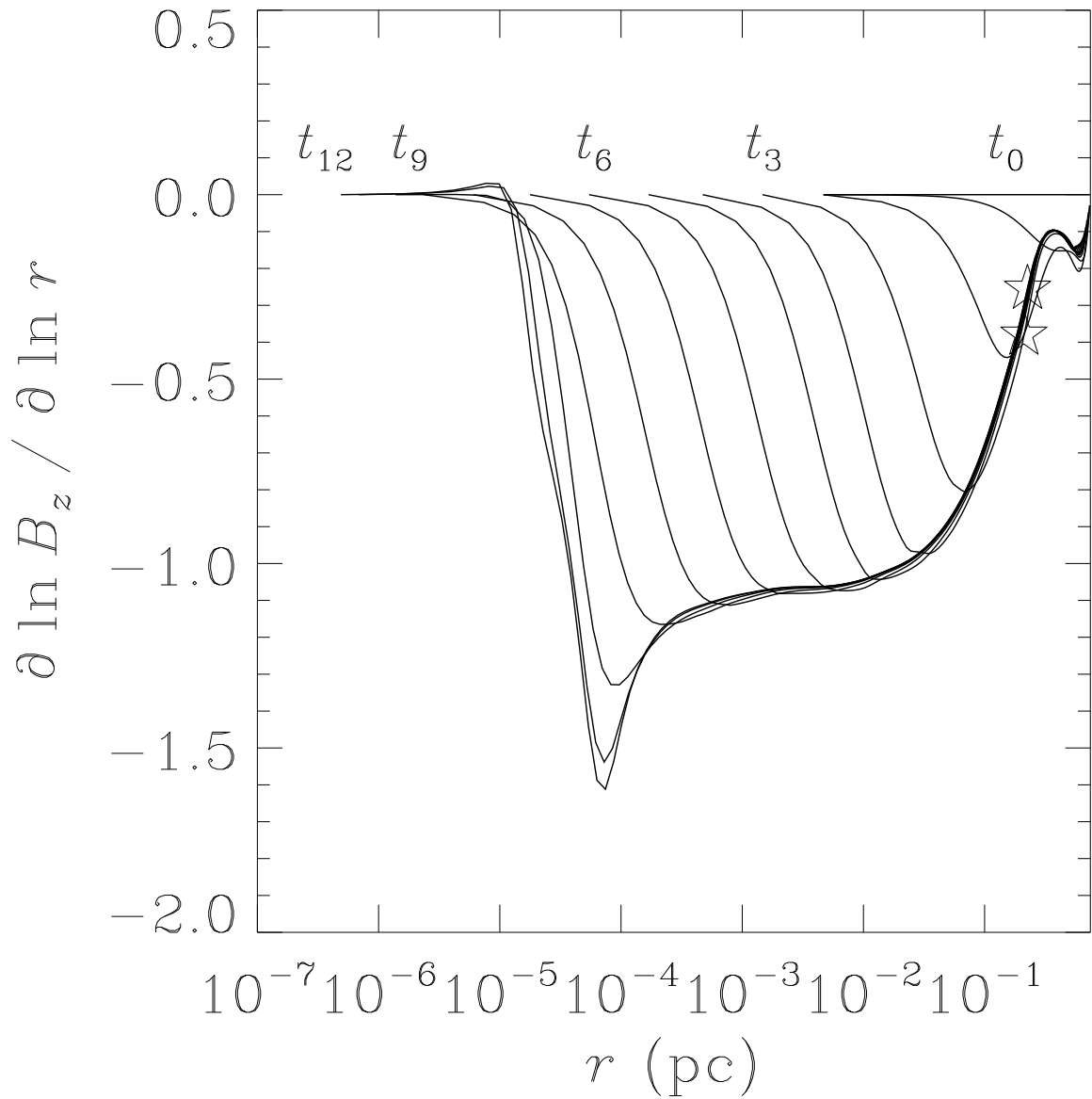


Figure 4.32: Radial derivative along the midplane of the z -component of the magnetic field, $\partial \ln B_z / \partial \ln r$, at different times, as in Fig. 4.27. The inner (outer) “star” on a radial profile curve, present only after a supercritical core forms, marks the initial (final) radius of the supercritical core.

uniform. Outside the supercritical core ($r \approx 0.4$ pc, marked by a “star”), where the gas is magnetically-supported, the profile flattens significantly and B_z is almost uniform. For radii in the range $\approx 10^{-3} - 10^{-2}$ pc the slope $\partial \ln B_z / \partial \ln r \simeq -1.1$ (see Figure 4.32). As the temperature increases at smaller radii, the slope approaches $\simeq -1.6$ until the location of the hydrostatic core boundary, inside of which the slope quickly asymptotes to zero. This zero slope is due to efficient Ohmic dissipation, which quickly erases any spatial variation in the magnetic field. The strength of the magnetic field inside the hydrostatic core is ≈ 0.2 G, in excellent agreement with the protosolar magnetic field strength as derived from meteoritic data (Levy 1988; Stacey et al. 1961; Herndon & Rowe 1974).

A closer inspection of Figures 4.31 and 4.32 reveals that the z -component of the magnetic field actually has a local maximum just outside of the hydrostatic core at $r \simeq 10^{-5}$ pc ($\simeq 2$ AU), where the inwardly-advected magnetic flux has piled up and formed a “magnetic wall.” This *local* concentration of magnetic flux outside the hydrostatic core boundary is due to efficient ambipolar diffusion and results in a magnetic shock, the consequences of which we will discuss in Sections 4.4.3 and 4.4.4. Tassis & Mouschovias (2005b) followed the formation and evolution of a series of these magnetic shocks and found that accretion onto the forming protostar occurs in a time-dependent, spasmodic fashion.

Figure 4.33 shows the maximum (in z) strength of the r -component of the magnetic field, generated as a result of field-line deformation during core contraction. Inside the inner flat region where the magnetic field is near uniform, $B_{r,\max}$ declines rapidly to very small values, reaching zero at the origin. The rapid contraction outside the hydrostatic core induces a strong field-line deformation, and $B_{r,\max}$ has a sharp local maximum at the boundary of the hydrostatic core, where its value becomes comparable to, although still smaller than, that of B_z ($B_r/B_z = 0.99$ at the location of $B_{r,\max}$). In fact, $B_z > B_r$ at all locations and for all times.

The ratio of the local Alfvén speed and the local isothermal sound speed, v_A/c_s , is shown in Figure 4.34. The behavior of this ratio may be understood by realizing that

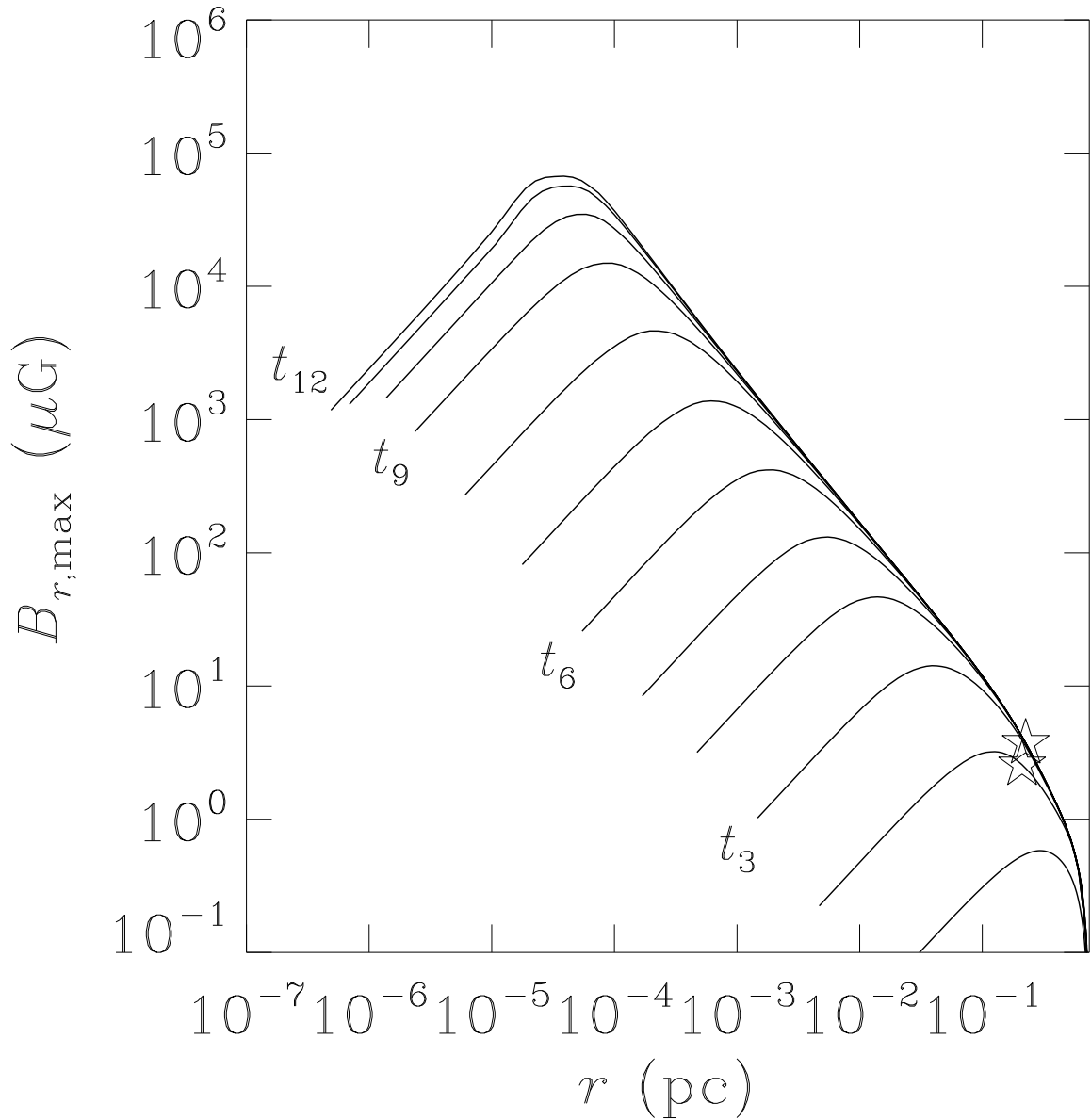


Figure 4.33: Radial profiles of the maximum (in z) strength of the r -component of the magnetic field at different times, as in Fig. 4.27. The inner (outer) “star”, present only after a supercritical core forms, marks the initial (final) radius of the supercritical core.

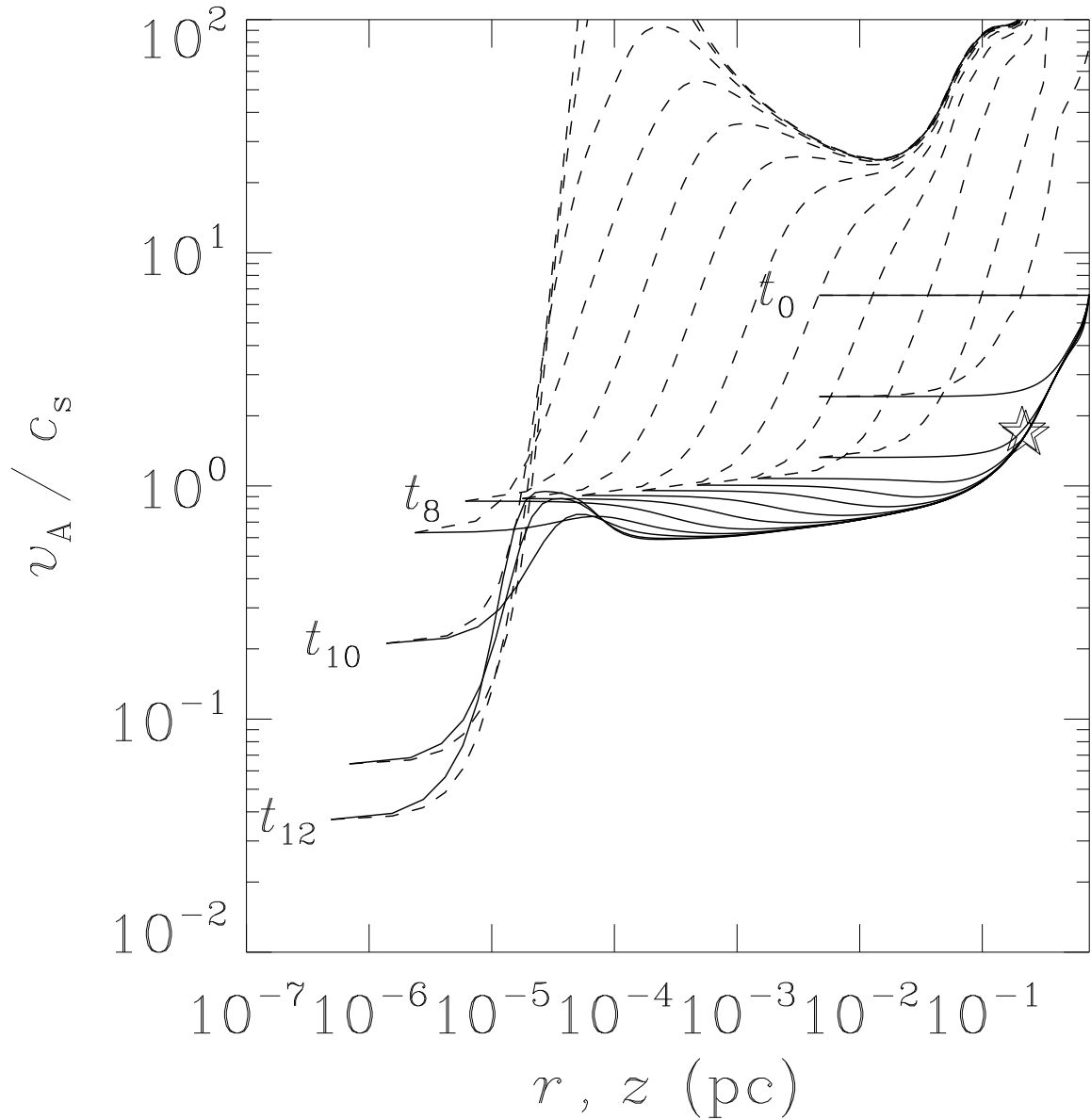


Figure 4.34: Radial midplane (solid line) and vertical symmetry-axis (dashed line) profiles of the ratio of the Alfvén speed and the local isothermal sound speed at different times, as in Fig. 4.27. The inner (outer) “star” on a radial profile curve, present only after a supercritical core forms, marks the initial (final) radius of the supercritical core.

$v_A/c_s \propto n_n^{\kappa - \gamma_{\text{eff}}/2}$. Outside of the magnetically-supercritical core (marked by a “star”) $\kappa \approx 0$ and so $v_A/c_s \propto n_n^{-1/2}$. This accounts for the large values of v_A/c_s in the cloud envelope and upper atmosphere. In the magnetically-supercritical core during the isothermal phase of contraction (when $\kappa \simeq 0.47$ and $\gamma_{\text{eff}} = 1$), the Alfvén speed varies only slightly with the isothermal sound speed and is approximately a constant of order unity. The fact that v_A becomes comparable to (or smaller than) the sound speed inside the supercritical core provides *an explanation for the thermalization of linewidths observed in molecular cloud cores* (Baudry et al. 1981; Myers & Benson 1983). In the theory of magnetic star formation, the material motions responsible for the observed linewidths are attributed to long-wavelength, standing Alfvén waves (Mouschovias 1987; Mouschovias & Psaltis 1995), with a remarkable quantitative agreement between theory and observations (Mouschovias et al. 2006).

A *local* maximum in v_A/c_s occurs just outside of the magnetic wall at $r \approx 10$ AU. There is a substantial decrease in v_A/c_s inside the hydrostatic core, where the gas is primarily thermally-supported, due to the increase in γ_{eff} and decrease in κ ; i.e., the gas begins to evolve near-adiabatically and the magnetic field begins to decouple from the matter. Once the magnetic field no longer significantly influences the matter, $\kappa \simeq (\gamma_{\text{eff}} - 1)/2$ and we immediately find that $v_A/c_s \propto n_n^{-1/2}$. This proportionality will approximately hold until the temperature reaches $\sim 10^3$ K, when thermal ionization and grain sublimation become important and the gas recouples to the magnetic field.

The radial profile of the mass-to-flux ratio (normalized to the central critical value for collapse) is given in Figure 4.35. It appears to exhibit a three-slope power law with a flat inner region, which corresponds to the flat-density uniform-magnetic-field core. The first power law (at small r) occurs just outside of hydrostatic core and marks the transition from the magnetically-decoupled hydrostatic core to the near flux-frozen magnetically-supercritical core. From radii $\sim 10^{-4}$ pc to a few $\times 10^{-2}$ pc, there is a second power law, which is relatively flat. In this region, the ions are still attached to the field lines

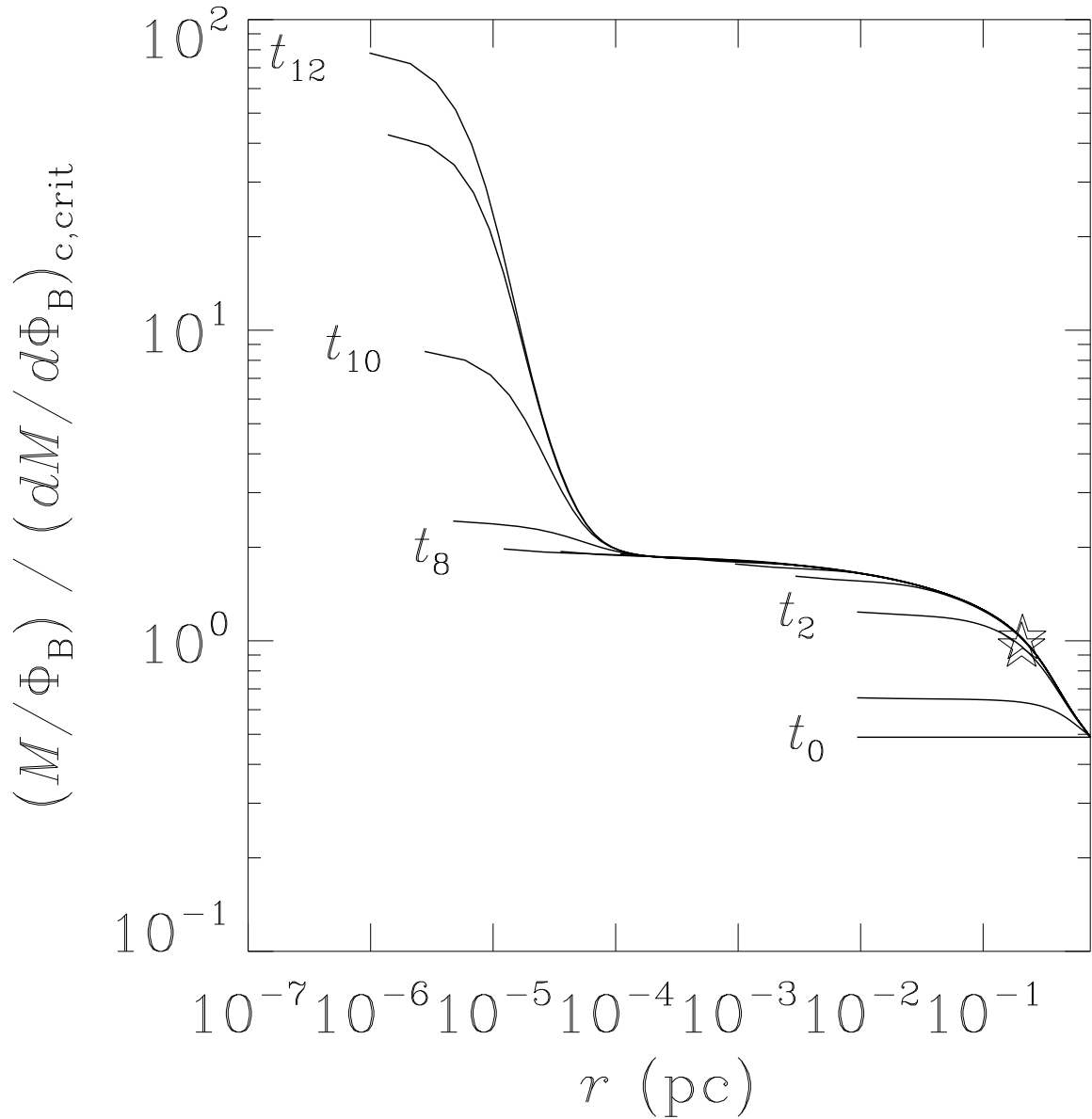


Figure 4.35: Radial profile of the mass-to-flux ratio (normalized to the central critical value for collapse) at different times, as in Fig. 4.27. The inner (outer) “star” on a radial profile curve, present only after a supercritical core forms, marks the initial (final) radius of the supercritical core.

and the mass-to-flux ratio only increases mildly. The third power law begins outside of magnetically-supercritical core, where magnetic fields continues to support the cloud envelope.

4.4.3 Forces

Figures 4.36 – 4.38 demonstrate the relative importance of thermal pressure, magnetic pressure and tension, and gravity in determining the magnitude of the local forces. In Figure 4.36, we give the ratio of thermal-pressure and gravitational forces. The gravitational force dominates the thermal force everywhere (since the cloud is thermally supercritical), except in the hydrostatic core ($r \lesssim 2$ AU). Just outside of the hydrostatic core, there is an abrupt increase in the thermal-pressure force that is ultimately responsible for the formation of a thermal shock there (see Section 4.4.4). At time t_{10} , the ratio of the thermal-pressure and gravitational forces inside the hydrostatic core is significantly larger than unity. This is because the collapsing core has overshoot its equilibrium, which results in radial (spherical) pulsations (see Section 4.4.4).

In Figure 4.37, we give the ratio of magnetic and gravitational forces. The magnetic force is an appreciable fraction of the gravitational force everywhere except inside the hydrostatic core (where efficient Ohmic dissipation operates — see Section 4.4.6). This is the case even inside the dynamically contracting magnetically-supercritical core. Hence, *the dynamical contraction of the magnetically-supercritical core is significantly slower than free-fall*. The magnetic force has a local maximum with respect to the gravitational force at ≈ 10 AU, just outside of the location of the maximum of the magnetic field seen in Figure 4.31. There the abrupt increase in the magnetic force by a factor $\gtrsim 2.5$ constitutes a magnetic wall and results in the formation of a magnetic shock (see Section 4.4.4).

In order to determine what agent is mainly responsible for diluting the effects of gravity at any given radius, we also give in Figure 4.38 the ratio of thermal-pressure and magnetic forces. The magnetic force is greater than the thermal-pressure force (and hence provides

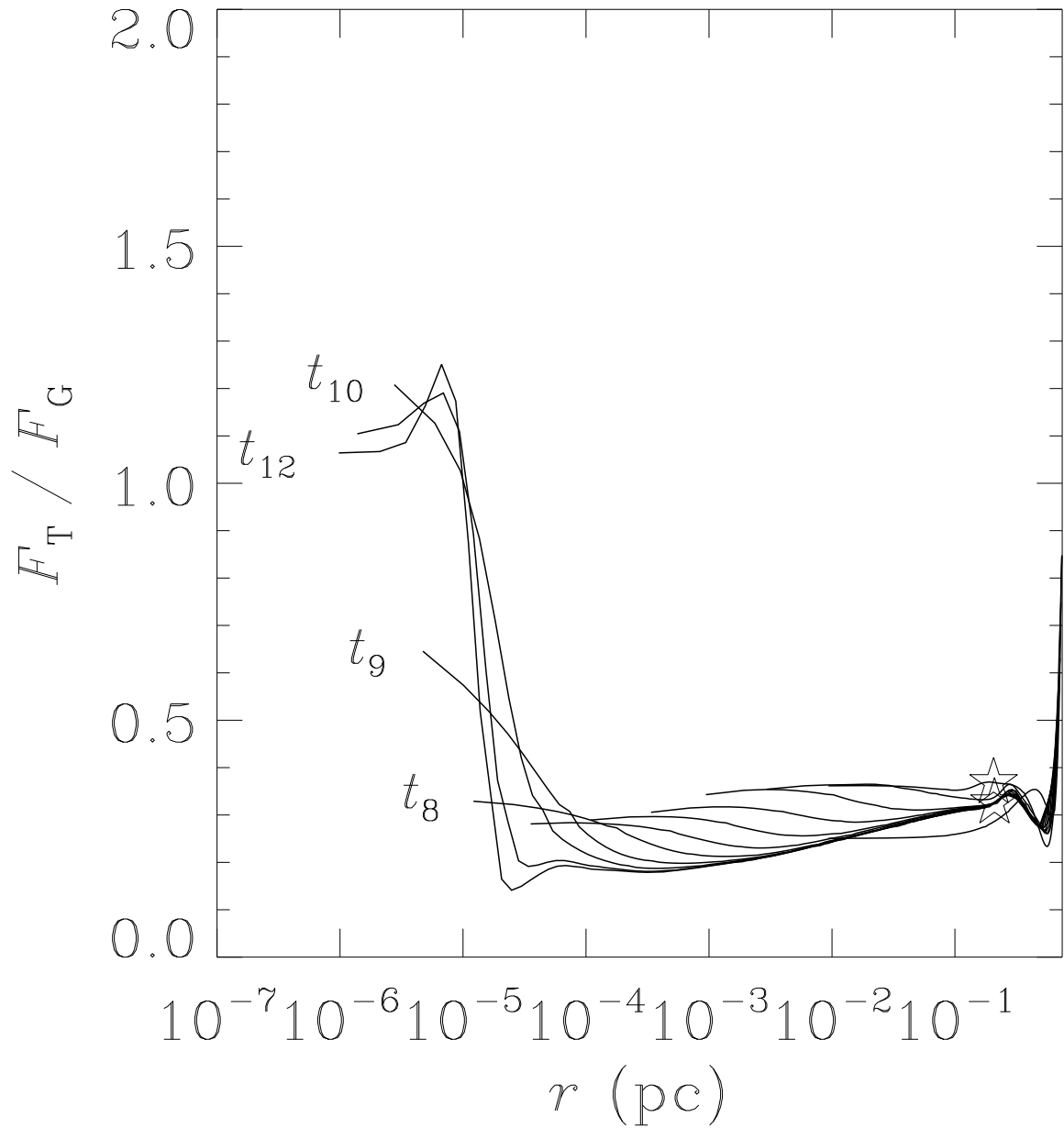


Figure 4.36: Radial midplane profile of the ratio of thermal-pressure and gravitational forces at different times, as in Fig. 4.27. The inner (outer) “star” on a radial profile curve, present only after a supercritical core forms, marks the initial (final) radius of the supercritical core.

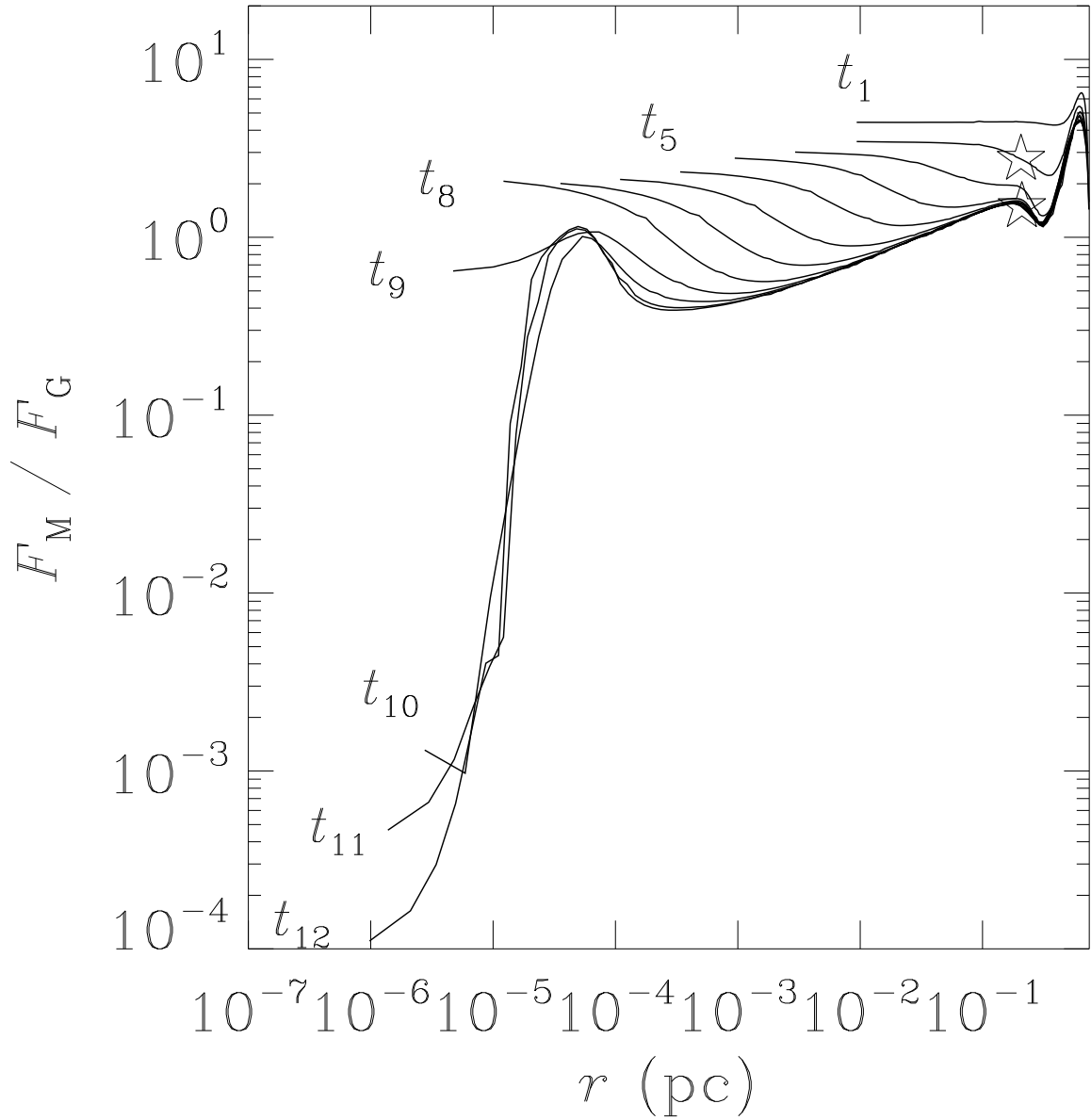


Figure 4.37: Radial midplane profile of the ratio of magnetic and gravitational forces at different times, as in Fig. 4.27. The inner (outer) “star” on a radial profile curve, present only after a supercritical core forms, marks the initial (final) radius of the supercritical core.

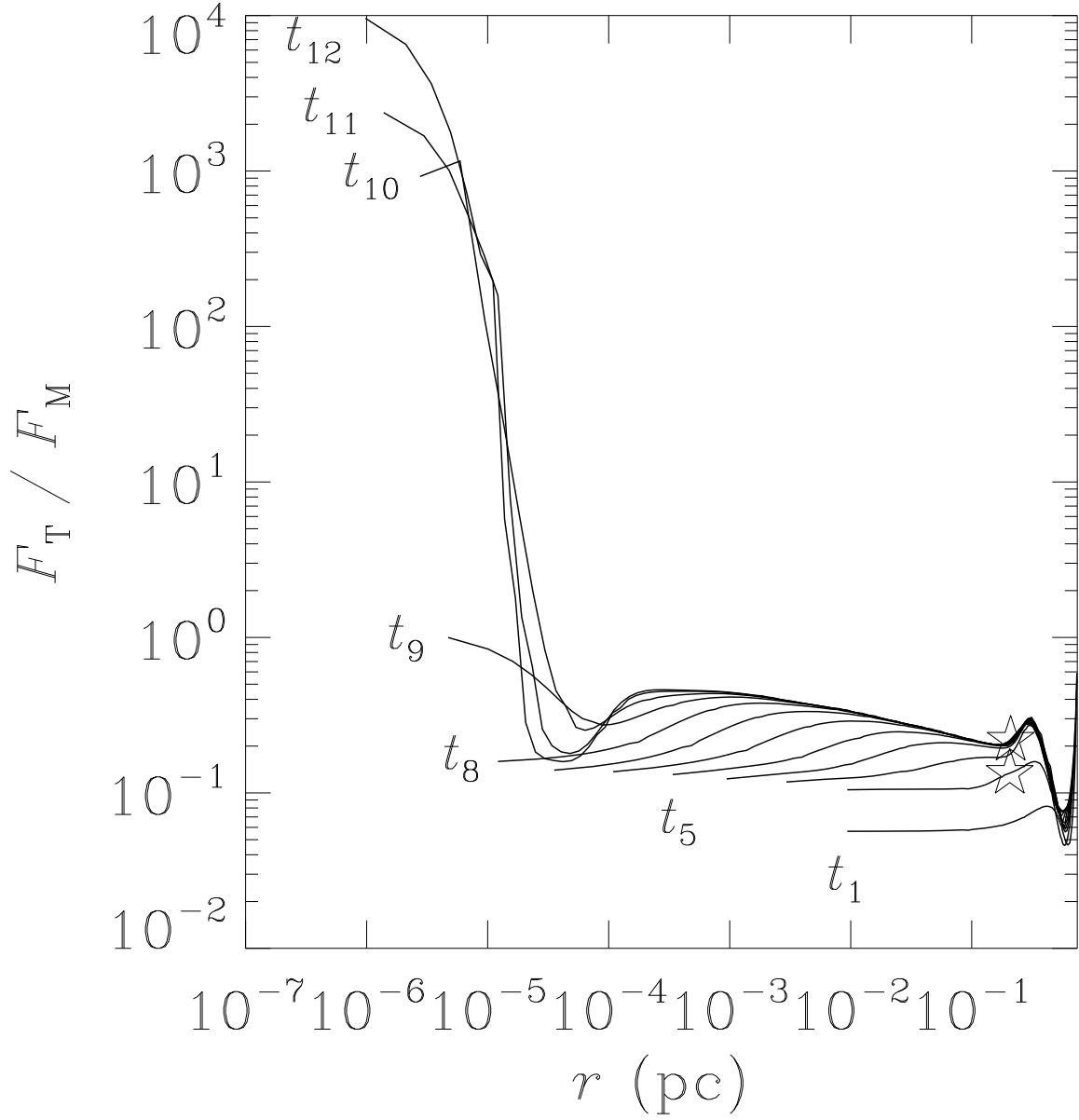


Figure 4.38: Radial midplane profile of the ratio of thermal-pressure and magnetic forces at different times, as in Fig. 4.27. The inner (outer) “star” on a radial profile curve, present only after a supercritical core forms, marks the initial (final) radius of the supercritical core.

the dominant opposition to gravity) everywhere except in the hydrostatic core, where the thermal-pressure force dominates the magnetic force by several orders of magnitude. There is a local minimum in the thermal-to-magnetic force ratio outside of the hydrostatic core, where the magnetic field strength increases briefly.

4.4.4 Velocities

The velocity of the neutrals is given in Figure 4.39. For comparison, the isothermal sound speed at a temperature of 10 K is 0.188 km s^{-1} . The ambipolar-diffusion-controlled, quasistatic phase is marked by small radial velocities ($\simeq 0.01 - 0.03 \text{ km s}^{-1}$). Once a magnetically- and thermally-supercritical core forms, dynamical contraction ensues inside the core and the radial velocity increases to $\simeq 0.5c_s - 1.0c_s$. It is of interest to note that the radial velocity is $\approx 0.1 \text{ km s}^{-1}$ at $r \sim 0.1 \text{ pc}$, in excellent agreement with the observed infall motions of L1544 by Tafalla et al. (1998). The predicted radial velocities also compare well with the observed infall motions near the starless molecular cloud core MC27 in Taurus, where speeds of $0.2 - 0.3 \text{ km s}^{-1}$ have been detected at $r \simeq 2000 - 3000 \text{ AU}$ ($\sim 10^{-2} \text{ pc}$) (Onishi et al. 1999). The radial velocities outside of the supercritical core, where the gas is magnetically supported, remain subsonic by a factor of a few.

At approximately the same time that isothermality breaks down in the supercritical core, the radial velocities become supersonic. The mass accumulating in the hydrostatic core causes an accelerated infall and the radial velocity approaches and exceeds $\sim 1 \text{ km s}^{-1}$. A shock forms near the boundary of the hydrostatic core due to rapid increases in the local magnetic and thermal pressure forces, and the velocity rapidly falls to zero inside the hydrostatic core. The large vertical velocities throughout the evolution result from the cloud collapsing along field lines and constantly responding to changes in the thermal-pressure gradient along magnetic field lines. At the boundary of the hydrostatic core, shocks appear along the vertical symmetry axis. Vertical velocities become positive after the core overshoots hydrostatic equilibrium, rebounds, and oscillates. Radial velocities remain negative,

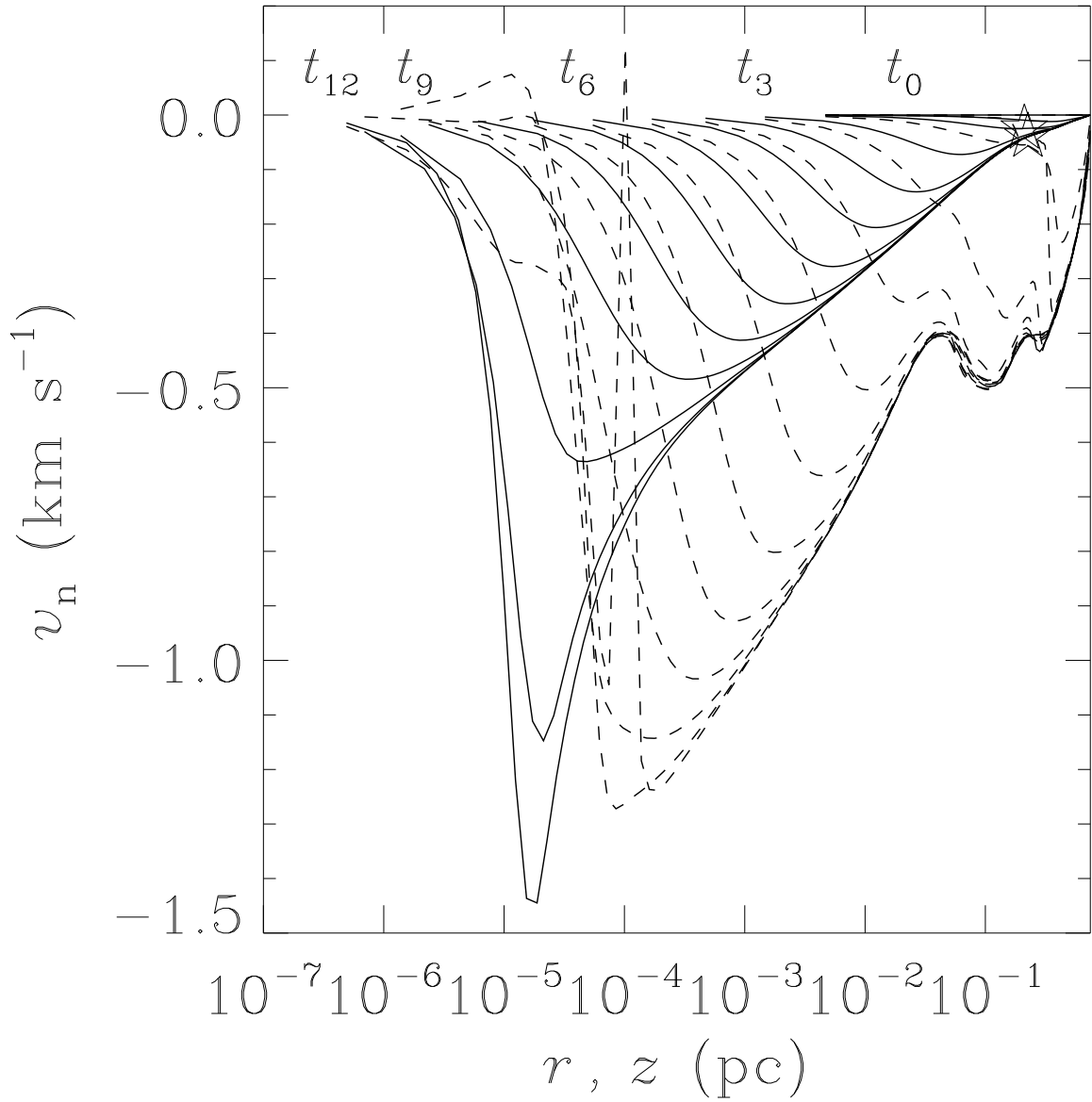


Figure 4.39: Radial midplane (solid line) and vertical symmetry-axis (dashed line) profiles of the velocity of the neutrals at different times, as in Fig. 4.27. The inner (outer) “star” on a radial profile curve, present only after a supercritical core forms, marks the initial (final) radius of the supercritical core.

but form a thermal and magnetic shock outside of the hydrostatic core.

The maximum radial velocities in this simulation are substantially larger than those found by Tassis & Mouschovias (2007b). In addition, there are significant differences in the structure and strength of the magnetic wall. Fortunately, the thorough parameter study by Tassis & Mouschovias (2007c) provides a valuable service by obviating the reasons for which these differences exist. They found that, if the onset of adiabaticity is delayed beyond its oft-assumed critical density 10^{11} cm^{-3} , as is naturally the case in the RMHD simulations presented here, the maximum infall velocity of both neutrals and magnetic field lines increases somewhat as the density at which adiabaticity sets in increases. This is because the delay of the onset of adiabaticity implies accelerated infall for longer times. Using the results from a simulation in which isothermality was assumed to always hold, Tassis & Mouschovias (2007c) found that the longer the gas remains isothermal, the weaker the magnetic shock is. In other words, the enhanced “pile-up” of matter and magnetic flux outside the hydrostatic core becomes increasingly absent. Given that the results of our RMHD simulations must necessarily be bracketed by those in which isothermal or adiabatic equations of state are assumed, the fact that our magnetic wall is more pronounced than found in their isothermal control run, yet less pronounced than found in their adiabatic run, is not surprising.

The velocity of the field lines is given in Figure 4.40. (Note the different velocity scaling on the ordinate.) Effective Ohmic dissipation in the hydrostatic core erases all spatial inhomogeneities in the magnetic field strength there and transports the magnetic flux outwards towards the magnetic wall where it accumulates. This is seen in the figure as a positive field-line velocity in the lab frame. Everywhere outside of the hydrostatic core, the velocity of the field lines remains negative at all times, indicating that the magnetic field there never diffuses outwards in the lab frame. Beyond the magnetically-supercritical core radius, the velocity of the field lines becomes vanishingly small, indicating stationary field lines and effective magnetic support in the envelope of the cloud.

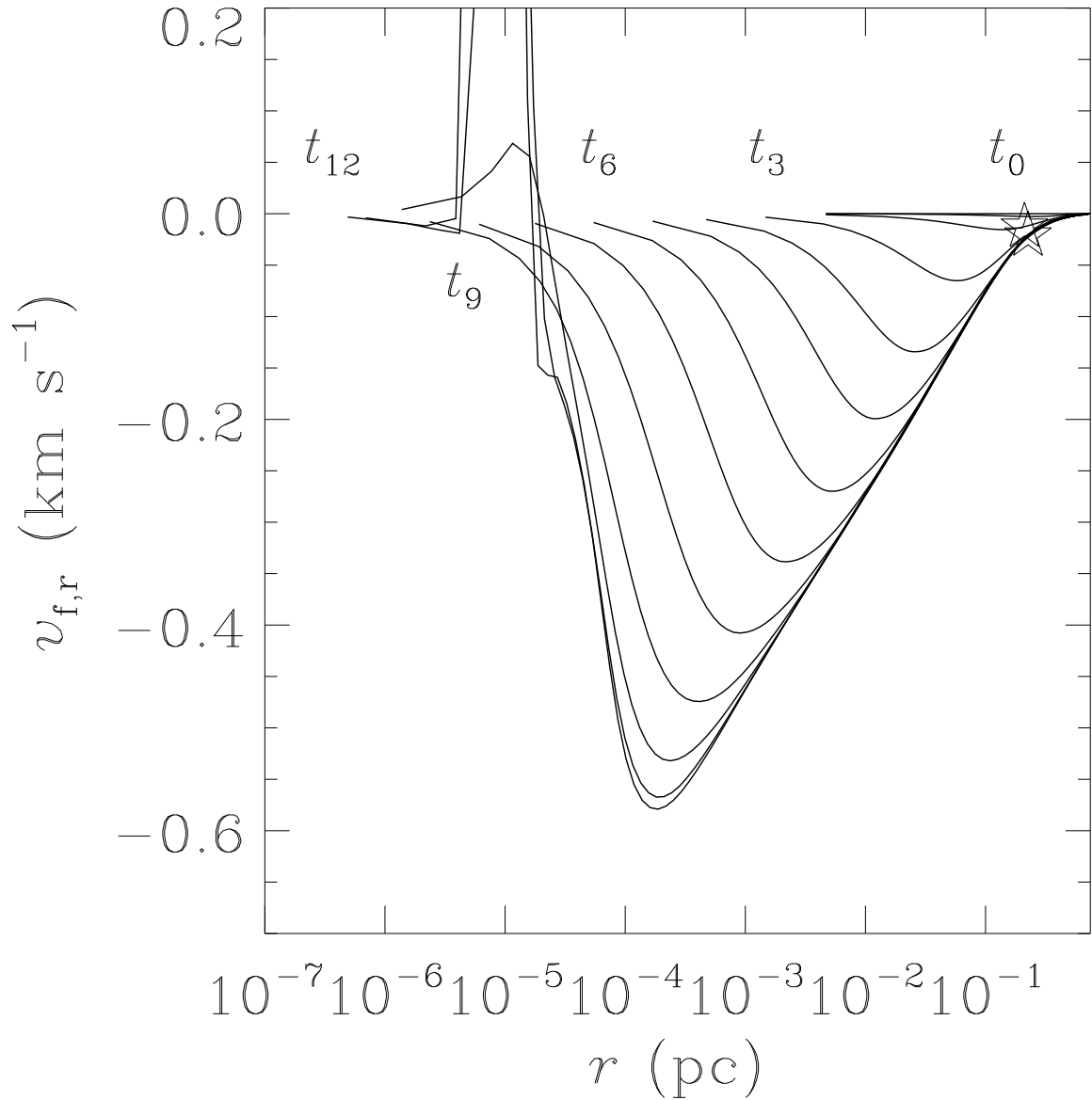


Figure 4.40: Radial midplane profile of the velocity of the magnetic field lines at different times, as in Fig. 4.27. The inner (outer) “star” on a radial profile curve, present only after a supercritical core forms, marks the initial (final) radius of the supercritical core.

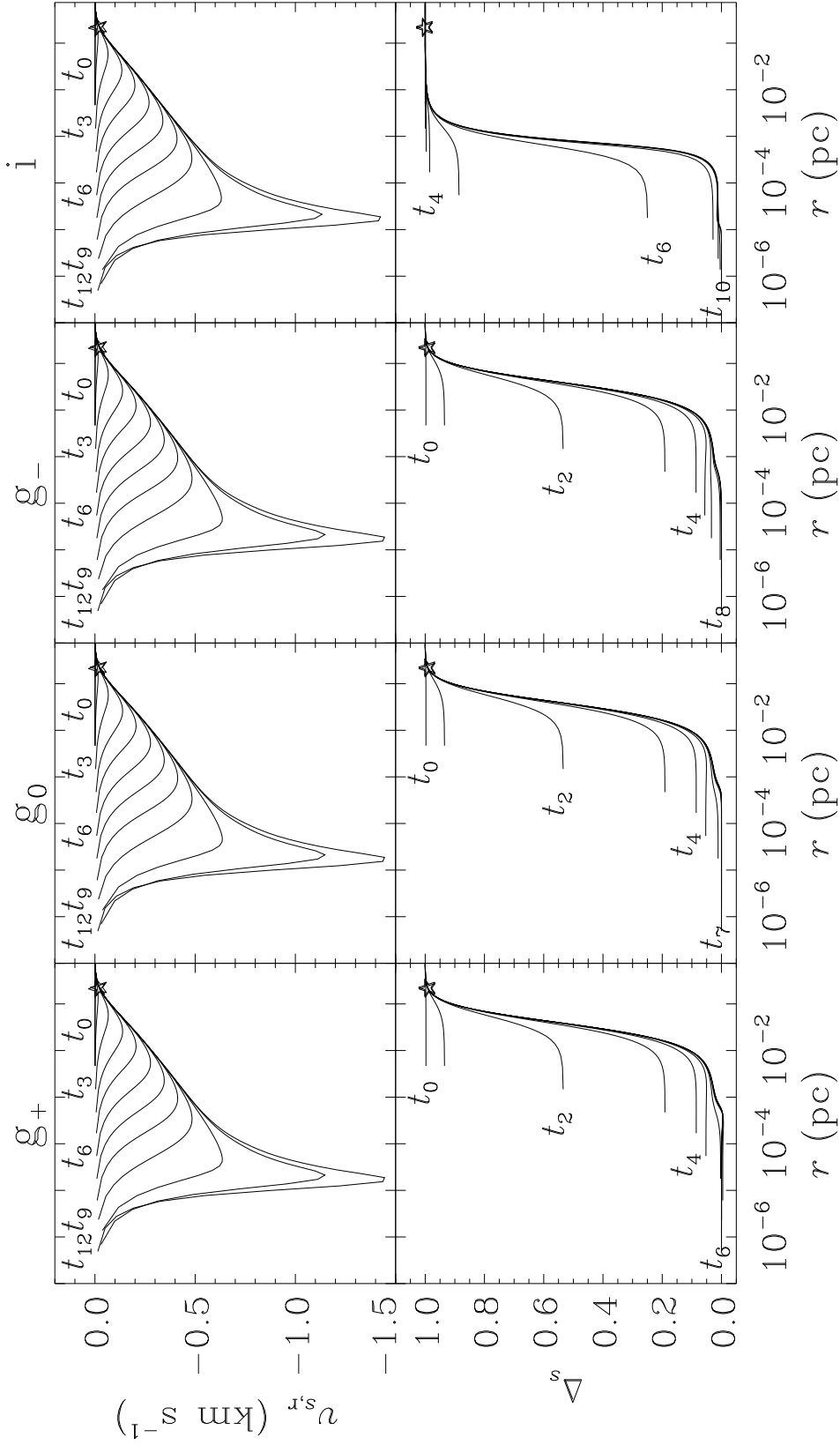


Figure 4.41: Radial midplane profiles of (top row) velocities and (bottom row) direct attachment parameters for (left to right) positively charged grains, neutral grains, negatively charged grains, and ions. Different curves correspond to different times, as in Fig. 4.27. The inner (outer) “star” on a radial profile curve, present only after a supercritical core forms, marks the initial (final) radius of the supercritical core.

Figure 4.41 shows radial profiles of the velocities and direct attachment parameters for the different species. (These profiles for the electrons are not given, since the electrons remain well-coupled to the magnetic field lines during the entire calculation.) The direct attachment parameter for species s is given by

$$\Delta_s \equiv \frac{v_{s,r} - v_{n,r}}{v_{f,r} - v_{n,r}} \quad (4.1)$$

and quantifies the degree to which species s is coupled to the magnetic field. If $\Delta_s \approx 1$, then species s is attached to the field lines, whereas if $\Delta_s \ll 1$, then species s is detached from the magnetic field lines and its motion follows that of the neutrals. It is more useful a diagnostic of magnetic attachment than the indirect attachment parameter, $\omega_s \tau_{sn}$, in that it takes into account more complicated physics than just cyclotron gyrations and elastic $s-n$ collisions (e.g., electrostatic attraction between the different charged species, inelastic collisions, etc.). In fact, it is straightforward to show from equations (C.1) and (C.2) that the two are related by

$$\Delta_s = \omega_s \tau_{sn} \left(\frac{\sigma_{\perp,s} \sigma_H - \sigma_{H,s} \sigma_{\perp}}{\sigma_s \sigma_{\perp}} \right), \quad (4.2)$$

where $\sigma_s = n_s q_s^2 \tau_{sn} / m_s$ is the conductivity of species s and the other quantities have the same meanings as in Figure 4.23.

Outside of the magnetically-supercritical core, all the species (except for the neutrals) remain well-attached to the magnetic field lines. It is only inside of the supercritical core that the different species begin to follow the neutrals, as each species is peeled away from the magnetic field via collisional forces. The negatively-charged grains are completely detached from the magnetic field by t_6 , the neutral grains by t_7 , and the positively-charged grains by t_8 . The ions do not begin to detach from the magnetic field until t_4 , well into the dynamical contraction phase, and do not fully detach until t_{10} . Indeed, at late times, the radial velocity profiles of these species appear identical to those of the neutrals.

A closer inspection of the direct attachment parameter profiles reveals more detailed

and interesting behavior than one would expect based solely on magnetic and collisional forces. These parameters do not simply asymptote directly to zero, but rather asymptote first to a small but nonzero value before finally settling at zero. For example, Δ_{g-} asymptotes to ≈ 0.05 before falling to zero. Thus, negatively-charged grains remain mildly attached to the field lines even when simpler estimates (e.g., $\omega_g \tau_{gn} \ll 1$) would suggest otherwise. This is a result of electrostatic attraction between negatively-charged grains and electron-shielded ions, which have yet to fully decouple from the magnetic field. Neutral grains also couple to the magnetic field by inelastic charge-capture processes. Slightly more complex behavior can be seen for the positively-charged grains, which are repelled from the field lines by electron-shielded ions. Even electrostatic attraction between ions and (fully-attached) electrons keeps the ions very mildly attached for $t_8 - t_{10}$, though this effect is much subtler than for the grains because of extremely low electron abundances at these high densities.

4.4.5 Contribution of Electric Current Density by Different Species

Figures 4.43 – 4.46 exhibit the contribution of different charged species to the total electric current density (in the midplane) as a function of radius at different times. The current density (in the midplane) carried by species s , $j_{s,\phi}$, may be obtained from equation (C.1) and written in terms of the total current density j_ϕ (shown in Figure 4.42) and various components of the resistivity tensor:

$$j_{s,\phi} \equiv n_s q_s v_{s,\phi} = (\sigma_{\perp,s} \eta_{\perp} + \sigma_{H,s} \eta_H) j_\phi. \quad (4.3)$$

(Absolute values have been taken; the cusps in the positive grain curves are due to the current passing through zero as it changes sign.)

At early times the contributions of electrons and ions to the electric current density are comparable and are approximately three orders of magnitude greater than the contribution

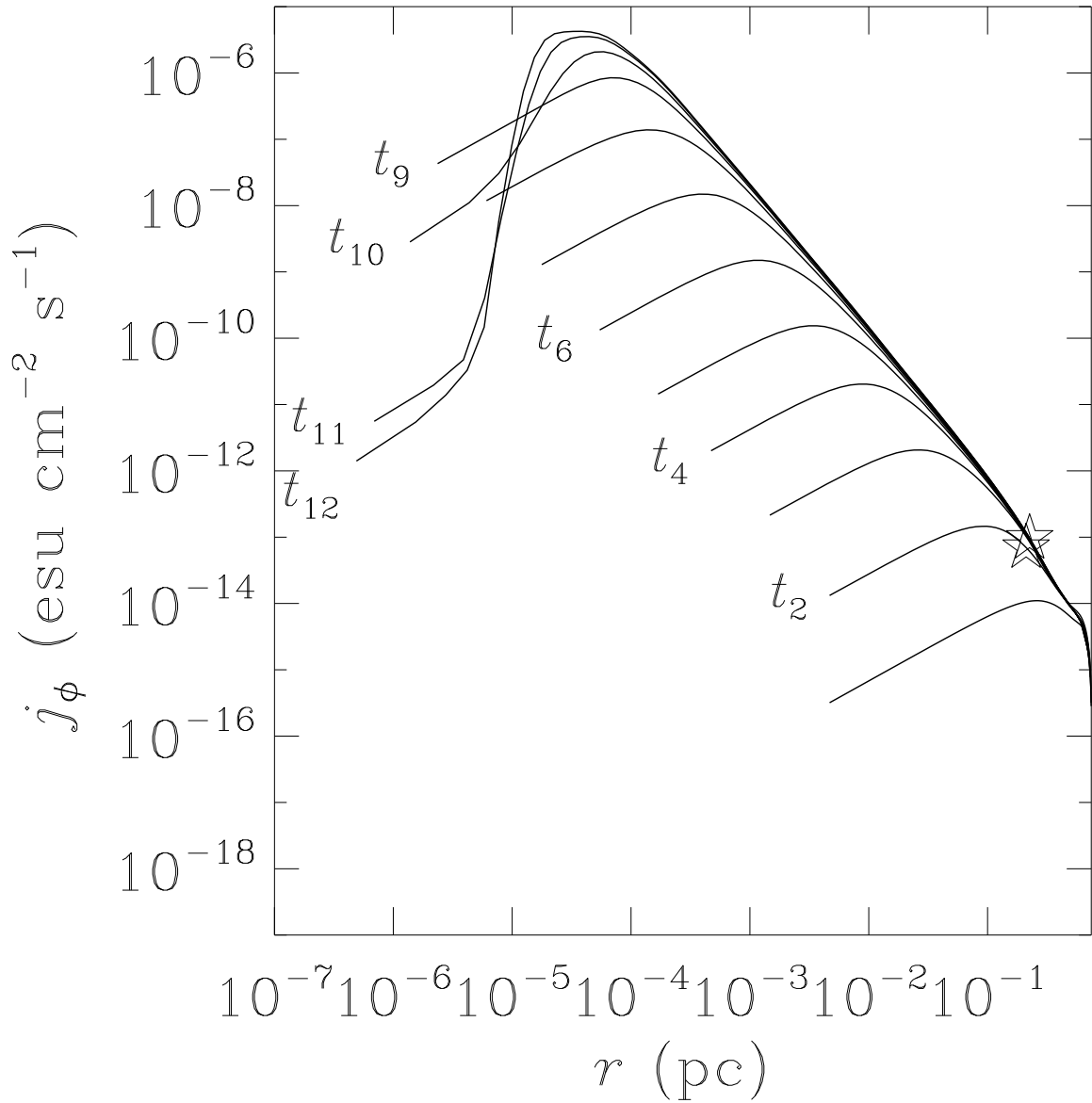


Figure 4.42: Radial midplane profile of the magnitude of the total electric current density in the ϕ -direction at different times, as in Fig. 4.27. The inner (outer) “star” on a radial profile curve, present only after a supercritical core forms, marks the initial (final) radius of the supercritical core.

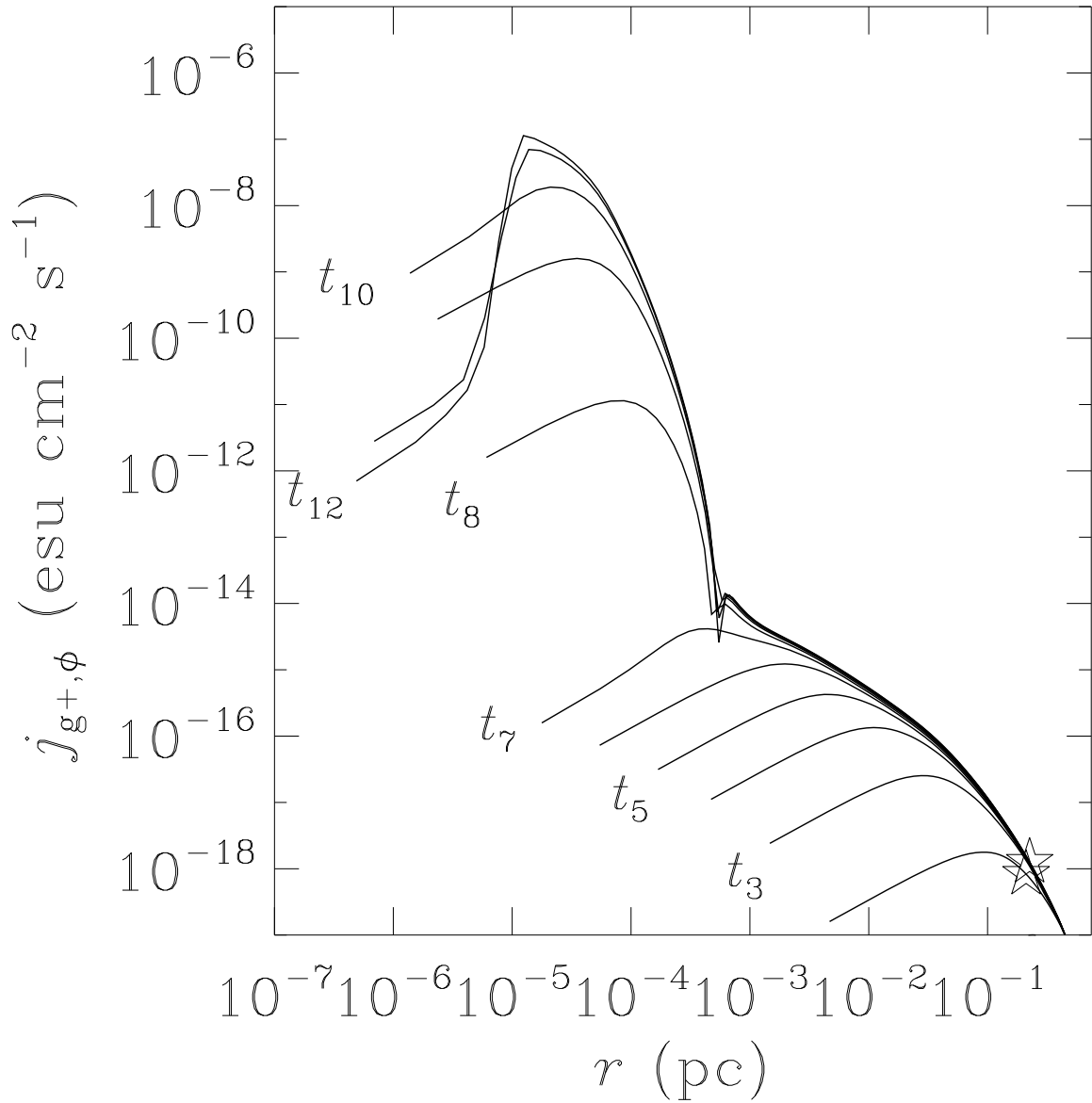


Figure 4.43: Radial midplane profile of the magnitude of the electric current density in the ϕ -direction carried by the positively-charged grains at different times, as in Fig. 4.27. The inner (outer) “star” on a radial profile curve, present only after a supercritical core forms, marks the initial (final) radius of the supercritical core.

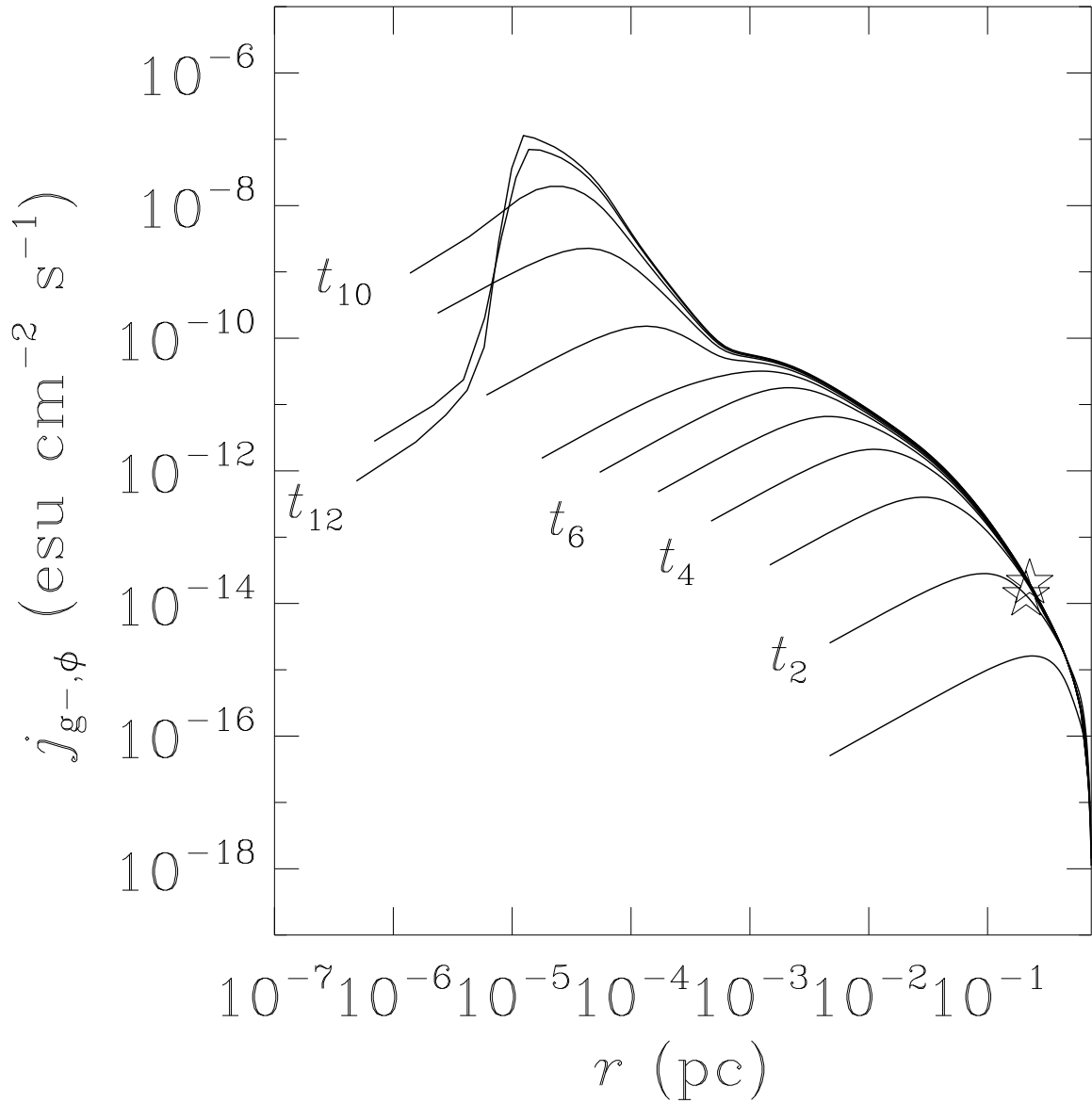


Figure 4.44: Radial midplane profile of the magnitude of the electric current density in the ϕ -direction carried by the negatively-charged grains at different times, as in Fig. 4.27. The inner (outer) “star” on a radial profile curve, present only after a supercritical core forms, marks the initial (final) radius of the supercritical core.

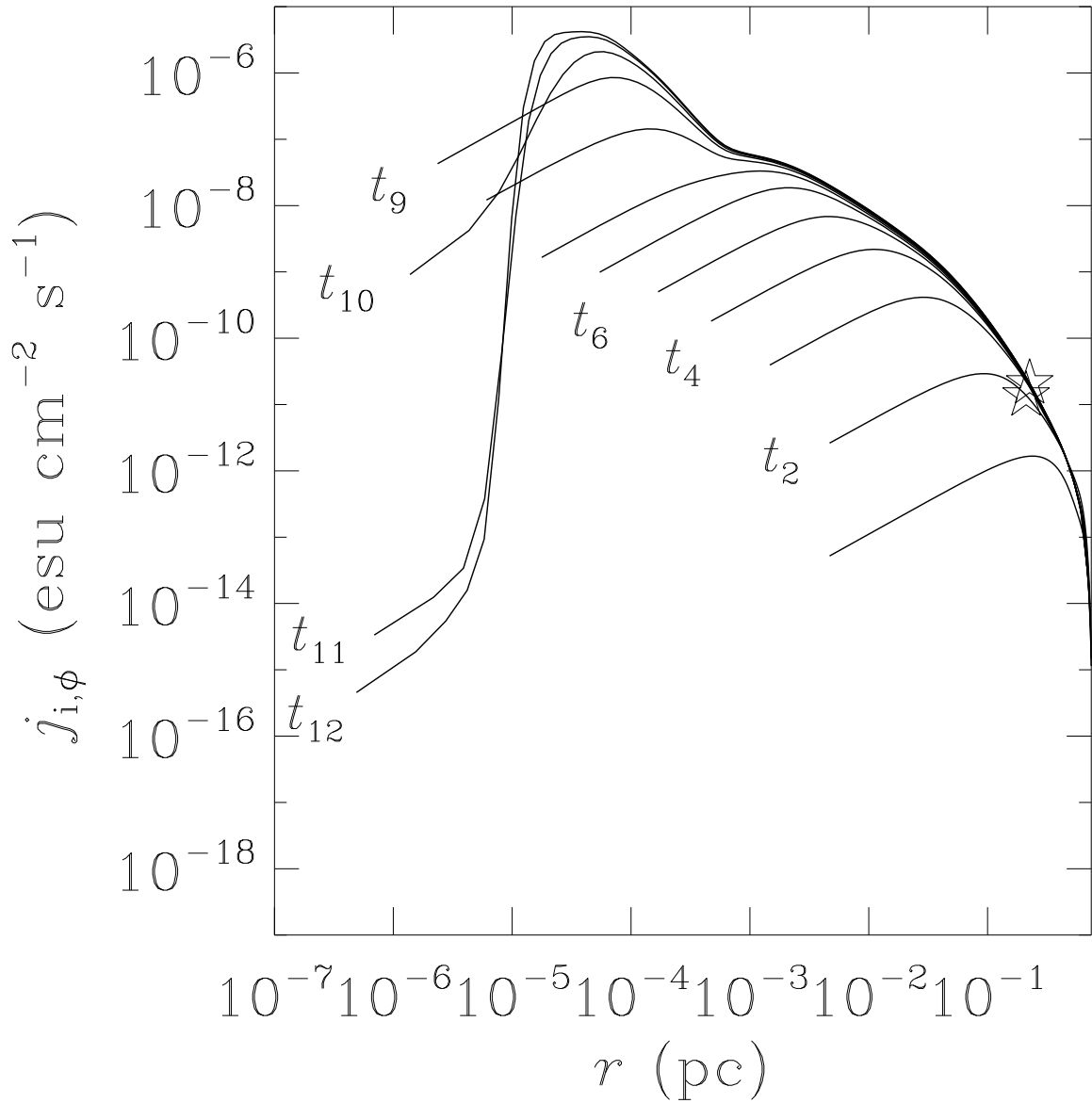


Figure 4.45: Radial midplane profile of the magnitude of the electric current density in the ϕ -direction carried by the ions at different times, as in Fig. 4.27. The inner (outer) “star” on a radial profile curve, present only after a supercritical core forms, marks the initial (final) radius of the supercritical core.

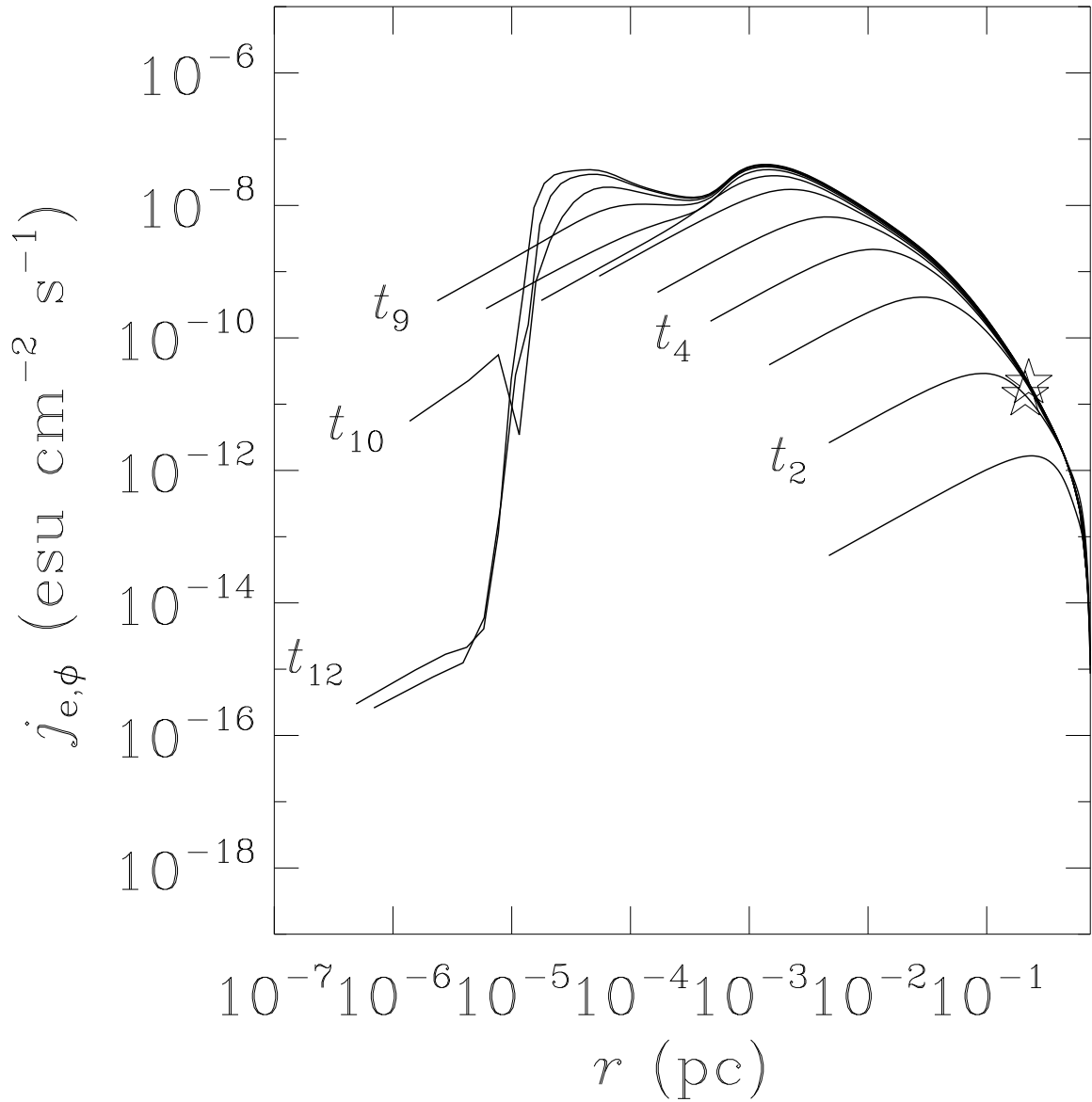


Figure 4.46: Radial midplane profile of the magnitude of the electric current density in the ϕ -direction carried by the electrons at different times, as in Fig. 4.27. The inner (outer) “star” on a radial profile curve, present only after a supercritical core forms, marks the initial (final) radius of the supercritical core.

from negatively-charged grains. By t_9 , the increasing disparity between electron and ion abundances (due to electron depletion onto grains) causes the ion current to become greater than the electron current by a factor ≈ 100 (recall that, at this stage, $x_i/x_e \simeq 125$ — see Figure 4.22). Finally, in the innermost region, the current density decays sharply due to the increasing effect of Ohmic dissipation (see Figure 4.47). As discussed in Section 4.3, grains become the main current carriers at roughly the same time as Ohmic dissipation becomes important. Their contribution to the electric current density is more than two (four) orders of magnitude greater than that of the ions (electrons).

4.4.6 Ambipolar Diffusion and Ohmic Dissipation

The relative importance of ambipolar diffusion and Ohmic dissipation as agents of magnetic diffusion is demonstrated in Figure 4.47, which shows radial midplane profiles of the ratio of the ambipolar-diffusion and Ohmic-dissipation resistivities. At low densities and large radii (and height), ambipolar diffusion dominates Ohmic dissipation. The two processes become equally important only at a density $\simeq 7 \times 10^{12} \text{ cm}^{-3}$, while at higher densities Ohmic dissipation operates on a timescale shorter than that of ambipolar diffusion. (See also Figure 4.23.) The region in which this occurs coincides with the region in which the electric currents diminish ($r \lesssim 2 \text{ AU}$). Note that magnetic decoupling is essentially complete by the time Ohmic dissipation becomes important; i.e., ambipolar diffusion is responsible for decoupling the gas from the magnetic field. Calculations that arrived at the conclusion that Ohmic dissipation is the cause of magnetic decoupling (e.g., Nakano & Umebayashi 1986a,b) were based on a value of the e-H₂ cross section which is too large by a factor of about 100 (see review by Mouschovias 1996, § 2.1).

4.4.7 Mass, Magnetic Flux, and Mass Infall Rate

In Figure 4.48 we show radial profiles of the cumulative mass within a radius r . There are two regions where the mass distribution is markedly different: outside the hydro-

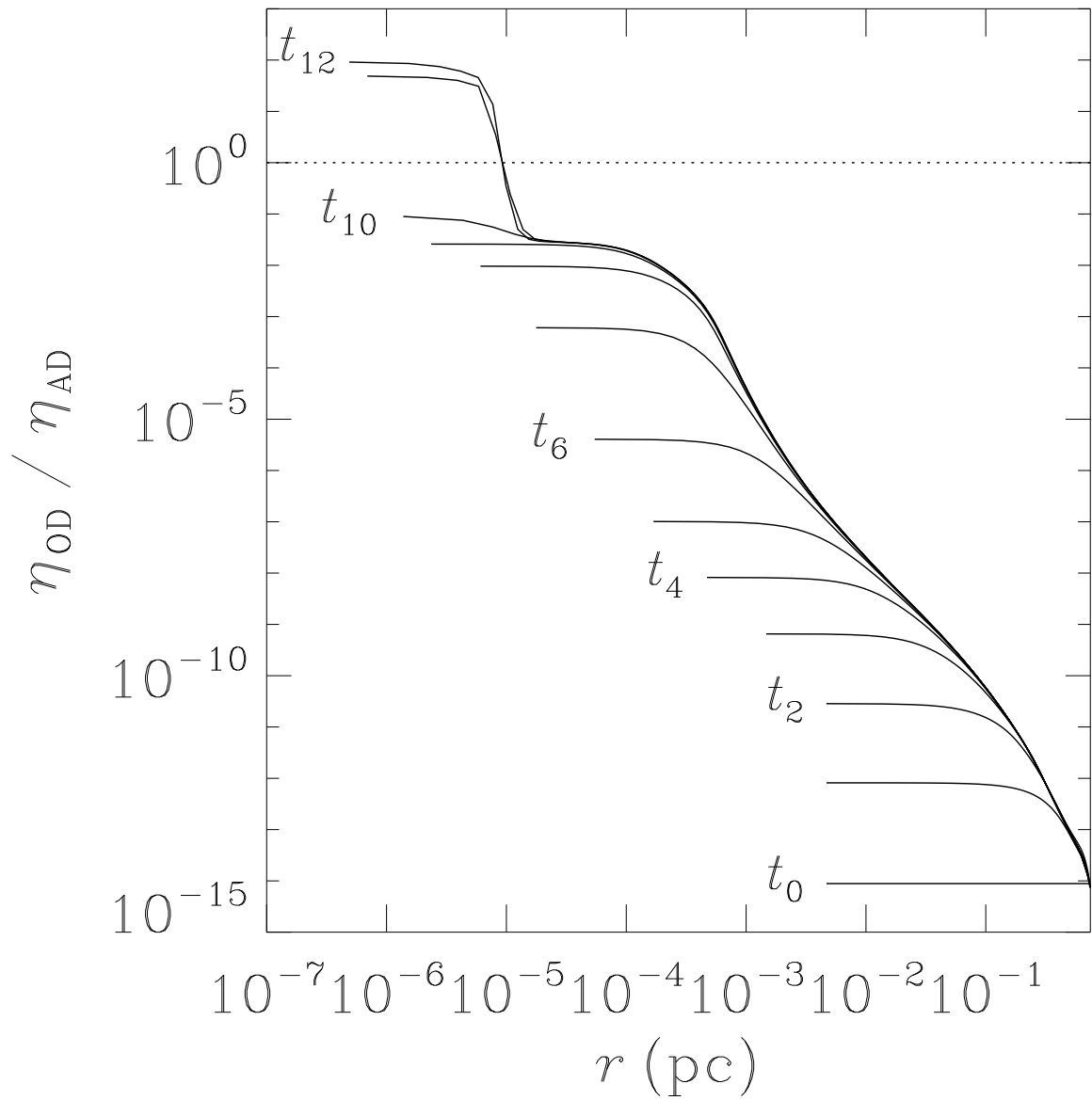


Figure 4.47: Radial midplane profiles of the ratio of Ohmic and ambipolar resistivities. The dotted line denotes the boundary when ambipolar diffusion and Ohmic dissipation become equally important magnetic diffusion mechanisms. Above (below) this line, Ohmic dissipation (ambipolar diffusion) dominates. Different curves correspond to different times, as in Fig. 4.27.

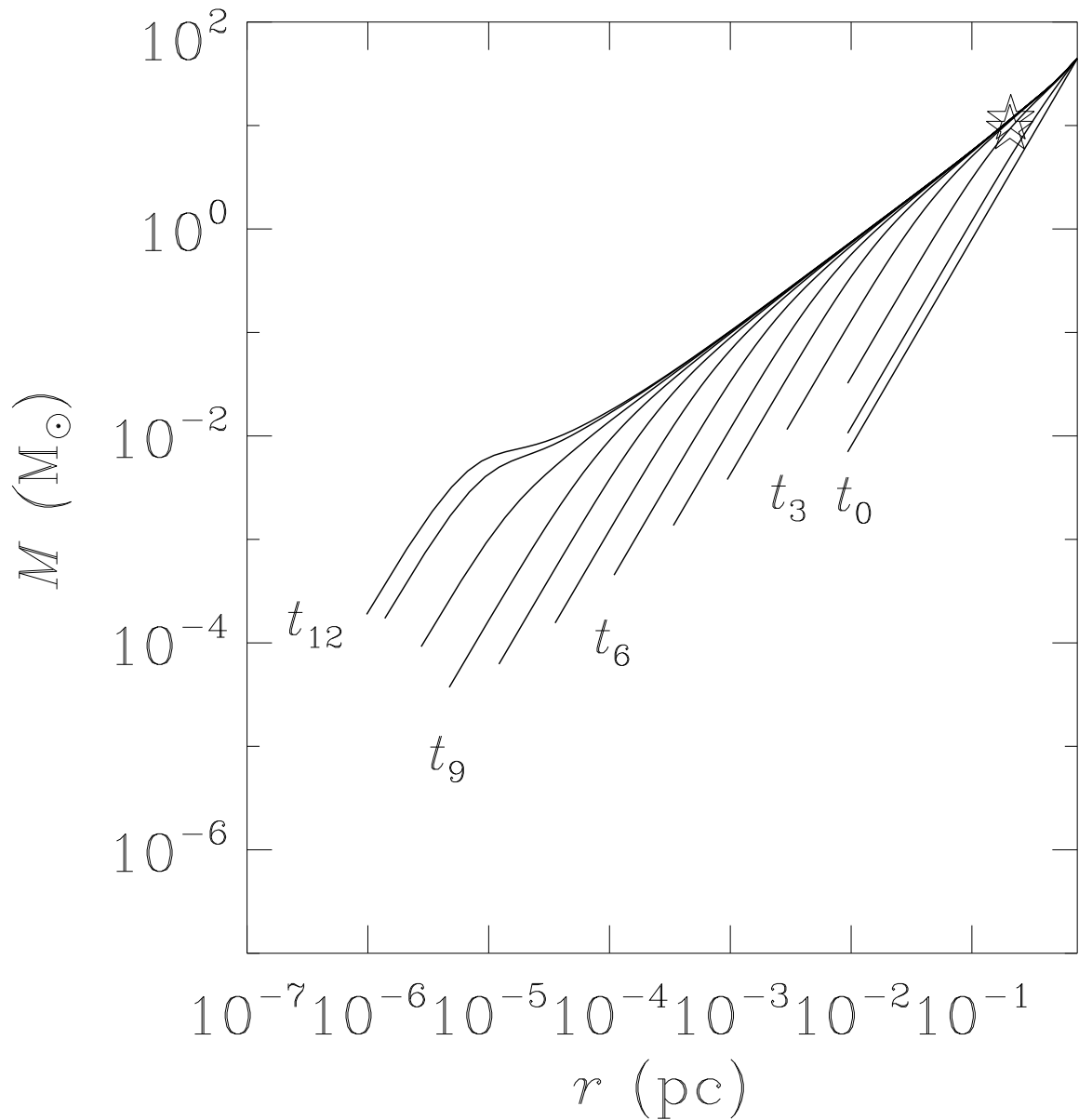


Figure 4.48: Radial profile of the cumulative mass within a (cylindrical) radius r at different times, as in Fig. 4.27. The inner (outer) “star” on a radial profile curve, present only after a supercritical core forms, marks the initial (final) radius of the supercritical core.

static core (or before the hydrostatic core forms), where the geometry is disklike and $\partial \ln M / \partial \ln r \simeq 2 + (1/2)(\partial \ln n_n / \partial \ln r) \approx 0.9$, and inside the hydrostatic core, where the geometry becomes spherical and $\partial \ln M / \partial \ln r \simeq 3 + (\partial \ln n_n / \partial \ln r) \approx -1/3$. For radii less than the instantaneous critical thermal lengthscale, $r \lesssim \lambda_{T,cr}(t)$, thermal-pressure forces smooth out any spatial structure in the density and $\partial \ln n_n / \partial \ln r \simeq 0$. By the end of the run, $\simeq 12 M_\odot$ has accumulated within the magnetically-supercritical core and $\simeq 0.006 M_\odot$ within the hydrostatic core.

Similar behavior is evident in Figure 4.49, which shows radial profiles of the cumulative magnetic flux within a radius r . Note, however, that the clear break in the mass-radius profile at the boundary of the hydrostatic core is hardly evident in the magnetic-flux–radius profile. The magnetic flux does not make the full transition to spherical geometry like the mass does, since the magnetic field is decoupled from every species except the tenuous electron fluid (see Section 4.41). The magnetic flux threading the hydrostatic core is $\approx 5 \times 10^{-5} \mu\text{G pc}^2 \approx 4.8 \times 10^{18} \text{ Wb}$. It is intriguing to note that this is relatively close to the magnetic flux of a typical Ap star such as θ Aurigae, which has a radius $4.5 R_\odot$ and magnetic field strength $B \sim 1 \text{ kG}$, giving a magnetic flux $\sim 3 \times 10^{18} \text{ Wb}$ (van Rensbergen et al. 1984). Ap stars are believed to avoid the convective stage as protostars and so retain the magnetic flux leftover from their formation. Coupled with θ Aurigae’s young age ($\sim 200 \text{ Myr}$), this suggests that its $\sim 1 \text{ kG}$ magnetic field is a fossil field.

The neutral density (Figure 4.27) and velocity (Figure 4.39) profiles are used to calculate the mass infall rate, $\partial M / \partial t$, through any (cylindrical) radius r , which is given in Figure 4.50. The mass infall rate varies considerably both spatially and temporally, a behavior also noted in magnetic calculations by Mouschovias & Morton (1992a,b), Ciolek & Mouschovias (1994), Basu (1997), and Desch & Mouschovias (2001) and in nonmagnetic calculations by Foster & Chevalier (1993). This behavior contrasts sharply with that of the singular isothermal sphere model, which would predict a *constant* and *uniform* mass infall rate of $0.975 C^3/G$ (Shu 1977). (The inclusion of magnetic fields to this model, which

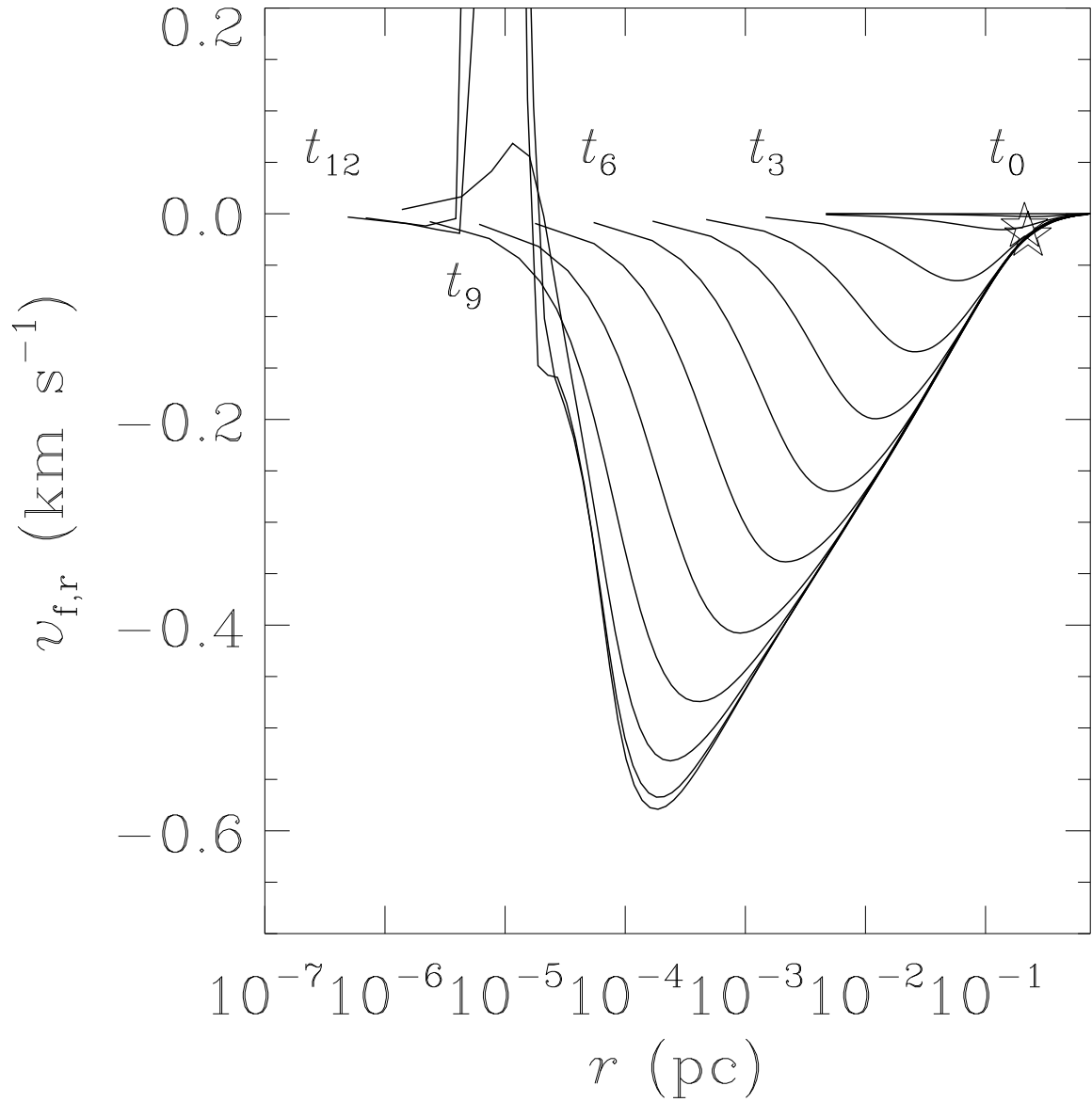


Figure 4.49: Radial profile of the cumulative magnetic flux within a (cylindrical) radius r at different times, as in Fig. 4.27. The inner (outer) “star” on a radial profile curve, present only after a supercritical core forms, marks the initial (final) radius of the supercritical core.

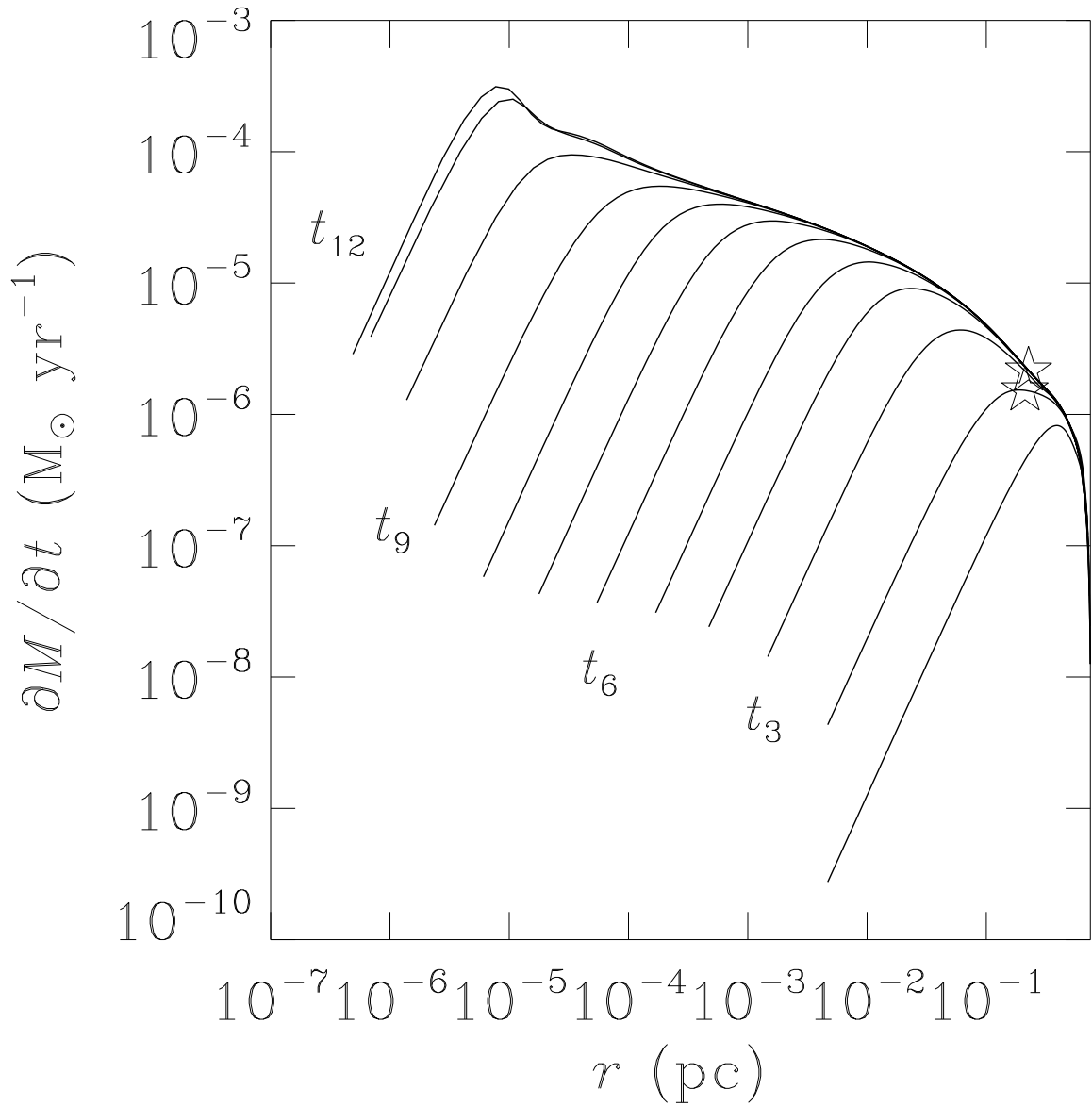


Figure 4.50: Radial profile of the mass infall rate through any (cylindrical) radius r in units of $M_{\odot} \text{ yr}^{-1}$ at different times, as in Fig. 4.27. The inner (outer) “star” on a radial profile curve, present only after a supercritical core forms, marks the initial (final) radius of the supercritical core.

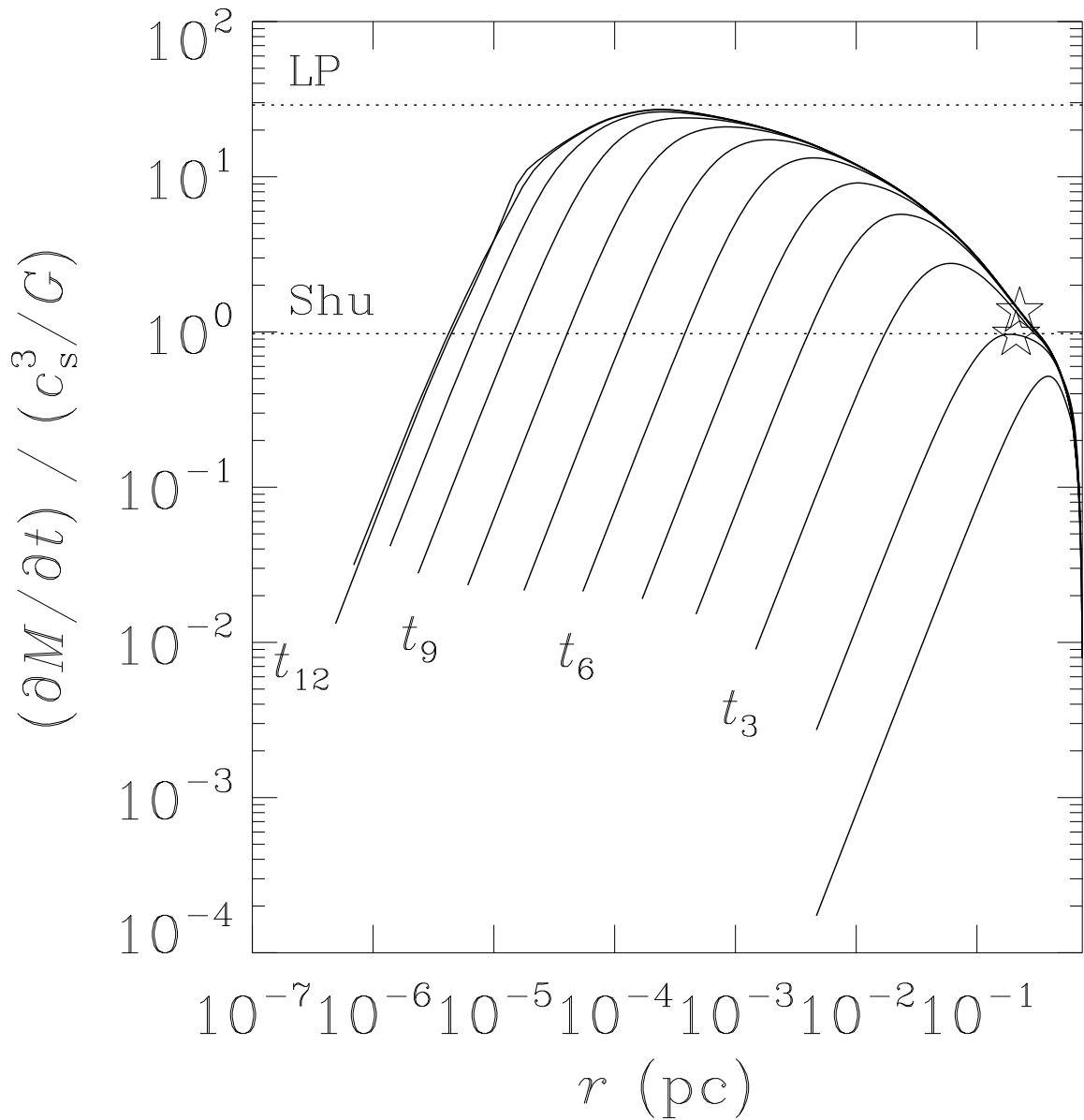


Figure 4.51: Radial profile of the mass infall rate through any (cylindrical) radius r normalized to the *local* value of c_s^3/G at different times, as in Fig. 4.27. The inner (outer) “star” on a radial profile curve, present only after a supercritical core forms, marks the initial (final) radius of the supercritical core. The horizontal dotted lines denote the constant mass infall rates predicted by the Shu (1977) and Larson-Penston (1969) solutions.

results in isothermal toroids, gives a larger but still time-independent and spatially uniform accretion rate — see Li & Shu 1996.)

In order to compare our mass infall rate more quantitatively with those predictions by the various self-similar solutions mentioned throughout this Thesis, we also plot in Figure 4.51 the mass infall rate normalized to c_s^3/G , where c_s is the instantaneous *local* isothermal sound speed in the model cloud. The horizontal dotted lines denote the constant mass infall rates predicted by the Shu (1977) and Larson-Penston (1969) solutions. At the boundary of the magnetically-supercritical core the mass infall rate is initially $1.53 \times 10^{-6} M_\odot \text{ yr}^{-1}$ ($= 0.96 c_s^3/G$), increasing to $2.00 \times 10^{-6} M_\odot \text{ yr}^{-1}$ ($= 1.26 c_s^3/G$) by the end of the run. The *maximum* infall rate is $3.13 \times 10^{-4} M_\odot \text{ yr}^{-1}$ ($= 27.18 c_s^3/G$) and occurs at $r \simeq 1.6 \text{ AU}$. That the early ambipolar-diffusion–controlled phase is characterized by a maximum mass infall rate comparable to the constant mass infall rate predicted by the Shu (1977) solution intuitively makes sense; the Shu (1977) solution was obtained by assuming quasi-static (i.e., negligible velocity) initial conditions, which is similar to the quasistatic (i.e., negligible acceleration) evolution of the early, ambipolar-diffusion–controlled phase that exists before the creation of a magnetically-supercritical core. Likewise, the mass infall rate in the Larson-Penston (1969) solution was obtained by assuming highly dynamical initial conditions, and so it is not surprising that the maximum mass infall rate found in our simulation, which occurs once a point mass (the hydrostatic core) is formed in the central region of the core, is limited by the (spatially-constant) mass infall rate found in the Larson-Penston (1969) solution.

4.4.8 Radiation Flux and Luminosity

Under the FLD approximation, the radiation flux is given by

$$\mathcal{F} = - \left(\frac{c\lambda_{\text{FLD}}}{\chi_{\text{R}}} \right) \nabla \mathcal{E} . \quad (4.4)$$

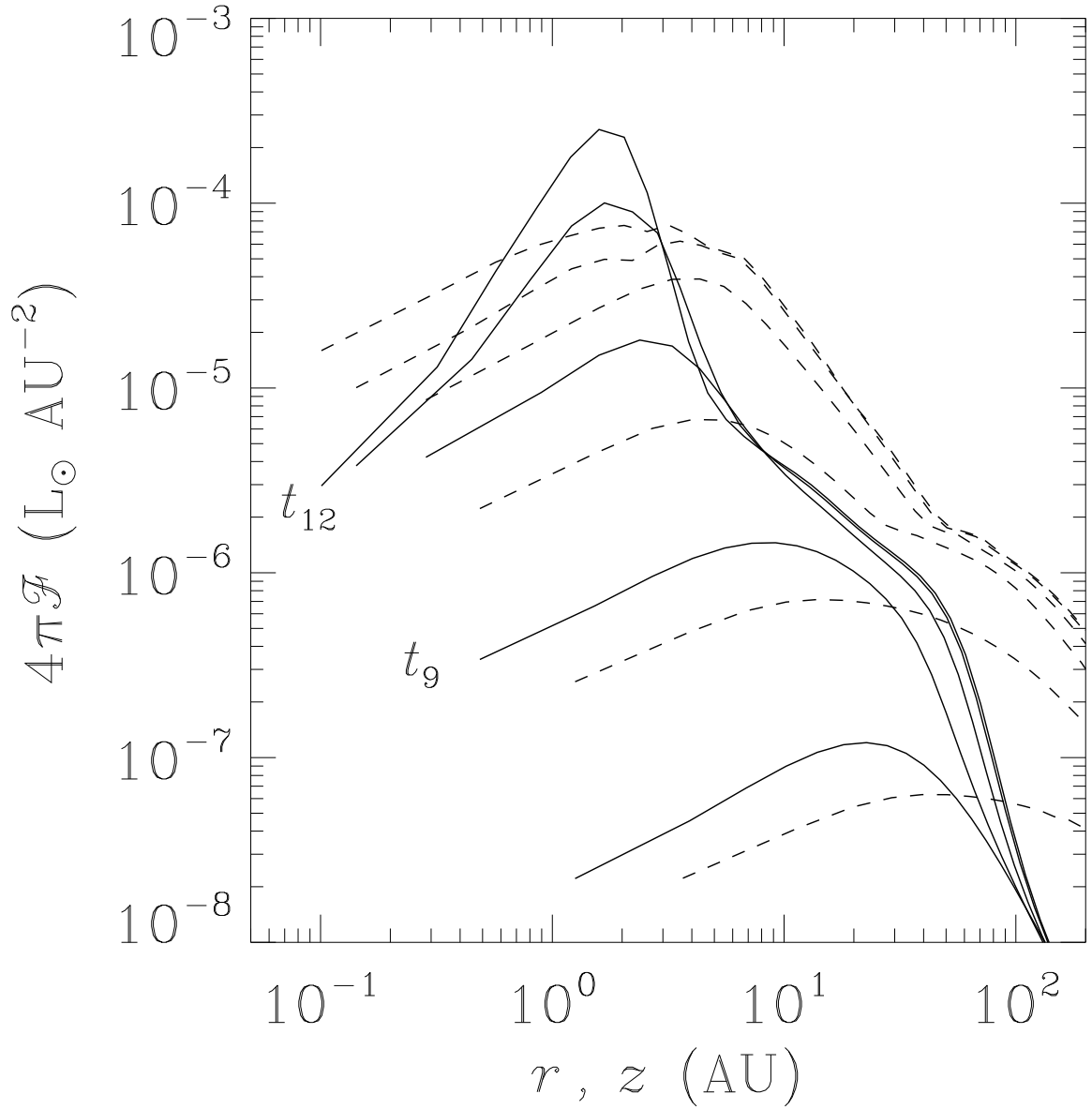


Figure 4.52: Radial midplane (solid line) and vertical symmetry-axis (dashed line) profiles of the radiation flux at different times, as in Fig. 4.27. To ease conversion to luminosity, we have multiplied the flux by 4π and have given it in units of $L_{\odot} \text{ AU}^{-2}$.

In Figure 4.52, we give the r -component of the radiation flux along the midplane (solid line) and the z -component of the radiation flux along the symmetry axis (dashed line). To ease conversion to luminosity,

$$L(z) = z^2 \oint \mathcal{F}(z, \theta) \cdot \hat{z} \, d\Omega, \quad (4.5)$$

in the figure we have multiplied the flux by 4π and given it in units of $L_{\odot} \text{ AU}^{-2}$. (To obtain the luminosity at the hydrostatic core boundary in L_{\odot} , simply multiply the value of the plotted quantity evaluated at $r \simeq 2 \text{ AU}$ by $\simeq 2^2$.) The radiation flux is substantially larger along the symmetry axis than along the midplane, because there is much less absorbing material in the former direction than the latter. Near the boundary of the hydrostatic core the two profiles attain a similar maximum $\simeq 2.5 \times 10^{-4} L_{\odot} \text{ AU}^{-2}$, corresponding to a luminosity $\simeq 10^{-3} L_{\odot}$.

Chapter 5

Parameter Study

5.1 Introduction

It is important to investigate the sensitivity of the above results to variations in the relevant free parameters of the problem, of which three are poorly constrained either observationally or experimentally: the initial mass-to-flux ratio of the parent molecular cloud, the grain size distribution, and the relative abundance of the short-lived yet extremely potent radionuclide ^{26}Al .

Tassis & Mouschovias (2007c) presented results from a parameter study that used numerical simulations to follow the detailed evolution of magnetic molecular cloud cores up to densities $\approx 10^{14} - 10^{16} \text{ cm}^{-3}$ under the assumption of an isothermal and/or piece-wise adiabatic equation of state. They showed that memory of the initial mass-to-flux ratio is completely lost at late times. By now, it is well known that the principal consequence of a larger (smaller) initial mass-to-flux ratio is to shorten (lengthen) the timescale for the formation of a magnetically-supercritical core (e.g., Ciolek & Basu 2001). While there are some small quantitative differences between simulations with varying initial mass-to-flux ratios (see Tassis & Mouschovias 2007c, § 3), the extreme demand of computer time required to produce a suitable μ_0 parameter study currently precludes this endeavor. Hence, we find it unnecessary to vary the initial mass-to-flux ratio as part of our parameter study at this time.

Grain size distributions in protostellar disks are notoriously difficult to constrain observationally (see, e.g., the introduction in McCabe et al. 2003). Analysis of spectral energy

distributions from disks has suggested that both grain growth and the settling of large grains to the disk midplane do, in fact, occur (Furlan et al. 2006). However, the degree of grain growth and settling varies widely across different circumstellar environments. Unfortunately, computational time constraints prevent a systematic study of the effects of various initial grain size distributions on our results at the moment. In a future publication, we will present results from a simulation that replaces our assumption of a single grain size with an MRN distribution of grain sizes.

For now, we focus only on the sensitivity of our results to the possible presence of ^{26}Al . While ^{26}Al is a powerful radioactive ionization source ($\zeta_{26} = 1.94 \times 10^{-19} \text{ s}^{-1}$), the fact that it is relatively short-lived compared with ^{40}K (half-life 0.716 Myr vs. 1.25 Gyr) suggests that it may only become important if the initial mass-to-flux ratio of the parent molecular cloud is relatively close to critical (so that the evolution is rapid) or if the core happens to become enriched because of a nearby Supernova explosion (e.g., Looney et al. 2006, Ouellette et al. 2007 — but see also Williams & Gaidos 2007 and Boss et al. 2008 for two different points of view). In the next section we compare the results discussed in Chapter 4 with those of a simulation in which ^{26}Al is assumed to dominate the high-density ionization rate.

5.2 ^{26}Al as an Alternative Radionuclide

Figures 5.1 and 5.2 are, respectively, the ^{26}Al -analogues of Figures 4.21 and 4.22, showing the evolution of quantities related to the chemistry as functions of central density: the ionization rate at the center of the cloud, ζ_c , due to all processes (UV radiation, cosmic rays, and radioactive decays) and the central abundances of different species, $x_{s,c} \equiv n_{s,c}/n_{n,c}$ (where $s = e, i, g_-, g_0, g_+$). The plateau reached by the ionization rate at high densities in the ^{26}Al model occurs at a value more than three orders of magnitude larger than in the ^{40}K model. As a result, the degree of ionization and the chemical abundances of all charged

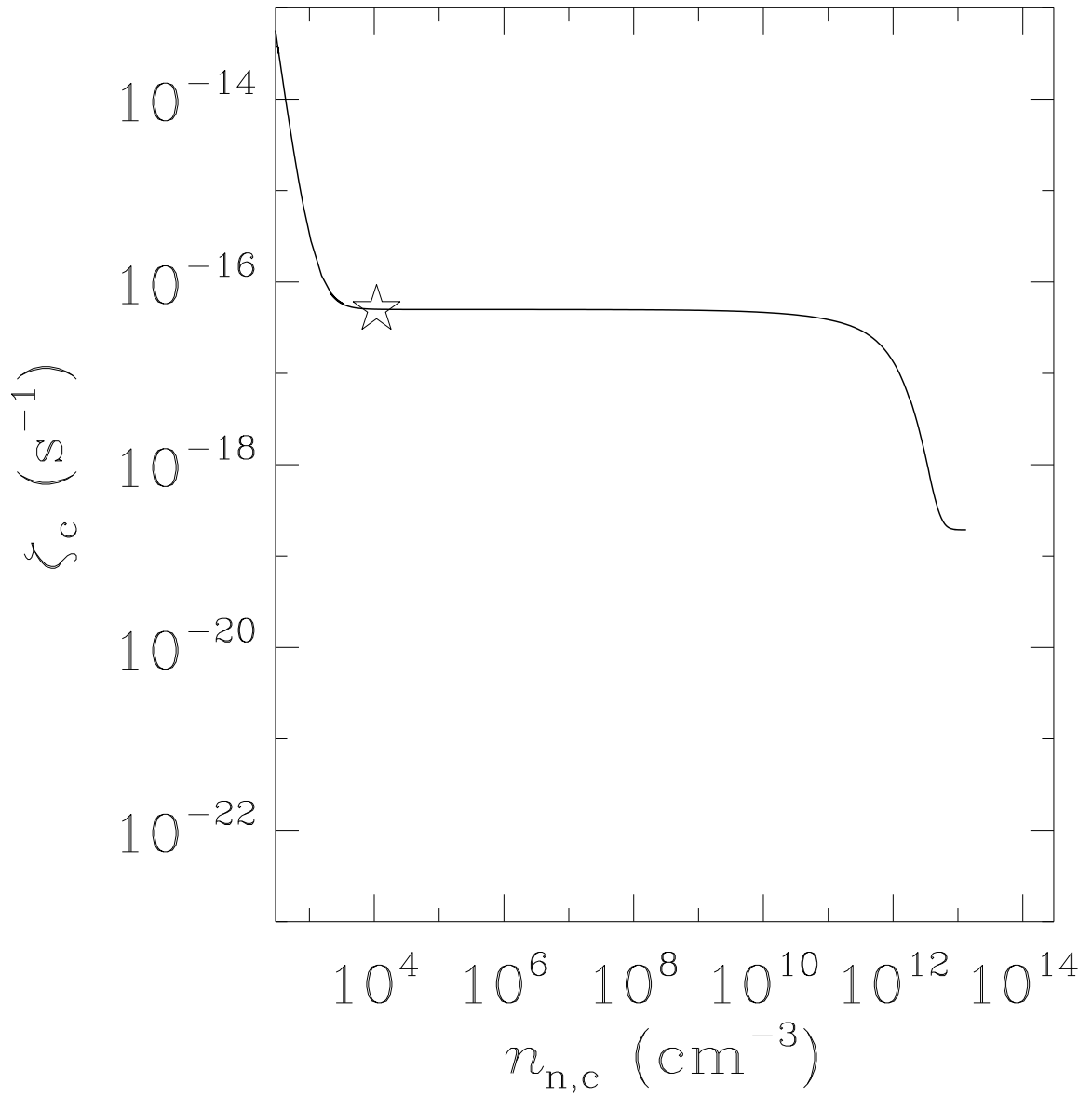


Figure 5.1: ^{26}Al as the dominant radionuclide. Evolution of the central ionization rate due to all processes (UV radiation, cosmic rays, and radioactive decays) as a function of the central number density of neutrals, $n_{n,c}$. The “star” marks the time at which a supercritical core forms.

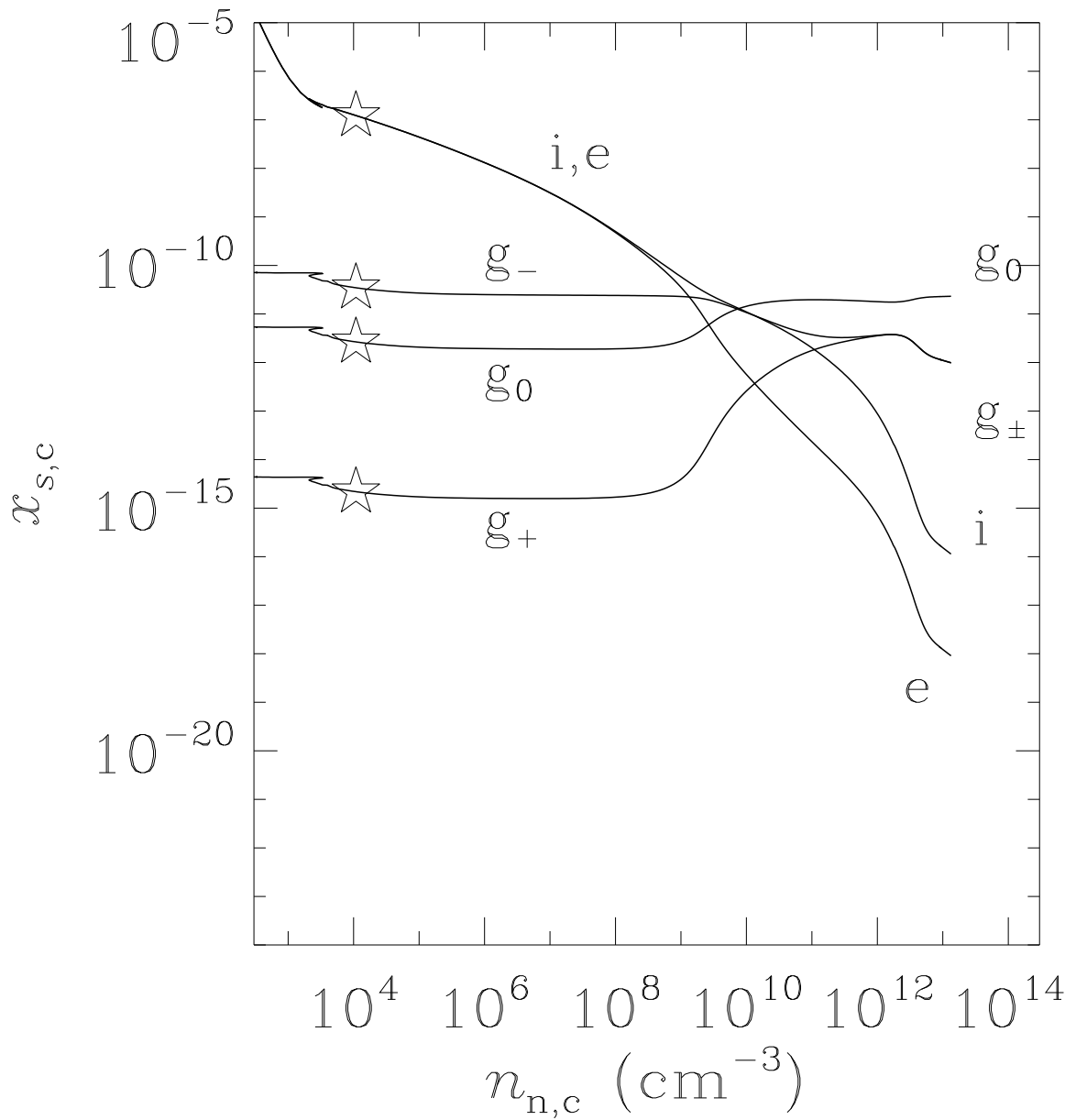


Figure 5.2: ^{26}Al as the dominant radionuclide. Evolution of the central abundances of species x_s (where $s = e, i, g_-, g_0, g_+$) as functions of the central number density of neutrals, $n_{n,c}$. The “star” marks the time at which a supercritical core forms.

species are significantly greater at high densities.

The larger abundances of ions and electrons have important effects on quantities related to the magnetic conductivity of the gas, which are given in Figures 5.3 – 5.6 as functions of central density. The magnetic diffusion coefficients related to ambipolar diffusion (AD), Ohmic dissipation (OD), and the Hall effect (H) are shown in Figure 5.3. While Ohmic dissipation becomes increasingly more important at high densities, ambipolar diffusion remains the dominant magnetic diffusion mechanism. This is reinforced in Figure 5.7, which shows the radial midplane profiles of the ratio of the ambipolar-diffusion and Ohmic-dissipation resistivities.

In Figure 5.4, we show the parallel (\parallel), perpendicular (\perp), and Hall (H) conductivities. Figures 5.5 and 5.6 show the fraction of the parallel and perpendicular conductivities, respectively, carried by each species. (Absolute values have been taken; the cusps in the positive grain curves are due to the conductivity passing through zero as it changes sign.) The larger electron abundances ensures that the electrons continue to dominate the parallel conductivity. However, the grains still dominate the perpendicular conductivity (and therefore the electric current) for central densities $\gtrsim 3 \times 10^{12} \text{ cm}^{-3}$, though by an appreciably smaller percentage of the total current.

All other quantities remained practically unchanged from their values given in Chapter 4. This is because (1) the magnetic field is largely decoupled from the gas by the time an ionization floor due to radioactivity is established and (2) the temperature evolution is independent of the ionization rate at these late times.

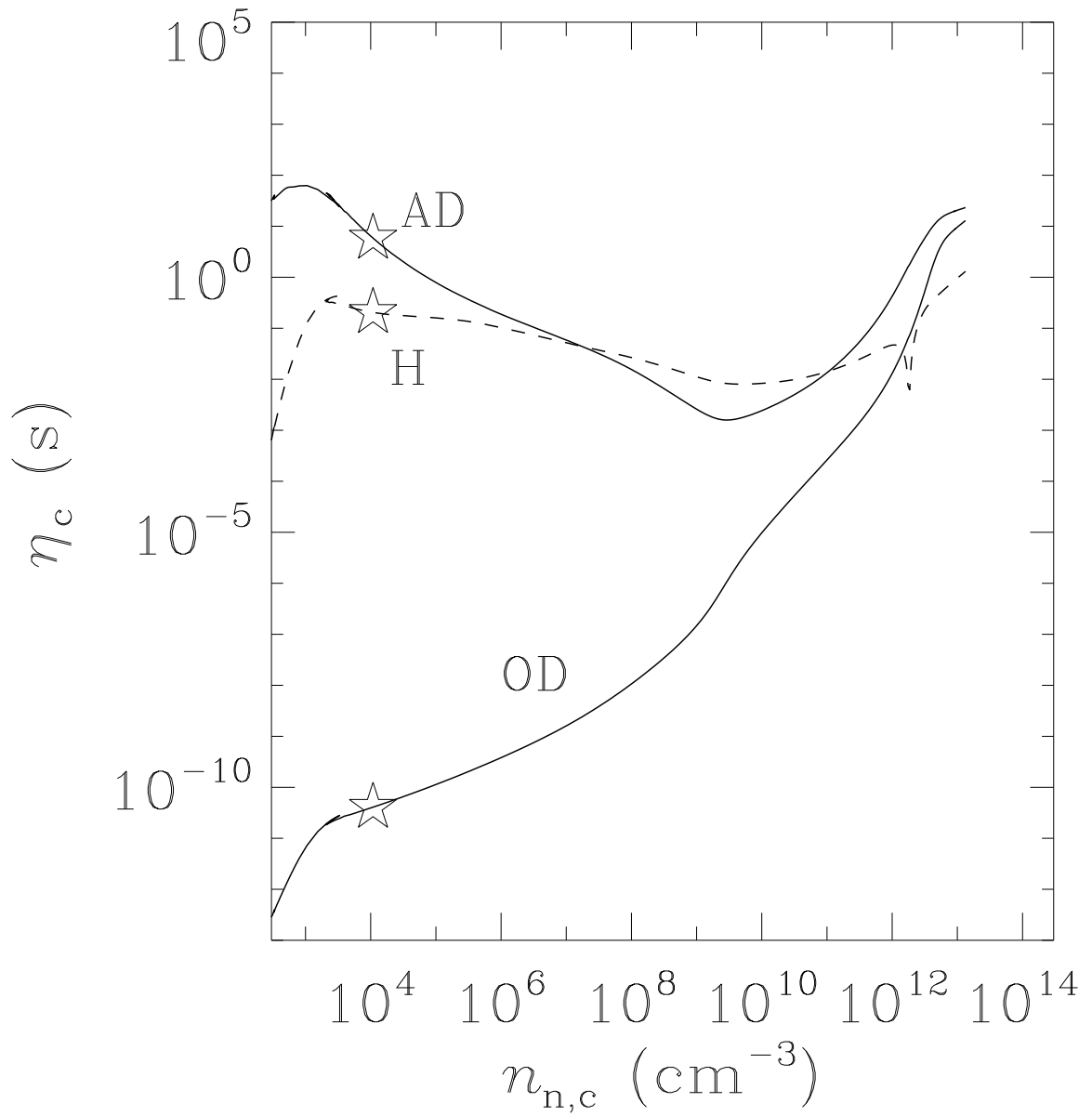


Figure 5.3: ^{26}Al as the dominant radionuclide. Evolution of the central magnetic resistivities associated with ambipolar diffusion (AD), Ohmic dissipation (OD), and the Hall effect (H) as functions of the central number density of neutrals, $n_{n,c}$. The "star" marks the time at which a supercritical core forms.

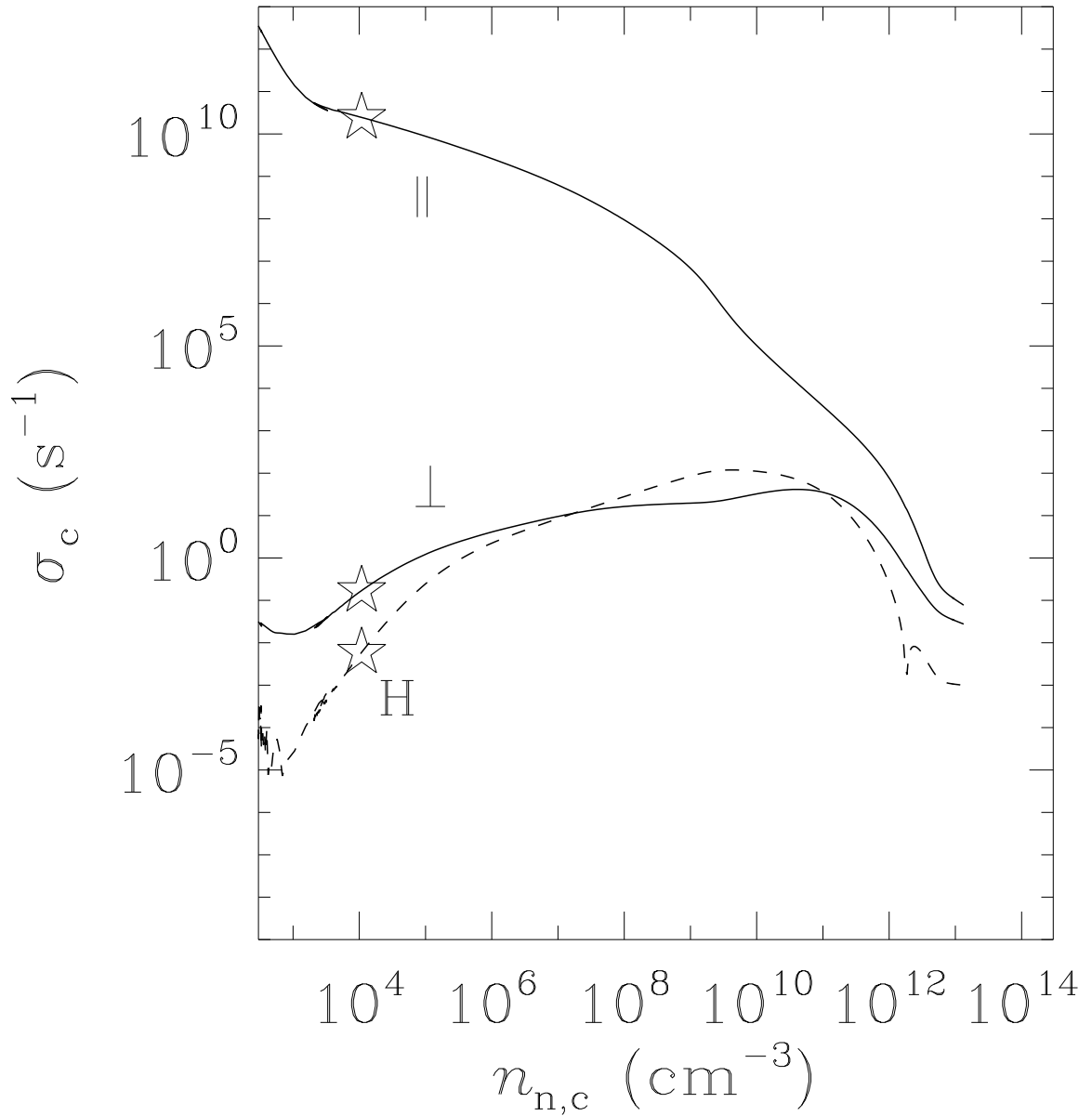


Figure 5.4: ^{26}Al as the dominant radionuclide. Evolution of the central parallel (\parallel), perpendicular (\perp), and Hall (H) magnetic conductivities as functions of the central number density of neutrals, $n_{n,c}$. The "star" marks the time at which a supercritical core forms.

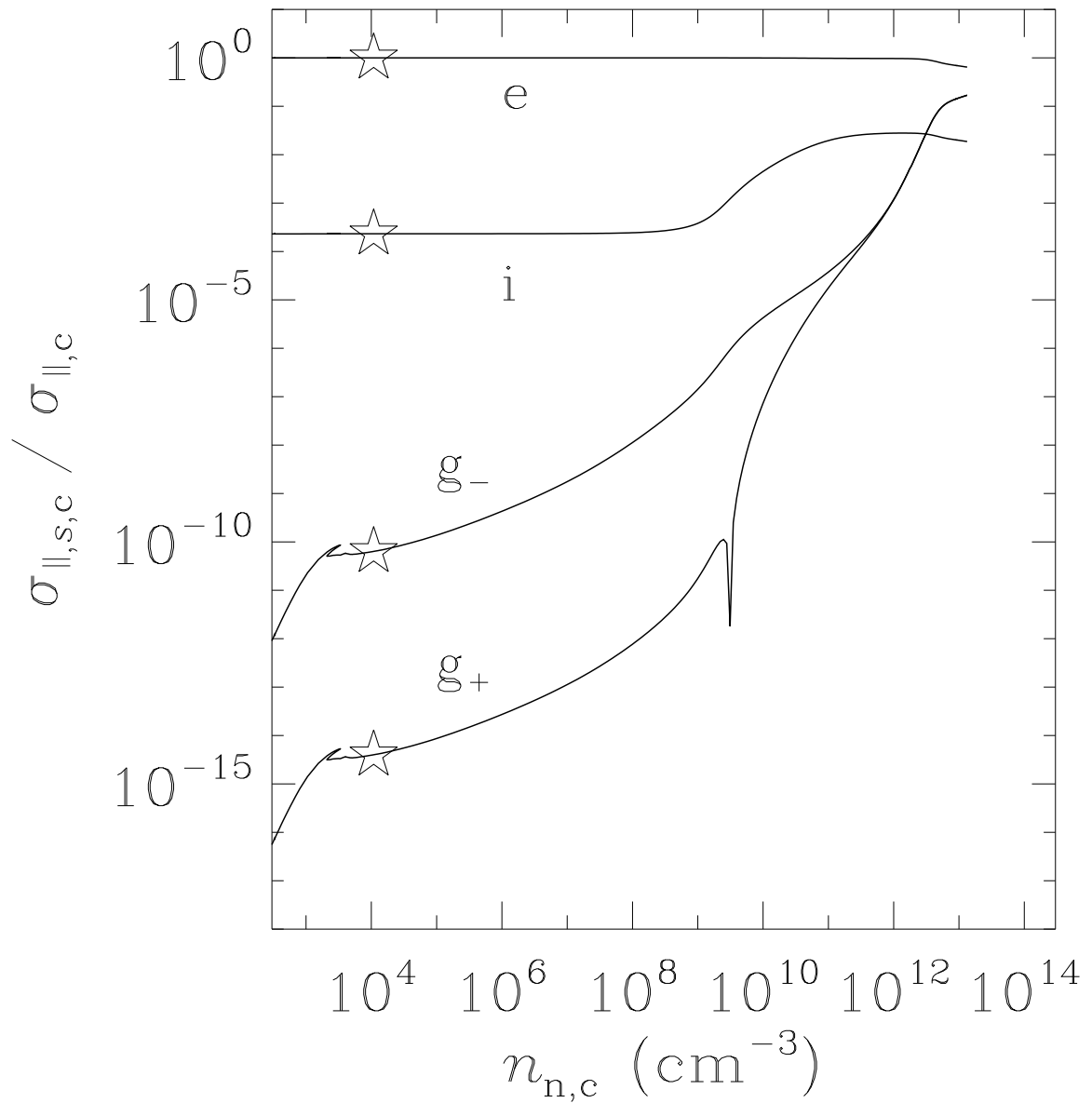


Figure 5.5: ^{26}Al as the dominant radionuclide. Evolution of the fraction of the central parallel magnetic conductivity carried by each species as a function of the central number density of neutrals, $n_{n,c}$. The "star" marks the time at which a supercritical core forms.

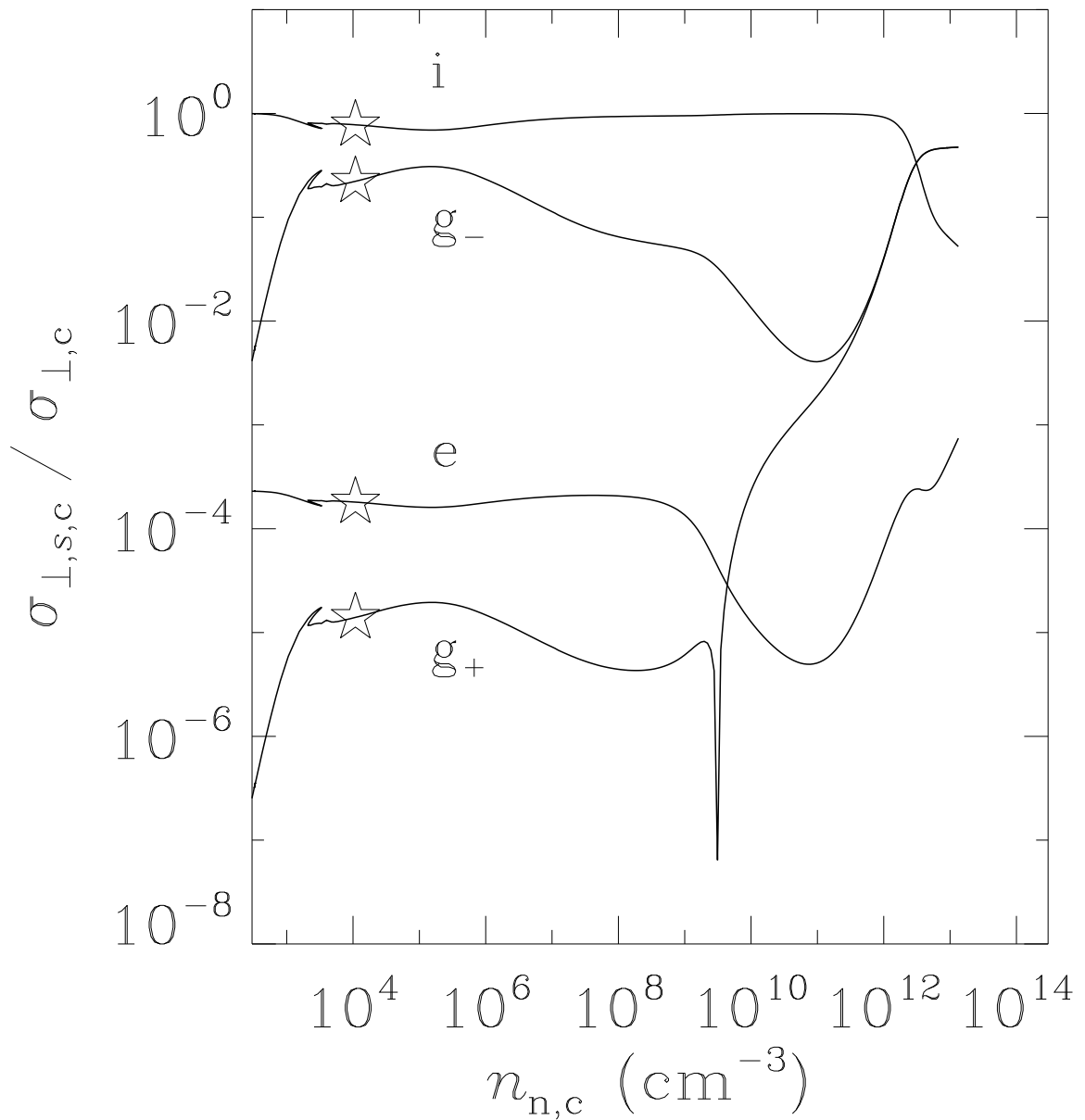


Figure 5.6: ^{26}Al as the dominant radionuclide. Evolution of the fraction of the central perpendicular magnetic conductivity carried by each species as a function of the central number density of neutrals, $n_{n,c}$. The "star" marks the time at which a supercritical core forms.

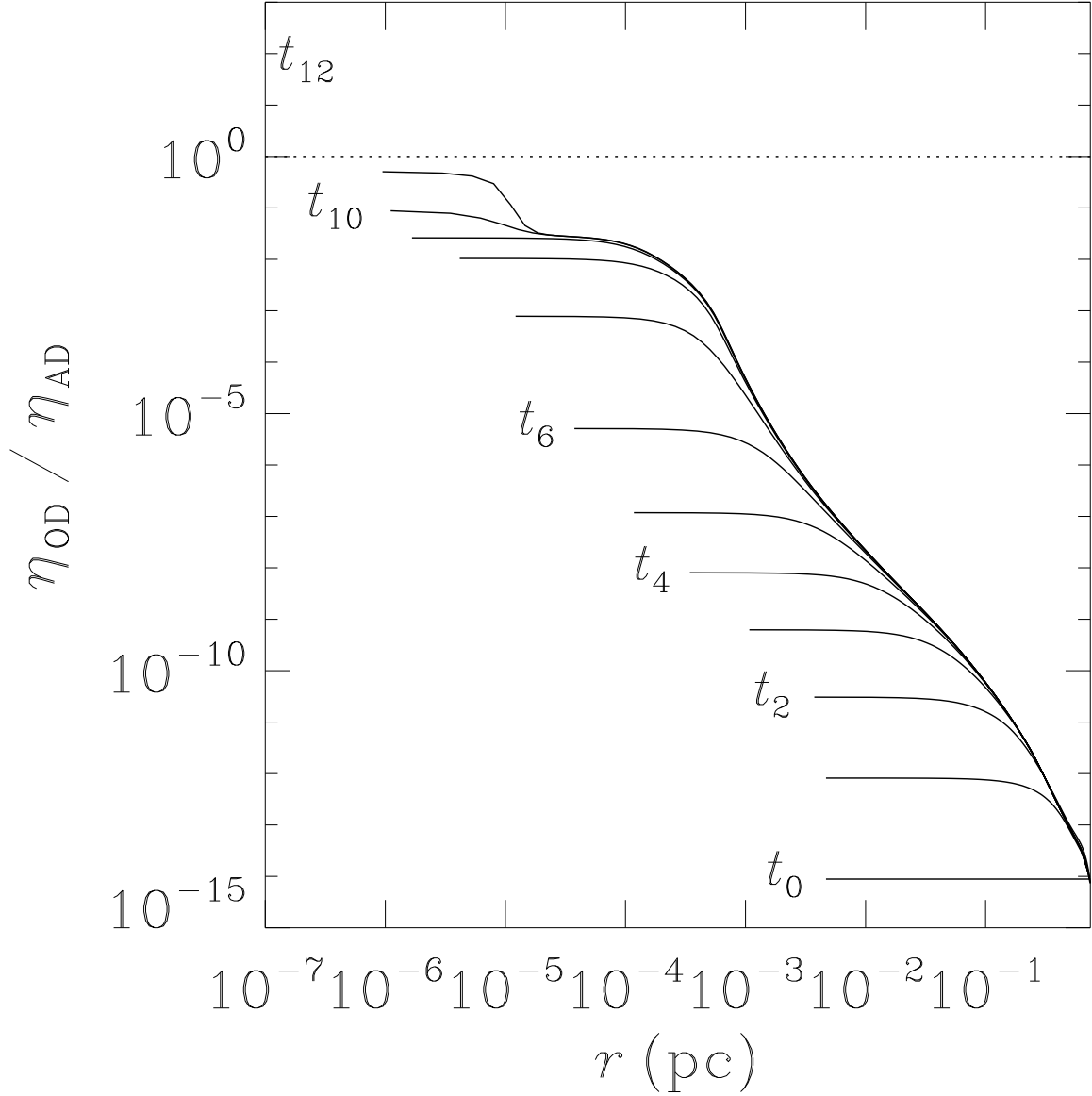


Figure 5.7: ^{26}Al as the dominant radionuclide. Radial midplane profiles of the ratio of Ohmic and ambipolar resistivities. The dotted line denotes the boundary when ambipolar diffusion and Ohmic dissipation become equally important magnetic diffusion mechanisms. Above (below) this line, Ohmic dissipation (ambipolar diffusion) dominates. Different curves correspond to different times, as in Fig. 4.27.

Chapter 6

Summary

We can now add to the evolutionary picture laid down at the close of Chapter 1. In an initially magnetically-subcritical cloud, ambipolar diffusion allows the neutrals to contract quasistatically via their own self-gravity through nearly-stationary magnetic field lines, redistributing the amount of mass in the central flux tubes of the cloud. Once the neutral infall creates a central region with a critical mass-to-flux ratio (at a central neutral number density $\simeq 10^4 \text{ cm}^{-3}$ under the conditions investigated in this Thesis), it begins to collapse more rapidly than its surroundings and is referred to as a supercritical core. The supercritical core evolves dynamically (though slower than free-fall) under near flux-freezing, until the resurrection of ambipolar diffusion causes magnetic decoupling to set in at a density $\approx 10^{10} \text{ cm}^{-3}$ and gradually, over several orders of magnitude, completely detach all but the electrons from the magnetic field. Dust grains play a crucial role in the evolution of both the cloud and the core, and by the time these densities are reached, the grains are largely responsible for the electric charge of the gas, despite the fact that most grains are charge-neutral. Perhaps more surprising, however, is the fact that the grains also carry the electric *current* for densities $\gtrsim 3 \times 10^{12} \text{ cm}^{-3}$. These densities are comparable to those for which Ohmic dissipation dominates ambipolar diffusion ($\gtrsim 7 \times 10^{12} \text{ cm}^{-3}$), which occurs in a central region of size $\approx 2 \text{ AU}$.

Once magnetic decoupling has effectively removed any ties between the bulk plasma and the magnetic field, the magnetic field is no longer dragged inwards, magnetic flux piles up at a radius of $\approx 10 \text{ AU}$, and a magnetic wall is formed. Inside this radius, the magnetic field becomes spatially uniform with a strength $\approx 0.2 \text{ G}$. Given the fact that the magnetic

field is completely unaffected by the motion of gas through it at these densities and on these lengthscales, it is not unreasonable to surmise that the protoplanetary disk that will eventually form will be exposed to a uniform magnetic field strength of ≈ 0.2 G. It may be no coincidence, therefore, that measurements of the remnant magnetization in meteorites imply magnetic fields in the early solar nebula of strength $\approx 0.1 - 0.2$ G.

Magnetic fields are also responsible for quickly establishing and maintaining a disk-like geometry all the way down to radial lengthscales on the order of 10 AU, inside of which thermal-pressure effects become important. This provides a natural explanation for observations of star-forming cores, such as L1551-IRS5, that reveal a disk-like geometry over a broad range of lengthscales.

Throughout the entire collapse phase, the liberated gravitational energy escapes from the gas only as efficiently as allowed by the dust grains, which are largely responsible for the opacity at temperatures $\lesssim 1500$ K. While the gas remains strictly isothermal only for central densities $\lesssim 10^7$ cm $^{-3}$, the temperature does not exhibit an appreciably rapid increase until densities $\approx 10^{11}$ cm $^{-3}$ are attained in the core. A central temperature of 100 K is reached when the central density $\simeq 6 \times 10^{12}$ cm $^{-3}$. For the densities considered in this Thesis ($\lesssim 10^{14}$ cm $^{-3}$), the gas never evolves adiabatically.

The dramatic temperature increase inside ≈ 4 AU leads to the formation of a hydrostatic core, in which approximate balance is achieved between thermal-pressure and gravitational forces. At the boundary of the hydrostatic core ($\simeq 2$ AU), there are prominent shocks, particularly along the vertical symmetry axis where velocities rapidly decrease from ≈ -1.2 km s $^{-1}$ to zero in only ≈ 8 AU. This abrupt deceleration causes the gas to rebound from overshooting hydrostatic force balance and subsequently oscillate about the equilibrium. Rapid Ohmic dissipation causes the magnetic field lines inside the hydrostatic core to move outwards, halting only at the location of the magnetic wall caused by ambipolar diffusion. A simple extrapolation of temperature based on our results indicates that a temperature of 1000 K will not be reached until a central density $\approx 3 \times 10^{15}$ cm $^{-3}$.

Therefore, the recoupling of the gas to the magnetic field, via thermal ionization and grain sublimation, will most likely not occur until central densities of at least several $\times 10^{15} \text{ cm}^{-3}$ are attained.

At the end of the calculation, the mass and magnetic flux in the hydrostatic core are $0.006 M_{\odot}$ and $5 \times 10^{-5} \mu\text{G pc}^2$, respectively. The mass-to-flux ratio in the central flux tube is $\simeq 80$ times the critical central value for collapse. The luminosity at the hydrostatic core boundary is $\simeq 10^{-3} L_{\odot}$. The mass infall rate is highly nonhomologous and time-dependent, rising from $\sim c_s^3/G$ at the boundary of the magnetically-supercritical core to a maximum value $\sim 27c_s^3/G$ at a radius of $\simeq 1.6 \text{ AU}$, near the boundary of the hydrostatic core. The quantitative similarity between the latter value and the (spatially constant) mass infall rate associated with the Larson-Penston-Hunter self-similar hydrodynamic collapse solution is no coincidence. By the time a spherical hydrostatic core is formed in our simulations, the infall velocities are dynamic and the magnetic field has largely decoupled from the gas.

In order to assess the relevancy of these calculations to actual star-forming molecular clouds and cores, a number of steps are being taken as this Thesis is being written. For example, we are currently collaborating with Professor Leslie Looney and his graduate student Hsin-Fang Chiang to perform synthetic interferometric observations of our simulations for comparison with 1 and 3 mm data of Class 0 sources from the Combined Array for Research in Millimeter Astronomy (CARMA). Simulation images will be convolved with the synthesized beam, multiplied by the primary beam attenuation, Fourier transformed into visibilities, and sampled with the same $u - v$ coverage as the observations themselves. Our simulations are also amenable to 7 mm studies once the Extended Very Large Array (EVLA) comes online in 2010. Another avenue that is currently being explored is the calculation of synthetic SEDs for quantitative comparison with observations of Class -I and Class 0 YSOs. Radiation from grains is responsible for the excess infrared and millimeter emission; grain density and temperature distributions are therefore important inputs to any SED calculation. These quantities are generated self-consistently by the simula-

tions presented in this Thesis. The construction of synthetic prestellar SEDs is particularly timely, since the Herschel Space Observatory will be the only space facility dedicated to the far-infrared and sub-millimeter part of the spectrum. In fact, prestellar SEDs peak in the *Herschel* “prime” band.

Despite a concerted effort to treat the nonisothermal stage of magnetic star formation as rigorously as possible, there still remains a great deal of work to be done, including both improvements to and extensions of what has already been accomplished for this Thesis. While much of this work deserves the undivided attention of a future graduate student or postdoctoral researcher of star formation theory, we outline here a few possibilities and give some idea of their feasibility.

First, dust coagulation ought to be computed in a time-dependent fashion. Unfortunately, the exact details of how and even when grain growth occurs in protostellar cores and disks are poorly constrained both experimentally and observationally. Due to recent improvements in instrumentation, however, observational prospects are becoming increasingly auspicious. A recent comprehensive study of the circumstellar disk surrounding the T Tauri star IM Lupi using photometry, spectroscopy, millimeter interferometry, and multi-wavelength imaging has obtained *quantitative* evidence of dust evolution in the disk (Pinte et al. 2008). The details may not be so essential, however, since the effect of grain size on the temperature evolution ought to be minimal, at least for the range of densities studied here; different grain sizes share roughly the same opacity for temperatures less than ≈ 400 K. On the other hand, the strength of the magnetic field at decoupling is a sensitive function of grain size (e.g., Desch & Mouschovias 2001). One possible way to circumvent the uncertainties of grain growth, at least at the present time, would be to adopt a nonuniform grain size distribution (such as the MRN distribution) and rerun the numerical simulations undertaken for this Thesis. As is evident from the discussion in Section 2.4.2, we have already modified the Zeus-MP code to handle such a distribution and preliminary code testing has begun.

Second, a relatively straightforward improvement that can be made to the numerical code used in this Thesis would be to upgrade the radiative transfer module from one that uses the grey FLD approximation to one that uses a multi-group FLD approximation. Rather than average radiation properties over the entire frequency spectrum, multi-group methods sort frequencies into different frequency bins, so that quantities associated with radiation are only averaged over the (much smaller) bin width. In some sense, it is a compromise between a grey calculation and a full frequency-dependent calculation, which is currently unrealizable.

Third, while the neglect of rotation was justifiably ignored in this Thesis, any calculation that endeavors to journey further along in the evolution of a protostellar core must include rotation. This would require modifying our numerical code to include both magnetic braking and Hall electromotive forces. The inclusion of rotation is particularly important to deciphering the formation and evolution of protoplanetary disks, including whether such disks form as the result of laminar contraction of disk-like clouds or by outward turbulent transfer of angular momentum. The answer to this question rests precariously on the presently-unknown strength and topology of protoplanetary disk magnetic fields. For example, magnetorotational instabilities (Balbus & Hawley 1991; Blaes & Balbus 1994; Jin 1996; Gammie 1996; Glassgold et al. 1997; Igea & Glassgold 1999; Wardle 1999; Sano & Miyama 1999; Sano et al. 2000; Balbus & Terquem 2001; Fleming & Stone 2003; Kunz & Balbus 2004; Salmeron & Wardle 2005; Fromang & Nelson 2006; Wardle 2007; Turner et al. 2007) and/or nonideal MHD shear instabilities (Kunz 2008) may be important for outward angular momentum transport within protoplanetary disks, provided that the magnetic field is sufficiently weak and not *too* decoupled from the gas to allow the instabilities to grow on a dynamical timescale. On the other hand, bipolar outflows and disk winds, which are thought to transport angular momentum away from disks, may be due in part to strong magnetic fields (Blandford & Payne 1982; Königl 1989; Wardle & Königl 1993; Shu et al. 1994; Li 1996; Salmeron et al. 2007). Determining which of these mechanisms dominates

the transport of angular momentum in protoplanetary disks is one of the most important unsolved problems in star and planet formation.

Finally, while there is a large body of work on star formation, very few studies attempt to unite what we already know about the star-formation process with current investigations into the physics of protoplanetary accretion disks. Disk studies often begin *in medias res*, using well-known physics to evolve the system from a more uncertain initial state. Recent advances in star formation calculations, including the ones presented in this Thesis, are enabling *ab initio* protostellar accretion disk studies to become feasible. There are already a few testaments to the promises of such an approach. For example, Dullemond et al. (2006) constructed a simple model of disk formation and evolution from collapsing star-forming cores. While this model relies upon an ad-hoc α -viscosity prescription to model angular momentum transport within the disk, it naturally reproduces the observed relation between the mass accretion rate and the stellar mass, $\dot{M}_{\text{acc}} \propto M_*^{1.8}$ (e.g., Natta et al. 2006). Vorobyov & Basu (2007) followed the hydrodynamics of a non-axisymmetric gravitating protostellar accretion disk (in the thin-disk approximation) that was formed self-consistently by simulating the collapse of a molecular cloud core. A subsequent paper by the same authors (Vorobyov & Basu 2008) studied the disk dynamics during the T Tauri phase, also finding considerable agreement with observations. Nevertheless, realistic models for *magnetic* protostellar accretion disks that self-consistently account for their formation do not presently exist.

Unfortunately, other than the possible inclusion of rotation and an MRN grain size distribution, all these improvements and extensions either will have to be attacked semi-analytically or must wait until future developments in computer hardware (e.g., NCSA's Blue Waters) or software (e.g., a fully-implicit nonideal RMHD code) render more rigorous calculations feasible. This is the price we pay for working in a field where so many nonlinear processes converge at once to produce what may otherwise be considered a relatively common occurrence and so taken for granted by anyone who has ever stared into the

night sky.

*So eine Arbeit wird eigentlich nie fertig,
man muß sie für fertig erklären,
wenn man nach Zeit und Umständen
das Möglichste getan hat.*

Such a work is actually never finished;
one must declare it finished
when, given time and circumstances,
one has done all that is possible.

Johann Wolfgang von Goethe, *Italienische Reise* (1787)

Appendix A

Rate Coefficients

For radiative recombination of atomic ions and electrons, $\alpha_{\text{rr}} = 2.8 \times 10^{-12} (300 \text{ K}/T)^{0.86} \text{ cm}^3 \text{ s}^{-1}$; for the dissociative recombination of electrons and HCO^+ ions, $\alpha_{\text{dr}} = 2.0 \times 10^{-7} (300 \text{ K}/T)^{0.75} \text{ cm}^3 \text{ s}^{-1}$ (Umebayashi & Nakano 1990). The rate coefficient adopted for charge exchange reactions between atomic and molecular ions is $\beta = 2.5 \times 10^{-9} \text{ cm}^3 \text{ s}^{-1}$ (Watson 1976).

The rate coefficients involving gas-phase species and grains are taken from Spitzer (1941, 1948), with refinements made by Draine & Sutin (1987) to account for the polarization of grains:

$$\alpha_{\text{ego}} = \pi a^2 \left(\frac{8k_{\text{B}}T}{\pi m_{\text{e}}} \right)^{1/2} \left[1 + \left(\frac{\pi e^2}{2ak_{\text{B}}T} \right)^{1/2} \right] \mathcal{P}_{\text{e}}, \quad (\text{A.1})$$

$$\alpha_{\text{igo}} = \pi a^2 \left(\frac{8k_{\text{B}}T}{\pi m_{\text{i}}} \right)^{1/2} \left[1 + \left(\frac{\pi e^2}{2ak_{\text{B}}T} \right)^{1/2} \right] \mathcal{P}_{\text{i}}, \quad (\text{A.2})$$

$$\alpha_{\text{eg}+} = \pi a^2 \left(\frac{8k_{\text{B}}T}{\pi m_{\text{e}}} \right)^{1/2} \left[1 + \left(\frac{e^2}{ak_{\text{B}}T} \right) \right] \left[1 + \left(\frac{2}{2 + (ak_{\text{B}}T/e^2)} \right)^{1/2} \right] \mathcal{P}_{\text{e}}, \quad (\text{A.3})$$

$$\alpha_{\text{ig}-} = \pi a^2 \left(\frac{8k_{\text{B}}T}{\pi m_{\text{i}}} \right)^{1/2} \left[1 + \left(\frac{e^2}{ak_{\text{B}}T} \right) \right] \left[1 + \left(\frac{2}{2 + (ak_{\text{B}}T/e^2)} \right)^{1/2} \right] \mathcal{P}_{\text{i}}. \quad (\text{A.4})$$

The sticking probabilities of electrons or ions onto grains, denoted \mathcal{P}_{e} and \mathcal{P}_{i} , are assigned the values 0.6 and 1.0, respectively (Umebayashi 1983). Other quantities in these equations have their usual meanings.

The rate coefficients for charge transfer between charged grains are given by

$$\alpha_{g_+^\alpha g_-^{\alpha'}} = \pi a_{\text{sum}}^2 \left(\frac{8k_B T}{\pi m_{\text{red}}} \right)^{1/2} \left[1 + \left(\frac{e^2}{a_{\text{sum}} k_B T} \right) \right] \left[1 + \left(\frac{2}{2 + (a_{\text{sum}} k_B T / e^2)} \right)^{1/2} \right], \quad (\text{A.5})$$

$$\alpha_{g_\pm^\alpha g_0^{\alpha'}} = \pi a_{\text{sum}}^2 \left(\frac{8k_B T}{\pi m_{\text{red}}} \right)^{1/2} \left[1 + \left(\frac{\pi e^2}{2a_{\text{sum}} k_B T} \right)^{1/2} \right] \mathcal{P}_{\alpha\alpha'}, \quad (\text{A.6})$$

where the reduced mass of the two grains (labeled α and α') is defined by

$$m_{\text{red}} = \frac{m_\alpha m_{\alpha'}}{m_\alpha + m_{\alpha'}}, \quad (\text{A.7})$$

and $a_{\text{sum}} = a_\alpha + a_{\alpha'}$ is the sum of the radii of two grains α and α' . The probability of two oppositely charged grains neutralizing each other upon contact is assumed to be unity.

The probability of charge being transferred to a neutral grain g_0^α from a charged grain $g_\pm^{\alpha'}$ is assumed to be proportional to the surface areas of the grains, so that $\mathcal{P}_{\alpha\alpha'} = a_{\alpha'}^2 / (a_\alpha^2 + a_{\alpha'}^2)$.

In other words, of all the collisions between a neutral grain, α , and a charged grain, α' , only a fraction \mathcal{P}_α lead to charge exchange. The complementary probability $\mathcal{P}_{\alpha'}$ leaves the charges unchanged.

Appendix B

Generalized Ohm's Law

B.1 Derivation

We consider equations (2.52) and (2.53), repeated here for convenience, which are to be solved for the species drift velocities \mathbf{w}_s relative to the neutrals:

$$0 = \frac{\omega_s \tau_{sn}}{1 + \varrho_s} \left(\frac{c}{B} \mathbf{E}_n + \mathbf{w}_s \times \mathbf{b} \right) - \mathbf{w}_s + \frac{\varrho_s}{1 + \varrho_s} \mathbf{w}_{g0}, \quad (\text{B.1})$$

$$0 = \mathbf{w}_{g0} - \sum_k \frac{\tau_0}{\tau_{k,\text{inel}}} \mathbf{w}_k. \quad (\text{B.2})$$

We define, for brevity and clarity of presentation, the following quantities

$$\Psi_{1,s} = \frac{\frac{\tau_0}{\tau_{s,\text{inel}}} \frac{\omega_s \tau_{sn}}{1 + \varrho_s}}{1 - \sum_k \frac{\tau_0}{\tau_{k,\text{inel}}} \frac{\varrho_k}{1 + \varrho_k}}, \quad \Psi_1 = \sum_k \Psi_{1,k}; \quad (\text{B.3a})$$

$$\Psi_{2,s} = \frac{\frac{\tau_0}{\tau_{s,\text{inel}}} \frac{\omega_s^2 \tau_{sn}^2}{(1 + \varrho_s)^2}}{1 - \sum_k \frac{\tau_0}{\tau_{k,\text{inel}}} \frac{\varrho_k}{1 + \varrho_k}}, \quad \Psi_2 = \sum_k \Psi_{2,k}; \quad (\text{B.3b})$$

$$\Psi_{3,s} = \frac{\frac{\tau_0}{\tau_{s,\text{inel}}} \frac{\omega_s \tau_{sn}}{1 + \varrho_s} \frac{\varrho_s}{1 + \varrho_s}}{1 - \sum_k \frac{\tau_0}{\tau_{k,\text{inel}}} \frac{\varrho_k}{1 + \varrho_k}}, \quad \Psi_3 = \sum_k \Psi_{3,k}. \quad (\text{B.3c})$$

We recall that the index k runs over all the charged species independently of the index s , which denotes the charged species in question. Note that the denominator in the above

expressions may be written with the help of equation (2.54b) as

$$\frac{\tau_0}{\tau_{\text{gon}}} + \sum_k \frac{\tau_0}{\tau_{k,\text{inel}}} \frac{1}{1 + \varrho_k}, \quad (\text{B.4})$$

which shows its positive definite nature.

We first multiply equation (B.1) by $\tau_0/\tau_{s,\text{inel}}$, sum over s , and use equation (B.2) to find that

$$\mathbf{w}_{\text{g0}} = \Psi_1 \frac{c}{B} \mathbf{E}_n + \sum_k \Psi_{1,k} \mathbf{w}_k \times \mathbf{b}, \quad (\text{B.5})$$

where we have switched the summation index to k to avoid confusion with the species in question, s . Next we take the cross product of equations (B.1) and (B.5) and the unit vector \mathbf{b} :

$$\mathbf{w}_s \times \mathbf{b} = \frac{\omega_s \tau_{sn}}{1 + \varrho_s} \left(\frac{c}{B} \mathbf{E}_n \times \mathbf{b} - \mathbf{w}_{s,\perp} \right) + \frac{\varrho_s}{1 + \varrho_s} \mathbf{w}_{\text{g0}} \times \mathbf{b}, \quad (\text{B.6})$$

$$\mathbf{w}_{\text{g0}} \times \mathbf{b} = \Psi_1 \frac{c}{B} \mathbf{E}_n \times \mathbf{b} - \sum_k \Psi_{1,k} \mathbf{w}_{k,\perp}. \quad (\text{B.7})$$

Equation (B.7) is now substituted into equation (B.6) to obtain

$$\mathbf{w}_s \times \mathbf{b} = \left(\frac{\omega_s \tau_{sn}}{1 + \varrho_s} + \frac{\varrho_s}{1 + \varrho_s} \Psi_1 \right) \frac{c}{B} \mathbf{E}_n \times \mathbf{b} - \left(\frac{\omega_s \tau_{sn}}{1 + \varrho_s} \mathbf{w}_{s,\perp} + \frac{\varrho_s}{1 + \varrho_s} \sum_k \Psi_{1,k} \mathbf{w}_{k,\perp} \right). \quad (\text{B.8})$$

Inserting this expression into equation (B.5), we find that

$$\mathbf{w}_{\text{g0}} = \Psi_1 \frac{c}{B} \mathbf{E}_n + (\Psi_2 + \Psi_3 \Psi_1) \frac{c}{B} \mathbf{E}_n \times \mathbf{b} - \sum_k (\Psi_{2,k} + \Psi_3 \Psi_{1,k}) \mathbf{w}_{k,\perp}, \quad (\text{B.9})$$

which is now ready to be inserted, along with equation (B.8), into equation (B.1):

$$\begin{aligned}
\mathbf{w}_s + \sum_k \left[\frac{\omega_s \tau_{sn}}{1 + \varrho_s} \left(\frac{\omega_k \tau_{kn}}{1 + \varrho_k} \delta_{sk} + \frac{\varrho_s}{1 + \varrho_s} \Psi_{1,k} \right) + \frac{\varrho_s}{1 + \varrho_s} (\Psi_{2,k} + \Psi_3 \Psi_{1,k}) \right] \mathbf{w}_{k,\perp} \\
= \left(\frac{\omega_s \tau_{sn}}{1 + \varrho_s} + \frac{\varrho_s}{1 + \varrho_s} \Psi_1 \right) \frac{c}{B} \mathbf{E}_n \\
+ \left[\frac{\omega_s \tau_{sn}}{1 + \varrho_s} \left(\frac{\omega_s \tau_{sn}}{1 + \varrho_s} + \frac{\varrho_s}{1 + \varrho_s} \Psi_1 \right) + \frac{\varrho_s}{1 + \varrho_s} (\Psi_2 + \Psi_3 \Psi_1) \right] \frac{c}{B} \mathbf{E}_n \times \mathbf{b}. \quad (\text{B.10})
\end{aligned}$$

The symbol δ_{sk} is the Kronecker delta. This is our first main result: it gives the velocity of each charged species in terms of the electric field in the frame of the neutrals. Another way of interpreting this equation is obtained by defining the velocity of the magnetic field lines with respect to the lab frame:

$$\mathbf{v}_f \equiv \frac{c}{B} \mathbf{E} \times \mathbf{b}. \quad (\text{B.11})$$

Then equation (B.10) provides the velocities of all the charged species in terms of the neutral velocity and the field-line velocity. We made use of this concept earlier in Section 2.5.3.

Equation (B.10) can be separated into components parallel and perpendicular to the magnetic field. The parallel component of the current density is easily obtained:

$$\mathbf{j}_{\parallel} = \sum_s n_s q_s \mathbf{w}_{s,\parallel} \quad (\text{B.12a})$$

$$= \sum_s n_s q_s \left(\frac{\omega_s \tau_{sn}}{1 + \varrho_s} + \frac{\varrho_s}{1 + \varrho_s} \Psi_1 \right) \frac{c}{B} \mathbf{E}_{n,\parallel} \quad (\text{B.12b})$$

$$= \sum_s \sigma_s (1 - \varsigma_s) \mathbf{E}_{n,\parallel} \quad (\text{B.12c})$$

$$\equiv \sigma_{\parallel} \mathbf{E}_{n,\parallel}, \quad (\text{B.12d})$$

where we have introduced the conductivity of species s , $\sigma_s = n_s q_s^2 \tau_{sn} / m_s$, and ς_s , given in Appendix D, is the factor by which the conductivity of species s is altered because of inelastic collisions. In the last step above, we have introduced the parallel conductivity, σ_{\parallel} ,

which is defined *in situ*. Note that $\varsigma_s \geq 0$ for all s . In other words, by interfering with the rate at which the charge carriers flow along the magnetic field, inelastic collisions are responsible for decreasing (increasing) the parallel conductivity (resistivity) of the gas.

Finding the perpendicular components of the current density is not as straightforward and amounts to solving a matrix equation. We first define the 4×1 column vectors \mathbf{C}^\perp and \mathbf{C}^H , whose entries are given by

$$(\mathbf{C}^\perp)_s = \omega_s \tau_{\text{sn}} (1 - \varsigma_s) \quad (\text{B.13a})$$

$$(\mathbf{C}^\text{H})_s = -\omega_s^2 \tau_{\text{sn}}^2 (1 - \varpi_s). \quad (\text{B.13b})$$

We also define the 4×4 matrix of coefficients \mathbf{A} whose entries are given by

$$(\mathbf{A})_{sk} = [1 + \omega_s^2 \tau_{\text{sn}}^2 (1 - \varphi_s)] \delta_{sk} + \omega_k^2 \tau_{\text{kn}}^2 \vartheta_{sk} (1 - \delta_{sk}). \quad (\text{B.14})$$

The expressions for ς_s , ϖ_s , φ_s , and ϑ_{sk} are given below in Appendix D. Then the perpendicular component of equation (B.10) takes on the form

$$\mathbf{C}^\perp \frac{c}{B} \mathbf{E}_{\text{n},\perp} - \mathbf{C}^\text{H} \frac{c}{B} \mathbf{E}_{\text{n}} \times \mathbf{b} = \mathbf{A} \mathbf{W}_\perp, \quad (\text{B.15})$$

where \mathbf{W}_\perp is the 4×1 column vector of unknown velocities of charge species relative to neutrals, $[\mathbf{w}_e, \mathbf{w}_i, \mathbf{w}_{g-}, \mathbf{w}_{g+}]^\text{T}$.

We use Cramer's method to solve the matrix equation (B.15). We define

$$D = \det[\mathbf{A}]. \quad (\text{B.16})$$

In addition, we use the notation D_s^\perp to represent the determinant of \mathbf{A} with the s th column of \mathbf{A} having been replaced by \mathbf{C}^\perp . Similarly, D_s^H is the determinant of \mathbf{A} with the s th

column having been replaced by C^H . Then, the solution of the system (B.15) is

$$\mathbf{w}_{s,\perp} = \frac{D_s^\perp}{D} \frac{c}{B} \mathbf{E}_{n,\perp} - \frac{D_s^H}{D} \frac{c}{B} \mathbf{E}_n \times \mathbf{b}. \quad (\text{B.17})$$

Once the determinants have been computed, the current density perpendicular to the magnetic field may be obtained:

$$\mathbf{j}_\perp = \sum_s n_s q_s \mathbf{w}_{s,\perp} \quad (\text{B.18a})$$

$$= \frac{\sum_s n_s q_s D_s^\perp}{D} \frac{c}{B} \mathbf{E}_{n,\perp} - \frac{\sum_s n_s q_s D_s^H}{D} \frac{c}{B} \mathbf{E}_n \times \mathbf{b} \quad (\text{B.18b})$$

$$= \sum_s \frac{\sigma_s (1 - \varsigma_s)}{1 + \omega_s^2 \tau_{sn}^2 (1 - \varphi_s)} \Upsilon_s(\varsigma) \mathbf{E}_{n,\perp} + \sum_s \frac{\sigma_s \omega_s \tau_{sn} (1 - \varpi_s)}{1 + \omega_s^2 \tau_{sn}^2 (1 - \varphi_s)} \Upsilon_s(\varpi) \mathbf{E}_n \times \mathbf{b} \quad (\text{B.18c})$$

$$\equiv \sigma_\perp \mathbf{E}_{n,\perp} - \sigma_H \mathbf{E}_n \times \mathbf{b}. \quad (\text{B.18d})$$

In the last step, we have defined the perpendicular conductivity σ_\perp and the Hall conductivity σ_H , which include the effects of inelastic collisions. The function Υ_s is given in Appendix D.

B.2 Modification due to a Grain Size Distribution

When considering a grain size distribution, rather than single-size grains, two changes must be made to the above derivation. First, the inelastic collision timescales given by equations (2.49) and (2.50) must be modified as follows:

$$\begin{aligned} \tau_{g_+, \text{inel}} \rightarrow \tau_{g_+^\alpha, \text{inel}} = & \left[\frac{1}{\tau_{g_0^\alpha \text{i}, \text{inel}}} + \frac{\rho_{g_+^\alpha}}{\rho_{g_0^\alpha}} \frac{1}{\tau_{g_+^\alpha \text{e}, \text{inel}}} \right. \\ & \left. + \sum_{\alpha'} \left(\frac{1}{\tau_{g_0^\alpha g_+^\alpha, \text{inel}}} + \frac{\rho_{g_+^\alpha}}{\rho_{g_0^\alpha}} \frac{1}{\tau_{g_+^\alpha g_0^{\alpha'}, \text{inel}}} + \frac{\rho_{g_+^\alpha}}{\rho_{g_0^\alpha}} \frac{1}{\tau_{g_+^\alpha g_+^{\alpha'}, \text{inel}}} \right) \right]^{-1}, \quad (\text{B.19a}) \end{aligned}$$

$$\tau_{g-,inel} \rightarrow \tau_{g_-^\alpha,inel} = \left[\frac{1}{\tau_{g_0^\alpha e,inel}} + \frac{\rho_{g_-^\alpha}}{\rho_{g_0^\alpha}} \frac{1}{\tau_{g_-^\alpha i,inel}} + \sum_{\alpha'} \left(\frac{1}{\tau_{g_0^\alpha g_-^{\alpha'},inel}} + \frac{\rho_{g_-^\alpha}}{\rho_{g_0^\alpha}} \frac{1}{\tau_{g_-^\alpha g_0^{\alpha'},inel}} + \frac{\rho_{g_-^\alpha}}{\rho_{g_0^\alpha}} \frac{1}{\tau_{g_-^\alpha g_+^{\alpha'},inel}} \right) \right]^{-1}. \quad (\text{B.19b})$$

The summations over α' (the grain size label) indicate that a grain of size α may give or receive charges not only from other grains of its own size, but also from all other different-size grains. Second, the summation index s in equations (B.12) and (B.18) should range over *all* charged species, including all sizes of charged grains.

Appendix C

Derivation of Species Velocities

En route to the derivation of a generalized Ohm's law, the differential velocity of every species can be obtained in terms of the current density:

$$\begin{aligned}
 n_s q_s \mathbf{w}_s &= \sigma_{\parallel, s} \mathbf{E}_{n, \parallel} + \sigma_{\perp, s} \mathbf{E}_{n, \perp} - \sigma_{H, s} \mathbf{E}_n \times \mathbf{b} \\
 &= \sigma_{\parallel, s} \eta_{\parallel} \mathbf{j}_{\parallel} + \sigma_{\perp, s} (\eta_{\perp} \mathbf{j}_{\perp} + \eta_H \mathbf{j} \times \mathbf{b}) - \sigma_{H, s} (\eta_{\perp} \mathbf{j} \times \mathbf{b} - \eta_H \mathbf{j}_{\perp}) \\
 &= \sigma_{\parallel, s} \eta_{\parallel} \mathbf{j}_{\parallel} + (\sigma_{\perp, s} \eta_{\perp} + \sigma_{H, s} \eta_H) \mathbf{j}_{\perp} + (\sigma_{\perp, s} \eta_H - \sigma_{H, s} \eta_{\perp}) \mathbf{j} \times \mathbf{b}. \quad (\text{C.1})
 \end{aligned}$$

Using equation (B.11), it is straightforward to show that

$$\mathbf{w}_f \equiv \mathbf{v}_f - \mathbf{v}_n = \frac{c \eta_{\perp}}{B} \mathbf{j} \times \mathbf{b} - \frac{c \eta_H}{B} \mathbf{j}_{\perp}. \quad (\text{C.2})$$

We may then write the components of the current density in terms of the differential velocity of the field lines as

$$\frac{c}{B} \mathbf{j} \times \mathbf{b} = \sigma_{\perp} \mathbf{w}_{f, \perp} - \sigma_H \mathbf{w}_f \times \mathbf{b}, \quad (\text{C.3a})$$

$$-\frac{c}{B} \mathbf{j}_{\perp} = \sigma_H \mathbf{w}_{f, \perp} + \sigma_{\perp} \mathbf{w}_f \times \mathbf{b}. \quad (\text{C.3b})$$

Defining the indirect coupling coefficient Θ_s implicitly by

$$\frac{\Theta_s}{\Theta_s + 1} \equiv \left(\frac{B}{c n_s q_s} \right) [\sigma_{\perp} (\sigma_{\perp, s} \eta_H - \sigma_{H, s} \eta_{\perp}) - \sigma_H (\sigma_{\perp, s} \eta_{\perp} + \sigma_{H, s} \eta_H)], \quad (\text{C.4})$$

and introducing

$$\Lambda_s \equiv - \left(\frac{B}{cn_s q_s} \right) \left[\sigma_{\perp} (\sigma_{\perp, s} \eta_{\perp} + \sigma_{H, s} \eta_H) + \sigma_H (\sigma_{\perp, s} \eta_H - \sigma_{H, s} \eta_{\perp}) \right], \quad (\text{C.5})$$

equation (C.1) may now be written in component form as

$$\mathbf{w}_{s, \perp} = \frac{\Theta_s}{\Theta_s + 1} \mathbf{w}_{f, \perp} + \Lambda_s \mathbf{w}_f \times \mathbf{b}, \quad (\text{C.6a})$$

$$\mathbf{w}_s \times \mathbf{b} = \frac{\Theta_s}{\Theta_s + 1} \mathbf{w}_f \times \mathbf{b} - \Lambda_s \mathbf{w}_{f, \perp}, \quad (\text{C.6b})$$

or, more explicitly,

$$\mathbf{v}_{s, \perp} = \mathbf{v}_{n, \perp} \frac{1}{\Theta_s + 1} + \mathbf{v}_{f, \perp} \frac{\Theta_s}{\Theta_s + 1} + (\mathbf{v}_f - \mathbf{v}_n) \times \mathbf{b} \Lambda_s, \quad (\text{C.7a})$$

$$\mathbf{v}_s \times \mathbf{b} = \mathbf{v}_n \times \mathbf{b} \frac{1}{\Theta_s + 1} + \mathbf{v}_f \times \mathbf{b} \frac{\Theta_s}{\Theta_s + 1} - (\mathbf{v}_{f, \perp} - \mathbf{v}_{n, \perp}) \Lambda_s. \quad (\text{C.7b})$$

These equations were discussed in Section 2.5.3.

Appendix D

Definitions

In the main text, as well as in the preceding appendices, we had delayed giving explicit definitions of ς_s , ϖ_s , φ_s , Υ_s , and ϑ_{sk} for all $(s, k) = e, i, g_-,$ and g_+ due to their complexity and length. Here we give explicit expressions for these quantities for all the charged species. Before we proceed, however, a few simplifications are in order. Since both $(\tau_{e,\text{inel}}/\tau_{en})$ and $(\tau_{i,\text{inel}}/\tau_{in}) \gg 1$ for the density regime of interest in this paper, we may neglect the influence of inelastic collisions on the electron and ion fluids. Using the results of Tassis & Mouschovias (2007b), we may also assume that the velocity difference between a given grain and a neutral particle is less than the sound speed of the gas. These are both excellent assumptions and lead to a much more compact form of the following definitions than would otherwise be possible.

The variable ς_s first appeared in the definition of the parallel conductivity (B.12) and again later in the definition of the perpendicular conductivity (B.18). For electrons and ions, $\varsigma_e = \varsigma_i = 0$, because of the negligible influence of inelastic collisions on the electron and ion fluids relative to that of elastic collisions. The expressions for the negative and positive grains are given by

$$\varsigma_{g\pm} = \frac{\varrho_{g\pm}}{1 + \varrho_{g\pm}} \left[\frac{\frac{\tau_0}{\tau_{g_0n}} + \frac{\tau_0}{\tau_{g_{\mp},\text{inel}}} \frac{2}{1 + \varrho_{g_{\mp}}} }{\frac{\tau_0}{\tau_{g_0n}} + \frac{\tau_0}{\tau_{g_+,\text{inel}}} \frac{1}{1 + \varrho_{g_+}} + \frac{\tau_0}{\tau_{g_-,\text{inel}}} \frac{1}{1 + \varrho_{g_-}}} \right], \quad (\text{D.1})$$

and are clearly positive. As mentioned in Section 2.5.2, by interfering with the rate at which the charge carriers flow along the magnetic field, inelastic collisions are responsible

for decreasing (increasing) the parallel conductivity (resistivity) of the gas.

The derivation of the perpendicular conductivity involved many more definitions, all of which are given below. For the same reason stated above for which $\varsigma_e = \varsigma_i = 0$, the expressions for ϖ_s and φ_s vanish when $s = e$ or i . The quantity Υ_s is equal to unity for these species. The nontrivial ϖ_s , φ_s , and Υ_s for $s = g_-, g_+$ are given by

$$\varpi_{g\pm} = \frac{\varsigma_{g\pm}}{1 + \varrho_{g\pm}} + \frac{\varrho_{g\mp}}{1 + \varrho_{g\mp}} \left[\frac{\frac{\tau_0}{\tau_{g_0n}} + \frac{\tau_0}{\tau_{g_+,inel}} \frac{\varsigma_{g_+}}{1 + \varrho_{g_+}} + \frac{\tau_0}{\tau_{g_-,inel}} \frac{\varsigma_{g_-}}{1 + \varrho_{g_-}}}{\frac{\tau_0}{\tau_{g_0n}} + \frac{\tau_0}{\tau_{g_+,inel}} \frac{1}{1 + \varrho_{g_+}} + \frac{\tau_0}{\tau_{g_-,inel}} \frac{1}{1 + \varrho_{g_-}}} \right]; \quad (D.2)$$

$$\begin{aligned} \varphi_{g\pm} = & \frac{\varrho_{g\pm}}{1 + \varrho_{g\pm}} \frac{2 + \varrho_{g\pm}}{1 + \varrho_{g\pm}} \left[\frac{\frac{\tau_0}{\tau_{g_0n}} + \frac{\tau_0}{\tau_{g_+,inel}} \frac{1}{1 + \varrho_{g_+}}}{\frac{\tau_0}{\tau_{g_0n}} + \frac{\tau_0}{\tau_{g_+,inel}} \frac{1}{1 + \varrho_{g_+}} + \frac{\tau_0}{\tau_{g_-,inel}} \frac{1}{1 + \varrho_{g_-}}} \right] \\ & + \frac{\tau_0}{\tau_{g_+,inel}} \frac{\varrho_{g\pm}}{(1 + \varrho_{g\pm})^2} \left[\frac{\frac{\tau_0}{\tau_{g_0n}} \frac{\varrho_{g\pm}}{1 + \varrho_{g\pm}} + \frac{\tau_0}{\tau_{g_+,inel}} \frac{1}{1 + \varrho_{g_+}} \left(\frac{\varrho_{g_+}}{1 + \varrho_{g_+}} + \frac{\varrho_{g_-}}{1 + \varrho_{g_-}} \right)}{\left(\frac{\tau_0}{\tau_{g_0n}} + \frac{\tau_0}{\tau_{g_+,inel}} \frac{1}{1 + \varrho_{g_+}} + \frac{\tau_0}{\tau_{g_-,inel}} \frac{1}{1 + \varrho_{g_-}} \right)^2} \right]; \end{aligned} \quad (D.3)$$

$$\Upsilon_{g\pm}(\varsigma) = \frac{1 + \frac{\omega_{g\mp}^2 \tau_{g\mp n}^2 \vartheta_{g\pm g\mp}}{1 + \omega_{g\mp}^2 \tau_{g\mp n}^2 (1 - \varphi_{g\mp})} \frac{1 - \varsigma_{g\mp}}{1 - \varsigma_{g\pm}}}{1 - \frac{\omega_{g_+}^2 \tau_{g_+ n}^2 \vartheta_{g_- g_+}}{1 + \omega_{g_+}^2 \tau_{g_+ n}^2 (1 - \varphi_{g_+})} \frac{\omega_{g_-}^2 \tau_{g_- n}^2 \vartheta_{g_+ g_-}}{1 + \omega_{g_-}^2 \tau_{g_- n}^2 (1 - \varphi_{g_-})}}; \quad (D.4)$$

$$\Upsilon_{g\pm}(\varpi) = \frac{1 + \frac{\omega_{g\mp}^2 \tau_{g\mp n}^2 \vartheta_{g\pm g\mp}}{1 + \omega_{g\mp}^2 \tau_{g\mp n}^2 (1 - \varphi_{g\mp})} \frac{1 - \varpi_{g\mp}}{1 - \varpi_{g\pm}}}{1 - \frac{\omega_{g_+}^2 \tau_{g_+ n}^2 \vartheta_{g_- g_+}}{1 + \omega_{g_+}^2 \tau_{g_+ n}^2 (1 - \varphi_{g_+})} \frac{\omega_{g_-}^2 \tau_{g_- n}^2 \vartheta_{g_+ g_-}}{1 + \omega_{g_-}^2 \tau_{g_- n}^2 (1 - \varphi_{g_-})}}. \quad (D.5)$$

In equation (B.14), we had introduced ϑ_{sk} as a measure of the inelastic collisional coupling between different pairs of charged species, $s \neq k$. This variable was also used in the definition of Υ_s above. Since the effect of inelastic collisions on the electron and ion fluids is negligible, ϑ_{sk} vanishes for $(s, k) = e$ or i . The only remaining nonzero values of ϑ_{sk}

involve the charged grain species, and are given by

$$\begin{aligned}
 \vartheta_{g_{\pm}g_{\mp}} &= \frac{\varrho_{g_{\pm}}}{1 + \varrho_{g_{\pm}}} \frac{\tau_0}{\tau_{g_{\mp},\text{inel}}} \frac{1}{1 + \varrho_{g_{\mp}}} \\
 &\times \left[\frac{\frac{1}{1 + \varrho_{g_{\mp}}} \left(1 - \frac{\tau_0}{\tau_{g_{\pm},\text{inel}}} \frac{\varrho_{g_{\pm}}}{1 + \varrho_{g_{\pm}}} \right) - \frac{1}{1 + \varrho_{g_{\pm}}} \left(1 - \frac{\tau_0}{\tau_{g_{\mp},\text{inel}}} \frac{\varrho_{g_{\mp}}}{1 + \varrho_{g_{\mp}}} \right)}{\left(\frac{\tau_0}{\tau_{g_0\text{n}}} + \frac{\tau_0}{\tau_{g_+, \text{inel}}} \frac{1}{1 + \varrho_{g_+}} + \frac{\tau_0}{\tau_{g_-, \text{inel}}} \frac{1}{1 + \varrho_{g_-}} \right)^2} \right]. \quad (\text{D.6})
 \end{aligned}$$

References

- Adams, F. C., Lada, C. J., & Shu, F. H. 1987, *ApJ*, 312, 788
- Adams, F. C., & Shu, F. H. 1985, *ApJ*, 296, 655
- . 1986, *ApJ*, 308, 836
- Alves, F. O., Franco, G. A. P., & Girart, J. M. 2008, *A&A*, 486, L13
- Andre, P., Ward-Thompson, D., & Barsony, M. 1993, *ApJ*, 406, 122
- . 2000, *Protostars and Planets IV*, 59
- Appenzeller, I., & Tscharnuter, W. 1975, *A&A*, 40, 397
- Arons, J., & Max, C. E. 1975, *ApJ*, 196, L77+
- Babcock, H. W., & Cowling, T. G. 1953, *MNRAS*, 113, 357
- Bacmann, A., André, P., Puget, J.-L., Abergel, A., Bontemps, S., & Ward-Thompson, D. 2000, *A&A*, 361, 555
- Baker, P. L. 1979, *A&A*, 75, 54
- Balbus, S. A., & Hawley, J. F. 1991, *ApJ*, 376, 214
- Balbus, S. A., & Terquem, C. 2001, *ApJ*, 552, 235
- Basu, S. 1997, *ApJ*, 485, 240
- Basu, S., & Ciolek, G. E. 2004, *ApJ*, 607, L39
- Basu, S., Ciolek, G. E., & Wurster, J. 2009, *New Astronomy*, 14, 221
- Basu, S., & Mouschovias, T. Ch. 1994, *ApJ*, 432, 720
- . 1995a, *ApJ*, 452, 386
- . 1995b, *ApJ*, 453, 271
- Bate, M. R. 1998, *ApJ*, 508, L95
- Baudry, A., Perault, M., de La Noe, J., Despois, D., & Cernicharo, J. 1981, *A&A*, 104, 101

- Bergin, E. A., Plume, R., Williams, J. P., & Myers, P. C. 1999, *ApJ*, 512, 724
- Binney, J., & Tremaine, S. 2008, *Galactic Dynamics: Second Edition*, ed. J. Binney & S. Tremaine (Princeton University Press)
- Black, D. C., & Bodenheimer, P. 1975, *ApJ*, 199, 619
- . 1976, *ApJ*, 206, 138
- Blaes, O. M., & Balbus, S. A. 1994, *ApJ*, 421, 163
- Blandford, R. D., & Payne, D. G. 1982, *MNRAS*, 199, 883
- Bodenheimer, P. 1968, *ApJ*, 153, 483
- Bodenheimer, P., Yorke, H. W., Rozyczka, M., & Tohline, J. E. 1990, *ApJ*, 355, 651
- Bonnor, W. B. 1956, *MNRAS*, 116, 351
- Boss, A. P. 1981, *ApJ*, 250, 636
- . 1984, *ApJ*, 277, 768
- . 1986, *ApJS*, 62, 519
- . 1988, *ApJ*, 331, 370
- . 1993, *ApJ*, 410, 157
- . 1997, *ApJ*, 483, 309
- . 1999, *ApJ*, 520, 744
- . 2002, *ApJ*, 568, 743
- . 2005, *ApJ*, 622, 393
- . 2007, *ApJ*, 658, 1136
- . 2009, *ApJ*, 697, 1940
- Boss, A. P., Ipatov, S. I., Keiser, S. A., Myhill, E. A., & Vanhala, H. A. T. 2008, *ApJ*, 686, L119
- Boss, A. P., & Myhill, E. A. 1995, *ApJ*, 451, 218
- Boss, A. P., & Yorke, H. W. 1990, *ApJ*, 353, 236
- . 1995, *ApJ*, 439, L55
- Caselli, P., Benson, P. J., Myers, P. C., & Tafalla, M. 2002, *ApJ*, 572, 238
- Caselli, P., Walmsley, C. M., Terzieva, R., & Herbst, E. 1998, *ApJ*, 499, 234

- Ceccarelli, C., Hollenbach, D. J., & Tielens, A. G. G. M. 1996, *ApJ*, 471, 400
- Chandrasekhar, S., & Fermi, E. 1953, *ApJ*, 118, 116
- Choi, M., Evans, II, N. J., Gregersen, E. M., & Wang, Y. 1995, *ApJ*, 448, 742
- Ciolek, G. E., & Basu, S. 2001, *ApJ*, 547, 272
- . 2006, *ApJ*, 652, 442
- Ciolek, G. E., & Königl, A. 1998, *ApJ*, 504, 257
- Ciolek, G. E., & Mouschovias, T. Ch. 1993, *ApJ*, 418, 774
- . 1994, *ApJ*, 425, 142
- . 1995, *ApJ*, 454, 194
- . 1996, *ApJ*, 468, 749
- . 1998, *ApJ*, 504, 280
- Clayton, D. D., & Leising, M. D. 1987, *Phys. Rep.*, 144, 1
- Consolmagno, G. J., & Jokipii, J. R. 1978, *Moon and Planets*, 19, 253
- Contopoulos, I., Ciolek, G. E., & Koenigl, A. 1998, *ApJ*, 504, 247
- Cortes, P., & Crutcher, R. M. 2006, *ApJ*, 639, 965
- Cortes, P. C., Crutcher, R. M., & Watson, W. D. 2005, *ApJ*, 628, 780
- Crutcher, R. M. 1999, *ApJ*, 520, 706
- Crutcher, R. M., & Kazès, I. 1983, *A&A*, 125, L23
- Crutcher, R. M., Mouschovias, T. Ch., Troland, T. H., & Ciolek, G. E. 1994, *ApJ*, 427, 839
- Crutcher, R. M., Nutter, D. J., Ward-Thompson, D., & Kirk, J. M. 2004, *ApJ*, 600, 279
- Crutcher, R. M., Roberts, D. A., Mehringer, D. M., & Troland, T. H. 1996, *ApJ*, 462, L79+
- Crutcher, R. M., Roberts, D. A., Troland, T. H., & Goss, W. M. 1999a, *ApJ*, 515, 275
- Crutcher, R. M., Troland, T. H., Goodman, A. A., Heiles, C., Kazès, I., & Myers, P. C. 1993, *ApJ*, 407, 175
- Crutcher, R. M., Troland, T. H., & Kazès, I. 1987, *A&A*, 181, 119
- Crutcher, R. M., Troland, T. H., Lazareff, B., Paubert, G., & Kazès, I. 1999b, *ApJ*, 514, L121
- Desch, S. J., & Mouschovias, T. Ch. 2001, *ApJ*, 550, 314

- Dotson, J. L., Davidson, J. A., Dowell, C. D., Hildebrand, R. H., Kirby, L., & Vaillancourt, J. E. 2008, *ApJS*, submitted
- Draine, B. T., & Sutin, B. 1987, *ApJ*, 320, 803
- Dullemond, C. P., Natta, A., & Testi, L. 2006, *ApJ*, 645, L69
- Ebert, R. 1957, *Zeitschrift fur Astrophysik*, 42, 263
- Elmegreen, B. G. 1979, *ApJ*, 232, 729
- Elmegreen, B. G. 1986, in *Astrophysics and Space Science Library*, Vol. 124, *Light on Dark Matter*, ed. F. P. Israel, 265–276
- Elmegreen, B. G., & Scalo, J. 2004, *ARA&A*, 42, 211
- Eng, C. 2002, PhD thesis, (Illinois Univ., Urbana-Champaign)
- Enoch, M. L., Young, K. E., Glenn, J., Evans, II, N. J., Golwala, S., Sargent, A. I., Harvey, P., Aguirre, J., Goldin, A., Haig, D., Huard, T. L., Lange, A., Laurent, G., Maloney, P., Maukopf, P., Rossinot, P., & Sayers, J. 2006, *ApJ*, 638, 293
- Evans, C. R., & Hawley, J. F. 1988, *ApJ*, 332, 659
- Evans, N. J., Dunham, M. M., Jørgensen, J. K., Enoch, M. L., Merín, B., van Dishoeck, E. F., Alcalá, J. M., Myers, P. C., Stapelfeldt, K. R., Huard, T. L., Allen, L. E., Harvey, P. M., van Kempen, T., Blake, G. A., Koerner, D. W., Mundy, L. G., Padgett, D. L., & Sargent, A. I. 2009, *ApJS*, 181, 321
- Fiedler, R. A., & Mouschovias, T. Ch. 1992, *ApJ*, 391, 199
- . 1993, *ApJ*, 415, 680
- Fleming, T., & Stone, J. M. 2003, *ApJ*, 585, 908
- Foster, P. N., & Chevalier, R. A. 1993, *ApJ*, 416, 303
- Fromang, S., & Nelson, R. P. 2006, *A&A*, 457, 343
- Furlan, E., Hartmann, L., Calvet, N., D'Alessio, P., Franco-Hernández, R., Forrest, W. J., Watson, D. M., Uchida, K. I., Sargent, B., Green, J. D., Keller, L. D., & Herter, T. L. 2006, *ApJS*, 165, 568
- Galli, D. 2005, *MNRAS*, 359, 1083
- Gammie, C. F. 1996, *ApJ*, 457, 355
- Gaustad, J. E. 1963, *ApJ*, 138, 1050
- Girart, J. M., Crutcher, R. M., & Rao, R. 1999, *ApJ*, 525, L109
- Girart, J. M., Rao, R., & Marrone, D. P. 2006, *Science*, 313, 812

- Glassgold, A. E. 1995, *ApJ*, 438, L111
- Glassgold, A. E., & Langer, W. D. 1974, *ApJ*, 193, 73
- Glassgold, A. E., Najita, J., & Igea, J. 1997, *ApJ*, 480, 344
- Goldreich, P., & Kwan, J. 1974, *ApJ*, 189, 441
- Goldreich, P., & Reisenegger, A. 1992, *ApJ*, 395, 250
- Goldsmith, P. F., & Arquilla, R. 1985, in *Protostars and Planets II*, ed. D. C. Black & M. S. Matthews, 137–149
- Goodman, A. A., Benson, P. J., Fuller, G. A., & Myers, P. C. 1993, *ApJ*, 406, 528
- Goodman, A. A., Crutcher, R. M., Heiles, C., Myers, P. C., & Troland, T. H. 1989, *ApJ*, 338, L61
- Goodwin, S. P., Ward-Thompson, D., & Whitworth, A. P. 2002, *MNRAS*, 330, 769
- Gregersen, E. M., Evans, II, N. J., Zhou, S., & Choi, M. 1997, *ApJ*, 484, 256
- Hawley, J. F., & Stone, J. M. 1995, *Computer Physics Communications*, 89, 127
- Hayashi, C. 1966, *ARA&A*, 4, 171
- Hayes, J. C., Norman, M. L., Fiedler, R. A., Bordner, J. O., Li, P. S., Clark, S. E., ud-Doula, A., & Mac Low, M.-M. 2006, *ApJS*, 165, 188
- Heiles, C. 1987, in *NATO ASIC Proc. 210: Physical Processes in Interstellar Clouds*, ed. G. E. Morfill & M. Scholer (Dordrecht: Reidel), 429–452
- Heiles, C., & Crutcher, R. 2005, in *Lecture Notes in Physics*, Berlin Springer Verlag, Vol. 664, *Cosmic Magnetic Fields*, ed. R. Wielebinski & R. Beck (Berlin: Springer)
- Herndon, J. M., & Rowe, M. W. 1974, *Meteoritics*, 9, 289
- Heyer, M., Krawczyk, C., Duval, J., & Jackson, J. M. 2008, *ArXiv e-prints*
- Heyer, M. H., & Brunt, C. M. 2004, *ApJ*, 615, L45
- Heyer, M. H., Vrba, F. J., Snell, R. L., Schloerb, F. P., Strom, S. E., Goldsmith, P. F., & Strom, K. M. 1987, *ApJ*, 321, 855
- Hildebrand, R. H., Dotson, J. L., Dowell, C. D., Schleuning, D. A., & Vaillancourt, J. E. 1999, *ApJ*, 516, 834
- Hollenbach, D. J., Werner, M. W., & Salpeter, E. E. 1971, *ApJ*, 163, 165
- Houde, M., Dowell, C. D., Hildebrand, R. H., Dotson, J. L., Vaillancourt, J. E., Phillips, T. G., Peng, R., & Bastien, P. 2004, *ApJ*, 604, 717

- Hunter, C. 1977, *ApJ*, 218, 834
- Igea, J., & Glassgold, A. E. 1999, *ApJ*, 518, 848
- Jackson, J. D. 1999, *Classical Electrodynamics* (3rd ed.) (New York: John Wiley & Sons, 1999)
- Jeans, J. H. 1902, *Royal Society of London Philosophical Transactions Series A*, 199, 1
- Jijina, J., Myers, P. C., & Adams, F. C. 1999, *ApJS*, 125, 161
- Jin, L. 1996, *ApJ*, 457, 798
- Johnstone, D., Fich, M., Mitchell, G. F., & Moriarty-Schieven, G. 2001, *ApJ*, 559, 307
- Johnstone, D., Matthews, H., & Mitchell, G. F. 2006, *ApJ*, 639, 259
- Johnstone, D., Wilson, C. D., Moriarty-Schieven, G., Joncas, G., Smith, G., Gregersen, E., & Fich, M. 2000, *ApJ*, 545, 327
- Jones, C. E., & Basu, S. 2002, *ApJ*, 569, 280
- Jones, C. E., Basu, S., & Dubinski, J. 2001, *ApJ*, 551, 387
- Kaifu, N., Hasegawa, T., Morimoto, M., Inatani, J., Nagane, K., Miyazawa, K., Chikada, Y., Kanzawa, T., Akabane, K., & Suzuki, S. 1984, *A&A*, 134, 7
- Kazès, I., & Crutcher, R. M. 1986, *A&A*, 164, 328
- Kirby, L. 2009, *ApJ*, 694, 1056
- Kittel, C. 1958, *Elementary Statistical Physics* (New York: John Wiley & Son, 1958)
- Königl, A. 1989, *ApJ*, 342, 208
- Krasnopolsky, R., & Königl, A. 2002, *ApJ*, 580, 987
- Kudoh, T., & Basu, S. 2003, *ApJ*, 595, 842
- . 2006, *ApJ*, 642, 270
- . 2008, *ApJ*, 679, L97
- Kudoh, T., Basu, S., Ogata, Y., & Yabe, T. 2007, *MNRAS*, 380, 499
- Kunz, M. W. 2008, *MNRAS*, 385, 1494
- Kunz, M. W., & Balbus, S. A. 2004, *MNRAS*, 348, 355
- Lada, C. J. 1987, in *IAU Symposium*, Vol. 115, *Star Forming Regions*, ed. M. Peimbert & J. Jugaku, 1–17
- Lada, C. J., & Wilking, B. A. 1984, *ApJ*, 287, 610

- Lada, E. A. 1992, *ApJ*, 393, L25
- Lai, S.-P., Crutcher, R. M., Girart, J. M., & Rao, R. 2001, *ApJ*, 561, 864
- . 2002, *ApJ*, 566, 925
- Lai, S.-P., Girart, J. M., & Crutcher, R. M. 2003, *ApJ*, 598, 392
- Larson, R. B. 1969, *MNRAS*, 145, 271
- . 1972a, *MNRAS*, 156, 437
- . 1972b, *MNRAS*, 157, 121
- . 1981, *MNRAS*, 194, 809
- Lay, O. P., Carlstrom, J. E., Hills, R. E., & Phillips, T. G. 1994, *ApJ*, 434, L75
- Lee, C. W., & Myers, P. C. 1999, *ApJS*, 123, 233
- Lequeux, J. 1975, *A&A*, 39, 257
- Leung, C. M., Kutner, M. L., & Mead, K. N. 1982, *ApJ*, 262, 583
- Levermore, C. D., & Pomraning, G. C. 1981, *ApJ*, 248, 321
- Levy, E. H. 1988, *Energetics of chondrule formation*, ed. J. F. Kerridge & M. S. Matthews, 697–711
- Li, H., Griffin, G. S., Krejny, M., Novak, G., Loewenstein, R. F., Newcomb, M. G., Calisse, P. G., & Chuss, D. T. 2006, *ApJ*, 648, 340
- Li, Z.-Y. 1996, *ApJ*, 465, 855
- Li, Z.-Y., & Nakamura, F. 2004, *ApJ*, 609, L83
- Li, Z.-Y., & Shu, F. H. 1996, *ApJ*, 472, 211
- Liszt, H. S., Wilson, R. W., Penzias, A. A., Jefferts, K. B., Wannier, P. G., & Solomon, P. M. 1974, *ApJ*, 190, 557
- Looney, L. W., Mundy, L. G., & Welch, W. J. 2003, *ApJ*, 592, 255
- Looney, L. W., Tobin, J. J., & Fields, B. D. 2006, *ApJ*, 652, 1755
- Mac Low, M.-M., & Klessen, R. S. 2004, *Reviews of Modern Physics*, 76, 125
- Mac Low, M.-M., Norman, M. L., Königl, A., & Wardle, M. 1995, *ApJ*, 442, 726
- Mac Low, M.-M., Smith, M. D., Klessen, R. S., & Burkert, A. 1998, *Ap&SS*, 261, 195
- Masunaga, H., Miyama, S. M., & Inutsuka, S.-I. 1998, *ApJ*, 495, 346

- Mathis, J. S., Rumpl, W., & Nordsieck, K. H. 1977, *ApJ*, 217, 425
- Matthews, B. C., Lai, S.-P., Crutcher, R. M., & Wilson, C. D. 2005, *ApJ*, 626, 959
- Matthews, B. C., & Wilson, C. D. 2002, *ApJ*, 574, 822
- McCabe, C., Duchêne, G., & Ghez, A. M. 2003, *ApJ*, 588, L113
- McDaniel, E. W., & Mason, E. A. 1973, *The Mobility and Diffusion of Ions and Gases* (New York: Wiley, 1973)
- McKee, C. F., Zweibel, E. G., Goodman, A. A., & Heiles, C. 1993, in *Protostars and Planets III*, ed. E. H. Levy & J. I. Lunine, 327–+
- Mellon, R. R., & Li, Z.-Y. 2009, *ApJ*, 698, 922
- Mestel, L. 1965, *QJRAS*, 6, 265
- . 1966, *MNRAS*, 133, 265
- Mestel, L., & Spitzer, Jr., L. 1956, *MNRAS*, 116, 503
- Mihalas, D., & Weibel Mihalas, B. 1984, *Foundations of radiation hydrodynamics* (New York: Oxford University Press, 1984)
- Morris, M., Zuckerman, B., Turner, B. E., & Palmer, P. 1974, *ApJ*, 192, L27+
- Morton, D. C. 1974, *ApJ*, 193, L35
- Mott, N. F., & Massey, H. S. W. 1971, *The Theory of Atomic Collisions* (3rd ed.) (Oxford: Oxford Univ. Press, 1971)
- Motte, F., Andre, P., & Neri, R. 1998, *A&A*, 336, 150
- Motte, F., André, P., Ward-Thompson, D., & Bontemps, S. 2001, *A&A*, 372, L41
- Mouschovias, T. Ch. 1975, PhD thesis, (California Univ., Berkeley.)
- . 1976a, *ApJ*, 206, 753
- . 1976b, *ApJ*, 207, 141
- . 1977, *ApJ*, 211, 147
- . 1978, Formation of stars and planetary systems in magnetic interstellar clouds (*Protostars and Planets: Studies of Star Formation and of the Origin of the Solar System*), 209–242
- . 1979, *ApJ*, 228, 475
- Mouschovias, T. Ch. 1983, in *IAU Symposium, Vol. 102, Solar and Stellar Magnetic Fields: Origins and Coronal Effects*, ed. J. O. Stenflo, 479–484

- Mouschovias, T. Ch. 1987, in NATO ASIC Proc. 210: Physical Processes in Interstellar Clouds, ed. G. E. Morfill & M. Scholer, 453–489
- . 1991a, *ApJ*, 373, 169
- Mouschovias, T. Ch. 1991b, in NATO ASIC Proc. 342: The Physics of Star Formation and Early Stellar Evolution, ed. C. J. Lada & N. D. Kylafis, 449–+
- Mouschovias, T. Ch. 1996, in *Solar and Astrophysical Magnetohydrodynamic Flows*, 505–538
- Mouschovias, T. Ch., & Morton, S. A. 1991, *ApJ*, 371, 296
- . 1992a, *ApJ*, 390, 144
- . 1992b, *ApJ*, 390, 166
- Mouschovias, T. Ch., & Paleologou, E. V. 1979, *ApJ*, 230, 204
- . 1980, *ApJ*, 237, 877
- Mouschovias, T. Ch., Paleologou, E. V., & Fiedler, R. A. 1985, *ApJ*, 291, 772
- Mouschovias, T. Ch., & Psaltis, D. 1995, *ApJ*, 444, L105
- Mouschovias, T. Ch., & Spitzer, Jr., L. 1976, *ApJ*, 210, 326
- Mouschovias, T. Ch., Tassis, K., & Kunz, M. W. 2006, *ApJ*, 646, 1043
- Myers, P. C. 1983, *ApJ*, 270, 105
- Myers, P. C. 1985, in *Protostars and Planets II*, ed. D. C. Black & M. S. Matthews, 81–103
- Myers, P. C., & Benson, P. J. 1983, *ApJ*, 266, 309
- Myers, P. C., Fuller, G. A., Goodman, A. A., & Benson, P. J. 1991, *ApJ*, 376, 561
- Myers, P. C., & Gammie, C. F. 1999, *ApJ*, 522, L141
- Myers, P. C., & Goodman, A. A. 1988, *ApJ*, 326, L27
- Myers, P. C., Linke, R. A., & Benson, P. J. 1983, *ApJ*, 264, 517
- Nakamura, F., & Li, Z.-Y. 2008, *ApJ*, 687, 354
- Nakano, T. 1979, *PASJ*, 31, 697
- . 1998, *ApJ*, 494, 587
- Nakano, T., & Umebayashi, T. 1980, *PASJ*, 32, 613
- . 1986a, *MNRAS*, 218, 663

- . 1986b, *MNRAS*, 221, 319
- Natta, A., Testi, L., & Randich, S. 2006, *A&A*, 452, 245
- Nishi, R., Nakano, T., & Umebayashi, T. 1991, *ApJ*, 368, 181
- Novak, G., Dotson, J. L., Dowell, C. D., Goldsmith, P. F., Hildebrand, R. H., Platt, S. R., & Schleuning, D. A. 1997, *ApJ*, 487, 320
- Novak, G., Gonatas, D. P., Hildebrand, R. H., Platt, S. R., & Dragovan, M. 1989, *ApJ*, 345, 802
- Nutter, D., & Ward-Thompson, D. 2007, *MNRAS*, 374, 1413
- Onishi, T., Mizuno, A., & Fukui, Y. 1999, *PASJ*, 51, 257
- Ostriker, E. C., Gammie, C. F., & Stone, J. M. 1999, *ApJ*, 513, 259
- Ostriker, E. C., Stone, J. M., & Gammie, C. F. 2001, *ApJ*, 546, 980
- Ouellette, N., Desch, S. J., & Hester, J. J. 2007, *ApJ*, 662, 1268
- Padoan, P., & Nordlund, Å. 1999, *ApJ*, 526, 279
- Paleologou, E. V., & Mouschovias, T. Ch. 1983, *ApJ*, 275, 838
- Parks, G. K. 1991, *Physics of Space Plasmas* (Redwood City Addison-Wesley, 1991. 283 p.)
- Penston, M. V. 1969, *MNRAS*, 144, 425
- Pinte, C., Padgett, D. L., Ménard, F., Stapelfeldt, K. R., Schneider, G., Olofsson, J., Panić, O., Augereau, J. C., Duchêne, G., Krist, J., Pontoppidan, K., Perrin, M. D., Grady, C. A., Kessler-Silacci, J., van Dishoeck, E. F., Lommen, D., Silverstone, M., Hines, D. C., Wolf, S., Blake, G. A., Henning, T., & Stecklum, B. 2008, *A&A*, 489, 633
- Pneuman, G. W., & Mitchell, T. P. 1965, *Icarus*, 4, 494
- Pollack, J. B., Hollenbach, D., Beckwith, S., Simonelli, D. P., Roush, T., & Fong, W. 1994, *ApJ*, 421, 615
- Preibisch, T., Sonnhalter, C., & Yorke, H. W. 1995, *A&A*, 299, 144
- Ryden, B. S. 1996, *ApJ*, 471, 822
- Saito, M., Kawabe, R., Ishiguro, M., Miyama, S. M., Hayashi, M., Handa, T., Kitamura, Y., & Omodaka, T. 1995, *ApJ*, 453, 384
- Salmeron, R., Königl, A., & Wardle, M. 2007, *Ap&SS*, 311, 81
- Salmeron, R., & Wardle, M. 2005, *MNRAS*, 361, 45

- Sano, T., & Miyama, S. M. 1999, *ApJ*, 515, 776
- Sano, T., Miyama, S. M., Umebayashi, T., & Nakano, T. 2000, *ApJ*, 543, 486
- Sargent, A. I., Beckwith, S., Keene, J., & Masson, C. 1988, *ApJ*, 333, 936
- Schleuning, D. A. 1998, *ApJ*, 493, 811
- Schleuning, D. A., Vaillancourt, J. E., Hildebrand, R. H., Dowell, C. D., Novak, G., Dotson, J. L., & Davidson, J. A. 2000, *ApJ*, 535, 913
- Scott, E. H., & Black, D. C. 1980, *ApJ*, 239, 166
- Scoville, N. Z., & Solomon, P. M. 1974, *ApJ*, 187, L67+
- Shu, F., Najita, J., Ostriker, E., Wilkin, F., Ruden, S., & Lizano, S. 1994, *ApJ*, 429, 781
- Shu, F. H. 1973, in *IAU Symposium, Vol. 52, Interstellar Dust and Related Topics*, ed. J. M. Greenberg & H. C. van de Hulst, 257–+
- Shu, F. H. 1977, *ApJ*, 214, 488
- Shu, F. H., Adams, F. C., & Lizano, S. 1987, *ARA&A*, 25, 23
- Simpson, R. J., Nutter, D., & Ward-Thompson, D. 2008, *MNRAS*, 391, 205
- Snow, Jr., T. P. 1976, *ApJ*, 204, 759
- Solomon, P. M., Rivolo, A. R., Barrett, J., & Yahil, A. 1987, *ApJ*, 319, 730
- Spitzer, Jr., L. 1941, *ApJ*, 93, 369
- . 1948, *ApJ*, 107, 6
- . 1968, *Diffuse matter in space* (New York: Interscience Publication, 1968)
- . 1978, *Physical processes in the interstellar medium* (New York Wiley-Interscience, 1978. 333 p.)
- Stacey, F. D., Lovering, J. F., & Parry, L. G. 1961, *J. Geophys. Res.*, 66, 1523
- Stanke, T., Smith, M. D., Gredel, R., & Khanzadyan, T. 2006, *A&A*, 447, 609
- Stone, J. M., Mihalas, D., & Norman, M. L. 1992, *ApJS*, 80, 819
- Stone, J. M., & Norman, M. L. 1992a, *ApJS*, 80, 753
- . 1992b, *ApJS*, 80, 791
- Stone, J. M., Ostriker, E. C., & Gammie, C. F. 1998, *ApJ*, 508, L99
- Strittmatter, P. A. 1966a, *MNRAS*, 131, 491

- . 1966b, *MNRAS*, 132, 359
- Tafalla, M., Mardones, D., Myers, P. C., Caselli, P., Bachiller, R., & Benson, P. J. 1998, *ApJ*, 504, 900
- Tang, Y.-W., Ho, P. T. P., Koch, P. M., Girart, J. M., Lai, S.-P., & Rao, R. 2009, *ArXiv e-prints*
- Tassis, K. 2007, *MNRAS*, 379, L50
- Tassis, K., & Mouschovias, T. Ch. 2004, *ApJ*, 616, 283
- . 2005a, *ApJ*, 618, 769
- . 2005b, *ApJ*, 618, 783
- . 2007a, *ApJ*, 660, 370
- . 2007b, *ApJ*, 660, 388
- . 2007c, *ApJ*, 660, 402
- Testi, L., & Sargent, A. I. 1998, *ApJ*, 508, L91
- Troland, T. H., Crutcher, R. M., Goodman, A. A., Heiles, C., Kazès, I., & Myers, P. C. 1996, *ApJ*, 471, 302
- Troland, T. H., Crutcher, R. M., & Kazès, I. 1986, *ApJ*, 304, L57
- Tscharnuter, W. 1975, *A&A*, 39, 207
- Tscharnuter, W. M. 1978, *Moon and Planets*, 19, 229
- Tscharnuter, W. M., & Winkler, K.-H. A. 1979, *Computer Physics Communications*, 18, 171
- Turner, N. J., Sano, T., & Dziourkevitch, N. 2007, *ApJ*, 659, 729
- Turner, N. J., & Stone, J. M. 2001, *ApJS*, 135, 95
- Umeyayashi, T. 1983, *Progress of Theoretical Physics*, 69, 480
- Umeyayashi, T., & Nakano, T. 1980, *PASJ*, 32, 405
- . 1990, *MNRAS*, 243, 103
- Vaillancourt, J. E., Dowell, C. D., Hildebrand, R. H., Kirby, L., Krejny, M. M., Li, H.-b., Novak, G., Houde, M., Shinnaga, H., & Attard, M. 2008, *ApJ*, 679, L25
- van Rensbergen, W., Hensberge, H., & Adelman, S. J. 1984, *A&A*, 136, 31
- Vorobyov, E. I., & Basu, S. 2007, *MNRAS*, 381, 1009

- . 2008, *ApJ*, 676, L139
- Vrba, F. J., Coyne, G. V., & Tapia, S. 1981, *ApJ*, 243, 489
- Ward-Thompson, D., André, P., Crutcher, R., Johnstone, D., Onishi, T., & Wilson, C. 2007, in *Protostars and Planets V*, ed. B. Reipurth, D. Jewitt, & K. Keil, 33–46
- Wardle, M. 1999, *MNRAS*, 307, 849
- . 2007, *Ap&SS*, 311, 35
- Wardle, M., & Königl, A. 1993, *ApJ*, 410, 218
- Watson, W. D. 1976, *Reviews of Modern Physics*, 48, 513
- Whitehouse, S. C., & Bate, M. R. 2006, *MNRAS*, 367, 32
- Williams, J. P., Bergin, E. A., Caselli, P., Myers, P. C., & Plume, R. 1998, *ApJ*, 503, 689
- Williams, J. P., & Gaidos, E. 2007, *ApJ*, 663, L33
- Winkler, K.-H. A., & Newman, M. J. 1980a, *ApJ*, 236, 201
- . 1980b, *ApJ*, 238, 311
- Yorke, H. W. 1977, *A&A*, 58, 423
- . 1979, *A&A*, 80, 308
- . 1980, *A&A*, 85, 215
- Yorke, H. W., Bodenheimer, P., & Laughlin, G. 1993, *ApJ*, 411, 274
- . 1995, *ApJ*, 443, 199
- Yorke, H. W., & Kruegel, E. 1977, *A&A*, 54, 183
- Yorke, H. W., & Shustov, B. M. 1981, *A&A*, 98, 125
- Yorke, H. W., & Sonnhalter, C. 2002, *ApJ*, 569, 846
- Zhou, S., Evans, II, N. J., Butner, H. M., Kutner, M. L., Leung, C. M., & Mundy, L. G. 1990, *ApJ*, 363, 168
- Zhou, S., Evans, II, N. J., Koempe, C., & Walmsley, C. M. 1993, *ApJ*, 404, 232
- . 1994, *ApJ*, 421, 854
- Zhou, S., Evans, II, N. J., & Wang, Y. 1996, *ApJ*, 466, 296
- Zuckerman, B., & Evans, II, N. J. 1974, *ApJ*, 192, L149
- Zuckerman, B., & Palmer, P. 1974, *ARA&A*, 12, 279
- Zweibel, E. G., & Josafatsson, K. 1983, *ApJ*, 270, 511

Vita

EDUCATION

- 2003 – 2009 **University of Illinois at Urbana-Champaign (UIUC)**
- Ph.D. in Physics candidate, thesis advisor: T. Ch. Mouschovias
 - M.S. in Physics (2004)
- 1999 – 2003 **University of Virginia (UVA)**
- B.A. in Astronomy-Physics with High Distinction
 - B.A. in Music
 - Minor in Mathematics

HONORS AND AWARDS

- 2003 – 2009 UIUC Excellent Teachers List (10/10 eligible semesters)
- 2005 – 2008 UIUC Outstanding Teachers List (4/10 eligible semesters)
- 2003 – 2004 Graduate Assistance in Areas of National Need Fellowship
- 2002 – 2003 UVA Lawn Resident (one of the top honors awarded by UVA)
- 2001 – 2002 David A. Harrison III Undergraduate Research Fellowship
- 2000 – 2003 UVA Echols Honors Program

SERVICE

- 2008 – Referee for ApJS
- 2007 – Referee for Ap&SS, MNRAS

RESEARCH EXPERIENCE

- 5/2004 – 8/2009 **Research Assistant** (Department of Physics, UIUC)
- Molecular cloud and star formation theory
 - Advisor: Telemachos Mouschovias
- 8/2002 – 8/2003 **Research Assistant** (Department of Astronomy, UVA)
- Magnetorotational instability in weakly-ionized accretion disks
 - Advisor: Steve Balbus
- 5/2002 – 8/2002 **Research Assistant** (Department of Astronomy, UVA)
- Radiative processes in MHD accretion disks
 - Advisor: Steve Balbus
- 5/2001 – 12/2001 **REU Student** (National Radio Astronomy Observatory, Socorro)
- High-mass star formation observation using the VLBA
 - Advisors: Claire Chandler and Lincoln Greenhill

TEACHING EXPERIENCE

Fall 2007 – Spr 2009	Teaching Assistant (Department of Physics, UIUC) • PHYS 505: Graduate Classical Electromagnetism
Fall 2006	Teaching Assistant (Department of Physics, UIUC) • PHYS 101: General Physics I (lab)
Spr 2006, Spr 2007	Head Teaching Assistant (Department of Physics, UIUC) • PHYS 102: General Physics II (discussion)
Fall 2005	Teaching Assistant (Department of Physics, UIUC) • PHYS 102: General Physics II (discussion)
Sum 2005, Fall 2008	Teaching Assistant (Department of Physics, UIUC) • PHYS 102: General Physics II (lab)
Fall 2004	Teaching Assistant (Department of Physics, UIUC) • PHYS 598AST: Graduate Astrophysics
Fall 2003, Spr 2005	Teaching Assistant (Department of Physics, UIUC) • PHYS 211: Mechanics (discussion)

PUBLICATIONS

1. **Kunz, M. W.**, & Mouschovias, T. Ch. 2009, in preparation:
The Nonisothermal Stage of Magnetic Star Formation. II. Results
2. Matthews, L. D., Greenhill, L. J. Goddi, C., Chandler, C. J., Humphreys, E. M. L., & **Kunz, M. W.** 2009, ApJ, in press:
A Feature Movie of SiO Emission 20-100 AU from the Massive Young Stellar Object Orion Source I
3. **Kunz, M. W.**, & Mouschovias, T. Ch. 2009, MNRAS-L, in press:
Ambipolar Diffusion and the Initial Core Mass Function in Molecular Clouds
4. Mouschovias, T. Ch., **Kunz, M. W.**, & Christie, D. A. 2009, MNRAS, 397, 14:
Formation of Interstellar Clouds: Parker Instability with Phase Transitions
5. **Kunz, M. W.**, & Mouschovias, T. Ch. 2009, ApJ:
The Nonisothermal Stage of Magnetic Star Formation. I. Formulation of the Problem and Method of Solution
6. **Kunz, M. W.** 2008, MNRAS, 385, 1494:
On the Linear Stability of Weakly Ionized, Magnetized Planar Shear Flows
7. Mouschovias, T. Ch., Tassis, K., & **Kunz, M. W.** 2006, ApJ, 646, 1043:
Observational Constraints on the Ages of Molecular Clouds and the Star-Formation Timescale: Ambipolar-Diffusion-Controlled or Turbulence-Induced Star Formation?
8. **Kunz, M. W.**, & Balbus S. A. 2004, MNRAS, 348, 355:
Ambipolar Diffusion in the Magnetorotational Instability